Lehrstuhl für Elektrische Energiespeichertechnik
Fakultät für Elektrotechnik und Informationstechnik
Technische Universität München

Linear and Nonlinear Aging of Lithium-Ion Cells

Dipl.-Ing. Univ. Jonas Peter Lothar Keil

Vollständiger Abdruck der von der Fakultät für Elektrotechnik und Informationstechnik der
Technischen Universität München zur Erlangung des akademischen Grades eines

Doktor-Ingenieur (Dr.-Ing.)

genehmigten Dissertation.

Vorsitzende: Prof. Dr. sc. Myriam Koch
Prüfer der Dissertation: 1. Prof. Dr.-Ing. Andreas Jossen
2. Prof. Dr. rer. nat. Jürgen Garche

Die Dissertation wurde am 15.06.2021 bei der Technischen Universität München eingereicht und durch
die Fakultät für Elektrotechnik und Informationstechnik am 02.09.2021 angenommen.

Abstract

The aging behavior of lithium-ion cells significantly defines their economic and sustainable usage. In particular, the transition from an early stage, linear to a later stage, nonlinear aging behavior is an ongoing research topic for designing and operating lithium-ion cells. The presented thesis investigates the linear and nonlinear aging based on laboratory experiments of industrially manufactured 18650-type lithium-ion cells composed of graphite as the negative electrode and lithium-nickel-cobalt-manganese-oxide as the positive electrode. The aging experiments reveal the impact of different operating strategies with varying charging currents, discharging currents and resting times. By means of electrochemical analysis and in-situ neutron diffraction, the underlying aging mechanisms are determined and the crystalline phases and lattice parameters of the negative and positive electrodes' active materials are characterized. For both linearly- and nonlinearly-aged cells, the loss of lithium inventory is the dominant degradation mode while the capacity loss in the edge area of the electrodes increases with ongoing aging. To describe the aging behavior, a physicochemical model is developed considering the dominant side reactions of solid electrolyte interphase (SEI) formation, SEI re-formation, lithium plating and lithium stripping. While SEI re-/formation defines linear aging, the onset and slope of nonlinear aging is simulated based on the ratio of reversibly and irreversibly plated lithium.

Kurzfassung

Das Alterungsverhalten von Lithium-Ionen-Zellen bestimmt maßgeblich deren wirtschaftlichen und nachhaltigen Einsatz. Vor allem der Übergang von einem anfangs linearen zu einem späteren nichtlinearen Alterungsverhalten ist im Fokus der aktuellen Forschung bei der Auslegung und dem Betrieb von Lithium-Ionen-Zellen. Die vorliegende Arbeit untersucht die lineare und nichtlineare Alterung anhand von Laborexperimenten von industriell gefertigten Lithium-Ionen-Zellen der Bauform 18650 mit Graphit als negative Elektrode und Lithium-Nickel-Kobalt-Mangan-Oxid als positive Elektrode. Die Alterungsexperimente zeigen den Einfluss unterschiedlicher Betriebsstrategien mit verschiedenen Ladeströmen, Entladeströmen und Ruhezeiten. Mit Hilfe elektrochemischer Analyse und in-situ Neutronendiffraktometrie werden die zugrunde liegenden Alterungsmechanismen bestimmt und die kristallinen Phasen und Kristallgitter der Aktivmaterialien der negativen und positiven Elektrode charakterisiert. Für sowohl linear als auch nichtlinear gealterte Zellen ist der Verlust des zyklisierbaren Lithiums die Hauptalterungsform, während der Kapazitätsverlust in den Randbereichen der Elektroden mit fortschreitender Alterung zunimmt. Um das Alterungsverhalten abzubilden, wurde ein physikalisch-chemisches Modell entwickelt, das die vorherrschenden Nebenreaktionen wie die Bildung der Solid Electrolyte Interphase (SEI), die SEI-Neubildung sowie die Abscheidung und die Auflösung von Lithium berücksichtigt. Während die SEI-Neu-/Bildung das lineare Alterungsverhalten bestimmt, wird das Einsetzen und der Verlauf der nichtlinearen Alterung durch das Verhältnis von reversibel und irreversibel abgeschiedenem Lithium beschrieben.

Vorwort und Danksagung

List of Contents

List of Abbreviations

$(LiOCO_2CH_2)_2$. lithium ethylene dicarbonate

Li_2CO_3 . . . . . . lithium carbonate

Li_2O . . . . lithium oxide

LiF . . . . lithium fluoride

$LiOCO_2CH_3$ . . . lithium methyl carbonate

BOL . . . . begin of life

CC . . . . constant current

CCCV . . . . . . constant current constant voltage

CEI . . . . cathode electrolyte interphase

CV . . . . constant voltage

DVA . . . . differential voltage analysis

ECM . . . . equivalent circuit model

EFC . . . . equivalent full cycle

EIS . . . . electrochemical impedance spectroscopy

EOL . . . . end of life

GEIS . . . . galvanostatic electrochemical impedance spectroscopy

ICA . . . . incremental capacity analysis

LAM . . . . loss of active material

LCO . . . . lithium cobalt oxide

LFP . . . . lithium iron phosphate

LLI . . . . loss of lithium-ion inventory

LMO . . . . lithium manganese oxide

ND . . . . neutron diffraction

NMC . . . . lithium nickel manganese cobalt oxide

NMR . . . . nuclear magnetic resonance

P2D . . . . pseudo two-dimensional

PEIS . . . . potentiostatic electrochemical impedance spectroscopy

RUL . . . . remaining useful life

SEI . . . . solid electrolyte interphase

SEM . . . . scanning electron microscopy

SOC . . . . state of charge

SOH . . . . state of health

SPM . . . . single particle model

SPODI . . . . . . structure powder diffractometer

XRD . . . . X-ray diffraction

List of Formula Symbols

a . . . . specific surface in m^{-1}

A_{cell} . . . . cell surface area in m^2

α_a . . . . anodic charge-transfer coefficient

α_c . . . . cathodic charge-transfer coefficient

c_l . . . . lithium-ion concentration in the electrolyte in $\text{mol}\,\text{m}^{-3}$

c_p . . . . specific heat capacity in $\text{J}\,\text{kg}^{-1}\,\text{K}^{-1}$

c_s . . . . lithium-ion concentration in the active material in $\text{mol}\,\text{m}^{-3}$

$c_{s,\text{max}}$ . . . . . . maximum lithium-ion concentration in the active material in $\text{mol}\,\text{m}^{-3}$

D_l . . . . diffusion coefficient in the electrolyte in $\text{m}^2\,\text{s}^{-1}$

D_s . . . . diffusion coefficient in the active material in $\text{m}^2\,\text{s}^{-1}$

E_a . . . . activation energy in $\text{J}\,\text{mol}^{-1}$

E_{Eq} . . . . thermodynamic equilibrium potential in V

ε_{th} . . . . surface emissivity

ε_l . . . . electrolyte volume fraction

ε_s . . . . active material volume fraction

ε_{na} . . . . volume fraction of non-active material

η . . . . overpotential in V

F . . . . Faraday's constant, $96\,485\,\text{C}\,\text{mol}^{-1}$

$f_\pm$ . . . . mean activity coefficient

h . . . . heat transfer coefficient in $\text{W}\,\text{m}^{-2}\,\text{K}^{-1}$

i . . . . charge-transfer current density in $\text{A}\,\text{m}^{-2}$

i_0 . . . . exchange current density in $\text{A}\,\text{m}^{-2}$

i_l . . . . current density in the electrolyte in $\text{A}\,\text{m}^{-2}$

i_s . . . . current density in the active material in $\text{A}\,\text{m}^{-2}$

i_{tot} . . . . total current density in $\text{A}\,\text{m}^{-2}$

j . . . . pore-wall flux in $\text{mol}\,\text{m}^{-2}\,\text{s}$

k_a . . . . anodic reaction rate constant in $\text{m}\,\text{s}^{-1}$

k_c . . . . cathodic reaction rate constant in $\text{m}\,\text{s}^{-1}$

κ . . . . conductivity in the electrolyte in $\mathrm{S\,m^{-1}}$

l_{cell} . . . . cell layer thickness in m

l_{neg} . . . . thickness of the negative electrode domain in m

l_{pos} . . . . thickness of the positive electrode domain in m

l_{sep} . . . . thickness of the separator domain in m

m_{cell} . . . . cell mass in kg

n . . . . number of electrons

N_l . . . . ionic flux in the electrolyte in $\mathrm{mol\,m^{-2}\,s}$

N_s . . . . ionic flux in the active material in $\mathrm{mol\,m^{-2}\,s}$

N_M . . . . MacMullin's number

$\nu_{\mathrm{Li\Theta}_s}$ . . . . stoichiometric coefficient $\mathrm{Li\Theta_s}$

$\nu_{\mathrm{Li^+}}$ . . . . stoichiometric coefficient $\mathrm{Li^+}$

Φ_l . . . . electrolyte potential in V

Φ_s . . . . electrode potential in the active material in V

$\dot{q}$ . . . . total heat power density in $\mathrm{W\,m^{-3}}$

$\dot{Q}_{conv}$ . . . . . . convected heat power in W

$\dot{q}_{ohm}$ . . . . ohmic heat power density in $\mathrm{W\,m^{-3}}$

$\dot{Q}_{rad}$ . . . . radiated heat power in W

$\dot{q}_{reac}$ . . . . reaction heat power density in $\mathrm{W\,m^{-3}}$

$\dot{q}_{rev}$ . . . . reversible heat power density in $\mathrm{W\,m^{-3}}$

$\dot{Q}_{th}$ . . . . cell thermal mass in W

R . . . . unviersal gas constant, $8.314\,\mathrm{J\,mol^{-1}\,K}$

R_l . . . . reaction term in $\mathrm{mol\,m^{-3}\,s^{-1}}$

r_p . . . . particle radius in m

σ . . . . conductivity in the active material $\mathrm{S\,m^{-1}}$

σ_B . . . . Stefan-Boltzmann constant, $5.67 \times 10^{-8}\,\mathrm{W\,m^{-2}\,K^{-4}}$

T . . . . absolute temperature in K

t_+ . . . . transport number of cations

T_∞ . . . . ambient temperature in K

v . . . . velocity in $\mathrm{m\,s^{-1}}$

V_{cell} . . . . . . cell volume in $\mathrm{m^3}$

1 Introduction, Objectives and Thesis Outline

Lithium-ion batteries are nowadays the most important battery energy storage technology. They are widely used both in mobile and stationary applications, such as consumer electronics, electric vehicles, and grid operations. The economic and sustainable usage of lithium-ion batteries is mainly defined by their aging behavior. Therefore, the determination, estimation and prediction of a battery's state of health (SOH), remaining useful life (RUL) and end of life (EOL) are current challenges.

In general, aging of lithium-ion batteries means the loss of capacity and the increase of impedance that results in a decrease in energy density and power capability [1–4]. The aging characteristic of lithium-ion batteries depends on the cell chemistry, their design and format, the operation mode which results in various stress conditions, the external thermal and mechanical boundary conditions and the underlying degradation mechanisms. Depending on these influencing variables, lithium-ion batteries can last up to several thousands of (partial) cycles as well up to some years [5–7]. The aging behavior can either be decelerated or accelerated as well as almost linear or nonlinear. Especially the transition from linear to nonlinear aging decides on first life and possible second life applications as well as the recycling of lithium-ion cells [8–13].

The aging of lithium-ion cells has been a major field of research for years. Studies cover a wide range of methods such as aging experiments, characterization measurements and modeling. The aim of this thesis is to investigate the linear and nonlinear aging behavior of lithium-ion cells. This also includes the transition from an early stage, linear to a later stage, nonlinear aging behavior.

Objectives

For the experimental and simulative investigation of the linear and nonlinear aging of lithium-ion cells, the following objectives and tasks have been set for this thesis:

1. Perform aging experiments on commercially produced lithium-ion cells under varying testing procedures considering linear and nonlinear aging

2. Experimentally investigate the underlying aging mechanisms of linearly and nonlinearly aged lithium-ion cells

3. Develop physicochemical side reaction models for solid electrolyte interphase (SEI) re-/formation, lithium plating and lithium stripping

4. Develop a physicochemical aging model considering the transition from linear to nonlinear aging

Thesis outline

The thesis is structured as depicted in Figure 1.1.

Chapter 2 introduces the fundamentals of lithium-ion cell aging, the underlying aging mechanisms and degradation modes, an overview of the methods for aging mechanism characterization, the definition of linear and nonlinear aging and finally the modeling of lithium-ion cell aging.

The applied methodology is presented in Chapter 3 and comprises the investigated lithium-ion cells, electrochemical analysis and neutron diffraction to experimentally characterize aging mechanisms as well as physicochemical modeling to simulate side reactions and their interaction – all applied to linear and nonlinear aging.

In Chapter 4, the aging mechanisms of linearly aged cells are experimentally revealed with electrochemical analysis and neutron diffraction. A physicochemical aging model considering SEI formation and re-formation is developed and correlated with the experimental results. The chapter references the scientific paper *Aging in 18650-type Li-ion cells examined with in-situ neutron diffraction, electrochemical analysis and physico-chemical modeling* [14].

An advanced physicochemical aging model considering SEI formation and re-formation and distinguishing between an electronic and an ionic conductivity of the SEI is shown in Chapter 5. This approach introduces the possibility to adapt the model to capacity as well as power fade. The scientific paper *A SEI Modeling Approach Distinguishing between Capacity and Power Fade* [15] is the reference of this chapter.

Chapter 6 references the scientific paper *Modeling of lithium plating and lithium stripping in lithium-ion batteries* [16] that presents a physicochemical model considering both lithium plating and lithium stripping side reactions. The model simulates reversible lithium plating as well as a characteristic voltage plateau due to lithium stripping and correlates with experimental data.

An aging study resulting in both linearly and nonlinearly aged cells is presented in Chapter 7. The cells and their underlying aging mechanisms are characterized by electrochemical analysis and in-situ neutron diffraction. The chapter references the scientific paper *Linear and Nonlinear Aging of Lithium-Ion Cells Investigated by Electrochemical Analysis and In-Situ Neutron Diffraction* [17].

In Chapter 8, a physicochemical aging model with SEI formation and re-formation, lithium plating and lithium stripping side reactions is presented. The model considers the transition from an early stage, linear to a later stage, nonlinear aging behavior. The chapter references the scientific paper *Electrochemical Modeling of Linear and Nonlinear Aging of Lithium-Ion Cells* [18].

The thesis completes with a conclusion and an outlook in Chapter 9.

Chapter 1: Introduction, Objectives and Thesis Outline

Chapter 2: Fundamentals of Lithium-Ion Cell Aging
Aging mechanisms in lithium-ion cells
Methods for aging mechanism characterization
Modeling of lithium-ion cell aging
Linear and nonlinear aging

Chapter 3: Methodology
Investigated cells
Aging experiments
Electrochemical analysis
Post-mortem analysis
Neutron diffraction
Physicochemical modeling

Experimental   Simulative   Linear aging   Nonlinear aging

Chapter 4: Aging in 18650-type Lithium-Ion Cells Examined with Neutron Diffraction,
Electrochemical Analysis and Physicochemical Modeling

Chapter 5: A SEI Modeling Approach Distinguishing between Capacity and Power Fade

Chapter 6: Modeling of Lithium Plating and Lithium Stripping in Lithium-Ion Batteries

Chapter 7: Linear and Nonlinear Aging of Lithium-Ion Cells Investigated by
Electrochemical Analysis and In-Situ Neutron Diffraction

Chapter 8: Electrochemical Modeling of Linear and Nonlinear Aging of Lithium-Ion Cells

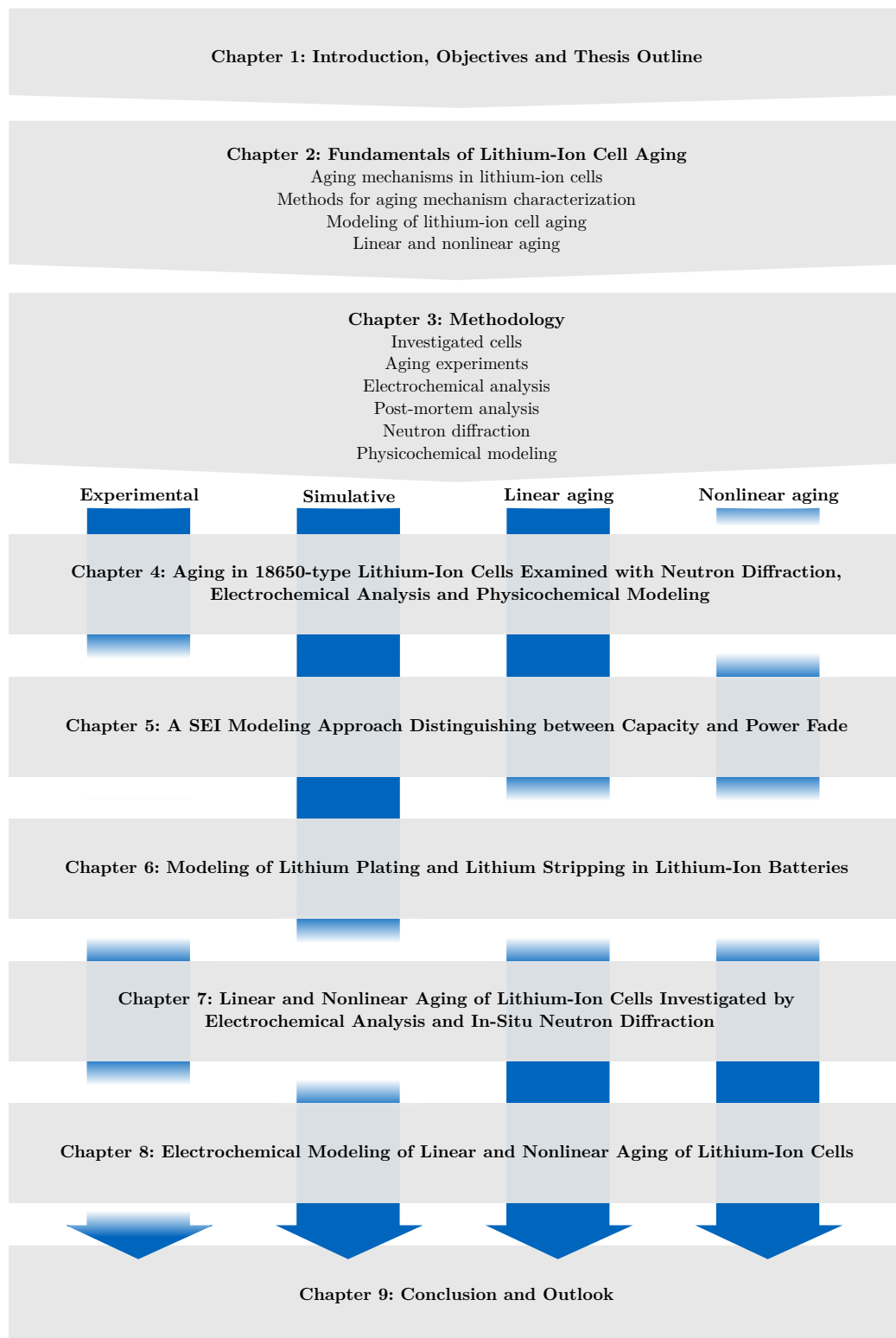Chapter 9: Conclusion and Outlook

Figure 1.1: Structure of the thesis. It shows in which chapters of the main part either linear or nonlinear aging or both are investigated experimentally or simulatively.

2 Fundamentals of Lithium-Ion Cell Aging

The following chapter gives an overview of the underlying aging mechanisms in lithium-ion cells, the methods to characterize those, the definition of linear and nonlinear aging and the state of the art of modeling lithium-ion cell aging.

2.1 Aging mechanisms in lithium-ion cells

In addition to the citations given, the following overview of aging mechanisms in lithium-ion cells is based on the reviews and publications by Agubra et al. [19; 20], Arora et al. [1], Aurbach et al. [21; 22], Birkl et al. [3], Broussely et al.[23], Edge et al. [4], Hausbrand et al. [24], Verma et al. [25], Vetter et al. [2] and Waldmann et al. [26].

Aging of lithium-ion cells in general means the loss of capacity and the increase of impedance that results in a decrease in energy density and power capability. These aging effects are caused by the degradation modes of the loss of lithium-ion inventory (LLI), the loss of active material (LAM) in the negative electrode and the LAM in the positive electrode.

For the LLI degradation mode, lithium ions are consumed by parasitic side reactions such as SEI formation and re-formation, electrolyte decomposition or lithium plating and thus are no longer available for the charge transport between the negative and positive electrode during cycling. The LAM in the negative electrode indicates that the active material of the negative electrode is no longer available for the de-/intercalation of lithium ions due to particle cracking and loss of electrical contact or blocking of active surfaces by resistive layers. Similarly, the LAM in the positive electrode means that the active material of the positive electrode is no longer available for the de-/intercalation of lithium ions due to structural disordering, particle cracking or loss of electrical contact. The described degradation modes can lead to either capacity or power fade or both. [3]

Figure 2.1 depicts the most commonly reported aging mechanisms in lithium-ion cells and their interdependencies. In the following, the main aging mechanisms are presented in more detail.

Solid electrolyte interphase formation   is one of the most dominant side reactions in lithium-ion cells and describes the reduction of the electrolyte, resulting in a passivation layer on the negative electrode's surface [27]. This passivation layer decreases the negative electrode's surface area and porosity. Both lithium metal and graphite electrodes suffer from SEI growth as their operating window exceeds the thermodynamic stability window of the electrolyte [4; 28]. During the first cycles of a lithium-ion cell, the initial SEI is formed resulting in a LLI of approximately 10 % that is considered beforehand while designing the cell and balancing the electrodes. The more the negative electrode is covered by the SEI passivation layer, the slower the additional SEI growth becomes. However, SEI formation never stops as it does not possess ideal properties, which would be a maximum conductivity for lithium ions and an insulating conductivity for electrons.
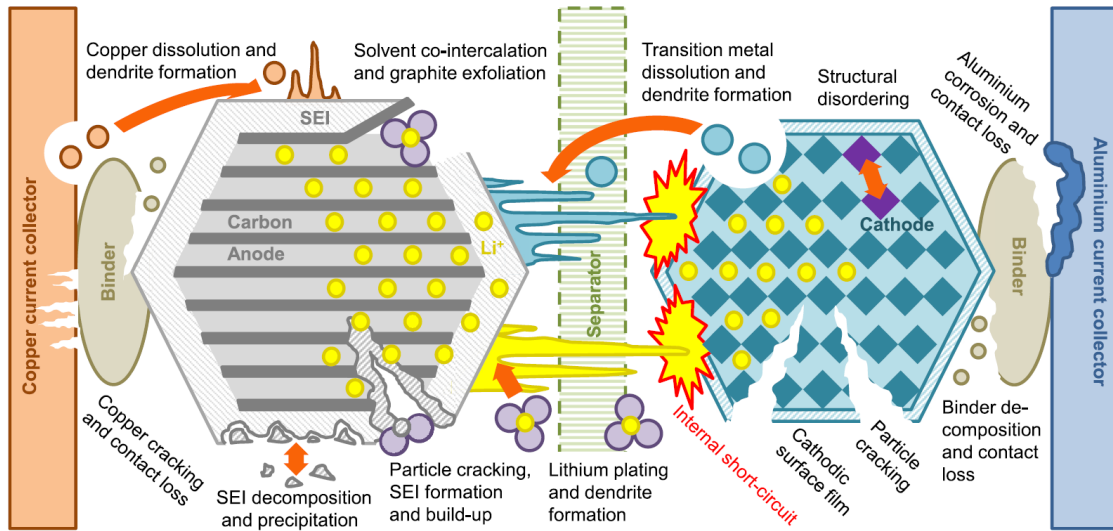
Figure 2.1: Schematic of aging mechanisms in lithium-ion cells. Figure taken from Birkl et al. [3].

Depending on the electrolyte mixture, which is composed of electrolyte salt, solvent and additives, various decomposition products have been observed within the SEI, such as lithium fluoride (LiF), lithium oxide (Li_2O), lithium carbonate (Li_2CO_3), lithium methyl carbonate ($LiOCO_2CH_3$) and lithium ethylene dicarbonate (($LiOCO_2CH_2)_2$) [4; 29].

Equivalently, the cathode oxidizes the electrolyte, exceeding its thermodynamic stability window and forming the so-called cathode electrolyte interphase (CEI).

Solid electrolyte interphase re-formation is caused by either cracking of the layer itself or exposing new and non-passivated surfaces on the negative electrode during graphite expansion. In comparison to the SEI formation that inhibits itself over time, the SEI re-formation side reaction is unaffected by any transport limitations through the film.

Lithium plating describes the side reaction where metallic lithium is formed on the surface of the negative electrode instead of intercalating into it [4]. The literature distinguishes, on the one hand, thermodynamic plating [13] where the surface of the negative electrode is fully lithiated and therefore lithium deposits. On the other hand, kinetic plating [30; 31] is the favored side reaction compared to the main reaction due to a high polarization. This high polarization is mainly caused by high charging currents at low temperatures and a high state of charge (SOC) [32–34]. However, even at moderate temperatures and charging rates, and due to temperature gradients and mechanical stress inside the cell, inhomogeneous current and potential distributions may cause lithium plating [35–37]. On the one hand, plated lithium can irreversibly react with the electrolyte forming additional SEI [4; 13]. On the other hand, lithium plating is partly reversible as long as the metallic lithium has an electrical contact to the active material of the negative electrode [38]. SEI re-/formation or lithium stripping can lead to plated lithium getting electrically disconnected which is then called dead lithium. Waldmann et al. [13] classify the terminology of lithium deposition and distinguish between homogeneous lithium plating and inhomogeneous, local or marginal, lithium deposition.

Lithium stripping is the reversible reaction of lithium plating which partly dissolves the plated lithium as soon as the overpotential becomes positive vs. Li/Li^+. In the literature, a distinction is made between two different reversible processes that are lithium stripping during a subsequent discharge and chemical intercalation during relaxation [13].

Particle fracture is caused by the significant volume change and resulting strain and stress in the electrodes' active materials during de-/intercalation of lithium [39; 40]. As a consequence, the electrical contact between active material particles, conductive additives and the current collector can be lost which results in a loss of the electronic conductivity [4]. Furthermore, particles can break into isolated islands and active material can get separated from the rest of the particle [41]. Subsequently, the cell exhibits a LAM and a LLI due to SEI and CEI re-formation. Especially, active materials with a high theoretical specific capacity like silicon reveal substantial volume changes and provoke severe particle fracture [4].

Positive electrode structural change and decomposition comprises phase changes, oxidation of lattice oxygen, electrolyte decomposition and loss, transition metal/Li^+ site exchange, acid attack and CEI formation leading mainly to LAM but also to LLI. The degradation mechanisms are highly dependent on the positive electrode's chemistry. Currently, various transition metal oxide materials are used which are divided into layered oxides such as lithium nickel manganese cobalt oxide (NMC) and lithium cobalt oxide (LCO), spinels such as lithium manganese oxide (LMO), and phospho-olivines such as lithium iron phosphate (LFP). [4]

2.2 Methods for aging mechanism characterization

There are various methods to characterize aging mechanisms and their underlying chemical, physical and mechanical processes. In general, a distinction is made between in-situ and ex-situ experiments. In-situ refers to measurements that are performed on materials in their original position, i.e. without disassembling the battery [42]. Ex-situ measurements involve cell opening and sample preparation. Major drawbacks of ex-situ measurements – also known as post-mortem analysis – are the high risk of altering or contaminating samples as well as the fact that cells can't be operated any further [26; 42; 43].

The most commonly used techniques are X-ray techniques, scanning probe microscopy, electron microscopy, optical techniques, magnetic (resonance) techniques and neutron techniques [42]. However, the metal casings of lithium-ion cells are generally impenetrable for electromagnetic waves, magnetic fields and electrons. Therefore, special cells including transparent windows are required for most spectroscopy and microscopy techniques [43; 44].

Electrochemical analysis such as electrochemical impedance spectroscopy (EIS) are applied for impedance analysis and to determine the cell's internal, SEI and charge transfer resistances. A wide frequency range can be assigned to examine the cell's ohmic, capacitive and inductive behavior. Depending on the excitation signal, a distinction is made between potentiostatic electrochemical impedance spectroscopy (PEIS) and galvanostatic electrochemical impedance spectroscopy (GEIS). Most techniques in electrochemistry are potentiostatic, which means the potential is controlled and the current is measured. In

contrast, the current is controlled and the potential is measured during GEIS.

Differential voltage analysis (DVA) and incremental capacity analysis (ICA) are applied to investigate degradation mechanisms [11; 34; 45–47]. Distinctive material markers refer to phase changes of the negative or positive electrode and reveal the degradation modes of LLI, LAM in the negative electrode or LAM in the positive electrode.

X-ray techniques comprise X-ray diffraction (XRD), X-ray absorption spectroscopy, X-ray tomographic microscopy and others. XRD is the most commonly used method in battery research and is based on the scattering of X-rays by periodically spaced atoms in a crystal, producing a diffraction pattern that yields information about the crystallographic structure. The method is used to monitor the structural evolution in an electrode as the electrochemical (aging) processes take place. [42]

Microscopy comprises scanning probe microscopy such as scanning electron microscopy (SEM), electron microscopy such as transmission electron microscopy and optical microscopy such as Raman spectroscopy. These methods are applied for direct visual measurements to investigate and compare surface morphologies. [42]

Neutron techniques comprise neutron diffraction (ND), neutron reflectometry, neutron radiography and neutron depth profiling [42; 48]. ND is the most used method and applied to investigate the atomic structure, lattice parameters and particle size of crystalline anode (e.g. graphite) and cathode active materials (e.g. spinels, layered metal oxides or phospho-olivines) [43]. Compared to XRD, ND shows a much higher sensitivity for light elements like lithium – especially in the vicinity of heavy elements – and is much more suitable for large cell formats due to the higher penetration depth of neutrons [43].

However, due to the difficulty in measuring neutron diffraction, only a few studies have been published so far. Dolotko et al. [49] investigated cell fatigue of linearly-aged commercial $C/LiCoO_2$ cells at $25\,°C$ and $50\,°C$, and observed a loss of mobile lithium due to SEI formation. This result is confirmed by Shiotani et al. [50] and Paul et al. [14] for 18650-type $C/LiNi_{0.33}Mn_{0.33}Co_{0.33}O_2$ cells. Paul et al. [43] also showed that LLI was the dominant aging mechanism for aged cells composed of different anode active materials such as mesocarbon microbeads and needle coke and an LFP-based cathode. Inhomogeneous lithium distribution affected by cell fatigue is shown by Cai et al. [51] and Mühlbauer et al. [52]. Furthermore, Zinth et al. [38] and von Lüders et al. [53] investigated chemical intercalation through changes in LiC_6 and LiC_{12} peak intensities during a rest time immediately after severe lithium deposition at low temperatures.

2.3 Modeling of lithium-ion cell aging

Lithium-ion cell models are used in a variety of applications ranging from cell design, electrode balancing, state estimation and prediction to describe and manage operating behavior. Cell models can be based on electrode models including material level and can be scaled to module, pack and system models. Ideally, simulation models require little parametrization effort, run very fast and provide very accurate results. Holistic models describe the cell's electrical, thermal and aging behavior including their interdependencies.

The literature distinguishes between first-principle, electrochemical, empirical, and machine learning models [4; 54; 55]. These model classes differ in terms of parametrization, simulation and validation effort, computational demand and predictability, and are appropriate for the simulation on different time and length scales.

First-principle models describe electrochemical effects on an atomic or molecular scale based on physical equations. Examples are the modeling approaches of molecular dynamics, density functional theory, and kinetic Monte Carlo. These models are used to investigate surface phenomena and interfacial chemistry. [56–59]

Electrochemical models also known as physicochemical models, describe surface and molecule processes in a phenomenological manner whereas the particle and electrode domain is described mechanistically. These models simulate cell characteristics including the main de-/intercalation as well as the side reactions based on electrochemical kinetics and transport equations. The best known electrochemical model is the pseudo two-dimensional (P2D) model developed by Newman and his co-workers Doyle and Fuller [60–63]. It applies the theory of porous electrodes and the theory of concentrated solutions [63; 64]. On the one hand, the model is computationally intensive, but on the other hand, it represents a very accurate model of lithium-ion cells. To reduce the computational time, the single particle model (SPM) was introduced as a simplification of the P2D. This model considers only one single particle per electrode and neither considers a spatial representation along the electrode nor of the liquid phase [65]. Therefore, the SPM is less accurate than the P2D model.

Empirical models describe the cell's behavior based on mathematical equations fitted to experimental data. The well-known (semi-)empirical equivalent circuit model (ECM) is parametrized on electrical, thermal and aging experiments to estimate and predict current and future states such as the state of charge (SOC) and the SOH. The advantages of these models are the simple implementation and fast computation. However, the disadvantage is that they can only describe a previously determined and implemented behavior. One should notice that the abbreviation ECM can be misleading as it is sometimes also used to abbreviate the term electrochemical models.

Machine learning models train the correlation between inputs and outputs – often also referred to as features and labels. Examples are methods of artificial intelligence like neural networks. These models need a lot of varied data. The model training can be computationally intensive, but applying the model can be very fast. Data-driven aging models, for instance, can get trained on the cell's current, voltage and temperature profiles in order to predict the capacity fade. [66–71]

State of the art of physicochemical aging modeling

In the following, the state of the art of physicochemical aging and side reaction modeling of lithium-ion cells – focusing on SEI re-/formation, lithium plating and lithium stripping – is presented chronologically:

Arora et al. [1; 72] introduced a mathematical model of lithium deposition on the negative electrode during overcharge of lithium-ion batteries. They described the side reaction by using a Butler-Volmer equation and – as firstly described by Doyle at al. [73] – included a passivating film growth on the graphite particles due to deposited lithium and the SEI forming decomposition product Li_2CO_3. The authors investigated lithium deposition and surface film growth under various operating conditions, cell designs and charging protocols.

Safari et al. [74] also presented a physicochemical aging model considering the growth of a SEI as the source of capacity fade. The rate of the SEI film growth depends on both solvent diffusion through the SEI film and solvent-reduction kinetics at the carbon surface.

Hein, Latz and co-workers [75; 76] introduced an electrochemical model that considers both lithium plating and lithium stripping. Their model shows a characteristic voltage plateau during discharge due to the dissolution of reversibly plated lithium. Furthermore, their 3D microstructure modeling approach reveals the most probable position for lithium plating [77].

Tang et al. [78] investigated the effect of lithium deposition on the electrode edges caused by local overpotentials. Under the assumptions of their model, an extension of 0.4 mm was sufficient to prevent the onset of lithium deposition after the cutoff potential was reached.

Legrand et al. [30] investigated lithium plating through charge transfer limitations that occur at short-time scales. However, diffusion limitations in the solid insertion compound occur at long-time scales and have not been examined.

Tippmann et al. [32] built up an electrochemical model that considers lithium plating for low-temperature charging. Their experimental results on degradation qualitatively correlate with the modeled anode potential.

The modeling of mechanical degradation in lithium-ion batteries during cycling based on SEI fracture is presented by Laresgoiti et al. [79]. In their model, SEI can break exposing active material to the electrolyte, leading to additional SEI layer formation.

A lithium plating model at subzero temperatures was introduced by Ge et al. [80] and validated by nuclear magnetic resonance (NMR) measurements. They showed that the lithium plating side reaction could occur even at low SOCs.

Yang et al. [12] presented an aging model considering SEI growth and lithium plating based on cathodic Tafel equations. While the anode porosity decreases during cycling, lithium plating exponentially increases and causes accelerated capacity loss and resistance rise. In a further work, Yang and co-workers [31] extended their model considering lithium stripping to model the characteristic voltage plateau during relaxation or discharge after severe lithium deposition. Differential voltage analysis assesses the amount of deposited lithium. This model is focused on one charging/discharging cycle and does not consider long-term cycling or aging.

Ren et al. [81] also modeled the characteristic voltage plateau due to lithium plating and lithium stripping side reactions at low temperatures. Differential voltage analysis is used as quantitative,

non-destructive lithium plating detection.

Xu et al. [82] modeled the effect of dead lithium on the cell's capacity and voltage. The dead lithium is modeled as an additional layer which restricts the transport of lithium ions.

Zhao et al. [83] modeled degradation considering lithium plating and lithium stripping side reactions at subzero ambient temperatures and used differential voltage analysis to calculate the amount of reversible lithium dissolution.

Finally, Müller et al. [84] investigated the influence of different porosity profiles in the graphite electrode on the battery's aging by two irreversible side reactions at the anode, namely SEI formation and lithium plating.

The state of the art SEI modeling approaches reveal no distinction between the transport of lithium ions, on the one hand, and electrons through the SEI, on the other hand. The models result in only one ohmic drop for the driving potential for both the main de-/intercalation and the SEI side reactions. The ideal SEI properties of a maximum conductivity for lithium ions (κ_{SEI}) and an insulating conductivity for electrons (σ_{SEI}) are not represented. Therefore, capacity and power fade are inextricably connected.

Lithium plating and lithium stripping models describe the characteristic voltage plateau during relaxation or discharge after severe lithium deposition. These models simulate only few cycles but no long-term cycling aging behavior.

A long-term cycling aging model considering SEI and lithium plating side reactions is presented by Yang et al. [12]. Their model also describes the transition to a nonlinear aging behavior. However, the lithium plating side reaction is modeled by a cathodic Tafel equation. Based on this modeling approach, lithium plating even takes place at positive overpotentials vs. Li/Li$^+$. To the best of our knowledge, no electrochemical long-term cycling aging model considering SEI, lithium plating and lithium stripping side reactions was presented so far showing the transition from an early stage, linear to a later stage, nonlinear aging behavior.

2.4 Linear and nonlinear aging

Figure 2.2 shows the aging behavior in terms of capacity loss of a commercial 18650-type C/LiNi$_{0.33}$Mn$_{0.33}$Co$_{0.33}$O$_2$ lithium-ion cell. The curve corresponds to the testing procedure #2 of the aging experiment in the publication *Linear and Nonlinear Aging of Lithium-Ion Cells Investigated by Electrochemical Analysis and In-Situ Neutron Diffraction* (see Table I and Figure 2) that is shown in Chapter 7.

Although the aging behavior depends on various factors such as cell chemistry, cell design and format, operating mode and stress conditions, external thermal and mechanical boundary conditions as well as underlying degradation mechanisms, an aging characteristic as presented here is very common. The formation of the initial SEI causes the degradation mechanism of LLI and the initial phase of aging. Thereafter, the cell ages moderately resulting in a square-root-shaped capacity loss over equivalent full cycles (EFCs). The degradation rate even decelerates until a turning point is reached where it accelerates again afterwards. A transition point marks an exceeding degradation rate which is approximately 0.5 ‰ capacity loss per EFC in this example. After this transition point, the degradation rate increases further and more strongly until the EOL criteria is reached at 80 % SOH. Although
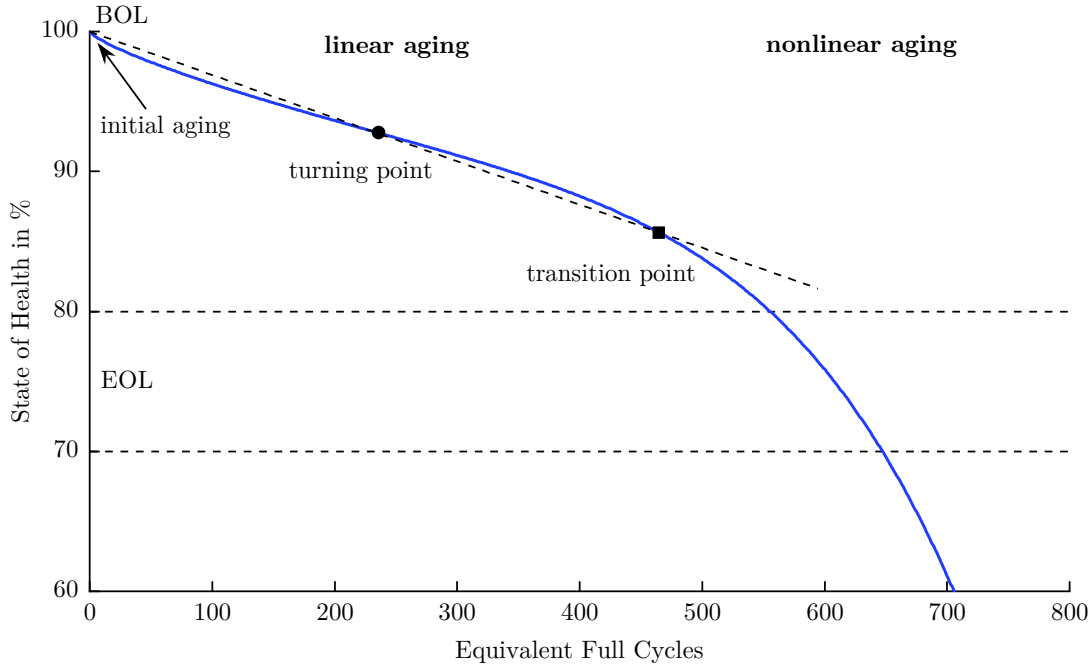
Figure 2.2: Linear and nonlinear aging behavior.

an EOL is often defined at 80 % SOH, no uniform standards exist so far [47]. This might result from different requirements on the performance of a battery depending on its application, which also demands a certain power capability next to the remaining capacity. Therefore, there are further EOL definitions such as 70 % SOH.

Overall, the aging behavior can be separated into an early stage, linear and a later stage, nonlinear aging [11]. The former indicates decelerating and moderately accelerating degradation rates, whereas the latter describes strongly accelerating degradation rates. Similar to the EOL, no standardized definition of linear and nonlinear aging exists, although these terms are often used in the literature [8–10; 12]. In this thesis, we define the early stage, linear aging from the cell's begin of life (BOL) to the transition point and the later stage, nonlinear aging from the transition point until the EOL is reached. We are aware that the linear aging does not coincide with a straight line.

Regardless of a first life or possible second life application, lithium-ion cells should age until their EOL is reached without a transition into a nonlinear aging behavior.

Schuster et al. [8; 9] presented aging experiments for different operating conditions and observed the transition to nonlinear aging. They suggested lithium deposition being the reason for the transition from linear to nonlinear aging. The lithium plating side reaction itself is caused by reduced kinetics of the graphite anode as a result of SEI growth and loss of graphite active material. A delay or even avoidance of nonlinear aging is suggested by operating the battery in optimum temperature, voltage and current windows. [8; 9; 13]

Bach et al. [10] investigated the same cell type as Schuster et al. [8; 9] by post-mortem analysis. They performed aging experiments at 20 °C with different charging and discharging currents. Uncycled as well as linearly and nonlinearly aged cells were disassembled and analyzed by XRD measurements. The authors found lithium loss and lithium excess and concluded that the main mechanism of capacity

loss originates from lithium which cannot be extracted from the anode, lithium which is bound in the SEI and lithium which has been deposited on the anode. They concluded that in case of accelerated capacity fade, local lithium deposition starts in unevenly compressed areas and then spreads over the whole anode of the cell. [13]

Anseán et al. [11] showed in-situ lithium plating analyses for a commercial C/LFP cell cycled under dynamic stress test. ICA and mechanistic model simulations were used to quantify the degradation modes and to relate their effects to lithium plating. They concluded that lithium deposition starts to become irreversible at the turning point of sudden capacity drop. [11; 13]

3 Methodology

The following chapter describes the investigated cells used in the aging experiments, the methods of electrochemical analysis and neutron diffraction to experimentally investigate the aging mechanisms and the physicochemical modeling of lithium-ion cells.

3.1 Investigated cells

In this thesis, we investigated mainly commercially produced lithium-ion cells. These are Sanyo UR18650E (see also Chapter 7 and Chapter 8), Samsung ICR18650-22F (see also Chapter 5) and Molicel IHR18650A (see also Chapter 6). Partly, we also tested lithium-ion cells manufactured under commercial standards (see also Chapter 4) in a joint venture between the Volkswagen and VARTA Microbattery companies. All cells have a cylindrical 18650 format. In general, these cells are composed of graphite as the anode and $LiNi_{0.33}Mn_{0.33}Co_{0.33}O_2$ as the cathode.

Table 3.1 exemplarily shows the specifications based on the datasheet of the investigated cell Sanyo UR18650E [85].

Table 3.1: Specifications of the lithium-ion cell Sanyo UR18650E [85].

Parameter	Symbol	Value
Nominal capacity	C_N	2.05 Ah
Nominal voltage	U_N	3.6 V
End-of-charge voltage	U_{ch}	4.2 V
End-of-discharge voltage	U_{dch}	2.75 V
Standard charging current	$I_{ch,std}$	1.435 A
Temperature range charge	$T_{amb,ch}$	0 to 40 °C
Temperature range discharge	$T_{amb,dch}$	−20 to 60 °C
Temperature range storage	$T_{amb,sto}$	−20 to 50 °C
Mass	m	44.5 g
Gravimetric energy density	E_{grav}	165 Wh kg^{-1}
Volumetric energy density	E_{vol}	443 Wh l^{-1}

3.2 Aging experiments

To perform the aging experiments, we used battery test systems (e.g. BaSyTec CTS) and environmental chambers (e.g. Binder MK 53) to keep the temperatures steady. The cells were cycled with synthetic charging/discharging cycles considering varying stress conditions (e.g. charging currents, discharging currents and resting times). The detailed testing procedures including information on constant current (CC) and constant voltage (CV) steps, charging and discharging cutoff currents and voltages as well

as resting times are presented in the Chapters 4 and 7. We tested at least three cells for every test procedure, except for the aging experiment shown in Chapter 4. At the beginning of the aging experiments and after a certain number of cycles (e.g. 100), checkup tests were performed to determine the cells' capacity and internal resistance.

3.3 Electrochemical analysis

We applied electrochemical analysis to determine the capacity loss and resistance increase. Additionally, we obtained DVA to investigate the underlying degradation mechanisms [17; 45]. Figure 3.1 exemplarily shows the measured differential voltage during aging. The figure depicts distinctive material markers that are phase changes of the lithiated graphite. According to Winter et al. [86], the first one shows the transition from phase III+IV to phase II+IIL and the second from phase II+IIL to II+I. As these markers do not shift and Q_C remains constant, anode active material loss cannot be confirmed. Distinctive material markers that refer to the cathode cannot be assigned in the DVA curves. The absolute irreversible capacity loss Q_{cell} at the remaining material markers of the anode reveal a loss of lithium inventory as the dominant aging mechanism in this example.
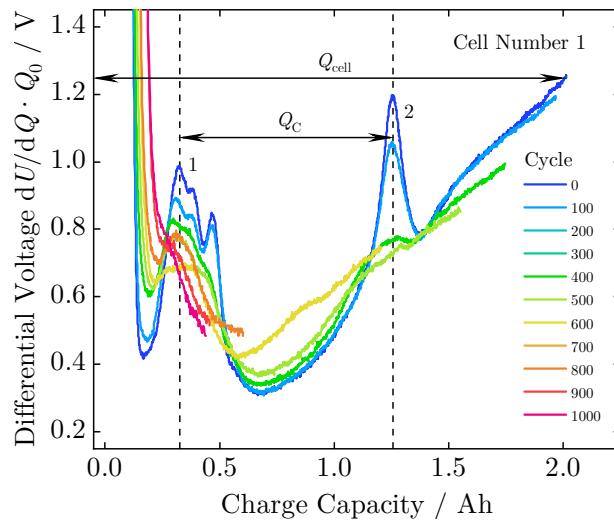

Figure 3.1: Measured differential voltage curves during aging.

Furthermore, we carried out EIS for impedance analysis and to determine the cell's internal, SEI and charge transfer resistances using a Biologic VMP3 potentiostat.

The electrochemical analysis is performed as a cross-validation of and in addition to the neutron diffraction results.

3.4 Post-mortem analysis

We used SEM to qualitatively investigate and compare the surface morphology of the electrodes from cycled and uncycled cells. We obtained images using a benchtop scanning electron microscope (JCM-6000, JEOL Ltd., Japan) with an acceleration voltage of 15 kV at Prof. Dr. Hubert A. Gasteiger's Chair of Technical Electrochemistry at the Technical University of Munich. In preparation for the mea-

surements, the cells were opened in a glove box (M. Braun Inertgas-Systeme GmbH, Germany) under an argon atmosphere, subsequent to the aging experiment. To consider the effects of inhomogeneous aging, we punched out electrode samples at different positions along the electrode.

3.5 Neutron diffraction

The neutron diffraction experiments in this thesis were performed using a Debye–Scherrer geometry under ambient conditions at the high-resolution powder diffractometer SPODI at the Heinz Maier-Leibnitz (FRM II) research reactor in Garching, Germany [87–90].

The high-resolution powder diffractometer SPODI is designed for structure solution and Rietveld refinement of structural parameters on crystalline powders. The instrument is characterized by a very high monochromator take-off angle of 155° with a detector array consisting of 80 position sensitive detector tubes. The sample environmental device enables lithium-ion cells to be measured in a rotating cell holder. [87–90]

Figure 3.2 a) shows the schematic of the instrument and the setup of the experiment. Neutrons with a wavelength of 0.1548 nm were incident on a rectangular cross section of 40 mm x 30 mm of the cell center, as shown in Figures 3.2 b) and c).
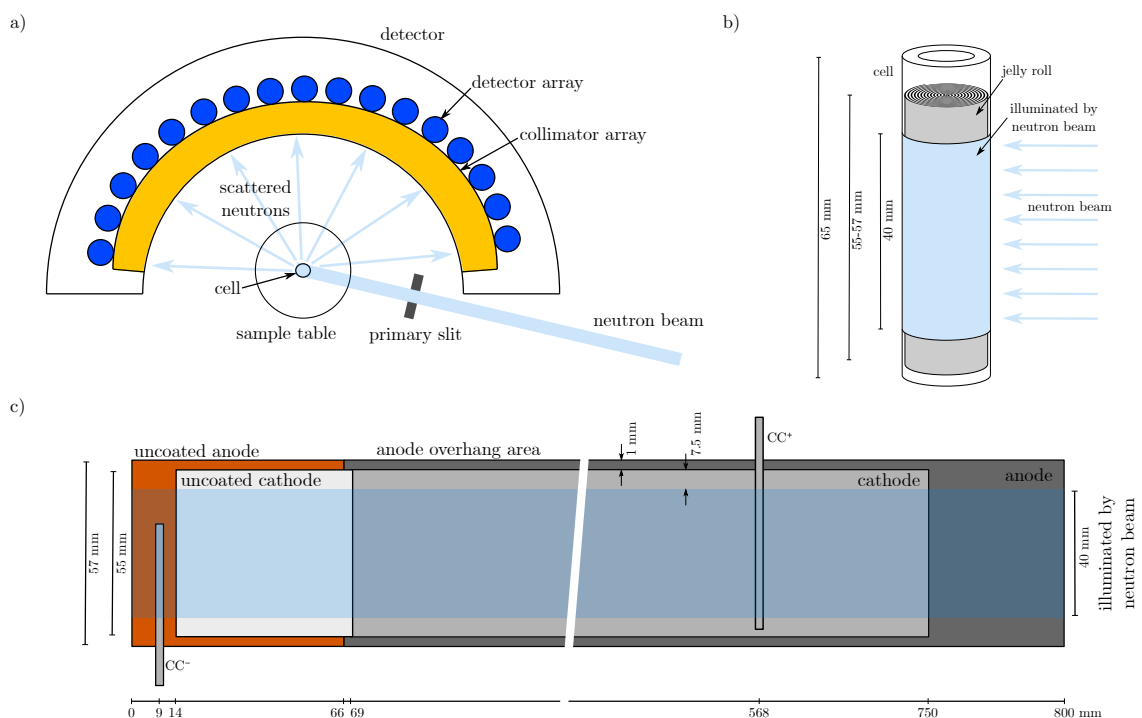

Figure 3.2: a) Schematic of high-resolution powder diffractometer SPODI and setup of neutron diffraction experiment, b) rectangular cross section of 40 mm height, illuminated by neutron beam, and c) schematic of electrode geometries of the investigated cell.

The top and bottom of the cell (approx. 25 mm in total) were not illuminated by the neutron beam, to avoid noisy signals from the cell holder and safety protection circuitry. A neutron detector array consisting of 80 vertical position-sensitive detectors with a Soller collimator in front of each, see Figure 3.2 a), recorded the neutrons scattered by the cell [87; 88]. The cells were continuously rotated

during the entire measurement to obtain an average signal over cell volume. Five succeeding diffractograms were measured for each cell, with an acquisition time of 36 min each. Therefore, the total integration time for the obtained diffractograms was 3 h for each cell. We determined an instrumental resolution function with a $Na_2Ca_3Al_2F_{14}$ reference material, in order to calculate the full widths at half the maximum reflections from the cell. To describe the peak profile shape, a Thompson-Cox-Hastings pseudo-Voigt function was used [91]. A linear interpolation between selected data points was used to fit the background. Multi-phase Rietveld refinements of structural models for the neutron diffraction data were carried out using the FullProf software package [92]. Due to significant overlap of diffraction peaks from the steel housing and current collectors, and the strong preferred orientations of crystallites for these phases, structure-independent profile fits were used.
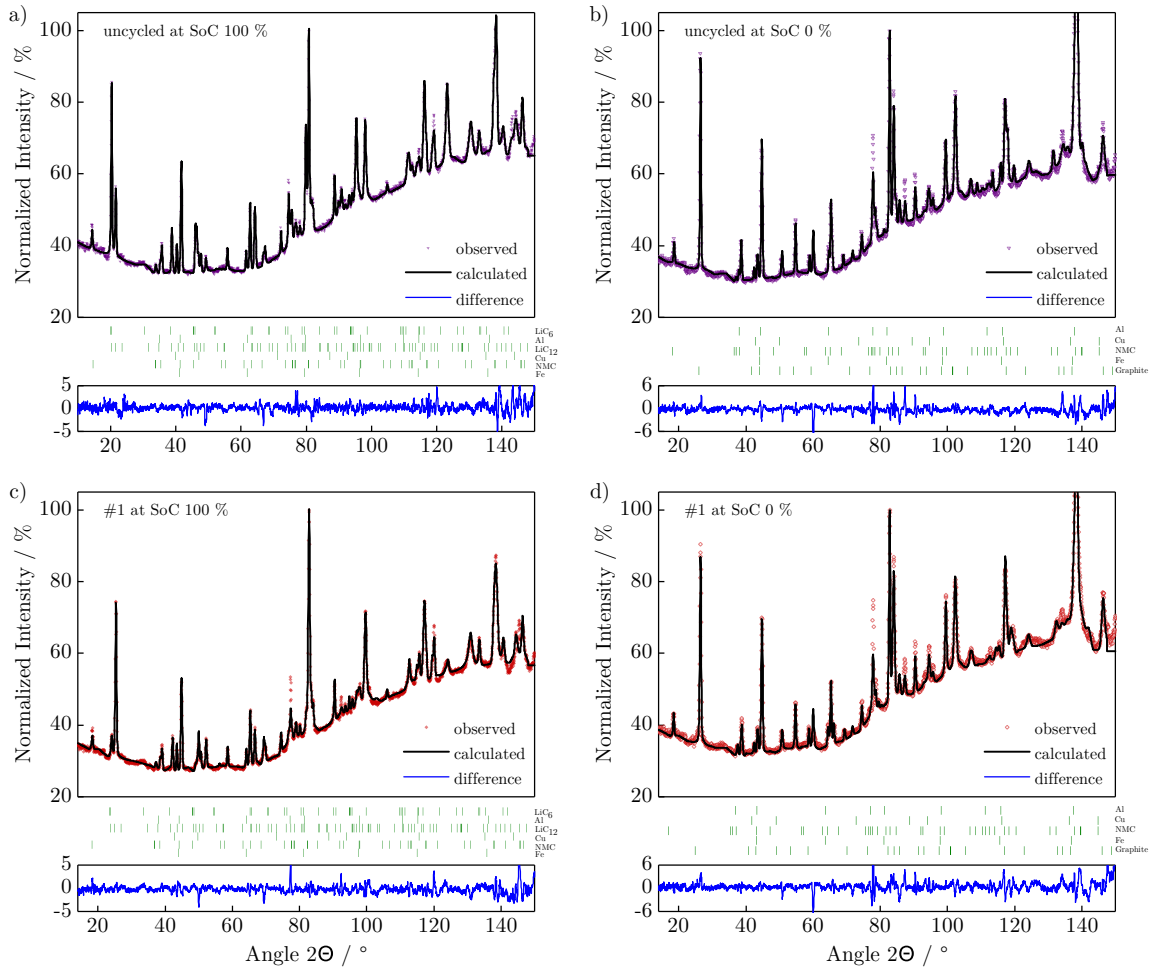

Figure 3.3: Neutron diffractograms with the full angular range of the a) uncycled cell at 100 % SOC, b) uncycled cell at 0 % SOC, c) nonlinearly-aged cell at 100 % SOC, d) nonlinearly-aged cell at 0 % SOC. The experimental data are shown by colored symbols whereas their Rietveld refinements are shown as black lines. The blue lines show differences between data and fit. The vertical bars (green) above the blue line indicate Bragg reflections corresponding to the crystalline phases in the cell (for 100 % SOC from top to bottom: LiC_6, Al, LiC_{12}, Cu, NMC and Fe, and for 0 % SOC from top to bottom: Al, Cu, NMC, Fe and graphite).

Figure 3.3 exemplarily shows full neutron diffractograms of uncycled (a) and b)) and nonlinearly-aged (test procedure # 1), c) and d)) cells in their fully charged and fully discharged state, along with their Rietveld refinements. The results corresponds to the aging experiment in the publication *Linear and Nonlinear Aging of Lithium-Ion Cells Investigated by Electrochemical Analysis and In-Situ Neutron Diffraction* that is shown in Chapter 7. A high background due to the incoherent scattering of neutrons due to the hydrogen present in the electrolyte and separator is observed for all cells, which tends to increase with angle. From the Rietveld refinement of all cells, electrochemically accessible lithium content in their electrodes and lattice parameters was extracted and compared.

Figure 3.4 depicts the selected angular range on the prominent LiC_6 (001), LiC_{12} (002) and C (002) reflections of the anode as well as the NMC (003), NMC (006) and NMC (012) reflections of the cathode.
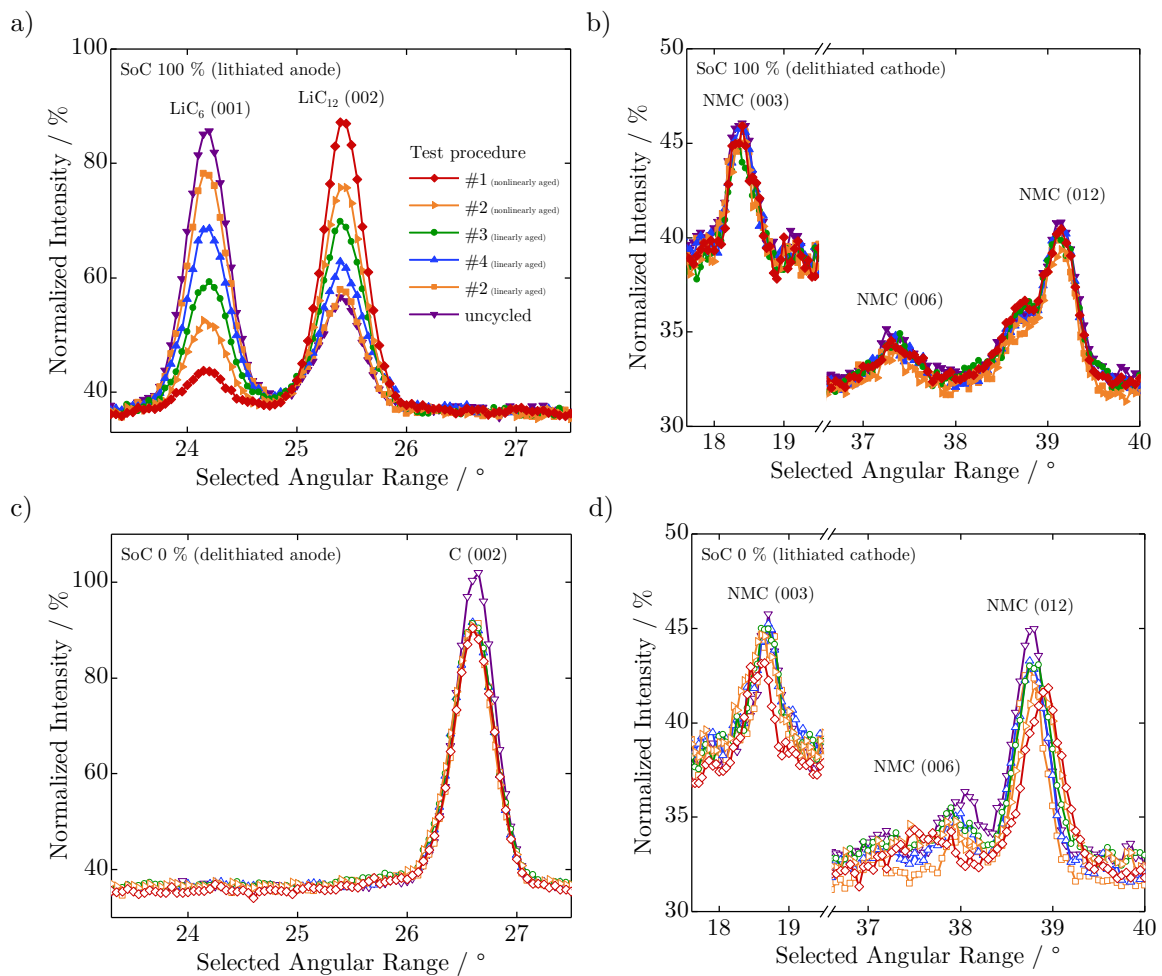

Figure 3.4: a) and c) present neutron diffraction data from a selected angular range, focusing on the prominent LiC_6 (001), LiC_{12} (002) and C (002) reflections of the anode, where changes in peak intensities of LiC_6 (001) and LiC_{12} (002) reflections indicate a reduction in lithium content in the anode on aging. b) and d) present selected angular range of neutron diffraction data, focusing on the NMC (003), NMC (006) and NMC (012) reflections of the cathode, which in spite of being weak in intensity, show angular shifts indicating a reduction in lithium content in the lithiated cathode on aging.

3.6 Physicochemical modeling

The physicochemical modeling in this thesis is based on the P2D model as introduced by Newman, Doyle and Fuller [60–63]. This so-called Newman model applies the theory of porous electrodes and the theory of concentrated solutions [64]. In this section, all governing equations and boundary conditions of the P2D model are introduced referring to the book *Electrochemical Systems* by John Newman and Karen E. Thomas-Alyea [63]. In addition, the coupling of the physicochemical model to a thermal model is introduced.

Porous electrode structure

The P2D model represents a one-dimensional model that passes through a cell layer along a perpendicular line that corresponds to the x-axis in Figure 3.5. At every point on that line in the negative and positive electrode, the model is extended by a pseudo dimension considering the lithium-ion concentration in the active material. This pseudo dimension represents the radial axis in spherical active material particles.
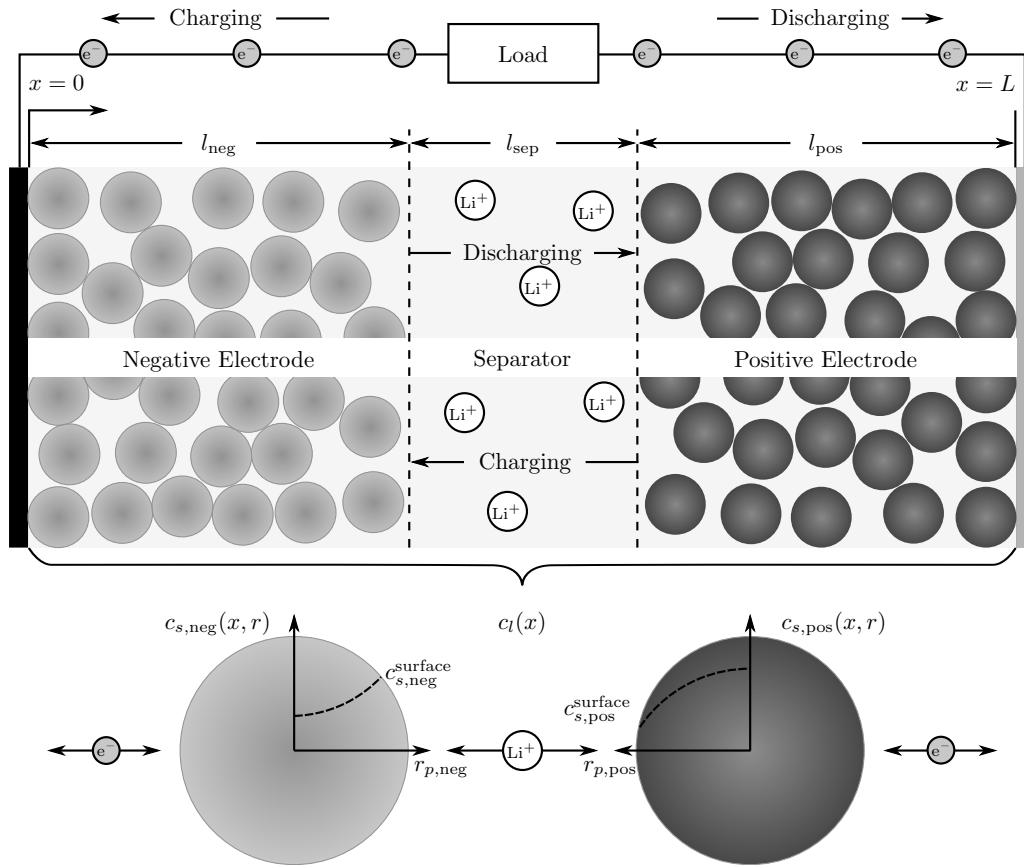

Figure 3.5: Schematic of the P2D model composed of the three domains negative electrode, separator and positive electrode, and their thicknesses l_{neg}, l_{sep} and l_{pos}. In each domain, the two phases liquid (electrolyte) and solid (active material) are distinguished. Lithium-ion transport takes place in the liquid phase as well as in the electrode's solid phase, whereas electron transport is only possible in the solid phase of the electrodes. The lithium de-/intercalation reaction takes place on the active material particles' surface causing lithium-ion diffusion inside the particles. [93; 94]

The modeling approach assumes both active material particles and electrolyte at every point of the porous electrodes due to very small and uniformly radially symmetric particles surrounded by electrolyte. The extent in y- and z-direction is accepted to be infinite compared to the cell's thickness and is thus neglected.

Based on the superposition of both the solid and the liquid phase at every point, it is possible to determine the potential and the concentration of the electrolyte as well as the potential and the concentration of the active materials. This results in four interdependent variables

$$c_l(x,t) \text{ in mol m}^{-3}, \quad \text{lithium-ion concentration in the electrolyte}$$
$$c_s(r,x,t) \text{ in mol m}^{-3}, \quad \text{lithium-ion concentration in the active material}$$
$$\Phi_l(x,t) \text{ in V}, \quad \text{electrolyte potential}$$
$$\Phi_s(x,t) \text{ in V}, \quad \text{electrode potential in the active material}$$

with each variable being spatially and temporally dependent. $c_s(r,x,t)$ and $\Phi_s(x,t)$ are only solved in the electrode domains, as no electron flux and thus no de-/intercalation reactions can take place in the separator domain.

The porous electrodes in lithium-ion cells are typically composed of active material, binder and conductive agent, filled with electrolyte. Therefore, the electrolyte volume fraction ε_l – also called porosity – describes the ratio between the electrolyte volume V_l and the entire electrode volume or separator volume V, respectively

$$\varepsilon_l = \frac{V_l}{V} \tag{3.1}$$

whereas the active material volume fraction ε_s is only defined in the two electrodes as the ratio between the volume of active material V_s and the electrode volume

$$\varepsilon_s = \frac{V_s}{V} \tag{3.2}$$

Including the non-active material volume fraction ε_{na}, the sum of all volume fractions results in

$$\varepsilon_l + \varepsilon_s + \varepsilon_{na} = 1 \tag{3.3}$$

for each domain.

The specific surface a couples the x- and r-dimension and is defined by

$$a = \frac{A_{\mathrm{p}}}{V_{\mathrm{p}}} = \frac{4\pi r_p^2}{\frac{4}{3}\pi \frac{r_p^3}{\varepsilon_s}} = \frac{3\varepsilon_s}{r_p} \tag{3.4}$$

with the particle's surface A_{p}, its volume V_{p} and its radius r_p, scaled with the active material volume fraction ε_s.

Electrode kinetics and rate of reaction

The lithium de-/intercalation reaction takes place on the active material particle surface according to the following scheme

$$\text{Li}^+ + \Theta_s + e^- \rightleftharpoons \text{Li}\Theta_s \tag{3.5}$$

where Θ_s symbolizes the delithiated host lattice and $\text{Li}\Theta_s$ the lithiated one. By rearranging Equation (3.5), the stoichiometric coefficients can be derived as $\nu_{\text{Li}^+} = -1$ and $\nu_{\text{Li}\Theta_s} = +1$

$$\nu_{\text{Li}^+}\text{Li}^+ + \nu_{\Theta_s}\Theta_s + \nu_{\text{Li}\Theta_s}\text{Li}\Theta_s \rightleftharpoons e^- \tag{3.6}$$

The rate of reaction is described by the Butler-Volmer equation

$$i = i_0 \left(\exp\left(\frac{\alpha_a n F}{RT}\eta \right) - \exp\left(-\frac{\alpha_c n F}{RT}\eta \right) \right) \tag{3.7}$$

with the surface overpotential η as the driving force of the reaction. The number of participating electrons n is 1 in lithium-ion batteries. α_a and α_c describe the anodic and cathodic charge-transfer coefficients. The overpotential η is calculated by the difference of the electrode potential in the active material Φ_s, the electrolyte potential Φ_l and the thermodynamic equilibrium potential E_{Eq}

$$\eta = \Phi_s - \Phi_l - E_{\text{Eq}} \tag{3.8}$$

While the overpotential refers to the magnitude of the potential drop caused by resistance to the passage of current, the term polarization generally refers to the departure of the potential from equilibrium conditions. Different types of resistances can cause overpotential.

The exchange current density i_0 is defined by

$$i_0 = F k_c^{\alpha_a} k_a^{\alpha_c} \left(c_{s,\max} - c_s|_{r=r_p} \right)^{\alpha_a} \left(c_s|_{r=r_p} \right)^{\alpha_c} \left(\frac{c_l}{1\,\text{mol m}^{-3}} \right)^{\alpha_a} \tag{3.9}$$

with $c_{s,\max}$ as the maximum concentration of lithium ions in the active material, c_s as the lithium-ion concentration in the active material – evaluated at the particle surface – and c_l as the concentration of lithium ions in the electrolyte. k_a and k_c describe reaction rate constants with subscripts a and c representing the anodic and cathodic direction, respectively. In the case of $\alpha_a = \alpha_c = 0.5$, the term $1\,\text{mol m}^{-3}$ simplifies the units of the reaction rates k_i which get reduced to m s^{-1}. This case is generally accepted in lithium-ion batteries and indicates that both forward and backward reactions proceed with the same rate.

By Faraday's law, the charge-transfer current density i results in the pore-wall flux j

$$j = \frac{i}{F} \tag{3.10}$$

The pore-wall flux and the specific surface determine the reaction term R_l in $\text{mol m}^{-3}\,\text{s}^{-1}$

$$R_l = aj \tag{3.11}$$

Mass transport and mass balance in the liquid phase

Diffusion, migration and convection are the transport mechanisms of lithium ions in the electrolyte and they define the ionic flux N_l by

$$N_l = N_{l,\text{diff}} + N_{l,\text{mig}} + N_{l,\text{con}} \tag{3.12}$$

Diffusion is caused by a concentration gradient and is described by Fick's law

$$N_{l,\text{diff}} = -D_l \nabla c_l \tag{3.13}$$

with D_l as the diffusion coefficient in the electrolyte. Lithium ions move from high to low concentrations.

Migration describes the transport of lithium ions in an electric field

$$N_{l,\text{mig}} = \frac{i_l t_+}{F} \tag{3.14}$$

where t_+ defines the transport number, as the amount of cations to the current density in the electrolyte i_l.

Finally, convection is caused by the flow of electrolyte with the concentration c_l and the velocity v

$$N_{l,\text{con}} = c_l v \tag{3.15}$$

The flow of electrolyte may be caused by a density or temperature gradient (natural convection), or by mechanical stirring or a pressure gradient (forced convection). In lithium-ion batteries, convection is mostly neglected. Thus, the ionic flux N_l can be written as

$$N_l = -D_l \nabla c_l + \frac{i_l t_+}{F} \tag{3.16}$$

The mass balance in the electrolyte is given by

$$\frac{\partial c_l}{\partial t} = -\nabla N_l + R_l \tag{3.17}$$

where the temporal change of the lithium-ion concentration in the electrolyte c_l correlates with the divergence of the ionic flux ∇N_l and the reaction term R_l.

Thus, the mass balance in the electrolyte, evaluated in the electrode domains, is described by

$$\varepsilon_{l,i} \frac{\partial c_l}{\partial t} = \nabla \left(D_{l,\text{eff}} \nabla c_l - \frac{i_l t_+}{F} \right) + R_l \tag{3.18}$$

that is scaled with the respective porosity $\varepsilon_{l,i}$ in each domain. The effective diffusion coefficient $D_{l,\text{eff}}$ and other effective transport parameters will be explained in Subsection 3.6.

In the separator domain, $R_l = 0$ and, therefore, the mass balance results in

$$\varepsilon_{l,i} \frac{\partial c_l}{\partial t} = \nabla \left(D_{l,\text{eff}} \nabla c_l - \frac{i_l t_+}{F} \right) \tag{3.19}$$

Mass transport and mass balance in the solid phase

In the solid phase, diffusion is the only transport mechanism of lithium ions. Therefore, Fick's law describes the ionic flux in the active material N_s by

$$N_s = -D_s \nabla c_s \tag{3.20}$$

with the diffusion coefficient in the active material D_s. Since no reaction takes place inside the particles, the mass balance in the active material is given by

$$\frac{\partial c_s}{\partial t} = -\nabla N_s \tag{3.21}$$

Within the spherical active material particles, lithium ions move along the r-axis. By transforming Cartesian coordinates into spherical coordinates, the mass balance results in

$$\frac{\partial c_s}{\partial t} = -\nabla N_s = D_s \left(\frac{\partial^2 c_s}{\partial r^2} + \frac{2}{r} \frac{\partial c_s}{\partial r} \right) \tag{3.22}$$

Charge balance

The current density in the active material i_s follows Ohm's law

$$i_s = -\sigma_{\text{eff}} \nabla \Phi_s \tag{3.23}$$

where σ_{eff} symbolizes the effective solid phase conductivity and $\nabla \Phi_s$ marks the divergence of the electrode potential in the active material.

In contrast, the current density in the electrolyte is described by a modified Ohm's law to account for interactions between anions and cations in the concentrated electrolyte

$$i_l = -\kappa_{\text{eff}} \nabla \Phi_l + \frac{2\kappa_{\text{eff}} RT}{F} \left(1 + \frac{\partial \ln f_\pm}{\partial \ln c_l} \right) (1 - t_+) \nabla \ln c_l \tag{3.24}$$

with the effective liquid phase conductivity κ_{eff}, the divergence of the electrolyte potential $\nabla \Phi_l$, the universal gas constant R, the temperature T, Faraday's constant F, the transport number of cations – that are lithium ions – t_+, the mean activity coefficient $f_\pm$ and the lithium-ion concentration in the electrolyte c_l.

Therefore, the total current density results in

$$i_{tot} = i_s + i_l \tag{3.25}$$

The charge balance in the electrode domains is given by

$$-\nabla i_l = \nabla i_s \tag{3.26}$$

and considers the equilibrium of incoming/outgoing charges (cations) in the liquid electrolyte and incoming/outgoing charges (electrons) in the solid active material.

However, no reaction takes place in the separator domain and the charge balance results in

$$-\nabla i_l = 0 \tag{3.27}$$

Boundary conditions

In order to solve the model equations, the following boundary conditions are implemented.

At the boundaries of the model, in particular the interface between electrode and current collector, the ionic flux N_l has to be terminated

$$\nabla c_l \big|_{x=0 \ \& \ x=l_{cell}} = 0 \tag{3.28}$$

with $l_{cell} = l_{\mathrm{neg}} + l_{\mathrm{sep}} + l_{\mathrm{pos}}$. Additionally, no current density in the electrolyte passes through these boundaries, so that the liquid phase potential is defined as

$$\nabla \Phi_l \big|_{x=0 \ \& \ x=l_{cell}} = 0 \tag{3.29}$$

Thus, the solid phase potential is given by

$$\nabla \Phi_s \big|_{x=0 \ \& \ x=l_{cell}} = -\frac{i_s}{\sigma_{\mathrm{eff}}} \tag{3.30}$$

In contrast, the current density in the active material is terminated at the interface between electrode and separator

$$\nabla \Phi_s \big|_{x=l_{\mathrm{neg}} \ \& \ x=l_{\mathrm{neg}}+l_{\mathrm{sep}}} = 0 \tag{3.31}$$

Furthermore, the pseudo-dimension is connected to the electrode kinetics by

$$-D_s \frac{\partial c_s}{\partial r}\bigg|_{r=r_p} = j \tag{3.32}$$

and the particles, and thus the concentration, is assumed to be symmetrical

$$-D_s \frac{\partial c_s}{\partial r}\bigg|_{r=0} = 0 \tag{3.33}$$

Effective transport parameters

The porous electrode structure elongates the transport path of lithium ions and electrons and requires the use of effective transport parameters. The ratio between the effective path length l_{eff} and the direct path length l defines the tortuosity as

$$\tau = \frac{l_{eff}}{l} \tag{3.34}$$

MacMullin's number N_M is given by the tortuosity and the volume fraction of the electrode or separator

$$N_M = \frac{\tau^n}{\varepsilon^m} \tag{3.35}$$

with geometrical empiric constants m and n. Per default $n = m = 1$. Based on MacMullin's number, the correction of transport parameters is calculated by

$$D_{l,\text{eff}} = \frac{1}{N_M} D_l \tag{3.36}$$

for the effective diffusion coefficient,

$$\kappa_{\text{eff}} = \frac{1}{N_M} \kappa \tag{3.37}$$

for the effective liquid phase conductivity as well as

$$\sigma_{\text{eff}} = \frac{1}{N_M} \sigma \tag{3.38}$$

to describe the effective solid phase conductivity.

Another correction was introduced by Bruggeman [95] that scales all transport parameters with the factor of $\varepsilon_l^{1.5}$ or $\varepsilon_s^{1.5}$, respectively.

Thermal Modeling

The physicochemical model is coupled to a 0D thermal model that simulates an evenly distributed heat in the cell. The total heat generation $\dot{q}$ is comprised of ohmic heat $\dot{q}_{ohm}$, reaction heat $\dot{q}_{reac}$ and reversible heat $\dot{q}_{rev}$

$$\dot{q} = \dot{q}_{ohm} + \dot{q}_{reac} + \dot{q}_{rev} = i_l \nabla \Phi_l + i_s \nabla \Phi_s + \sum_k a_k i_k \left(\eta_k + T \frac{\partial E_{eq,k}}{\partial T} \right) \tag{3.39}$$

with the current density in the electrolyte i_l and the current density in the active material i_s. Here, the index k symbolizes the partial reactions at the negative and positive electrode. The heat transfer is considered by convection

$$\dot{Q}_{conv} = h A_{\text{cell}} (T - T_\infty) \tag{3.40}$$

with the heat transfer coefficient h and the cell's surface area A_{cell}. T marks the absolute temperature and T_∞ the ambient temperature. The radiation is calculated by

$$\dot{Q}_{rad} = \varepsilon_{th} \sigma_B A_{\text{cell}} \left(T^4 - T_\infty^4 \right) \tag{3.41}$$

in which ε_{th} describes the surface emissivity and σ_B the Stefan-Boltzmann constant. In addition, the cell's thermal mass is considered by

$$\dot{Q}_{th} = m_{\text{cell}} c_p \frac{\partial T}{\partial t} \tag{3.42}$$

with its mass m_{cell} and specific heat capacity c_p. Thus, the governing equation is described by

$$m_{\text{cell}} c_p \frac{\partial T}{\partial t} = V_{\text{cell}} \frac{1}{l_{\text{cell}}} \int_{x=0}^{l_{\text{cell}}} \dot{q}\ \mathrm{d}l - h A_{\text{cell}} \left(T - T_\infty \right) - \varepsilon_{th} \sigma_B A_{\text{cell}} \left(T^4 - T_\infty^4 \right) \tag{3.43}$$

with the cell volume V_{cell} and the thickness of a cell layer l_{cell}.

Arrhenius

The temperature dependency of the anodic and cathodic reaction rate constants (k_a and k_c) and the diffusion coefficients in the negative and positive active material ($D_{s,\text{neg}}$ and $D_{s,\text{pos}}$) are described by the Arrhenius equation

$$\Psi = \Psi_{\text{ref}} \exp \left(\frac{E_{a,\Psi}}{R} \left(\frac{1}{T_{\text{ref}}} - \frac{1}{T} \right) \right) \tag{3.44}$$

with $E_{a,\Psi}$ as the activation energy. Ψ marks the dependent variable and Ψ_{ref} its reference value at the reference temperature T_{ref}.

The temperature dependency of the diffusion coefficient in the electrolyte D_l, the liquid phase conductivity κ and the thermodynamic factor $\frac{\partial \ln f_\pm}{\partial \ln c_l}$ are often taken from Valøen et al. [96].

Modeling environment

We used the software COMSOL Multiphysics® [97] (versions 5.2a-5.4) including its physics interfaces and multiphysics couplings to develop our electrical, thermal and aging models. To run the simulations in general and the cyclic aging models in particular and to analyze the simulation results, we applied MATLAB® [98] and the interface LiveLink™ [99].

4 Aging in 18650-type Li-Ion Cells Examined with Neutron Diffraction, Electrochemical Analysis and Physicochemical Modeling

Within this chapter, the article *Aging in 18650-type Li-ion cells examined with neutron diffraction, electrochemical analysis and physico-chemical modeling* is presented.

In this paper, we showed the aging behavior of 18650-type lithium-ion cells examined with neutron diffraction and electrochemical analysis. Furthermore, we developed a physico-chemical aging model considering the early stage, linear capacity fade.

The investigated cells were composed of graphite as the negative electrode and $LiNi_{0.33}Mn_{0.33}Co_{0.33}O_2$ (NMC) as the positive electrode and were manufactured under commercial standards in a joint venture between Volkswagen and VARTA Microbattery.

The aging experiment was performed for 1000 cycles at a controlled temperature of 23 °C. The general test procedure was as follows: CC discharge with 1C to a cutoff voltage of 2.5 V, followed by a CC charge with 1C to a cutoff voltage of 4.1 V and a CV charge with a cutoff current of C/20 using a Maccor battery tester. This results in a capacity loss of 21 % relative to the cell's initial capacity.

We performed in-situ neutron diffraction measurements under ambient conditions at the high-resolution powder diffractometer SPODI and carried out Rietveld refinements to identify crystalline phases, estimated their phase fractions and derived lattice parameters to thus analyze the cyclable lithium content in the electrodes and structural changes caused by aging. Both uncycled and cycled cells were investigated in their charged and discharged states.

For the lithiated negative electrode, the neutron diffraction experiment revealed a decrease in the intensity of the LiC_6 (001) reflection peak and an increase in the intensity of the LiC_{12} (002) reflection peak on aging. Based on the Rietveld refinement of the complete neutron diffractogram of the lithiated negative electrode, we extracted phase fractions of the LiC_6 and LiC_{12} phases. From the phase fractions, we calculated molar ratios to thus derive the electrode's stoichiometry that relates to its lithium content. Here, we observed a shift in stoichiometry from $x = 0.84 \pm 0.02$ for the uncycled cell to $x = 0.65 \pm 0.02$ for the cycled cell. For the delithiated negative electrode, only a pure C (002) phase is visible for both the cycled and the uncycled cell indicating a complete extraction of lithium. The lattice parameters of the hexagonal graphite (space group $P6_3/mmc$) C_6, LiC_6 and LiC_{12} phases show no appreciable differences between the cycled and the uncycled cell except for a slight change in the c lattice parameter of the C_6 phase.

The lithiated positive electrode shows shifts in the angular positions of the NMC (003), NMC (012) and NMC (006) reflections on aging caused by changing lattice parameters. Based on the c/a lattice parameter ratio, the stoichiometry y in $Li_yNi_{0.33}Mn_{0.33}Co_{0.33}O_2$ is calculated based on a linear regression by Buchberger et al. [100] as $y = 0.89 \pm 0.02$ for the uncycled cell and $y = 0.81 \pm 0.02$ for the

cycled cell. For the delithiated positive electrode, the neutron diffraction experiment revealed similar angular positions of these NMC reflections and thus no differences in lattice parameters. From the c/a ratio, we calculated a stoichiometry of $y = 0.54 \pm 0.02$ for both the cycled and the uncycled cell.

After the ND experiment, we carried out cycling experiments at low currents of C/50 to derive the cell's equilibrium potential for model parametrization and DVA as well as GEIS at 100 % SOC for frequencies ranging from 5 mHz to 1 kHz for impedance analysis using a Biologic VMP3 potentiostat. Based on the equilibrium potential, the aged cell shows an increased polarization due to higher overpotentials. This is consistent with an increase in the internal resistance from 16 mΩ for the uncycled cell to 28 mΩ for the cycled cell derived from the GEIS measurements. Additionally, we observed increasing SEI and charge transfer resistances as seen in broadening semi-circles in their Nyquist plot. The DVA reveals distinctive material markers that are phase changes of the lithiated graphite. [86] A first batch of peaks at lower charge states of the cell corresponds to low lithiation stages such as LiC_{24} and LiC_{48}. Furthermore, a second peak at about 50 % SOC marks the transition of these stages into a pure LiC_{12} phase with a coexistance of LiC_6 and LiC_{12} phases thereafter. Based on the DVA results, negative electrode active material loss cannot be confirmed. Distinctive material markers that refer to the positive electrode cannot be assigned in the DVA curves.

We developed a physicochemical model as introduced in Section 3.6 and included SEI re-/formation in the negative electrode as aging mechanism. SEI formation on intact graphite particles is considered as a first side reaction and SEI re-formation due to cracking of the SEI layer caused by the expansion and contraction of the graphite particles during cycling as a second side reaction. Both side reactions are considered to be irreversible and implemented by cathodic Tafel equations. Integrating the side reaction current gives a charge quantity that results in the thickness of the SEI layer. The resistance of the SEI layer is proportional to the thickness and increases over time. It causes an additional overpotential for the main and side reactions. The model parameters are measured by the cell manufacturer (e.g. geometry parameters), deduced from the ND measurements (e.g. initial state of charge) or taken from the literature (e.g. transport parameters). We ran the simulations according to the testing procedure of the aging experiment and reproduced a capacity loss of 21 % after 1000 cycles. The simulated voltage of a C/50 discharge agrees with the measured ones for the uncycled and cycled cells with a maximum deviation of 15 mV. Furthermore, the model reveals a shift in the stoichiometry of the lithiated negative electrode from $x = 0.84$ for the uncycled cell to $x = 0.67$ for the cycled cell. For the lithiated positive electrode, the stoichiometry decreases from $y = 0.89$ to $y = 0.81$ on aging. The stoichiometries of the delithiated negative and positive electrodes remain unchanged.

These results reveal the dominant aging mechanism to be LLI as experimentally investigated by in-situ ND and confirmed by physicochemical modeling. Additional aging mechanisms that cause deactivation or undesirable phase transformations of electrode materials are excluded from the detailed evaluation of neutron diffractograms, within the experimental accuracy of the method.

his expertise in the field of electrochemical modeling. The manuscript was written by Neelima Paul, Jonas Keil and Ludwig Kraft and was edited by Frank M. Kindermann, Ralph Gilles and Andreas Jossen. All authors discussed the data and commented on the results.

Aging in 18650-type Li-ion cells examined with neutron diffraction, electrochemical analysis and physico-chemical modeling
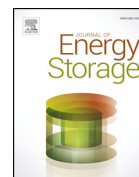
Neelima Paul, Jonas Keil, Frank M. Kindermann, Sebastian Schebesta, Oleksandr Dolotko,
Martin J. Mühlbauer, Ludwig Kraft, Simon V. Erhard, Andreas Jossen, Ralph Gilles

Permanent weblink:
`https://doi.org/10.1016/j.est.2018.03.016`

Aging in 18650-type Li-ion cells examined with neutron diffraction, electrochemical analysis and physico-chemical modeling

Neelima Paul[a,*], Jonas Keil[b], Frank M. Kindermann[b], Sebastian Schebesta[c], Oleksandr Dolotko[a], Martin J. Mühlbauer[a,d,e], Ludwig Kraft[b], Simon V. Erhard[b], Andreas Jossen[b], Ralph Gilles[a]

[a] Heinz Maier-Leibnitz Zentrum, Technical University of Munich (TUM), 85747 Garching, Germany
[b] Institute for Electrical Energy Storage Technology, Technical University of Munich (TUM), 80333 Munich, Germany
[c] VW-VM Forschungsgesellschaft mbH and Co. KG, 73479 Ellwangen, Germany
[d] Institute for Applied Materials (IAM), Karlsruhe Institute of Technology (KIT), Hermann-von-Helmholtz-Platz 1, 76344 Eggenstein-Leopoldshafen, Germany
[e] Helmholtz-Institute Ulm for Electrochemical Energy Storage (HIU), P.O. Box, 76021 Karlsruhe, Germany

ABSTRACT

Aging in NMC/C cells (NMC-$Li_y(Ni_{0.33}Mn_{0.33}Co_{0.33})O_2$), cycled 1000 times at a $1C$ rate, has been characterized by *in situ* neutron diffraction and electrochemical analysis. These experimental results have been validated by a physico-chemical aging model, which attributes capacity fade to growth of a continuous SEI film on the anode. Neutron diffraction of the cells indicate a cyclable lithium loss corresponding to a capacity fade of about 23% in both electrodes of the cycled cell. The cycled cell suffers an anode stoichiometry shift from $x = 0.84$ to $x = 0.65$ in Li_xC_6 ($0 \leqslant x \leqslant 1$) in its fully charged state and a cathode stoichiometry shift from $y = 0.89$ to $y = 0.81$ in $Li_y(Ni_{0.33}Mn_{0.33}Co_{0.33})O_2$ ($0 < y \leqslant 1.05$) in its fully discharged state. Anode ($x = 0$) as well as cathode stoichiometries ($y = 0.54$) remain practically unchanged in the cell's fully discharged and charged states, respectively. These stoichiometry shifts match well with those derived from the model, and both neutron diffraction and model are in good agreement to the electrically determined capacity fade of 21%. In fact, cyclable lithium losses slightly exceed this value. Thus, capacity fade in these cells is mainly due to loss of cyclable lithium into the continuous growth of a SEI film on the anode surface.

1. Introduction

Due to their high energy and power densities, Li-ion batteries are the most favored rechargeable systems in portable electronic devices [1]. Nowadays they are gaining popularity in electric transportation and stationary grid storage systems as well. These large-scale applications demand much longer battery lifespans and thus an understanding of aging mechanisms responsible for reducing lifetime or cycle life is essential [2,3]. The most common cathode material used in commercial portable Li-ion batteries is $LiCoO_2$ (LCO) due to its high energy density and good cycling performance. However, Co is expensive and considered toxic. For electric vehicles, $Li_y(Ni_{0.33}Mn_{0.33}Co_{0.33})O_2$ (NMC) seems to be the more preferred cathode materials as their layered structure is more stable, changes in lattice volume are smaller (for $y > 0.5$), and thereby safety and lifetime are enhanced. At the cost of a comparatively lower energy density, $LiFePO_4$ (LFP) cathodes offer an even better cycling performance and safety, and are usually the optimal choice for stationary grid storage systems.

Several experimental methods are being used to understand Li-ion

batteries during storage as well as during operation [4]. Analytical methods such as electrochemical impedance spectroscopy, microscopy, X-ray and neutron diffraction addressed aging and attributed loss of cyclable lithium and decay of electrode materials as the most important capacity fade mechanisms [5–12]. These occurred due to solid-electrolyte interphase (SEI) layer growth, volume changes in the electrodes during Li-ion intercalation/deintercalation, blockage and structural degradation, Li plating, as well as undesirable phase transformations of active electrode materials. There are several studies which have investigated battery aging by comparing experimental results with simulation models [13–17]. For example, a SEI electron tunneling model, which attributed electron tunneling through the inner SEI layer as the rate determining step, was proposed and simulated to explain capacity fade during storage and cycling by Li et al. [15,16]. This model was validated by experiments on commercial prismatic LFP/C cells. However, no study compared results from aging models to neutron diffraction data. In particular, there is no reported investigation where experimentally observed capacity fading results in 18650-type NMC/C cells using neutron diffraction are compared with a physico-chemical

---

model. For non-destructive *in situ* studies of such large format Li-ion cells, neutron diffraction is a suitable and powerful method. Several types of Li-ion cells, such as LCO/C [18,19], NMC/C [20,21] and LFP/C [22–24] have been investigated using neutrons as a probe. These investigations addressed Li plating on the anode [25,26], structural changes within the cathode [21] and spatially resolved inhomogeneities in current densities [27–29] in both prismatic as well as 18650-type cells. However, aging studies in 18650-type cells with neutron diffraction are rare [11,30,12,31,32]. In a recent investigation of aging in commercial 18650-type NMC/C cells with neutrons, capacity fade was attributed to loss of cyclable lithium and cathode material degradation [12]. Our studies investigate the cycling induced aging in similar cell chemistry in more details using additionally physico-chemical modeling and electrochemical analysis.

2. Experimental techniques

2.1. Cell description

Cylindrical 18650-type NMC/C cells, produced under commercial standards, were provided by the battery manufacturer (VW-VM Forschungsgesellschaft mbH and Co. KG, a joint venture between Volkswagen and VARTA Microbattery GmbH). Each cell consisted of a $Li_{1.05}(Ni_{0.33}Mn_{0.33}Co_{0.33})_{0.95}O_2$ cathode, an organic carbonate based electrolyte (containing 1 M $LiPF_6$ conducting salt as well as SEI forming and overcharge protecting additives), a monolayer polyolefin-based separator and a graphite anode. The single cathode and anode layers were 63 μm and 47 μm thick, contained about 2 wt.% binder and were coated double-sided on Al-foil and Cu-foil respectively. The cathode contained 3 wt.% highly graphitic carbon as well. The cell balancing was adjusted to obtain an anode/cathode capacity ratio of 1.06. The active material densities of the positive and negative electrodes were 3.28 g cm^{-3} and 1.50 g cm^{-3}, respectively. The cell formation was done by charging and discharging the pristine cells at $C/10$ followed by micro short-circuit detection and cycles for capacity and inner resistance measurement. After cell formation, one cell (labelled as 'uncycled cell' in this work) was stored in a 20% state of charge (SOC) at 23 °C, which relates to 20% of the initial cell capacity. The other cell (labelled as 'cycled cell' in this work) was cycled for 1000 cycles between 2.5 V and 4.1 V (with a $1C$ rate at 23 °C) by the battery manufacturer. Simultaneously, two other similar cells were stored and cycled to check the reproducibility of the capacity fade behavior for the cells used in the manuscript. After long term cycling procedure and an additional waiting period of about two years, neutron diffractograms of both uncycled and cycled cells were taken in their fully charged and fully discharged states. Due to the additional waiting period, both cells underwent calendric aging which resulted in a 6% individual capacity fade. For one of the cells, neutron diffractogram was taken at 20% SOC as well, to check the structure at an intermediate state. This particular intermediate SOC was chosen as cells are usually kept in this condition during storage.

2.2. Electrochemical techniques

Long term cycling for 1000 cycles was performed with a CCCV charge (constant current charging to 4.1 V, followed by a constant voltage hold at 4.1 V until a current corresponding to $C/20$ is reached) and a CC discharge (to 2.5 V) with a rate of $1C$, using a Maccor battery tester. After about two years, neutron diffraction experiments were performed. Thereafter, charging and discharging experiments at low current (corresponding to a $C/50$ rate), and galvanostatic electrochemical impedance spectroscopy (GEIS) on both cells, were carried out with a Biologic VMP3 potentiostat. Electrical behavior of the cells were always compared in response to the same currents (C rates).

2.3. Neutron diffraction

Neutron diffraction measurements were performed in a Debye–Scherrer geometry under ambient conditions at the high-resolution powder diffractometer SPODI, MLZ Garching [33]. Neutrons having a wavelength of 0.1548 nm were incident on a rectangular cross section of 40 mm × 30 mm of the cell. The cell edges (about 10 mm) at the top and bottom were not illuminated by the neutron beam, to avoid signals in the diffractograms from the cell holder at the top and the remaining cell plastic cover at the bottom. A neutron detector array consisting of 80 vertical position sensitive detectors collected the neutrons scattered by the cell [34,35]. The cells were continuously rotated during the entire measurement to reduce texture effects and obtain an average signal over cell volume. Five diffractograms were measured for each cell with an acquisition time of 48 min each. Therefore, the total integration time for the averaged diffractograms for each cell was approximately 4 h. Instrumental resolution function was determined with a $Na_2Ca_3Al_2F_{14}$ reference material to calculate full widths at half maximum of reflections from the cell. To describe the peak profile shape, a Thompson–Cox–Hastings pseudo-Voigt function was used [36]. A linear interpolation between selected data points was used to fit the background. Multi-phase Rietveld refinements of structural models for the neutron diffraction data were carried out with FullProf software package [37]. For the steel housing and the current collectors, structure independent profile fits had to be used to get a better quality pattern refinement because their crystallites had strong preferred orientations.

3. Experimental results

3.1. Electrical behavior

The aging procedure of cycling the NMC/C cell was initiated after the cell formation protocol was completed. A steady and an approximately linear decrease in the discharge capacity was observed as can be seen in Fig. 1. After completing 1000 cycles, the cycled cell had suffered a capacity loss of 21% relative to the capacity of the uncycled cell. A similar approximately linear trend was seen in the other set of cells which were simultaneously stored and cycled, which supports the reproducibility of this aging study. In general, the value of discharge capacity is strongly dependent on the cycling conditions, e.g. on the C rate and the voltage limits. In this aging study, the upper voltage limit was restricted to 4.1 V and a C rate of 1 C was used. Cycling the cell with a lower C rate and with a upper voltage limit of 4.2 V would have lead to a higher value discharge capacity for these cells. In order to compare experimental studies with the model, potential profiles of the cells had to be obtained at a low current. Thus both cells underwent one more cycle, this time with a $C/50$ rate between 2.5 and 4.1 V. The
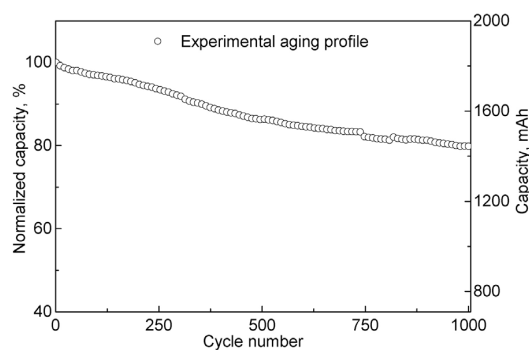

Fig. 1. Experimental aging profile of the NMC/C cell at a $1C$ rate during the long term cycling procedure. Both normalized capacity as well as discharge capacity of the cell versus the cycle number is shown.
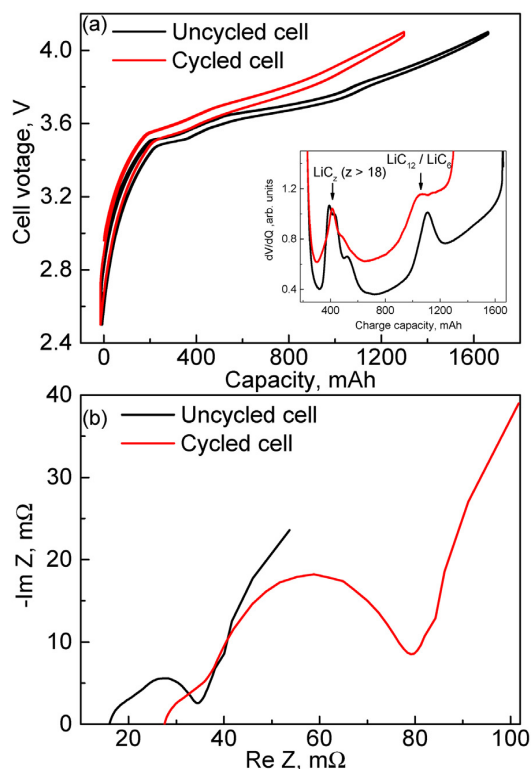
Fig. 2. (a) Experimental potential profiles of the uncycled (black line) and cycled NMC/C (red line) cells at a low current (C/50 rate). The corresponding differential voltage curves are shown in the inset. (b) Experimental Nyqist plots of charged NMC/C cells at room temperature. (For interpretation of the references to color in this figure legend, the reader is referred to the web version of this article.)

behavior of both cells was always compared at the same C rate and current, be it $1C$ in the long term cycling or C/50 in the electrical tests and model, to exclude contributions to capacity fade from dissimilar currents [38]. Fig. 2(a) compares the voltage profiles of both cells cycled with a C/50 rate and they appear similar except for the capacity difference. The change in charge/discharge overpotential or cell polarization of the cycled NMC/C cell is minor and a consequence of its larger internal resistance, which is shown in Fig. 2(b). In a recent study of 18650-type LFP/C cells, only a minimal cell polarization change was seen for cells wherein the sole aging contributer was cyclable lithium loss [31]. Moreover recent aging studies of NMC/C pouch cells under different temperature and upper cutoff potentials also indicated the same effect [39]. Thus, we already have a first indication that the capacity loss for cycled cells in this study may also be mainly due to loss of cyclable lithium.

The inset in Fig. 2(a) shows the differential voltage curves for the two cells at this low current, which indicate the phase transitions occurring in the anode during charge. Contributions from cathode can be ruled out because previous studies on NMC/C cells have shown that peaks in differential voltage curves, particularly for voltages higher than 3 V, may be exclusively attributed to staging phenomena in the negative electrode material [10]. The observed peaks are related to availability of specific Li-ion intercalation sites and result from transitions between regions of two coexisting lithiated graphite phases. The first batch of peaks, indicated by an arrow at lower charge states of the cell, corresponds to low lithiation stages (such as LiC_{24}, LiC_{48} and so on). The second arrow points to a region about 50% SOC, and corresponds to a complete transformation of these lithiation stages into a

pure LiC_{12} phase. Beyond this region, coexistence of LiC_6 (denoted as Stage I) and LiC_{12} (denoted as stage II) phases is observed. In the cycled cell, these peaks have reduced in intensity, broadened and slightly shifted in position. Speculatively, these are a consequences of local inhomogenities due to a slower rate of Li-ion intercalation into graphene layers, or increase in the available surface area of graphite (due to microstructural changes), leading to a virtual reduction in the amount of active graphite participating in the formation of the LiC_{12} phase.

In Fig. 2(b), GEIS data, acquired at 100% SOC for frequencies ranging from 5 mHz to about 1 kHz, are shown. The uncycled and cycled cells show internal resistances of about 16 mΩ and 28 mΩ, respectively. Their charge-transfer resistances, indicated by the semi-circles are predominantly due to the SEI and active surface area in the two cells. The uncycled cell shows a charge-transfer resistance of 13 mΩ whereas the cycled cell shows a higher charge-transfer resistance of about 43 mΩ. Such an impedance rise in the mid frequency region, noticable as a increase in the diameter of the semi-circles, is generally attributed to electrolyte decomposition towards SEI growth [8,12] Therefore the observed increase in impedance could be due to hinderance to the electronic/ionic transfer from continual growth and reconstruction of the SEI layer during cycling. Though these electrical measurements imply that capacity fade is mainly from reduction in cyclable lithium content due to the continual growth of an SEI layer, possibilities of a slowed diffusion rate and active material loss cannot be completely ruled out. Neutron diffraction can shed light on the possible structural degradation of the electrode materials, active material loss (within the experimental accuracy), and on the change in the amount of cyclable lithium.

3.2. Structural behavior

Both anode and cathode materials undergo structural changes due to the Li intercalation/deintercalation process. Neutron diffraction measurements as well as Rietveld refinements were done on the uncycled and cycled cells to identify crystalline phases, estimate their phase fractions, lattice parameters, and consequently cyclable Li content in the electrodes. The complete diffractograms for the fully charged state and the fully discharged state are shown in Figs. 3 and 4, along with their Rietveld refinements. A high background is observed due to the incoherent scattering of neutrons by hydrogen in the electrolyte and separator. It has a tendency to slightly increase with angle but is basically similar for all cells.

3.2.1. Anode

In both cells, LiC_6 and LiC_{12} reflections of the lithiated anode material are clearly visible in the fully charged state. No LiC_z reflections with $z > 12$, corresponding to phases with low lithium content such as LiC_{18} or LiC_{24}, are observed in either cell for this state of charge. From Fig. 5(a), one notes a decrease in the intensity of the $LiC_6(001)$ reflection peak and an increase in the $LiC_{12}(002)$ reflection peak on aging. It is difficult to say if the tiny C(002) reflection at $2\theta = 26.6°$ is from the anode or from the graphitic carbon of the cathode. Its intensity is similar in both cells and seems unaffected by aging. The mean lithium content in a carbon anode in its charged state can be estimated from phase fractions of lithiated anode phases (LiC_6 and LiC_{12}). For example, for anode/cathode capacity ratio of 1, existence of a sole LiC_6 phase would correspond to 100% lithiation of the carbon anode and existence of a sole LiC_{12} phase would correspond to a 50% lithiation of the carbon anode [25]. The mean lithium content can be described by a parameter x in Li_xC_6 ($0 \leqslant x \leqslant 1$). Differences in mean lithium content or anode stoichiometry for fully charged and fully discharged anodes of the uncycled and cycled cells provide an estimation of cyclable lithium losses in the anode. Phase fractions of LiC_6 and LiC_{12} phases were extracted from Rietveld refinement of the complete neutron diffractogram, converted into molar ratios and finally into mean lithium contents, as
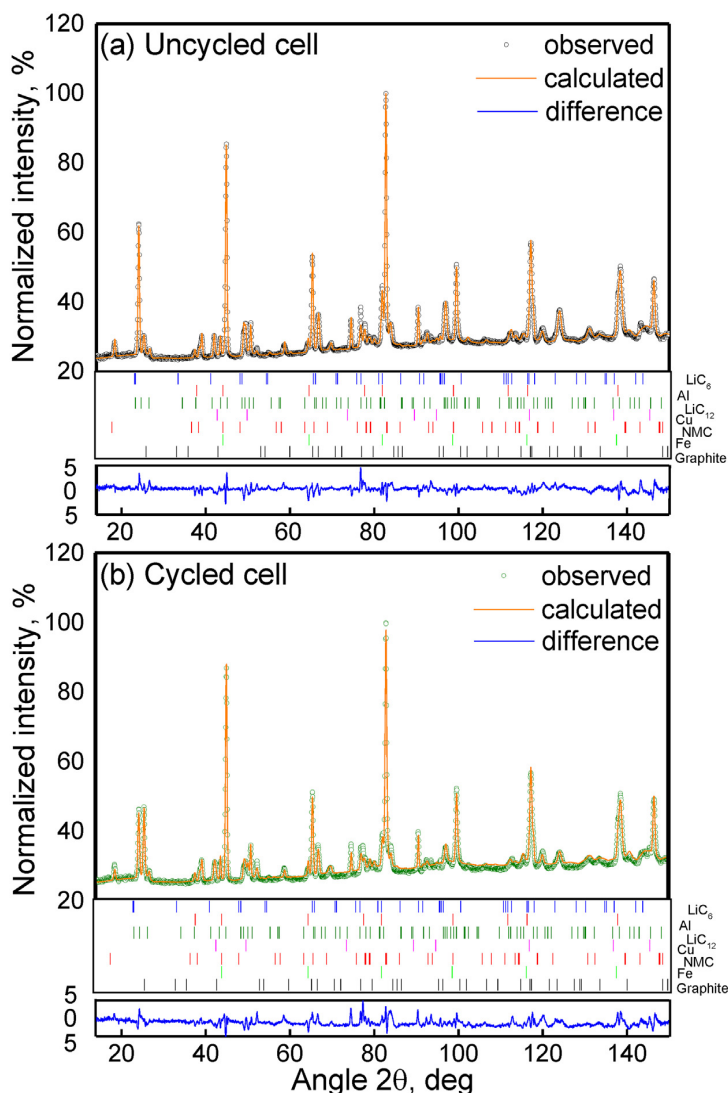
Fig. 3. Neutron diffractograms of the (a) uncycled and (b) cycled NMC/C cells, measured in their fully charged states. Experimental data are shown in circles (black – uncycled and green – cycled) along with their Rietveld refinements (orange line). The blue lines mark the difference between data and fit. Vertical bars above the blue line indicate Bragg reflections corresponding to crystalline phases in the cell (from top to bottom: LiC_6, Al, LiC_{12}, Cu, NMC, Fe and graphite). (For interpretation of the references to color in this figure legend, the reader is referred to the web version of this article.)

shown in Tables 1 and 2. For the uncycled cell, mean lithium content was $x = 0.84 \pm 0.02$ and for the cycled cell, it was $x = 0.65 \pm 0.02$.

In Fig. 4, diffraction data for the cells in their fully discharged state is shown. The anode is completely delithiated as only the pure graphite phase is visible. This is clearly evident in Fig. 5(b) where only a pure C(002) reflection is visible, indicating a complete extraction of lithium from the anode. Anode stoichiometry in the discharged state corresponds to a mean lithium content, $x = 0$ for both cells. A slight broadening (FWHM: 0.428° to 0.443°) in the graphite peak was observed for the aged cell, which might correspond either to a reduction in the crystallite size of the anode material or microcrack formation. Such a microstructural change would result in an increase of available graphite surface for Li intercalation/deintercalation, which could explain the increased consumption of cyclable lithium for SEI growth on the newly formed graphite area. Table 3 shows the lattice parameters of the hexagonal graphite (space group $P6_3/mmc$) C_6, LiC_6 and LiC_{12} phases as determined by Rietveld refinement of the neutron diffraction

data in Figs. 3 and 4, according to their structural models. Other than a slight increase in the c lattice parameter for the C_6 phase, no appreciable differences in lattice parameters for any phase are observed upon cycling.

Fig. 6(a)–(c) are a zoom into a selected region of the neutron diffractograms, and show the prominent reflections of anode at three different states of charge. At SOC 100, LiC_6 (001) and LiC_{12} (002) reflections are seen along with a small C(002) reflection. At SOC 20, these reflections are replaced by a higher stage lithiated graphite reflection – LiC_z ($z > 12$) ($d = 0.3480 \pm 0.0003$), which some designate as a LiC_{24} reflection [22] while others designate it as LiC_{18} reflection [38]. As per Dahn et al., its angular position would suggest an anode stoichiometry of $Li_{0.35}C_6$ [40]. For the fully discharged cell, only the C(002) reflection can be seen. This shifting of the (002) graphite related reflections towards higher angles on discharge, is due to the contraction of c-axis on expulsion of lithium from the lithiated graphite and continues till a pure graphite phase is formed.
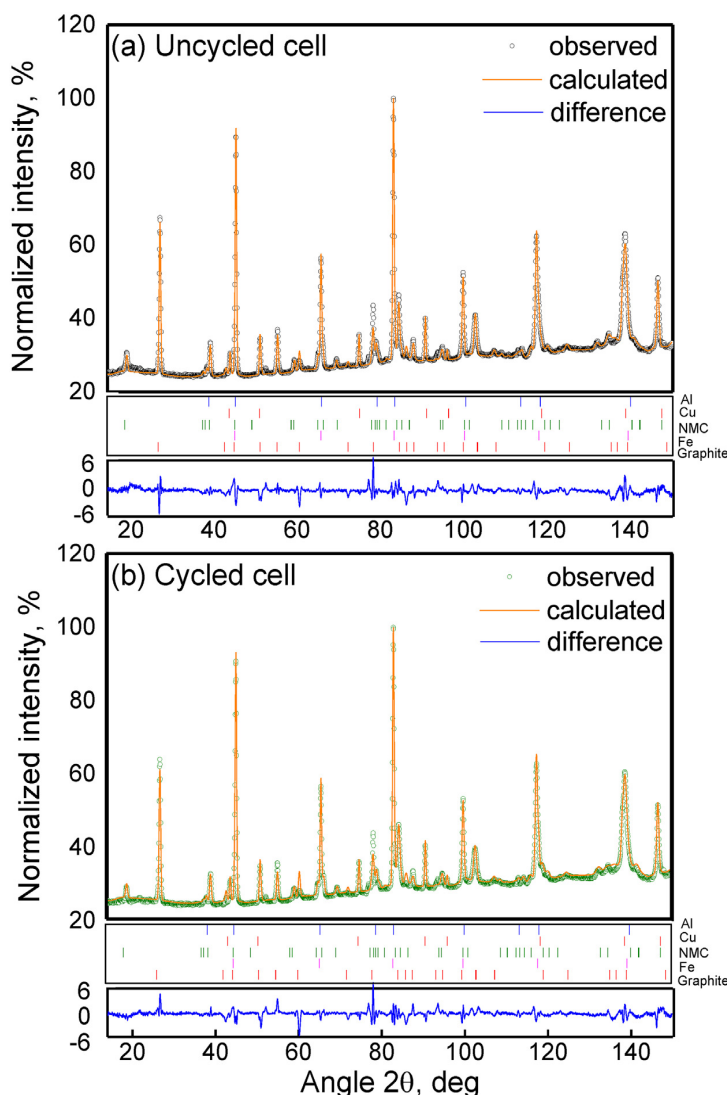
Fig. 4. Neutron diffractograms of the (a) uncycled and (b) cycled NMC/C cells, measured in their fully discharged state. Although (a) and (b) appear similar, significant differences are observable in a magnified view. Experimental data are shown in circles (black – uncycled and green – cycled) along with their Rietveld refinements (orange line). The blue lines mark the difference between data and fit. Vertical bars above the blue line indicate Bragg reflections corresponding to crystalline phases in the cell (from top to bottom: Al, Cu, NMC, Fe and graphite.) (For interpretation of the references to color in this figure legend, the reader is referred to the web version of this article.)

3.2.2. Cathode

For the fully charged state of the cells, the well-known NMC (003) and NMC (012) reflections, shown in Fig. 5(c), are at similar angular position of $2\theta = 18.45°$ and $2\theta = 39.13°$ for both cells. From Table 4, no differences in lattice parameters between the uncycled and the cycled cell for their charged state can be seen. Rietveld refinements also result in a constant value of $z/c = 0.236$ for the refined fractional coordinate of the oxygen atoms on the 6c site (0,0,z) for both cells. This parameter gives an estimation of interlayer distances between the oxygen layers and the value obtained here is similar to the value obtained by Dolotko et al. for NMC based 18650 cells [11]. Thus, the average charge at the oxygen ions is similar due to an identical lithium content in the cathodes. From the c/a value, which is about 5.135 in both cells, lithium content corresponding to $y = 0.54$ in $Li_y(Ni_{0.33}Mn_{0.33}Co_{0.33})O_2$ is calculated as per the procedure given by Buchberger et al. for NMC based pouch cells [39]. Interestingly, the Li content within the cathode (in its fully charged state) does not change on cell aging. Note that the same amount of charging current had been provided to both cells. No unidentified isolated peaks are observed in the diffractograms. These results rule out any deterioration or

undesirable phase transformation of the cathode material on aging. On going from charged state to a discharged state, the Li-O bond length of the uncycled cell decreases from 0.2149 nm to 0.2126 nm whereas the M–O bond lengths increases from 0.1915 nm to 0.1941 nm due to increase in ionic radius of the transition metals. A similar trend, but with a smaller magnitude, is seen for the cycled cell. A decrease in the Li–O interatomic distances on lithiation or lithium insertion, typical for such transition metal oxides, is related to the reduction in the c lattice parameter.

A complete discharge of the uncycled cell causes the NMC (003) reflection to shift from $2\theta = 18.45°$ to $2\theta = 18.72°$ (see Fig. 5(d)) corresponding to a contraction of unit cell in the c direction. This is a consequence of reduction in the electrostatic repulsion between the oxygen layers due to reduction in the partial screening of charge by lithium ions. On the other hand, the a lattice parameter, which is influenced by M–O bond lengths, is increased. From Table 4, although a similar trend is seen for the cycled cell, the c lattice parameter is not reduced to the same magnitude as in the uncycled cell. The cycled cell has, in comparison, a larger c lattice parameter and a slightly smaller a lattice parameter. Such changes typically indicate a reduction in
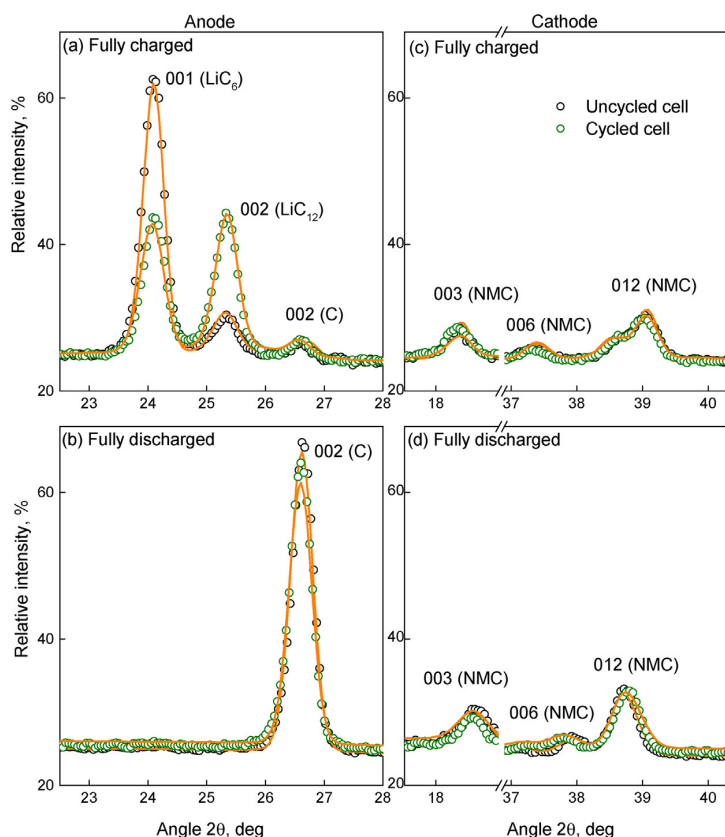
Fig. 5. Selected regions of the neutron diffractograms from Figs. 3 and 4 showing (a) a significant decrease in the LiC_6 (001) reflection intensity and an increase in LiC_{12} (002) reflection intensity in the charged cell on aging. The weak C (002) reflection is unchanged and could be due to conductive carbon in the cathode. (b) Discharged cells show only C (002) reflection indicating a complete extraction of lithium from the anode. (c) The Bragg positions of the NMC (003), NMC (006) and NMC (012) reflections are unaltered in the charged state upon aging. (d) In the discharged state, Bragg positions of the NMC (003), NMC (006) and NMC (012) reflections are slightly shifted due to reduced cyclable lithium content in the aged cell.

Table 1
Molar fractions of the LiC_6 and LiC_{12} phases, as obtained by Rietveld refinement of neutron diffractograms of the charged cells according to their structural models.

Molar fractions	Uncycled	Cycled
LiC_6	0.81 ± 0.02	0.45 ± 0.02
LiC_{12}	0.19 ± 0.02	0.55 ± 0.02

Table 2
Lithium content x in Li_xC_6 as obtained from LiC_6 and LiC_{12} phase fractions by Rietveld refinement of neutron diffractograms.

Li content anode	Uncycled	Cycled
Charged cells:		
x in Li_xC_6	0.84 ± 0.02	0.65 ± 0.02
Discharged cells:		
x in Li_xC_6	0	0

Table 3
Lattice parameters of the anode, as determined by Rietveld refinement of neutron diffractograms according to the structural models of the C_6 phase in the discharged cell and LiC_6 and LiC_{12} phases in the charged cell.

Lattice parameters – anode	Uncycled cell	Cycled cell
C_6-a, nm	0.2462 ± 0.0002	0.2463 ± 0.0002
C_6-c, nm	0.6712 ± 0.0002	0.6718 ± 0.0002
LiC_{12}-a, nm	0.4282 ± 0.0003	0.4286 ± 0.0003
LiC_{12}-c, nm	0.7047 ± 0.0003	0.7044 ± 0.0003
LiC_6-a, nm	0.4319 ± 0.0002	0.4318 ± 0.0002
LiC_6-c, nm	0.3700 ± 0.0002	0.3701 ± 0.0002

amount of cyclable lithium content in the cathode and have also been reported earlier for LCO/C cells [30]. From the different c/a values (5.011 for the uncycled cell and 5.039 for the cycled cell), Li contents corresponding to $y = 0.89$ and $y = 0.81$ in $Li_y(Ni_{0.33}Mn_{0.33}Co_{0.33})O_2$ were calculated and are displayed in Table 5.

Fig. 6(d)–(f) shows selected regions of the neutron diffractograms containing reflections from cathode at three different states of charge. The Bragg positions corresponding to the NMC (003), NMC (006) reflections shift towards higher angles due to a contraction in the c axis on Li-ion incorporation. On the other hand, the NMC (012) reflection shifts towards lower angles. For the cycled cell at SOC 20, lithium content $y = 0.69$ in $Li_y(Ni_{0.33}Mn_{0.33}Co_{0.33})O_2$ can be extracted from its c/a value of 5.082.

4. Development of a physico-chemical model

Physico-chemical modeling of Li-ion cells gains insights to investigate and describe the cell's behavior based on particle and electrode effects [41]. In contrast to first-principle or empirical models, physico-chemical models are suitable not only to describe surface and molecule processes in a phenomenological manner but also to describe particle and electrode domains in a mechanistical manner. We developed a physico-chemical aging model on the basis of a one-dimensional intercalation model approach based on the work of Fuller, Doyle and Newman [42–44]. The developed model is a one-dimensional representation of the cell, which is coupled to a second dimension representing the active material particles, hence it is also referred to as a pseudo two-dimensional (p2D) model. Fig. 7 shows a schematic drawing of this one-dimensional model of the cell with its x-direction perpendicular to the cell layers. As one can see, only one particle size and no size distribution is assumed for particles of each electrode. The
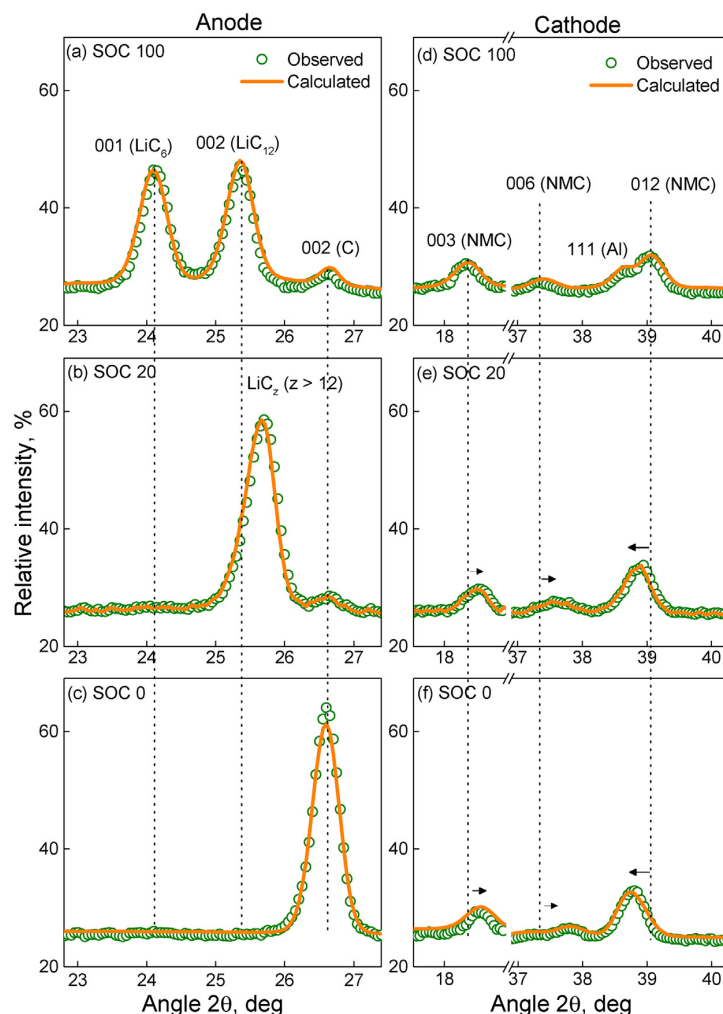
Fig. 6. Selected regions of the neutron diffractograms from cycled cells at three different states of charge. (a) At SOC 100, LiC$_6$ (001) and LiC$_{12}$ (002) reflections are seen along with a small C (002) reflection. (b) At SOC 20, these reflections are replaced by a higher stage lithiated graphite reflection LiC$_z$ ($z > 12$). (c) At SOC 0, only the C(002) reflection is visible. (d), (e) and (f) Bragg reflections of the NMC (003), NMC (006) shift towards higher angles whereas NMC (012) reflections shift towards lower angles during cell discharge.

Table 4
Lattice parameters of the cathode, as determined by Rietveld refinement of neutron diffractograms according to the structural models of the NMC phase.

Lattice parameters – cathode	Uncycled cell	Cycled cell
Charged cells:		
NMC-*a*, nm	0.2819 ± 0.0002	0.2819 ± 0.0002
NMC-*c*, nm	1.4480 ± 0.0002	1.4484 ± 0.0002
Discharged cells:		
NMC-*a*, nm	0.2848 ± 0.0002	0.2843 ± 0.0002
NMC-*c*, nm	1.4273 ± 0.0002	1.4323 ± 0.0002

Table 5
Lithium content in the Li$_y$(Ni$_{0.33}$Mn$_{0.33}$Co$_{0.33}$)O$_2$ (NMC) phases, as obtained from their c/a ratios by Rietveld refinement of their neutron diffractograms.

Li content	Uncycled	Cycled
Charged cells:		
y in Li$_y$(Ni$_{0.33}$Mn$_{0.33}$Co$_{0.33}$)O$_2$	0.54 ± 0.02	0.54 ± 0.02
Discharged cells:		
y in Li$_y$(Ni$_{0.33}$Mn$_{0.33}$Co$_{0.33}$)O$_2$	0.89 ± 0.02	0.81 ± 0.02

model describes inhomogeneous current densities along the *x*-direction effecting inhomogeneous lithium distributions both in the solid and liquid phase. As a result, the SEI growth is much more pronounced next to the separator than it is next to the current collector. Inhomogeneities along the *y*- and *z*-directions of the electrodes are neglected within this model. The model takes a Li-ion reduction side reaction describing SEI growth into account, which results both in a loss of cyclable lithium as well as an increase of the SEI resistance. In a recent paper, we had

shown a good agreement between experimental and simulation results for various temperatures as well as potential windows with a similar aging model for the same cell chemistry [45]. In this work, we focus on the dependencies between neutron diffraction measurements, electrochemical analysis and physicochemical modeling. We use measured cell parameters (e.g. electrodes thickness and particle radii) and values from literature (e.g. solid diffusivity and conductivity) and validate the model with electrochemical measurements as well as neutron diffraction data for the initial uncycled cell. After simulation of aging processes during 1000 cycles is carried out, cyclable lithium loss and the
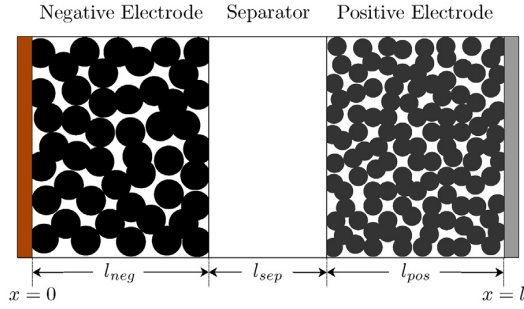
Fig. 7. Schematic drawing of the physico-chemical Li-ion model.

shift in the electrodes stoichiometries can be extracted. If loss of cyclable lithium is the sole aging mechanism as predicted from neutron diffraction measurements, the model would predict a similar reduction in lithium content within both electrodes of the cycled cell as well as reproduce a similar capacity fade and potential profiles as obtained experimentally from electrochemical measurements.

4.1. Description of the one-dimensional intercalation model

The model consists of a negative electrode, a separator and a positive electrode. The total length of the model is the summation of the three domains

$$l = l_{neg} + l_{sep} + l_{pos} \tag{1}$$

All domains are considered as porous media. The electrolyte fills the gaps between the particles and carries the Li-ions in the cell. The transportation of Li-ions is caused by three mechanisms: diffusion, migration and convection. However, convection plays only a minor role in Li-ion cells and can be neglected. A charge transfer can take place at the boundary of electrolyte and active material. The electrolyte and the active material are expressed by liquid and solid phase, respectively. The solid phase of the separator has no active material for intercalation/deintercalation, so the charge transfer can only take place in the two electrodes. The model assumes that at each point on the one-dimensional axis in the electrodes there can be a charge transfer between the liquid electrolyte phase and the solid particle phase. The extension to the particle dimension is the reason why the model is also regarded as a pseudo two-dimensional model. The intercalation/deintercalation process of the charge transfer is modeled via Butler–Volmer kinetics [44], which yields a charge transfer current density i depending on the overpotential η

$$i = i_0 \left(\exp\left(\frac{\alpha_a F}{RT} \eta \right) - \exp\left(-\frac{\alpha_c F}{RT} \eta \right) \right) \tag{2}$$

where i_0 describes the exchange current density of the reaction and α_a and α_c the anodic and cathodic charge transfer coefficients, respectively. F is Faraday's constant, R the universal gas constant and T the local temperature. The overpotential is calculated as the difference between the electrode potential and the electrode equilibrium potential. The electrode potential again results from the difference between the solid phase potential Φ_s and the liquid phase potential Φ_l. In our case the overpotential furthermore has to be adapted to the voltage drop over the SEI layer which is caused by its resistance R_{SEI}

$$\eta = \Phi_s - \Phi_l - E_{eq} - iR_{SEI} \tag{3}$$

The equilibrium potential for intercalation electrodes depends on the material combination and the SOC. The model considers a graphite anode and NMC cathode as described for the experiments above. Equilibrium potential curves from previous research of Safari et al. [46] and Tippmann et al. [47] were used to describe the anode and the cathode, respectively. The exchange current density in Eq. (2) is a

function that depends on the local concentration of Li-ions at the electrode-electrolyte interface in the solid and liquid phase

$$i_0 = F (k_c)^{\alpha_a} (k_a)^{\alpha_c} (c_{s,\max} - c_s)^{\alpha_a} (c_s)^{\alpha_c} \left(\frac{c_l}{c_{l,\text{ref}}} \right)^{\alpha_a} \tag{4}$$

k_c and k_a represent the cathodic and anodic reaction rate constant, respectively. c_s is the concentration of intercalated Li-ions at the solid phase particle surface of the corresponding electrode, c_l is the concentration of Li-ions in the liquid phase and $c_{s,max}$ is the maximum concentration of intercalated Li-ions. $c_{l,ref}$ is a reference concentration of the liquid phase, which is set to $1{,}000 \, \text{mol/m}^3$.

4.2. Validation of the model

The main aging mechanism that is modeled is the growth of the SEI layer at the negative electrode because this has been predicted in previous experimental studies [11]. Various papers use Tafel equations – a simplification of the Butler–Volmer equation for large values of the overpotential – to model irreversible side reactions [48–54]. A linear combination of all side reaction exchange currents generates the total side reaction exchange current

$$i_{\text{side}} = \sum_k i_{\text{side},k} \tag{5}$$

In our model, two side reactions are implemented in the anode besides the main intercalation/deintercalation reaction described in Eq. (2). The first one is a SEI layer growth on intact particles ($i_{side,1}$) and the second reaction models SEI layer cracking, due to expansion and contraction of the particles during cycling, that results in a new SEI layer formation ($i_{side,2}$). These two reactions are considered to be irreversible reductions that consume Li-ions and deposit species on the anode

$$\text{Li}^+ + e^- + \text{S} \rightarrow \text{P} \tag{6}$$

where S refers to the solvent and P to the product that is deposited. Each side reaction current can be described by a cathodic Tafel equation

$$i_{\text{side},k} = -a_k \, i_{0,\text{side}} \exp\left(-\frac{\alpha \eta F}{RT} \right) \tag{7}$$

where a_k represents a proportionality factor for the corresponding side reaction. The exchange current density $i_{0,side}$ is a constant, fitted to the capacity loss over the desired lifetime, because it cannot directly be determined. The overpotential for the side reaction is the same as stated in Eq. (3). A common redox potential for such side reactions, used by various researchers, and feasible for the considered electrolyte is 0.4 V [49,52,53,55–57]. The proportionality factor of the covered particles is a constant set to $a_1 = 0.3$. This represents the porosity of the SEI layer. The volume expansion of graphite particles during cycling is about 10% ($k_{exp} = 0.1$) [58,59]. However, cracking only takes place during charging of the cell when Li-ions are intercalated in the negative electrode and the particles expand. Additionally, it depends on the stoichiometry x in Li_xC_6 due to the different graphite stages: If $x < 0.3$ and $x > 0.7$ particle cracking is most probable [51,60,61]. Therefore, proportionality factor for cracking is defined during the charging process and is for $x < 0.3$

$$a_2 = k_{\text{exp}} \exp\left(-2 \frac{i_{\text{side},2}}{i_{1C}} \right) \tag{8}$$

and for $x > 0.7$

$$a_2 = k_{\text{exp}} \exp\left(-\frac{i_{\text{side},2}}{i_{1C}} \right) \tag{9}$$

where i_{1C} is the current density for a 1C discharge. The integrated side reaction current generates a charge density q_{SEI} that is used to describe the SEI layer growth [49,51–53,55]

$$\delta_{\text{SEI}} = \frac{q_{\text{SEI}} M_{\text{SEI}}}{\rho_{\text{SEI}} F (1 - a_1)} \tag{10}$$

M_{SEI} is the molar mass of the species depositing on the particles and creating the porous SEI layer with its density ρ_{SEI}. The porosity of the SEI layer is taken into account, which results in a thicker layer. The resistance of the SEI layer used in Eq. (3) is proportional to its thickness and thus increasing over time

$$R_{\text{SEI}} = \frac{\delta_{0,\text{SEI}} + \delta_{\text{SEI}}}{\sigma_{\text{SEI}}} \tag{11}$$

As the physico-chemical model describes the cell behavior based on electrochemical kinetics and transport equations, several geometry, thermodynamic, kinetic and transport parameters are needed. A lot of them have been measured by the battery manufacturer exactly for these cells, in particular all geometry parameters (e.g. thickness of electrodes and separator as well as mean particle radii). Other parameters like the initial state of charge can be deduced from the neutron diffraction measurements. Although we know a lot about the cells, some parameters cannot be measured or can only be measured with specific measuring instruments. These parameters (e.g. solid diffusivity of anode and cathode) are taken from literature as they describe similar used materials. All parameters are listed in Table 6.

The simulation was carried out with COMSOL Multiphysics 5.2a [66]. The cell was cycled in the range of 2.5–4.1 V with a current of $1C$

Table 6

Physico-chemical model parameters. Superscript m indicates measured values, f indicates fitted values.

Parameter	Anode (LiC$_6$)	Separator	Cathode (LiNiMnCoO$_2$)
Geometry			
Thickness l	47 μm^m	20 μm^m	63 μm^m
Particle radius r_p	17 μm^m		10 μm^m
Solid phase fraction ϵ_s	0.68^m		0.70^m
Liquid phase fraction ϵ_l	0.31^m	0.48^m	0.29^m
Thermodynamics			
Equilibrium voltage E_{eq}	See Eq. (A.1) [46]		See Eq. (A.2) [47]
Maximum Li concentration $c_{s,max}$	31,370 mol/m^3 [46]		51,385 mol/m^3 [47]
Initial state of charge $\frac{c_{s,0}}{c_{s,max}}$	0.84^m		0.52^m
Kinetics			
Reaction rate k_{ref}	1×10^{-11} m/s [45]		1×10^{-11} m/s [45]
Anodic charge-transfer coefficient α_a	0.5 [62]		0.5 [62]
Cathodic charge-transfer coefficient α_c	0.5 [62]		0.5 [62]
Transport			
Solid diffusivity $D_{s,ref}$	3.9×10^{-14} m^2/s [63]		8×10^{-14} m^2/s [64]
Solid conductivity σ	100 S/m [62]		1 S/m [62]

Parameter	Electrolyte
Electrolyte diffusivity D_l	See Eq. (A.3) [65]
Electrolyte conductivity κ	See Eq. (A.4) [65]
Activity dependency $\frac{\partial \ln f_\pm}{\partial \ln c_l}$	See Eq. (A.5) [65]
Transport number t_+	0.38 [65]

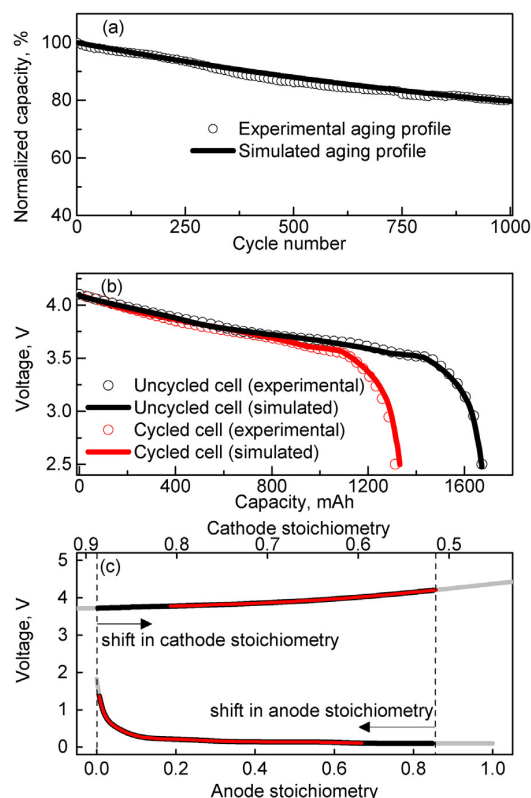| Parameter	SEI layer
Side reaction equilibrium potential $E_{eq,side}$	0.4 V [49]
Side reaction exchange current density $i_{0,side}$	2.0×10^{-6} A/m^2^{f}
Solid conductivity σ_{SEI}	5×10^{-4} S/m^f
Density ρ_{SEI}	1690 kg/m^3 [49]
Molar mass M_{SEI}	0.162 kg/mol [49]
Initial resistance $R_{0,SEI}$	1×10^{-3} Ωm^2 [49]
Initial thickness $\delta_{0,SEI}$	5 nm [49]

Fig. 8. (a) Comparison of experimental (empty circles) and simulated (solid line) normalized capacity during aging of NMC/C 18650-type cell. (b) Comparison of the experimental (empty circles) and simulated (solid lines) potential profiles of uncycled and cycled NMC/C 18650-type cells. (c) Simulated cycling range for the anode and cathode of the uncycled (black line) and cycled (red line) cells. (For interpretation of the references to color in this figure legend, the reader is referred to the web version of this article.)

using a constant current (CC) discharge followed by a constant current constant voltage (CCCV) charge phase. In this main cycling process, discharge capacity for each $1C$ discharge of the simulation was recorded. Fig. 8(a) shows the comparison of the capacity fade (or aging) profiles of the simulation and the experimental data. The simulation data is in good agreement with the capacity fade of the real cell. Additionally, $C/50$ checkup discharges corresponding to the beginning and end of the cycling process were performed. That is, capacity of the uncycled cell was measured with a $C/50$ discharge. After 1000 cycles, another $C/50$ discharge was applied and the capacity of the cycled cell was measured. These voltage profiles of the $C/50$ discharges are displayed in Fig. 8(b), together with the measured voltage profiles of the real cell. The measured and simulated voltage curves show only a slight deviation with a maximum value of about 15 mV due to the selected equilibrium voltage curves for the anode and cathode from literature. The good agreement between the modeled and the experimental aging as well as potential profiles conclude that cyclable lithium loss into SEI layer growth is the main aging mechanism for this cell. Fig. 8(c) shows the shifts in anode and cathode stoichiometry predicted from the model that fit good to neutron diffraction data in Tables 2 and 5.

5. Discussion

For large format cells, neutron diffraction is one of the few experimental techniques that can give stoichiometric information of light elements like lithium without opening the cell. The anode

stoichiometry shift, or reduction of x in Li_xC_6 ($0 \leqslant x \leqslant 1$) on aging, was directly obtained from the phase fractions of LiC_6 and LiC_{12} phases, which were the only lithiated graphite phases in the diffractogram. The cathode stoichiometry shift, or reduction in y in $Li_y(Ni_{0.33}Mn_{0.33}Co_{0.33})O_2$ ($0 < y \leqslant 1.05$) on aging, was indirectly obtained from the c/a lattice parameter ratio.

In this section, we compare these experimentally extracted stoichiometry shifts from neutron diffraction data to those predicted by the physico-chemical model. According to the model, cyclable lithium can only be lost into the growth and reconstruction of an SEI layer at the anode. This loss in the amount of cyclable lithium results in shifts in electrode stoichiometries as shown in Fig. 8(c). The model predicts that anode stoichiometry decreases from 0.84 to 0.67 on aging whereas the cathode stoichiometry remains practically unchanged for the fully charged cell. On the other hand, for the fully discharged cell, the model predicts that cathode stoichiometry decreases from 0.89 to 0.81 on aging whereas the anode stoichiometries are unchanged. Therefore, from the model an anode stoichiometry shift of $\Delta x = 0.17$ in Li_xC_6 and a cathode stoichiometry shift of $\Delta y = 0$ in $Li_y(Ni_{0.33}Mn_{0.33}Co_{0.33})O_2$ at SOC 100% are predicted from loss of cyclable lithium into the SEI layer. This is in reasonable agreement to the anode stoichiometry shift of $\Delta x = 0.19 \pm 0.02$ and cathode stoichiometry shift of $\Delta y = 0$ obtained from Rietveld refinement of neutron diffractograms in Fig. 3. For SOC 0%, the model predicts a cathode stoichiometry shift of $\Delta y = 0.08$ and an anode stoichiometry corresponding to $\Delta x = 0$. This is in a very good agreement to the cathode stoichiometry shift of $\Delta y = 0.08 \pm 0.02$ and anode stoichiometry shift of $\Delta x = 0$ obtained from the neutron diffractogram in Fig. 4.

As mentioned earlier, a good estimation of the available cyclable lithium is the difference in Li content within an electrode between its charged and discharged state. From neutron diffraction, a 23% loss in cyclable lithium in the anode and a 23% loss in cyclable lithium in the cathode can be estimated. Overall, capacity fade due to loss of cyclable lithium in both electrodes here slightly exceeds the relative discharge capacity fade of 21%, obtained from electrical tests (from Fig. 1). Note that information from the neutron diffraction is restricted to the central part of the cylindrical cell only. Thus, a slightly higher cyclable lithium loss may be a consequence of inhomogenieties in lithium distribution in the cycled cell which results in a lower lithium concentration in the central part of the cycled cell compared to its edges. No structural deterioration of active electrode materials was detected by neutron diffraction in the charged state of the cells. These results indicate that loss of cyclable lithium is the dominant factor contributing to the observed capacity fade. In the discharged state, minor structural differences are seen in the cathode. The lattice parameter c for the cycled cathode material undergoes a decrease by 1.1% upon discharging, which is lower than the corresponding decrease in the uncycled material (1.5%). The corresponding increase in a lattice parameters are 0.8% and 1.0%

Table 7

Relative capacity loss in the cells due to cyclable lithium loss, measured by neutron diffraction and estimated by physico-chemical modelling.

Relative capacity loss	Neutron diffraction	Physico-chemical model
Cyclable Li loss in anode	23%	21%
Cyclable Li loss in cathode	23%	21%

for the cycled and uncycled cells, respectively. These differences are a result of the reduced amount of available cyclable lithium in the cathode of the cycled cell on discharge.

The relative capacity losses from anode and cathode, experimentally determined by neutron diffraction and theoretically calculated by a model predicting capacity losses due to loss of cyclable lithium into a continual SEI layer growth at the anode, are summarized in Table 7. The good agreement in capacity fade determination between these methods concludes that loss of cyclable lithium into SEI layer formation at the anode is indeed the main aging mechanism contributing to the observed capacity fade in these cells.

6. Conclusion

In this study, the capacity loss in 18650-type NMC/C cells, produced under commercial standards, was experimentally investigated with *in situ* neutron diffraction and electrical tests, as well as physico-chemically modeling. The comparison of neutron diffraction experiments with electrochemical characterization reveals that the entire 21% capacity loss upon cycling is dominantly due to loss of cyclable lithium, which is evident from a reduction in available cyclable lithium in anode as well as cathode. Detailed evaluation of neutron diffractograms could exclude other contributions to aging such as deactivation or undesirable phase transformations of electrode materials, within the experimental accuracy of the method. Physico-chemical modeling confirms that the capacity fade is caused by consumption of cyclable lithium in ongoing SEI growth. This continual SEI growth is attributed to the fact that the electrode-electrolyte interface morphology at the anode of the cycled cell changes due to the repeated expansion and contraction of the anode with each cycle. A good agreement between the experimentally determined electrode stoichiometry shifts and those predicted by the model is demonstrated.

Appendix A. Analytical model input

Equilibrium voltage curves dependent on the degree of lithiation x for the negative electrode $E_{eq,neg}$ based on Safari et al. [46] and the positive electrode $E_{eq,pos}$ by Tippmann et al. [47]

$$
\begin{aligned}
E_{eq,neg} =\ & 0.6635 + (2.988 \exp(-33.52x)) \\
& + 0.02014 \tanh+(\frac{-x+0.6246}{0.06227}) + 0.9562 \tanh(\frac{x-0.01663}{0.03467}) \\
& - 1.461 \tanh(\frac{x-2.876}{-0.1853}) - 0.03768 \tanh(\frac{x-0.2755}{0.07276})
\end{aligned}
\tag{A.1}
$$

$$
E_{eq,pos} = \frac{(-3249y^3 + 10789y^2 - 9090y + 2929)}{(y^4 - 532y^3 + 2088y^2 - 1767y + 587)}
\tag{A.2}
$$

Electrolyte dependencies as measured by Valøen et al. [65] for diffusion coefficient D_l, conductivity κ and activity dependence as a function of temperature T and concentration c_l

$$
D_l = 10^{-4.43 - \frac{54}{T-(229+5\,c_l)} - 0.22c_l} \times 10^{-4}
\tag{A.3}
$$

$$\kappa = 0.1 \, c_l(-10.5 + 0.074T - 6.96 \times 10^{-5}T^2 + 0.668c_l - 0.0178c_l T$$
$$+ 2.8 \times 10^{-5}c_l T^2 + 0.494c_l^2 - 8.86 \times 10^{-4}c_l^2 T)^2 \tag{A.4}$$

$$\frac{\partial \ln f_\pm}{\partial \ln c_l} = \frac{0.601 - 0.24c_l^{0.5} + 0.982c_l^{1.5}(1 - 0.0052(T - 294))}{1 - t_{\text{plus}}} - 1 \tag{A.5}$$

References

[1] J.M. Tarascon, M. Armand, Issues and challenges facing rechargeable lithium batteries, Nature 414 (6861) (2001) 359–367, http://dx.doi.org/10.1038/35104644.

[2] F.T. Wagner, B. Lakshmanan, M.F. Mathias, Electrochemistry and the future of the automobile, J. Phys. Chem. Lett. 1 (14) (2010) 2204–2219, http://dx.doi.org/10.1021/jz100553m.

[3] D. Andre, S.-J. Kim, P. Lamp, S.F. Lux, F. Maglia, O. Paschos, B. Stiaszny, Future generations of cathode materials: an automotive industry perspective, J. Mater. Chem. A 3 (13) (2015) 6709–6732, http://dx.doi.org/10.1039/C5TA00361J.

[4] P. Harks, F.M. Mulder, P. Notten, In situ methods for Li-ion battery research: a review of recent developments, J. Power Sources 288 (2015) 92–105, http://dx.doi.org/10.1016/j.jpowsour.2015.04.084.

[5] V. Agubra, J. Fergus, Lithium ion battery anode aging mechanisms, Materials 6 (4) (2013) 1310–1325, http://dx.doi.org/10.3390/ma6041310.

[6] M. Dubarry, B.Y. Liaw, M.-S. Chen, S.-S. Chyan, K.-C. Han, W.-T. Sie, S.-H. Wu, Identifying battery aging mechanisms in large format Li ion cells, J. Power Sources 196 (7) (2011) 3420–3425, http://dx.doi.org/10.1016/j.jpowsour.2010.07.029.

[7] M. Kassem, J. Bernard, R. Revel, S. Pélissier, F. Duclaud, C. Delacourt, Calendar aging of a graphite/LiFePO$_4$ cell, J. Power Sources 208 (2012) 296–305, http://dx.doi.org/10.1016/j.jpowsour.2012.02.068.

[8] V.A. Sethuraman, L.J. Hardwick, V. Srinivasan, R. Kostecki, Surface structural disordering in graphite upon lithium intercalation/deintercalation, J. Power Sources 195 (11) (2010) 3655–3660, http://dx.doi.org/10.1016/j.jpowsour.2009.12.034.

[9] K. Jalkanen, J. Karppinen, L. Skogström, T. Laurila, M. Nisula, K. Vuorilehto, Cycle aging of commercial NMC/graphite pouch cells at different temperatures, Appl. Energy 154 (2015) 160–172, http://dx.doi.org/10.1016/j.apenergy.2015.04.110.

[10] M. Ecker, N. Nieto, S. Käbitz, J. Schmalstieg, H. Blanke, A. Warnecke, D.U. Sauer, Calendar and cycle life study of Li(NiMnCo)O$_2$-based 18650 lithium-ion batteries, J. Power Sources 248 (2014) 839–851, http://dx.doi.org/10.1016/j.jpowsour.2013.09.143.

[11] O. Dolotko, A. Senyshyn, M.J. Muhlbauer, K. Nikolowski, F. Scheiba, H. Ehrenberg, Fatigue process in Li-ion cells: an in situ combined neutron diffraction and electrochemical study, J. Electrochem. Soc. 159 (12) (2012) A2082–A2088, http://dx.doi.org/10.1149/2.080212jes.

[12] S. Shiotani, T. Naka, M. Morishima, M. Yonemura, T. Kamiyama, Y. Ishikawa, Y. Ukyo, Y. Uchimoto, Z. Ogumi, Degradation analysis of 18650-type lithium-ion cells by operando neutron diffraction, J. Power Sources 325 (2016) 404–409, http://dx.doi.org/10.1016/j.jpowsour.2016.06.026.

[13] D. Li, D.L. Danilov, L. Gao, Y. Yang, P.H. Notten, Degradation mechanisms of C$_6$/LiFePO$_4$ batteries: experimental analyses of cycling-induced aging, Electrochim. Acta 210 (2016) 445–455, http://dx.doi.org/10.1016/j.electacta.2016.05.091.

[14] J. Christensen, J. Newman, Cyclable lithium and capacity loss in Li-ion cells, J. Electrochem. Soc. 152 (4) (2005) A818, http://dx.doi.org/10.1149/1.1870752.

[15] D. Li, D. Danilov, Z. Zhang, H. Chen, Y. Yang, P.H.L. Notten, Modeling the SEI-formation on graphite electrodes in LiFePO$_4$ batteries, J. Electrochem. Soc. 162 (6) (2015) A858–A869, http://dx.doi.org/10.1149/2.0161506jes.

[16] D. Li, D. Danilov, Z. Zhang, H. Chen, Y. Yang, P.H.L. Notten, (Invited) Electron tunneling based SEI formation model, ECS Trans. 62 (1) (2014) 1–8, http://dx.doi.org/10.1149/06201.0001ecst.

[17] C. Delacourt, M. Safari, Mathematical modeling of aging of Li-ion batteries, in: A.A. Franco, M.L. Doublet, W.G. Bessler (Eds.), Physical Multiscale Modeling and Numerical Simulation of Electrochemical Devices for Energy Conversion and Storage, Green Energy and Technology, Springer London, London, 2016, pp. 151–190, , http://dx.doi.org/10.1007/978-1-4471-5677-2_5.

[18] M.A. Rodriguez, D. Ingersoll, S.C. Vogel, D.J. Williams, Simultaneous in situ neutron diffraction studies of the anode and cathode in a lithium-ion cell, Electrochem. Solid-State Lett. 7 (1) (2004) A8, http://dx.doi.org/10.1149/1.1628664.

[19] N. Sharma, V.K. Peterson, M.M. Elcombe, M. Avdeev, A.J. Studer, N. Blagojevic, R. Yusoff, N. Kamarulzaman, Structural changes in a commercial lithium-ion battery during electrochemical cycling: an in situ neutron diffraction study, J. Power Sources 195 (24) (2010) 8258–8266, http://dx.doi.org/10.1016/j.jpowsour.2010.06.114.

[20] X.-L. Wang, K. An, L. Cai, Z. Feng, S.E. Nagler, C. Daniel, K.J. Rhodes, A.D. Stoica, H.D. Skorpenske, C. Liang, W. Zhang, J. Kim, Y. Qi, S.J. Harris, Visualizing the chemistry and structure dynamics in lithium-ion batteries by in-situ neutron diffraction, Sci. Rep. 2 (2012) 747, http://dx.doi.org/10.1038/srep00747.

[21] O. Dolotko, A. Senyshyn, M.J. Mühlbauer, K. Nikolowski, H. Ehrenberg, Understanding structural changes in NMC Li-ion cells by in situ neutron diffraction, J. Power Sources 255 (2014) 197–203, http://dx.doi.org/10.1016/j.jpowsour.2014.01.010.

[22] M.A. Rodriguez, M.H. van Benthem, D. Ingersoll, S.C. Vogel, H.M. Reiche, In situ analysis of LiFePO$_4$ batteries: signal extraction by multivariate analysis, in: C. Binns (Ed.), Introduction to Nanoscience and Nanotechnology, vol. 25, John Wiley &

[23] Sons, Inc, Hoboken, NJ, USA, 2010, pp. 143–148, , http://dx.doi.org/10.1154/1.3393786.

[23] C.-W. Hu, N. Sharma, C.-Y. Chiang, H.-C. Su, V.K. Peterson, H.-W. Hsieh, Y.-F. Lin, W.-C. Chou, B.-Y. Shew, C.-H. Lee, Real-time investigation of the structural evolution of electrodes in a commercial lithium-ion battery containing a V-added LiFePO$_4$ cathode using in-situ neutron powder diffraction, J. Power Sources 244 (2013) 158–163, http://dx.doi.org/10.1016/j.jpowsour.2013.02.074.

[24] I.A. Bobrikov, A.M. Balagurov, C.-W. Hu, C.-H. Lee, T.-Y. Chen, S. Deleg, D.A. Balagurov, Structural evolution in LiFePO$_4$-based battery materials: in-situ and ex-situ time-of-flight neutron diffraction study, J. Power Sources 258 (2014) 356–364, http://dx.doi.org/10.1016/j.jpowsour.2014.02.060.

[25] V. Zinth, C. von Lüders, M. Hofmann, J. Hattendorff, I. Buchberger, S. Erhard, J. Rebelo-Kornmeier, A. Jossen, R. Gilles, Lithium plating in lithium-ion batteries at sub-ambient temperatures investigated by in situ neutron diffraction, J. Power Sources 271 (2014) 152–159, http://dx.doi.org/10.1016/j.jpowsour.2014.07.168.

[26] C. von Lüders, V. Zinth, S.V. Erhard, P.J. Osswald, M. Hofmann, R. Gilles, A. Jossen, Lithium plating in lithium-ion batteries investigated by voltage relaxation and in situ neutron diffraction, J. Power Sources 342 (2017) 17–23, http://dx.doi.org/10.1016/j.jpowsour.2016.12.032.

[27] A. Senyshyn, M.J. Mühlbauer, O. Dolotko, M. Hofmann, T. Pirling, H. Ehrenberg, Spatially resolved in operando neutron scattering studies on Li-ion batteries, J. Power Sources 245 (2014) 678–683, http://dx.doi.org/10.1016/j.jpowsour.2013.06.158.

[28] L. Cai, K. An, Z. Feng, C. Liang, S.J. Harris, In-situ observation of inhomogeneous degradation in large format Li-ion cells by neutron diffraction, J. Power Sources 236 (2013) 163–168, http://dx.doi.org/10.1016/j.jpowsour.2013.02.066.

[29] A. Senyshyn, M.J. Muhlbauer, O. Dolotko, M. Hofmann, H. Ehrenberg, Homogeneity of lithium distribution in cylinder-type Li-ion batteries, Sci. Rep. 5 (2015) 18380, http://dx.doi.org/10.1038/srep18380.

[30] A. Senyshyn, M.J. Mühlbauer, K. Nikolowski, T. Pirling, H. Ehrenberg, "In-operando" neutron scattering studies on Li-ion batteries, J. Power Sources 203 (2012) 126–129, http://dx.doi.org/10.1016/j.jpowsour.2011.12.007.

[31] N. Paul, J. Wandt, S. Seidlmayer, S. Schebesta, M.J. Mühlbauer, O. Dolotko, H.A. Gasteiger, R. Gilles, Aging behavior of lithium iron phosphate based 18650-type cells studied by in situ neutron diffraction, J. Power Sources 345 (2017) 85–96, http://dx.doi.org/10.1016/j.jpowsour.2017.01.134.

[32] M.J. Mühlbauer, O. Dolotko, M. Hofmann, H. Ehrenberg, A. Senyshyn, Effect of fatigue/ageing on the lithium distribution in cylinder-type Li-ion batteries, J. Power Sources 348 (2017) 145–149, http://dx.doi.org/10.1016/j.jpowsour.2017.02.077.

[33] M. Hoelzel, A. Senyshyn, N. Juenke, H. Boysen, W. Schmahl, H. Fuess, High-resolution neutron powder diffractometer SPODI at research reactor FRM II, Nucl. Instrum. Methods Phys. Res. Sect. A: Accel. Spectrom. Detect. Assoc. Equip. 667 (2012) 32–37, http://dx.doi.org/10.1016/j.nima.2011.11.070.

[34] M. Hoelzel, A. Senyshyn, O. Dolotko, SPODI: high resolution powder diffractometer, J. Large-Scale Res. Facil. JLSRF 1 (2015), http://dx.doi.org/10.17815/jlsrf-1-24.

[35] R. Gilles, B. Krimmer, H. Boysen, H. Fuess, Status of the new structure powder diffractometer (SPODI) at the FRM-II in Garching, Appl. Phys. A: Mater. Sci. Process. 74 (0) (2002) s148–s150, http://dx.doi.org/10.1007/s003390201739.

[36] P. Thompson, D.E. Cox, J.B. Hastings, Rietveld refinement of Debye–Scherrer synchrotron X-ray data from Al$_2$O$_3$, J. Appl. Crystallogr. 20 (2) (1987) 79–83, http://dx.doi.org/10.1107/S0021889887087090.

[37] T. Roisnel, J. Rodríguez-Carvajal, WinPLOTR: a windows tool for powder diffraction pattern analysis, Mater. Sci. Forum 378–381 (2001) 118–123, http://dx.doi.org/10.4028/www.scientific.net/MSF.378-381.118.

[38] N. Sharma, V.K. Peterson, Current-dependent electrode lattice fluctuations and anode phase evolution in a lithium-ion battery investigated by in situ neutron diffraction, Electrochim. Acta 101 (2013) 79–85, http://dx.doi.org/10.1016/j.electacta.2012.09.101.

[39] I. Buchberger, S. Seidlmayer, A. Pokharel, M. Piana, J. Hattendorff, P. Kudejova, R. Gilles, H.A. Gasteiger, Aging analysis of graphite/LiNi$_{1/3}$Mn$_{1/3}$Co$_{1/3}$O$_2$ cells using XRD, PGAA, and AC impedance, J. Electrochem. Soc. 162 (14) (2015) A2737–A2746, http://dx.doi.org/10.1149/2.0721514jes.

[40] J.R. Dahn, R. Fong, M.J. Spoon, Suppression of staging in lithium-intercalated carbon by disorder in the host, Phys. Rev. B 42 (10) (1990) 6424–6432, http://dx.doi.org/10.1103/PhysRevB.42.6424.

[41] A. Jokar, B. Rajabloo, M. Désilets, M. Lacroix, An inverse method for estimating the electrochemical parameters of lithium-ion batteries, J. Electrochem. Soc. 163 (14) (2016) A2876–A2886, http://dx.doi.org/10.1149/2.0191614jes.

[42] T.F. Fuller, M. Doyle, J. Newman, Simulation and optimization of the dual lithium ion insertion cell, J. Electrochem. Soc. 141 (1) (1994) 1–10.

[43] M. Doyle, T.F. Fuller, J. Newman, Modeling of galvanostatic charge and discharge of the lithium/polymer/insertion cell, J. Electrochem. Soc. 140 (6) (1993) 1526–1533.

[44] J. Newman, K.E. Thomas-Alyea, Electrochemical Systems, 3rd ed., John Wiley & Sons, Inc., Hoboken, New Jersey, 2004.

[45] F.M. Kindermann, J. Keil, A. Frank, A. Jossen, A SEI modeling approach distinguishing between capacity and power fade, J. Electrochem. Soc. 164 (12) (2017) E287–E294, http://dx.doi.org/10.1149/2.0321712jes.

[46] M. Safari, C. Delacourt, Modeling of a commercial graphite/LiFePO$_4$ cell, J. Electrochem. Soc. 158 (5) (2011) A562, http://dx.doi.org/10.1149/1.3567007.

[47] S. Tippmann, D. Walper, L. Balboa, B. Spier, W.G. Bessler, Low-temperature charging of lithium-ion cells Part I: Electrochemical modeling and experimental investigation of degradation behavior, J. Power Sources 252 (2014) 305–316, http://dx.doi.org/10.1016/j.jpowsour.2013.12.022.

[48] P. Arora, R.E. White, M. Doyle, Capacity fade mechanisms and side reactions in lithium-ion batteries, J. Electrochem. Soc. 145 (10) (1998) 3647–3667, http://dx.doi.org/10.1149/1.1838857.

[49] A. Awarke, S. Pischinger, J. Ogrzewalla, Pseudo 3D modeling and analysis of the SEI growth distribution in large format Li-ion polymer pouch cells, J. Electrochem. Soc. 160 (1) (2012) 172–181, http://dx.doi.org/10.1149/2.022302jes.

[50] G. Ning, R.E. White, B.N. Popov, A generalized cycle life model of rechargeable Li-ion batteries, Electrochim. Acta 51 (10) (2006) 2012–2022, http://dx.doi.org/10.1016/j.electacta.2005.06.033.

[51] H. Ekström, G. Lindbergh, A model for predicting capacity fade due to SEI formation in a commercial graphite/LiFePO$_4$ cell, J. Electrochem. Soc. 162 (6) (2015) 1003–1007, http://dx.doi.org/10.1149/2.0641506jes.

[52] P. Ramadass, B. Haran, P.M. Gomadam, R. White, B.N. Popov, Development of first principles capacity fade model for Li-ion cells, J. Electrochem. Soc. 151 (2) (2004) 196–203, http://dx.doi.org/10.1149/1.1634273.

[53] R.P. Ramasamy, J.-W. Lee, B.N. Popov, Simulation of capacity loss in carbon electrode for lithium-ion cells during storage, J. Power Sources 166 (1) (2007) 266–272, http://dx.doi.org/10.1016/j.jpowsour.2006.12.086.

[54] R. Fu, S.-Y. Choe, V. Agubra, J. Fergus, Development of a physics-based degradation model for lithium ion polymer batteries considering side reactions, J. Power Sources 278 (2015) 506–521, http://dx.doi.org/10.1016/j.jpowsour.2014.12.059.

[55] G. Ning, B.N. Popov, Cycle life modeling of lithium-ion batteries, J. Electrochem. Soc. 151 (10) (2004) 1584–1591, http://dx.doi.org/10.1149/1.1787631.

[56] M. Safari, M. Morcrette, A. Teyssot, C. Delacourt, Multimodal physics-based aging model for life prediction of Li-ion batteries, J. Electrochem. Soc. 156 (3) (2009) 145–153, http://dx.doi.org/10.1149/1.3043429.

[57] A.V. Randall, R.D. Perkins, X. Zhang, G.L. Plett, Controls oriented reduced order modeling of solid-electrolyte interphase layer growth, J. Power Sources 209 (2012) 282–288, http://dx.doi.org/10.1016/j.jpowsour.2012.02.114.

[58] J. Vetter, P. Novák, M.R. Wagner, C. Veit, K.-C. Möller, J.O. Besenhard, M. Winter, M. Wohlfahrt-Mehrens, C. Vogler, A. Hammouche, Ageing mechanisms in lithium-ion batteries, J. Power Sources 147 (1–2) (2005) 269–281, http://dx.doi.org/10.1016/j.jpowsour.2005.01.006.

[59] Y. Qi, H. Guo, L.G. Hector, A. Timmons, Threefold increase in the Young's modulus of graphite negative electrode during lithium intercalation, J. Electrochem. Soc. 157 (5) (2010) 558–566, http://dx.doi.org/10.1149/1.3327913.

[60] J.B. Siegel, A.G. Stefanopoulou, P. Hagans, Y. Ding, D. Gorsich, Expansion of lithium ion pouch cell batteries: observations from neutron imaging, J. Electrochem. Soc. 160 (8) (2013) 1031–1038, http://dx.doi.org/10.1149/2.011308jes.

[61] I. Laresgoiti, S. Käbitz, M. Ecker, D.U. Sauer, Modeling mechanical degradation in lithium ion batteries during cycling: solid electrolyte interphase fracture, J. Power Sources 300 (2015) 112–122, http://dx.doi.org/10.1016/j.jpowsour.2015.09.033.

[62] S.V. Erhard, P.J. Osswald, J. Wilhelm, A. Rheinfeld, S. Kosch, A. Jossen, Simulation and measurement of local potentials of modified commercial cylindrical cells – Part II: Multi-dimensional modeling and validation, J. Electrochem. Soc. 162 (14) (2015) A2707–A2719, http://dx.doi.org/10.1149/2.0431514jes.

[63] M. Doyle, J. Newman, G.S. Antoni, S.N. Caroline, T. Jean-Marie, Comparison of modeling predictions with experimental data from plastic lithium ion cells, J. Electrochem. Soc. 143 (6) (1996) 1890, http://dx.doi.org/10.1149/1.1836921.

[64] C.X. Ding, Y.C. Bai, X.Y. Feng, C.H. Chen, Improvement of electrochemical properties of layered LiNi$_{1/3}$Co$_{1/3}$Mn$_{1/3}$O$_2$ positive electrode material by zirconium doping, Solid State Ion. 189 (1) (2011) 69–73, http://dx.doi.org/10.1016/j.ssi.2011.02.015.

[65] L.O. Valøen, J.N. Reimers, Transport properties of LiPF$_6$-based Li-ion battery electrolytes, J. Electrochem. Soc. 152 (5) (2005) 882–891, http://dx.doi.org/10.1149/1.1872737.

[66] COMSOL Multiphysics 5.2a, https://www.comsol.com/.

5 A SEI Modeling Approach Distinguishing between Capacity and Power Fade

Within this chapter, the article *A SEI modeling approach distinguishing between capacity and power fade* is presented.

In this work, we introduced a P2D physicochemical model with SEI growth as the dominant aging mechanism. By distinguishing between an electronic and an ionic conductivity of the SEI, this approach introduces the possibility to adapt the model to capacity as well as power fade.

The model is based on a Samsung ICR18650-22F cell composed of graphite as the negative electrode and NMC as the positive electrode. We derived the cell's equilibrium potential by cycling with a low current at controlled room temperature. Geometric parameters (e.g. thicknesses of electrodes and separator) were measured at the battery research center *Münster Electrochemical Energy Technology* (MEET).

We implemented SEI formation due to their non-ideal insulation properties and SEI re-formation after their cyclic cracking during graphite expansion. For the implementation of SEI growth, we introduced a new approach that distinguishes between the transport of lithium ions, on the one hand, and of electrons through the SEI, on the other hand. This is in accordance with the assumption that the SEI possesses two ideal properties – a maximum conductivity for lithium ions (κ_{SEI}) and an insulating conductivity for electrons (σ_{SEI}). With this approach, we assume that new SEI is formed at the SEI/electrolyte interface. The model results in different ohmic drop for the driving potential of the main intercalation reaction at the negative electrode and the SEI forming reaction. This results in a more accurate representation of the SEI and enables us to differentiate between capacity and power fade, which is inextricably connected in a single conductivity modeling approach as presented in 4.

Additionally, we implemented active material dissolution as aging mechanism in the positive electrode that reduces its solid volume fraction. This aging mechanism corresponds to the degradation mode of LAM.

We fitted the relevant parameters and validated the model on experimental data from Ecker et al. [101]. The exchange current density of SEI formation was determined at different temperatures at $50\,\%$ SOC in a calendar aging mode. Lithium ions for the reaction are taken from the electrolyte but to keep the charge balance valid in calendar aging, lithium ions also have to deintercalate from the negative electrode whereas during cyclic aging those lithium ions are deintercalated from the positive electrode.

Both calendar and cyclic aging result in a square-root-shaped capacity loss over time or cycles. With increasing SEI growth and hence increasing SEI resistance, the SEI current density decreases until a state is reached where resistance increase and current density decrease keep the overpotential effectively steady. Due to that quasi-steady state, SEI formation never stops but decelerates to result in an almost linear capacity fade. The again accelerating or nonlinear aging behavior is simulated based on the active material dissolution side reaction in the positive electrode and occurs as soon as LAM becomes larger

than the LLI.

The simulated capacity fade during cyclic aging agrees well with the linear as well as with the transition to a nonlinear aging behavior, whereas the slope of nonlinear aging is underestimated by the model. Furthermore, the shifts in stoichiometry and the half-cell behavior depict the change from a limitation of the negative electrode to a limitation of the positive electrode and also agree well with the measurements and conclusions reported by Kleiner et al. [102].

With our modeling approach we are able to differentiate between capacity fade and power fade which is inextricably connected in a single conductivity approach.

Author contribution Frank M. Kindermann and Jonas Keil initiated the idea of the SEI modeling approach and developed, parametrized and validated the SEI model. Alexander Frank helped to carry out the simulation studies and to process the data. The manuscript was written by Frank M. Kindermann and was edited by Jonas Keil and Andreas Jossen. All authors discussed the data and commented on the results.

A SEI Modeling Approach Distinguishing between Capacity and Power Fade

Frank M. Kindermann, Jonas Keil, Alexander Frank, Andreas Jossen

Permanent weblink:

https://doi.org/10.1149/2.0321712jes

A SEI Modeling Approach Distinguishing between Capacity and Power Fade

Frank M. Kindermann,*,z Jonas Keil,* Alexander Frank, and Andreas Jossen

Technical University of Munich (TUM), Institute for Electrical Energy Storage Technology, Munich, Germany

In this paper we introduce a pseudo two-dimensional (P2D) model for a common lithium-nickel-cobalt-manganese-oxide versus graphite (NCM/graphite) cell with solid electrolyte interphase (SEI) growth as the dominating capacity fade mechanism on the anode and active material dissolution as the main aging mechanism on the cathode. The SEI implementation considers a growth due to non-ideal insulation properties during calendar as well as cyclic aging and a re-formation after cyclic cracking of the layer during graphite expansion. Additionally, our approach distinguishes between an electronic (σ_{SEI}) and an ionic (κ_{SEI}) conductivity of the SEI. This approach introduces the possibility to adapt the model to capacity as well as power fade. Simulation data show good agreement with an experimental aging study for NCM/graphite cells at different temperatures introduced in literature.

Lithium-ion batteries are one of the most promising candidates for energy storage in future stationary storage systems and electric vehicles.[1–3] Enormous research efforts have been conducted to get a thorough understanding of the system "lithium-ion cell" and to further develop it for higher energy and power density, higher safety standards as well as longer cycle life.[4]

The aging behavior of lithium-ion batteries has been a focus issue of battery research since the introduction of lithium-ion cells by Sony in 1991.[5] Reviews by Agubra et al.,[6,7] Arora et al.,[8] Aurbach et al.,[9,10] Birkl et al.,[11] Broussely et al.,[12] Verma et al.[13] and Vetter et al.[14] are just a few examples of the extensive literature regarding aging behavior. Commonly accepted and experimentally verified aging phenomena as mentioned in the previously cited literature are electrolyte decomposition leading to solid electrolyte interphase (SEI) and cathode electrolyte interphase (CEI) growth, solvent co-intercalation, gas evolution with subsequent cracking of particles, a decrease of accessible surface area and porosity due to SEI growth, contact loss of active material particles due to volume changes during cycling, binder decomposition, current collector corrosion, metallic lithium plating and transition-metal dissolution from the cathode.

The listed aging mechanisms can be assigned to three different categories that are a loss of lithium-ions (LLI), an impedance increase and a loss of active material (LAM).[12,15–18] The LLI is synonymous to a decrease in the amount of cyclable lithium-ions as they are trapped in a passivating film on either of the electrodes or in plated metallic lithium. Due to the growth of the passivating layers and/or the formation of rock-salt in the cathode (residue of the cathode active material after transition-metal dissolution), kinetic transport of lithium-ions through those inactive areas is limited and results in an impedance rise. An LAM can be caused by the dissolution of transition-metal-ions from the cathode bulk material, changes in the electrode composition and/or changes in crystal structure of the active material which all diminish the amount of host structure for lithium-ion intercalation. Also mechanical strain during de-/intercalation can contribute to LAM as particles from both electrodes can crack and get electronically separated from the bulk material.

For investigating or describing the behavior of lithium-ion cells, different model categories can be implemented and those can be classified into first-principle, electrochemical engineered and empirical models.[19,20]

Atomistic models based molecular dynamics (MD)[21,22] and density functional theory (DFT)[23–25] try to recreate molecular behavior on an atomic scale. As they use fundamental physics-based approaches for atom-atom interactions, these models are also called first-principle models.[21] This category of models becomes of greater importance in future research efforts for better understanding interfacial chemistry as it can predict species in the interphases that might be hidden or changed due to poor empirical characterization. The drawback of first-principle models is that they cannot properly handle cycling of intercalation electrodes as the consideration of the bulk structure is necessary which cannot be represented with a traditional surface thermodynamics approach.[26,27] MD and DFT consider clean surfaces and influences of close subsurface layers, so they do not consider structural changes in the electrodes during cycling.

A step closer to modeling complete cell behavior are electrochemical engineered models that are often also known as physicochemical models. Within this class, surface and molecule processes are modeled in a phenomenological manner but the particle and electrode domain are described mechanistically. Based on electrochemical kinetics and transport equations they can simulate cell characteristics and intercalation as well as side reactions.[19,20] The best-known electrochemistry-based models are the pseudo two-dimensional (P2D) model developed by Newman and co-workers[28–30] and the single particle model (SPM) first introduced by Zhang et al.[31] The often proved accuracy and agreement with experimental data of the P2D model originate from its basic implementation of porous electrode theory as well as concentrated solution theory.[28,32] Up to today, the P2D model represents the most precise and – though computationally costly – most popular model in lithium-ion battery research.[28] The SPM represents a simplification of the P2D model in order to decrease computational time. As the spatial representation of the liquid phase are neglected and transport phenomena are just considered in one single representative particle, the SPM lacks the accuracy of the P2D model but still shows good agreement with experimental data.[20,31,33]

Empirical models are based on implementing behavioral trends from past experiments and predicting future states such as state-of-charge (SOC) and state-of-health (SOH) from there. The best known models of that category are equivalent circuit models and neural network models.[20,34] As they are relatively simple to implement and computationally fast, empirical models are frequently found in literature.[34–42] However, their application is limited as they can only describe a previously seen and implemented behavior, so an adaption to another cell or even chemistry needs a completely new database.[19,20]

Previous literature described several degradation mechanisms on anode as well as cathode in a P2D model. Ashwin et al.[43,44] investigated the porosity change in the negative electrode due to SEI growth under different cycle and temperature conditions. Fu et al.[45] ascribed capacity fade to SEI growth as well as active material degradation and found an extra deposit layer on the anode near the separator. Lawder et al.[46] studied the influence of different driving cycle profiles on the capacity fade of electric vehicle batteries and ascribed the total capacity fade to SEI growth. The effects of gas evolution due to SEI growth were modeled by Rashid et al.[47] On the cathode side, Cai et al.[48] implemented an SOC independent manganese disproportionation which

*Electrochemical Society Student Member.
zE-mail: f.kindermann@tum.de

increased the cathodic resistance and lead to a change both in porosity as well as particle radius. A combination of SEI growth and cathode dissolution in a lithium-cobalt-oxide (LCO) cell was shown by Lam et al.[49] and optimal discharge parameters were derived. Another very extensive model that included manganese dissolution from a lithium-manganese-oxide cathode and the effects of manganese-ions incorporated into the anodic SEI was presented by Lin et al.[50]

In this paper we introduce a P2D model for a common NCM/graphite cell with SEI growth as the dominating capacity fade mechanism on the graphite anode and active material dissolution as the main aging mechanism on the cathode. The SEI implementation considers a growth due to imperfections in its insulating properties as well as new SEI formation due to cracking of the layer during graphite expansion when cycling the cell. The novelty of our approach is that we include two separate conductivities within the SEI for lithium-ions (κ_{SEI}) and electrons (σ_{SEI}) leading to distinct overpotentials driving the main and side reaction. Simulation data is compared to experimental studies on NCM/graphite cells performed by Ecker et al.[51]

Model Development

To analyze the behavior of the most important aging mechanisms and their impact on capacity fade, we implemented a P2D physico-chemical model for a common NCM/graphite cell using COMSOL Multiphysics 5.2a. As the basic equations of the P2D model have been extensively shown in literature,[28–30] a brief overview of the model and all used parameters (see Table AI) are given in the Appendix. The basic assumptions of the implemented aging mechanisms in the presented model are introduced and discussed subsequently.

Implementation of SEI growth.—For the implementation of SEI growth we introduce a new approach that distinguishes between the transport of two species through the SEI – lithium-ions on the one hand and electrons on the other hand (refer to Figure 1a). This is in accordance with the assumption that the SEI possesses two ideal properties – a maximum conductivity for lithium-ions and an insulating conductivity for electrons.[13,52] We are aware that literature[53–55] still debates whether new SEI is formed at the SEI/electrolyte or the graphite/SEI interface. With our approach, we assume that new SEI is formed at the SEI/electrolyte interface. In the case of an SEI formation at the graphite/SEI interface solvent particles would need to be the second species migrating through the SEI besides lithium-ions. As our P2D model treats the SEI as an interface phenomenon influencing charge-transfer, both cases would lead to the same cell behavior, so we stick to electron migration through the SEI for SEI formation.

Our new approach results in a different ohmic drop (iR) for the driving overpotential of the main intercalation reaction at the negative electrode η_{neg} and the SEI forming side reaction η_{SEI}.

$$\eta_i = \Phi_s - \Phi_l - E_{Eq,i} - i_i \cdot R_i \quad [1]$$

Both resistances R_{neg} and R_{SEI} are dependent on the SEI's initial thickness $\delta_{0,SEI}$, the thickness increase $\Delta\delta_{SEI}$ and the respective conductivity. The initial thickness is assumed to be 20 nm which is considered a fully formed SEI[56] and the thickness increase is due to the non-ideal insulating properties as well as an SEI re-formation after cracking.

$$R_{neg} = \frac{\delta_{0,SEI} + \Delta\delta_{SEI}}{\kappa_{SEI}} \quad [2]$$

$$R_{SEI} = \frac{\delta_{0,SEI} + \Delta\delta_{SEI}}{\sigma_{SEI}} \quad [3]$$

As no measurements of the SEI's electronic conductivity σ_{SEI} are known,[56] we assume σ_{SEI} to be 10^{-8} S m^{-1} which is considered an insulating behavior.[57] In contrast, the ionic conductivity κ_{SEI} is presumed to be 10^{-2} S m^{-1} which is approximately the conductivity of a liquid lithium-ion battery electrolyte.[57]

With the introduced overpotentials we implemented a growth due to imperfections in the SEI's insulating properties by Butler-Volmer
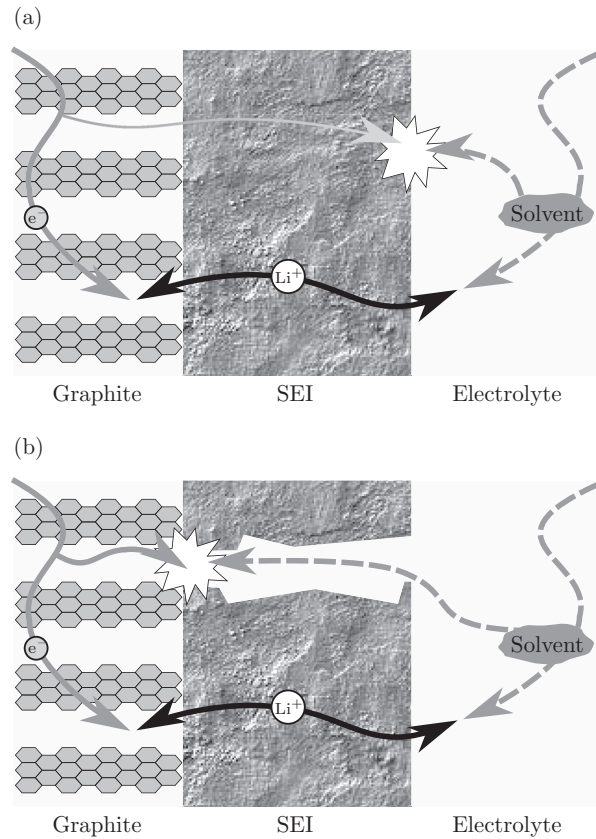

Figure 1. (a) SEI growth at SEI/electrolyte interface by electron flux through the interphase. Lithium-ion transport for (de-)intercalation reaction has a different conductivity than the electron transport. (b) SEI growth in cracks without hindrance of interphase.

kinetics with an anodic charge-transfer coefficient $\alpha_{a,SEI} = 0.05$ and a cathodic charge-transfer coefficient $\alpha_{c,SEI} = 0.95$. This implementation is close to the often used cathodic Tafel expression[8,15] but considers also dissolution reactions during cycling.[58]

$$i_{SEI,n} = i_{0,SEI} \cdot \left[\exp\left(\frac{\alpha_{a,SEI} \cdot F \cdot \eta_{SEI}}{RT} \right) - \exp\left(\frac{-\alpha_{c,SEI} \cdot F \cdot \eta_{SEI}}{RT} \right) \right] \quad [4]$$

The index n in $i_{SEI,n}$ symbolizes LiF and Li$_2$CO$_3$ as we included the two most important SEI products in the model.[59,60] F, R and T represent Faraday's constant, the universal gas constant and the absolute temperature, respectively. Specific values for $i_{0,SEI}$ will be given in the Results and discussion section by Equation 11.

Additionally, we implemented an SEI re-formation after cracking due to graphite expansion during intercalation of lithium-ions.[61,62] As we only assume a new formation without dissolution by cracking, the anodic part in the Butler-Volmer equation is omitted and the overpotential η_{crack} considers no iR-drop.

$$\eta_{crack} = \Phi_s - \Phi_l - E_{Eq,SEI} \quad [5]$$

The current density computation considers a cracking function dependent on intercalation degree x that is depicted in Figure 2 which is the gradient of a graphite expansion curve as previously introduced by Laresgoiti et al.[62] Furthermore, we included an empirical factor $\frac{i_{neg}}{i_{C/100}}$ to scale the cracking for utilization at different intercalation current densities.

$$i_{crack} = -i_{0,SEI} \cdot \left(\frac{i_{neg}}{i_{C/100}} \right) \cdot f_{crack}(x) \cdot \exp\left(\frac{-F \cdot \eta_{crack}}{RT} \right) \quad [6]$$
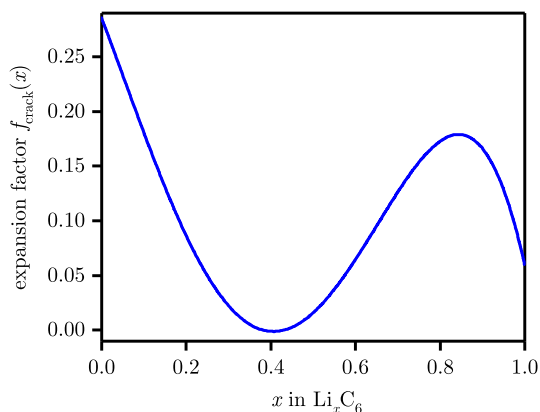
Figure 2. Function $f_{\text{crack}}(x)$ of the expansion gradient over lithiation degree x to scale the amount of SEI cracking during different stages of intercalation.

For simplicity, we assume that only Li_2CO_3 is formed in the cracks. The overall increase in SEI thickness $\Delta\delta_{\text{SEI}}$ after integrating the respective current densities is calculated with the molar masses M_i and densities ρ_i by

$$\Delta\delta_{\text{SEI}} = \frac{(Q_{\text{crack}} + Q_{Li_2CO_3}) \cdot M_{Li_2CO_3}}{\rho_{Li_2CO_3} \cdot F} + \frac{Q_{LiF} \cdot M_{LiF}}{\rho_{LiF} \cdot F} \quad [7]$$

The lithium-ions consumed in the three SEI forming charge quantities are subtracted from the total amount of cyclable lithium-ions and represent the LLI in the model.

We assume that the known aging behavior of a lithium-ion battery cannot be represented completely by a mere implementation of SEI growth. In literature, models with SEI growth as their only capacity fade mechanism do not show the typical non-linear aging behavior – i.e. the sudden decrease – in usable capacity after several hundred cycles.[53,55,59,61,63] In these models, this non-linear aging behavior can be emulated by a high power fade, though, which shortens charging and discharging due to high overpotentials that decrease the usable capacity.[43,61] Measurements in literature ascribe this non-linear aging behavior to lithium plating[64,65] as well as to degradation mechanisms on the cathode.[5,48,50] For the here introduced model we chose to implement a cathode dissolution reaction as the responsible mechanism for the non-linear aging behavior. As we lack any information on that topic from the chosen experimental data, including a mechanism on the positive electrode seems sensible in regard of the possible interactions between the two mechanisms (SEI growth and lithium plating) at the negative electrode.

We are aware that dissolved transition-metal ions from the cathode have been reported to be incorporated in the anodic SEI and have altering effects on its properties.[66–68] Including those effects will be part of future investigations, as they are not crucial for the general improvement of the introduced SEI model representation by two conductivities.

Cathode dissolution reaction.—The implemented dissolution reaction, is reducing the solid phase volume fraction $\varepsilon_{s,pos}$ depending on the cathode's intercalation degree. Hence, the reduction of $\varepsilon_{s,pos}$ corresponds to the LAM in our model. Acid attack by HF is one of the dominating causes for active material dissolution at the cathode[50,69,70] and is implemented as an irreversible kinetics expression in the positive electrode domain. As HF evolution is promoted at potentials above 4.0 V,[69] this potential is used as the equilibrium potential $E_{\text{Eq,diss}}$.

$$i_{\text{diss}} = i_{0,\text{diss}} \cdot \exp\left(\frac{F \cdot \eta_{\text{diss}}}{RT}\right) \quad [8]$$

$$\eta_{\text{diss}} = \Phi_s - \Phi_l - E_{\text{Eq,diss}} \quad [9]$$

Table I. Parameters for the side reaction definitions. The superscript e indicates estimated values.

Symbol	Parameter	Value
SEI layer		
$E_{\text{Eq,SEI}}$	SEI formation equilibrium potential	0.4 V [71]
κ_{SEI}	Li^+ conductivity	1×10^{-2} S m^{-1} [57]
σ_{SEI}	e^- conductivity	1×10^{-8} S m^{-1} [57]
$\delta_{0,\text{SEI}}$	Initial thickness	20 nm [56]
$\rho_{\text{SEI},Li_2CO_3}$	Density of Li_2CO_3	2110 kg m^{-3}
M_{SEI,Li_2CO_3}	Molar of mass Li_2CO_3	73.89 g mol^{-1}
$\rho_{\text{SEI,LiF}}$	Density of LiF	2640 kg m^{-3}
$M_{\text{SEI,LiF}}$	Molar mass of LiF	25.94 g mol^{-1}
Transition-metal dissolution		
$E_{\text{Eq,diss}}$	Dissolution equilibrium potential	4.0 V [69]
$i_{0,\text{diss}}$	Dissolution exchange current density	6.05×10^{-6} A m^{-2} ^{e}

The volume fraction of the cathode active material is continuously calculated by the integrated dissolution current density Q_{diss} of HF dissolving transition-metals from the active material.

$$\varepsilon_{s,pos} = \varepsilon_{s,pos,0} - \frac{Q_{\text{diss}}}{c_{s,max,pos} \cdot l_{pos} \cdot F} \quad [10]$$

In conclusion to the introduction of the side reaction modeling approach, an overview of all parameters for the previously shown side reactions can be found in Table I.

Results and Discussion

Determination of SEI formation exchange current density.—As mentioned before, we used the experimental data for a NCM/graphite cell from Ecker et al.[51] to test our model and fit relevant parameters. By simulating our model in a calendar aging mode (i.e. no applied external current density), we are able to determine the exchange current density of SEI formation. Electrons for forming the SEI are provided by the anode in calendar as well as cyclic aging. Lithium-ions for the reaction are taken from the electrolyte but to keep the charge balance valid in calender aging, lithium-ions also have to deintercalate from the negative electrode whereas during cyclic aging those lithium-ions are deintercalated from the positive electrode. With the provided data for 35, 40 and 50°C at 50% SOC, we determined the SEI formation exchange current density $i_{0,\text{SEI}}$ depending on temperature T in an Arrhenius-like behavior as we expect a negligible influence of the cathodic dissolution reaction at this SOC.

$$i_{0,\text{SEI}} = 14.7 \times 10^4 \text{ A m}^{-2} \exp\left(\frac{-86.2 \text{ kJ mol}^{-1}}{RT}\right) \quad [11]$$

The exchange current density for SEI formation calculates to 3.6, 6.1 and 17.1 × 10^{-10} A m^{-2} for 35, 40 and 50°C respectively and is in agreement with an exchange current density smaller than 1×10^{-7} A m^{-2} as proposed by Fu et al.[45]

The agreement of experimental and simulation data can be seen in Figure 3.

Quantitatively LiF and Li_2CO_3 are formed at the same rate in the calendric regime of the introduced model. This is to be expected as the same reduction potential and an overall side reaction exchange current density $i_{0,\text{SEI}}$ is assumed. The incorporation of the two main degradation products is still advisable as it influences the thickness prediction of the SEI by the different molar volumes of LiF and Li_2CO_3 ($V_{\text{m,LiF}} = 9.8 \times 10^{-6}$ m^3 mol^{-1}; $V_{\text{m},Li_2CO_3} = 3.5 \times 10^{-5}$ m^3 mol^{-1}).

Capacity fade based on SEI growth during cyclic and calendar aging.—When applying a cyclic aging regime with a 1C rate between 2.75 and 4.2 V (constant current (CC) discharge and constant
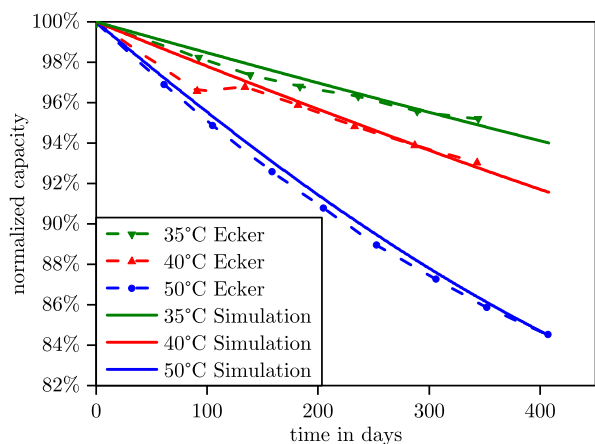
Figure 3. Comparison of experimental data taken from Ecker et al.[51] and data from the proposed model for calendar aging at 50% SOC as a result of SEI formation.

Figure 5. Comparison of the modeled SEI thickness close to the current collector over 1000 cycles with and without an implemented cathode dissolution. The cell was cycled with a 1C rate between 2.75 and 4.2 V.

current-constant voltage (CC-CV) charge), we observe a higher capacity fade due to SEI growth than during calendar aging. One might expect that this increase in capacity fade is solely due to the cracking and re-formation of the SEI which is not occurring during calendar aging. However, as also shown by Purewal et al.[72] the increase in SEI growth is mainly due to the differing overpotentials during cycling and the cracking of the SEI accounts for only a small amount of the total SEI formed.

The overall SEI growth close to the separator and close to the current collector as well as the overall capacity fade as shown in Figure 4 follows a $\sqrt{t}$-behavior. In contrast to Lin et al.,[50] this behavior is not modeled by an exponential decay pre-factor limiting the exchange current density but is based on a different utilized range in the $i_{\text{SEI},n}$-η_{SEI}-curve determining the kinetics of SEI growth. As the kinetics dependency has an exponential shape and the overpotential changes due to the increasing R_{SEI}, the SEI formation current decreases until a state is reached where resistance increase and current density decrease keep the overpotential effectively steady. Due to that quasi-steady state, SEI formation never stops for reasons of the SEI being insulating enough but changes to a linear growth behavior.
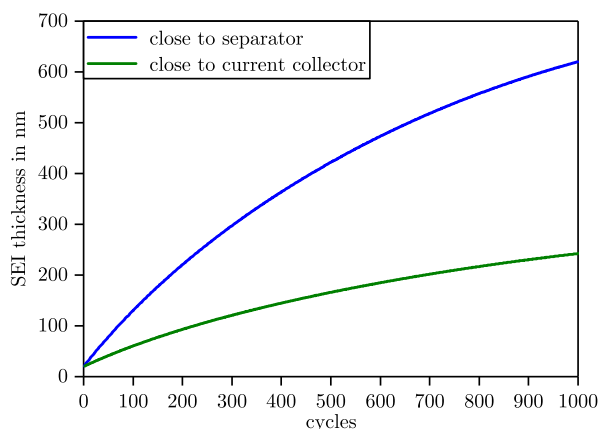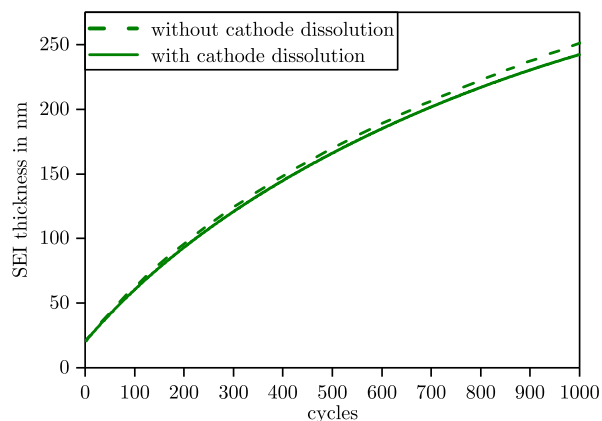
Non-linear aging behavior due to cathode dissolution.—As the SEI is not stopping to grow due to kinetic limitations as discussed in the previous section, another effect has to serve as a limiting condition. Our simulations show that the "stabilization" of SEI growth is influenced by the degradation of the positive electrode. This fact – which seems contradictory to what one would expect – is caused by a straightforward circumstance. As cathode degradation outpaces the amount of lost cyclable lithium-ions contributing to SEI growth, less and less lithium-ions are moved from the anode to the cathode during discharge.[5,50] This effect leads to shorter charging times and, therefore, shorter times during which SEI can grow which results in a decrease of SEI growth in each cycle[75] (see Figure 5). The same would hold true with lithium plating as a source of LLI and the consequent decrease of cyclable lithium-ions.

Figure 5 compares the decrease of SEI growth over 1000 cycles close to the current collector with and without an implemented cathode dissolution reaction. The difference in SEI thickness after 1000 cycles is about 10 nm. This thickness difference seems to be very small in comparison to the difference in the corresponding overall capacity fade as depicted in Figure 6 (blue and red line). The reason for the behavior of the model with cathode dissolution is a prolonged
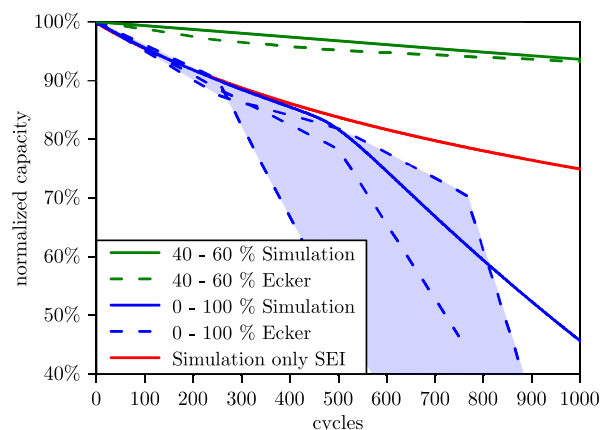

Figure 4. Comparison of the modeled SEI thickness close to the separator and close to the current collector over 1000 cycles. The cell was cycled with a 1C rate between 2.75 and 4.2 V. The difference in growth is due to inhomogeneous current density distribution through the electrodes.[73,74]

Figure 6. Comparison of experimental data taken from Ecker et al.[51] and data from the proposed model for cyclic aging as a result of SEI formation and cathode dissolution. The light blue color covers the range of the three measurements by Ecker et al.[51] Additionally, the red line shows the capacity fade behavior of the model when disabling the cathode dissolution reaction.
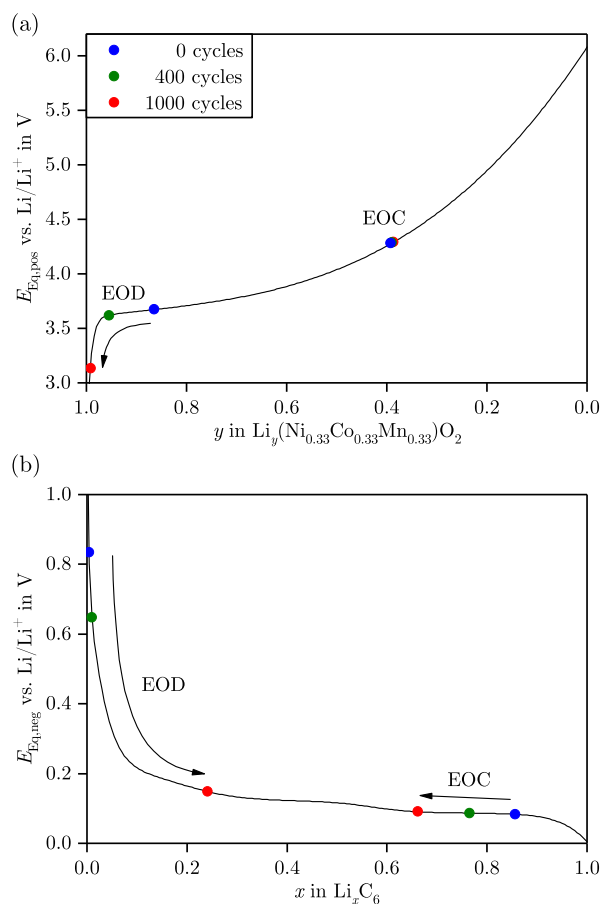
Figure 7. Cathode (a) and anode (b) stoichiometry for initial starting conditions (blue), before the transition to non-linear behavior in the capacity fade curve (green) and after 1000 cycles (red). (For interpretation of the references to color in this figure legend, the reader is referred to the web version of the article.)

Figure 8. (a) Comparison of voltage curve taken from Ecker et al.[51] for 0.25C discharge and data from the proposed model. (b) Exemplary different power fade behavior by changing κ_{SEI} to 1×10^{-7} S m^{-1}.

CV phase during charging due to the side reactions. The CV phase keeps the SEI reaction below the reduction potential and the cathode dissolution reaction above the oxidation potential, so the current does not drop below the stopping criterion of C/20 due to the side reactions. Therefore, the longer CV phase counterbalances the shorter charging time for the intercalation reaction and does not limit the SEI growth as much as expected.

Figure 6 compares the simulated non-linear behavior in usable capacity with experimental results by Ecker et al.[51] The non-linearity in usable capacity occurs as soon as the LAM in the cathode becomes larger than the LLI. Whereas the decrease in the beginning of the capacity fade and the position of the transition zone from linear to non-linear aging behavior are in good agreement, the slope after the transition zone is underestimated by the model. This could be caused by the exclusion of implementing lithium plating as a second source of LLI and will, therefore, be a task for future work.

Figure 7 depicts consequences of the capacity fade on the shift within the stoichiometry – which is the intercalation degree – at the end-of-charge (EOC) and end-of-discharge (EOD). Besides the initial conditions of a non-aged cell, the values of an aged cell before and after the transition to non-linear behavior in the capacity curve of Figure 6 are shown. As expected, the stoichiometry of the anode at the EOC decreases due to LLI (shift from blue to red in Figure 7b). In contrast, the stoichiometry of the cathode at the EOC stays (almost) the same as the anode stays in a stage-1 potential plateau and the
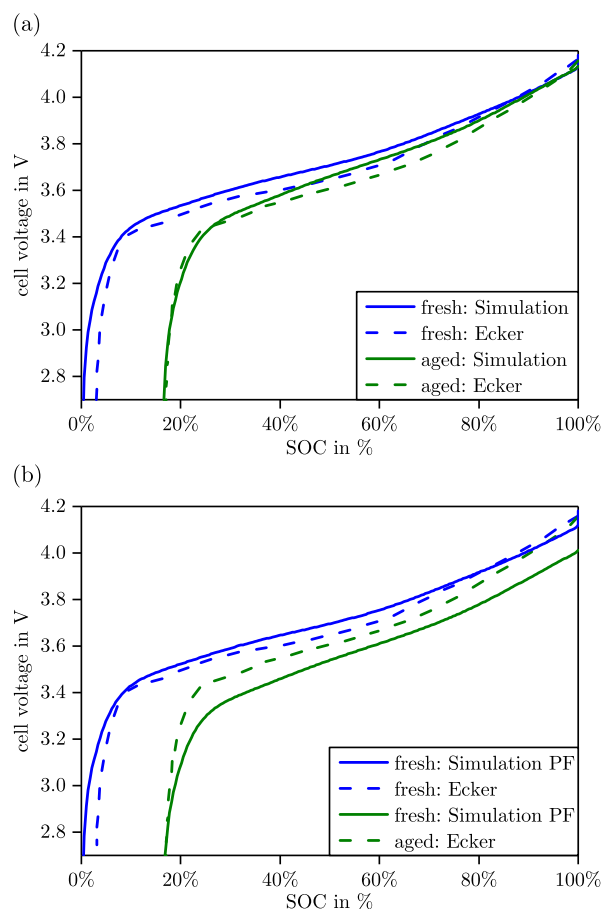
EOC is defined by the cutoff-voltage of the cell at 4.2 V which is the difference between anode and cathode potential.

At the EOD, we see that the cathode stoichiometry increases (shift from blue to red in Figure 7a) as the LAM is higher than the LLI and percentagewise more lithium-ions intercalate in a smaller cathode active material volume. When the cathode stoichiometry at EOD is reaching 1, the anode stoichiometry also increases as the discharge is terminated before all lithium-ions are deintercalated from the anode. Therefore, at this point we see a change from an anode limitation to a cathode limitation of the cell. Those shifts and the half-cell behavior are also in good agreement with measurements and conclusions reported by Kleiner et al.[76] for an NCA/graphite cell.

Capacity and power fade behavior with new model.—Depicted in Figure 8a is the voltage discharge curve of the simulated cell prior and after aging at 100 % SOC and 50 °C compared to data reported in the paper of Ecker et al.[51] As can be seen, the cell shows a capacity fade – recognizable by shorter discharge time – but no significant power fade as voltage levels are almost equal.

Figure 8b shows the exemplary behavior of a cell with a uniform conductivity κ_{SEI} of 1×10^{-7} S m^{-1} for lithium-ions and electrons within the SEI in the order of often used values in literature.[47,77] The plot shows that we get a totally different power behavior as a result and, therefore, prediction of available energy with a model that does not distinguish between the conductivity of electrons and lithium-ions in the SEI – although we calculate the same capacity fade.

With our modeling approach we are able to differentiate between capacity fade and power fade, both resulting in an energy loss during aging. We thereby get the possibility to gain new insights into SEI properties for different cell systems and material combinations in future work.

Conclusions

In this paper we introduced a new approach for modeling aging behavior that distinguishes between electronic (σ_{SEI}) and ionic (κ_{SEI}) conductivity of the SEI. By this approach we do not only represent the SEI in a way that is more accurate but we can also differentiate between capacity and power fade which is inextricably connected in a single conductivity approach.

The model shows good agreement with experimental data from Ecker et al.[51] as not only an SEI growth due to non-ideal insulation properties and re-formation after cyclic cracking but also a cathode dissolution reaction is implemented. With this cathodic aging mechanism, the transition to non-linear behavior in retrievable capacity can be explained.

Future work will add further aging mechanisms on both electrodes, like e.g. lithium plating and a cathode electrolyte interphase (CEI) formation, to the existing model to get a more thorough understanding of the interactions between the different mechanisms.

Appendix

The P2D model is based on porous electrode and concentrated solution theory and solves lithium-ion concentration c_i and potential Φ_i within the liquid electrolyte (subscript $i = l$) and the solid active material (subscript $i = s$) phase. The model geometry is defined as a one dimensional interval divided into three main domains corresponding to the graphite electrode, the separator and the NCM electrode. An additional dimension is set for the description of species intercalation within the particle domain. For a detailed model description, the reader is referred to Reference 29. The main equations are mass balance for lithium-ions in the electrolyte c_l

$$\varepsilon_l \frac{\partial c_l}{\partial t} = \nabla \left(D_{l,eff} \nabla c_l - \frac{i_l t_+}{F} \right) + a_s j_n \qquad [A1]$$

and charge balance

$$\nabla \left(-\kappa_{eff} \nabla \Phi_l + \frac{2\kappa_{eff} RT}{F} \left(1 + \frac{\partial \ln f_\pm}{\partial \ln c_l} \right) (1 - t_+) \nabla \ln c_l \right) = F a_s j_n \qquad [A2]$$

throughout the electrode domain. The current within the liquid phase is described by the current density i_l and potential Φ_l, while the pore wall flux at the electrode-electrolyte interface is named j_n. R describes the universal gas constant, F the Faraday's constant and T the local absolute temperature. Within the separator domain the equations simplify to

$$\varepsilon_l \frac{\partial c_l}{\partial t} = \nabla \left(D_{l,eff} \nabla c_l - \frac{i_l t_+}{F} \right) \qquad [A3]$$

and

$$\nabla \left(-\kappa_{eff} \nabla \Phi_l + \frac{2\kappa_{eff} RT}{F} \left(1 + \frac{\partial \ln f_\pm}{\partial \ln c_l} \right) (1 - t_+) \nabla \ln c_l \right) = 0 \qquad [A4]$$

To couple solid and liquid phase, Butler-Volmer kinetics are assumed for the pore wall flux

$$j_n = k_c^{\alpha_a} k_a^{\alpha_c} \left(c_{s,max} - c_s|_{r=r_p} \right)^{\alpha_a} \left(c_s|_{r=r_p} \right)^{\alpha_c} \left(\frac{c_l}{1\,\text{mol m}^{-3}} \right)^{\alpha_a} \left(e^{\frac{\alpha_a F}{RT} \eta} - e^{-\frac{\alpha_c F}{RT} \eta} \right) \qquad [A5]$$

including the lithium-ion concentration at the particle's surface c_s and the overpotential

$$\eta = \Phi_s - \Phi_l - E_{Eq} \qquad [A6]$$

where Φ_s corresponds to the solid phase potential.

Effective transport parameters are used to account for tortuosity in the homogenized P2D model by scaling material parameters with MacMullin's number – a function of

---

Table AI. Physicochemical model parameters measured and estimated from a Samsung ICR-22F 18650-cell. Superscript *m* indicates measured values and *e* estimated values.

Parameter	Anode	Separator	Cathode
Geometry			
Thickness l	$77\,\mu\text{m}^{\,m}$	$18\,\mu\text{m}^{\,m}$	$79\,\mu\text{m}^{\,m}$
Particle radius r_p	$10\,\mu\text{m}^{\,m}$		$4\,\mu\text{m}^{\,m}$
Solid phase fraction ε_s	$0.56^{\,m}$		$0.59^{\,m}$
Liquid phase fraction ε_l	$0.33^{\,m}$	$0.4^{\,m}$	$0.33^{\,m}$
Thermodynamics			
Equilibrium voltage E_{Eq}	see Equation A8 [81]		see Equation A9 [80]
Maximum Li$^+$ concentration $c_{s,max}$	$31363\,\text{mol m}^{-3}$		$51385\,\text{mol m}^{-3}$
Initial state of charge $\frac{c_{s,0}}{c_{s,max}}$	$0.85^{\,e}$		$0.395^{\,e}$
Kinetics			
Reaction rate constant k_{ref}	$1 \times 10^{-11}\,\text{m s}^{-1\,e}$		$1 \times 10^{-11}\,\text{m s}^{-1\,e}$
Anodic charge-transfer coefficient α_a	$0.5^{\,e}$		$0.5^{\,e}$
Cathodic charge-transfer coefficient α_c	$0.5^{\,e}$		$0.5^{\,e}$
Transport			
Solid diffusivity D_s	$3.9 \times 10^{-14}\,\text{m}^2\,\text{s}^{-1\,e}$		$8 \times 10^{-14}\,\text{m}^2\,\text{s}^{-1\,e}$
Solid conductivity σ	$100\,\text{S m}^{-1\,e}$		$2\,\text{S m}^{-1\,e}$
MacMullin number N_M	12 [82]	10 [82]	10 [82]

Parameter	Electrolyte
Electrolyte concentration c_l	$1000\,\text{mol m}^{-3\,e}$
Electrolyte diffusivity D_l	see Equation A10 [79]
Electrolyte conductivity κ	see Equation A11 [79]
Activity dependency $\frac{\partial \ln f_\pm}{\partial \ln c_l}$	see Equation A12 [79]
Transport number t_+	0.38 [79]

porosity ε_l and tortuosity τ[78]

$$\Psi_{l,eff} = \frac{\varepsilon_l}{\tau} \Psi_l = \frac{1}{N_M} \Psi_l \quad \text{[A7]}$$

To describe the electrolyte's characteristics properly, a concentration dependence is implemented for conductivity, diffusivity and mean molar activity coefficient of the electrolyte. These are taken from fittings to measurements[79] while presuming a constant transport number. The applied diffusion coefficients are estimated from various literature sources.[29,30,80,81] The equilibrium potential is taken from literature[81] as well as the maximum concentration of lithium within active material particles.[71,81] Additional parameters such as reaction rate constants[80,81] are assumed based on references from literature.

The chosen parameters for the above introduced model – measured or taken from literature – are summarized in Table AI.

Equilibrium voltage curves dependent on the degree of lithiation x or y for the negative electrode $E_{Eq,neg}$ by Safari et al.[81] and the positive electrode $E_{Eq,pos}$ by Stewart et al.[80]

$$E_{Eq,neg} = 0.6379 + (0.5416 \cdot \exp(-305.5309 \cdot x)) + 0.044 \cdot \tanh\left(\frac{-x + 0.1958}{0.1088}\right)$$

$$- 0.1978 \cdot \tanh\left(\frac{x - 1.0571}{0.0854}\right) - 0.6875 \cdot \tanh\left(\frac{x + 0.0117}{0.0529}\right)$$

$$- 0.0175 \cdot \tanh\left(\frac{x - 0.5692}{0.0875}\right) \quad \text{[A8]}$$

$$E_{Eq,pos} = 6.0826 - 6.9922 \cdot y + 7.1062 \cdot y^2 - 0.54549 \cdot 10^{-4} \cdot \exp(124.23 \cdot y - 114.2593)$$

$$- 2.5947 \cdot y^3 \quad \text{[A9]}$$

Analytical dependencies for electrolyte diffusivity D_l, conductivity κ and activity $\frac{\partial \ln f_\pm}{\partial \ln c_l}$ as functions of temperature T, lithium-ion concentration in the liquid phase c_l and transport number t_+ as measured by Valøen et al.[79]

$$D_l = 10^{-4.43 - \frac{54}{T - (229 + 5 \cdot c_l)} - 0.22 \cdot c_l} \cdot 10^{-4} \quad \text{[A10]}$$

$$\kappa = 0.1 \cdot c_l \cdot (-10.5 + 0.074 \cdot T - 6.96 \cdot 10^{-5} \cdot T^2 + 0.668 \cdot c_l - 0.0178 \cdot c_l \cdot T$$

$$+ 2.8 \cdot 10^{-5} \cdot c_l \cdot T^2 + 0.494 \cdot c_l^2 - 8.86 \cdot 10^{-4} \cdot c_l^2 \cdot T)^2 \quad \text{[A11]}$$

$$\frac{\partial \ln f_\pm}{\partial \ln c_l} = \frac{0.601 - 0.24 \cdot c_l^{0.5} + 0.982 \cdot c_l^{1.5} \cdot (1 - 0.0052 \cdot (T - 294))}{1 - t_+} - 1 \quad \text{[A12]}$$

References

1. M. Armand and J.-M. Tarascon, *Nature*, **451**, 652 (2008).
2. J.-M. Tarascon, *Electrochemical Society Interface*, **25**, 79 (2016).
3. B. Scrosati and J. Garche, *Journal of Power Sources*, **195**, 2419 (2010).
4. S. Passerini and B. Scrosati, *Electrochemical Society Interface*, **25**, 85 (2016).
5. R. M. Spotnitz, *Journal of Power Sources*, **113**, 72 (2003).
6. V. A. Agubra and J. W. Fergus, *Materials*, **6**, 1310 (2013).
7. V. A. Agubra and J. W. Fergus, *Journal of Power Sources*, **268**, 153 (2014).
8. P. Arora, R. E. White, and C. M. Doyle, *Journal of The Electrochemical Society*, **145**, 3647 (1998).
9. D. Aurbach, *Journal of Power Sources*, **89**, 206 (2000).
10. D. Aurbach, B. Markovsky, G. Salitra, E. Markevich, Y. Talyossef, M. Koltypin, L. F. Nazar, B. Ellis, and D. Kovacheva, *Journal of Power Sources*, **165**, 491 (2007).
11. C. R. Birkl, M. R. Roberts, E. McTurk, P. G. Bruce, and D. A. Howey, *Journal of Power Sources*, **341**, 373 (2017).
12. M. Broussely, P. Biensan, F. Bonhomme, P. Blanchard, S. Herreyre, K. Nechev, and R. J. Staniewicz, *Journal of Power Sources*, **146**, 90 (2005).
13. P. Verma, P. Maire, and P. Novák, *Electrochimica Acta*, **55**, 6332 (2010).
14. J. Vetter, P. Novák, M. R. Wagner, C. Veit, K.-C. Möller, J. O. Besenhard, M. Winter, M. Wohlfahrt-Mehrens, C. Vogler, and A. Hammouche, *Journal of Power Sources*, **147**, 269 (2005).
15. J. Christensen and J. S. Newman, *Journal of The Electrochemical Society*, **152**, A818 (2005).
16. Q. Zhang and R. E. White, *Journal of Power Sources*, **179**, 793 (2008).
17. X. Han, M. Ouyang, L. Lu, J. Li, Y. Zheng, and Z. Li, *Journal of Power Sources*, **251**, 38 (2014).
18. M. Dubarry, C. Truchot, and B. Y. Liaw, *Journal of Power Sources*, **219**, 204 (2012).
19. V. Ramadesigan, Paul W. C. Northrop, S. De, S. Santhanagopalan, R. D. Braatz, and V. R. Subramanian, *Journal of The Electrochemical Society*, **159**, R31 (2012).
20. A. Jokar, B. Rajabloo, M. Désilets, and M. Lacroix, *Journal of Power Sources*, **327**, 44 (2016).
21. P. Ganesh, P. R. C. Kent, and D.-e. Jiang, *The Journal of Physical Chemistry C*, **116**, 24476 (2012).
22. D. Marrocchelli, C. Merlet, and M. Salanne In *Physical Multiscale Modeling and Numerical Simulation of Electrochemical Devices for Energy Conversion and Storage*; A. A. Franco, M. L. Doublet, and W. G. Bessler, Eds.; Green Energy and Technology; Springer: London, 2016; pp 61–89.
23. S. Ogata, N. Ohba, and T. Kouno, *The Journal of Physical Chemistry C*, **117**, 17960 (2013).
24. E. Zvereva, D. Caliste, and P. Pochet, *Carbon*, **111**, 789 (2017).
25. M. Saubanère, J.-S. Filhol, and M. L. Doublet In *Physical Multiscale Modeling and Numerical Simulation of Electrochemical Devices for Energy Conversion and Storage*; A. A. Franco, M. L. Doublet, and W. G. Bessler, Eds.; Green Energy and Technology; Springer: London, 2016; pp 1–36.
26. N. G. Hörmann, M. Jäckle, F. Gossenberger, T. Roman, K. Forster-Tonigold, M. Naderian, S. Sakong, and A. Groß, *Journal of Power Sources*, **275**, 531 (2015).
27. K. Ushirogata, K. Sodeyama, Z. Futera, Y. Tateyama, and Y. Okuno, *Journal of The Electrochemical Society*, **162**, A2670 (2015).
28. J. S. Newman and K. E. Thomas-Alyea *Electrochemical systems*, 3rd ed.; Wiley-Interscience: Hoboken, NJ, 2004.
29. T. F. Fuller, C. M. Doyle, and J. S. Newman, *Journal of The Electrochemical Society*, **141**, 982 (1994).
30. C. M. Doyle, T. F. Fuller, and J. S. Newman, *Journal of The Electrochemical Society*, **140**, 1526 (1993).
31. D. Zhang, B. N. Popov, and R. E. White, *Journal of The Electrochemical Society*, **147**, 831 (2000).
32. J. S. Newman and C. W. Tobias, *Journal of The Electrochemical Society*, **109**, 1183 (1962).
33. S. Santhanagopalan, Q. Guo, P. Ramadass, and R. E. White, *Journal of Power Sources*, **156**, 620 (2006).
34. L. Kang, X. Zhao, and J. Ma, *Applied Energy*, **121**, 20 (2014).
35. W. Waag, S. Käbitz, and D. U. Sauer, *Applied Energy*, **102**, 885 (2013).
36. U. Tröltzsch, O. Kanoun, and H.-R. Tränkler, *Electrochimica Acta*, **51**, 1664 (2006).
37. H. Schranzhofer, J. Bugajski, H. J. Santner, C. Korepp, K.-C. Möller, J. O. Besenhard, M. Winter, and W. Sitte, *Journal of Power Sources*, **153**, 391 (2006).
38. D. Andre, M. Meiler, K. Steiner, H. Walz, T. Soczka-Guth, and D. U. Sauer, *Journal of Power Sources*, **196**, 5349 (2011).
39. D. Andre, M. Meiler, K. Steiner, C. Wimmer, T. Soczka-Guth, and D. U. Sauer, *Journal of Power Sources*, **196**, 5334 (2011).
40. J. C. Burns, R. Petibon, K. J. Nelson, N. N. Sinha, A. Kassam, B. M. Way, and J. R Dahn. *Journal of The Electrochemical Society*, **160**, A1668 (2013).
41. H. Dai, T. Xu, L. Zhu, X. Wei, and Z. Sun, *Applied Energy*, **184**, 119 (2016).
42. K. Fang, D. Mu, S. Chen, B. Wu, and F. Wu, *Journal of Power Sources*, **208**, 378 (2012).
43. T. R. Ashwin, Y. M. Chung, and J. Wang, *Journal of Power Sources*, **328**, 586 (2016).
44. T. R. Ashwin, A. McGordon, and P. A. Jennings, *Electrochimica Acta*, **232**, 203 (2017).
45. R. Fu, S.-Y. Choe, V. A. Agubra, and J. W. Fergus, *Journal of Power Sources*, **278**, 506 (2015).
46. M. T. Lawder, Paul W. C. Northrop, and V. R. Subramanian, *Journal of The Electrochemical Society*, **161**, A2099 (2014).
47. M. Rashid and A. Gupta, *ECS Electrochemistry Letters*, **3**, A95 (2014).
48. L. Cai, Y. Dai, M. Nicholson, R. E. White, K. Jagannathan, and G. Bhatia, *Journal of Power Sources*, **221**, 191 (2013).
49. L. L. Lam and R. B. Darling, *Journal of Power Sources*, **276**, 195 (2015).
50. X. Lin, J. Park, L. Liu, Y. K. Lee, A. M. Sastry, and W. Lu, *Journal of The Electrochemical Society*, **160**, A1701 (2013).
51. M. Ecker, N. Nieto, S. Käbitz, J. Schmalstieg, H. Blanke, A. Warnecke, and D. U. Sauer, *Journal of Power Sources*, **248**, 839 (2014).
52. K. Xu, *Chemical Reviews*, **104**, 4303 (2004).
53. D. Li, D. Danilov, Z. Zhang, H. Chen, Y. Yang, and P. H. L. Notten, *Journal of The Electrochemical Society*, **162**, A858 (2015).
54. J. Yan, B.-J. Xia, Y.-C. Su, X.-Z. Zhou, J. Zhang, and X.-G. Zhang, *Electrochimica Acta*, **53**, 7069 (2008).
55. M. B. Pinson and M. Z. Bazant, *Journal of The Electrochemical Society*, **160**, A243 (2013).
56. S. J. Harris and P. Lu, *The Journal of Physical Chemistry C*, **117**, 6481 (2013).
57. J. B. Goodenough and Y. Kim, *Chemistry of Materials*, **22**, 587 (2010).
58. S. Ramesh and B. Krishnamurthy, *Journal of The Electrochemical Society*, **162**, A545 (2015).
59. L. Liu, J. Park, X. Lin, A. M. Sastry, and W. Lu, *Journal of Power Sources*, **268**, 482 (2014).
60. M. Gauthier, T. J. Carney, A. Grimaud, L. Giordano, N. Pour, H.-H. Chang, D. P. Fenning, S. F. Lux, O. Paschos, C. Bauer, F. Maglia, S. Lupart, P. Lamp, and Y. Shao-Horn, *The Journal of Physical Chemistry Letters*, **6**, 4653 (2015).
61. H. Ekström and G. Lindbergh, *Journal of The Electrochemical Society*, **162**, A1003 (2015).
62. I. Laresgoiti, S. Käbitz, M. Ecker, and D. U. Sauer, *Journal of Power Sources*, **300**, 112 (2015).
63. H. J. Ploehn, P. Ramadass, and R. E. White, *Journal of The Electrochemical Society*, **151**, A456 (2004).
64. S. F. Schuster, T. C. Bach, E. Fleder, J. Müller, M. J. Brand, G. Sextl, and A. Jossen, *Journal of Energy Storage*, **1**, 44 (2015).
65. T. C. Bach, S. F. Schuster, E. Fleder, J. Müller, M. J. Brand, H. Lorrmann, A. Jossen, and G. Sextl, *Journal of Energy Storage*, **5**, 212 (2016).
66. Y. Domi, T. Doi, T. Ochida, T. Yamanaka, T. Abe, and Z. Ogumi, *Journal of The Electrochemical Society*, **163**, A2849 (2016).

67. I. Buchberger, S. Seidlmayer, A. Pokharel, M. Piana, J. Hattendorff, P. Kudejova, R. Gilles, and H. A. Gasteiger, *Journal of The Electrochemical Society*, **162**, A2737 (2015).
68. B. Vortmann-Westhoven, M. Winter, and S. Nowak, *Journal of Power Sources*, **346**, 63 (2017).
69. A. Bhandari and J. Bhattacharya, *Journal of The Electrochemical Society*, **164**, A106 (2017).
70. A. Banerjee, Y. Shilina, B. Ziv, J. M. Ziegelbauer, S. Luski, D. Aurbach, and I. C. Halalay, *Journal of The Electrochemical Society*, **164**, A6315 (2017).
71. P. Ramadass, B. S. Haran, P. M. Gomadam, R. E. White, and B. N. Popov, *Journal of The Electrochemical Society*, **151**, A196 (2004).
72. J. Purewal, J. S. Wang, J. Graetz, S. Soukiazian, H. Tataria, and M. W. Verbrugge, *Journal of Power Sources*, **272**, 1154 (2014).
73. F. M. Kindermann, P. J. Osswald, S. Klink, G. Ehlert, J. Schuster, A. Noel, S. V. Erhard, W. Schuhmann, and A. Jossen, *Journal of Power Sources*, **342**, 638 (2017).
74. F. M. Kindermann, P. J. Osswald, G. Ehlert, J. Schuster, A. Rheinfeld, and A. Jossen, *Journal of The Electrochemical Society*, **164**, E3105 (2017).
75. A. M. Colclasure, K. A. Smith, and R. J. Kee, *Electrochimica Acta*, **58**, 33 (2011).
76. K. Kleiner, P. Jakes, S. Scharner, V. Liebau, and H. Ehrenberg, *Journal of Power Sources*, **317**, 25 (2016).
77. G. Ning, R. E. White, and B. N. Popov, *Electrochimica Acta*, **51**, 2012 (2006).
78. M. J. Martínez-Rodríguez, S. Shimpalee, and J. W. van Zee, *Journal of The Electrochemical Society*, **156**, B80 (2009).
79. L. O. Valøen and J. N. Reimers, *Journal of The Electrochemical Society*, **152**, A882 (2005).
80. S. G. Stewart, V. Srinivasan, and J. S. Newman, *Journal of The Electrochemical Society*, **155**, A664 (2008).
81. M. Safari and C. Delacourt, *Journal of The Electrochemical Society*, **158**, A562 (2011).
82. J. Landesfeind, A. Ehrl, M. Graf, W. A. Wall, and H. A. Gasteiger, *Journal of The Electrochemical Society*, **163**, A1254 (2016).

6 Modeling of Lithium Plating and Lithium Stripping in Lithium-Ion Batteries

This chapter introduces the paper *Modeling of Lithium Plating and Lithium Stripping in Lithium-ion Batteries.*

In this study, we present a physicochemical model considering both lithium plating and lithium stripping side reactions. The model simulates reversible lithium plating and the characteristic voltage plateau due to lithium stripping during a subsequent discharge after lithium plating in a previous charge.

The model is based on a Molicel IHR18650A lithium-ion cell with a nominal capacity of 1.95 Ah which is composed of graphite as the negative electrode and NMC as the positive electrode. We carried out characterization and validation measurements at various C-rates (0.1 C, 0.2 C, 0.5 C, 1 C) at a controlled temperature of 25 °C and 0 °C. To investigate the voltage plateau caused by lithium stripping during a 0.2 C discharge, we induced lithium plating using a constant current constant voltage (CCCV) charging protocol at various C-rates (0.2 C, 0.5 C, 0.7 C, 1 C) with a cut-off current of 0.05 C at a controlled temperature of 0 °C.

The lithium plating side reaction is described by a Butler-Volmer equation as reported by Arora et al. [72] and takes place as soon as the potential of the negative electrode becomes negative vs. Li/Li^+. Once the potential becomes positive again, the subsequent lithium stripping side reaction proceeds by dissolving the plated lithium. This side reaction is also described by a Butler-Volmer equation including an additional correction term that considers the amount of reversibly plated and stripped lithium. The correction term allows the stripping reaction to be stopped, when the reversibly amount of plated lithium has been dissolved. The equilibrium potential of both lithium plating and lithium stripping side reactions is regarded as 0 V vs. Li/Li^+ and the exchange current density is considered to be concentration and reaction rate dependent. We assume a fully reversible lithium deposition reaction that is valid for a few cycles as simulated in this work.

While the lithium de-/intercalation reactions as well as lithium plating and lithium stripping side reactions depend on the temperature, we coupled the physicochemical model with a 0D thermal model considering the thermal mass of the lithium-ion cell and the heat transfer by convection and radiation. The heat generation is comprised of irreversible heat.

The simulated cell voltage and surface temperature agrees well with the validation experiments for different C-rates at a controlled temperature of 25 °C and 0 °C.

The lithium plating simulation results agree to the state of the art and show more severe plating with increasing C-rate, stronger plating at the negative electrode/separator interface and strongest plating when switching from the CC to the CV charging mode. The amount of deposited lithium predicted by the simulation is in the same range as the ones measured in a previous neutron diffraction study by von Lüders et al. [53] under nearly the same conditions.

With the novel lithium stripping modeling approach, we simulated the characteristic voltage plateau during discharge that is in good agreement with the experimental data for different C-rates. Finally, the voltage plateau increases with higher C-rates and therefore with an increasing amount of deposited lithium.

Author contribution Jonas Keil initiated the idea of an electrochemical lithium stripping modeling approach, developed, parametrized and validated the model and initiated the experimental work. Christian von Lüders helped to develop the model based on his expertise on lithium plating and literature based lithium plating modeling approaches, initiated and coordinated the experimental work and carried out the simulation studies. The data was analyzed by Jonas Keil and Christian von Lüders, while Markus Webersberger helped to process the data. The manuscript was written by Christian von Lüders and Markus Webersberger and was edited by Jonas Keil and Andreas Jossen. All authors discussed the data and commented on the results.

Modeling of lithium plating and lithium stripping in lithium-ion batteries

Christian von Lüders, Jonas Keil, Markus Webersberger, Andreas Jossen

Permanent weblink:
`https://doi.org/10.1016/j.jpowsour.2018.12.084`

Modeling of lithium plating and lithium stripping in lithium-ion batteries

Christian von Lüders[*], Jonas Keil, Markus Webersberger, Andreas Jossen

Institute for Electrical Energy Storage Technology (EES), Technical University of Munich (TUM), Arcisstr. 21, 80333, Munich, Germany

HIGHLIGHTS

- A physicochemical model for lithium plating and lithium stripping is developed.
- The characteristic voltage plateau due to lithium stripping is simulated.
- The voltage plateau corresponds to the amount of previously plated lithium.
- Simulated amount of plated lithium corresponds to a former neutron diffraction study.

ARTICLE INFO

ABSTRACT

In this study, we present a physicochemical model considering both lithium plating and lithium stripping side reactions in lithium-ion batteries. The model shows the amount of reversibly plated lithium dependent on the charging current on the surface of the graphite anode. In the subsequent discharge, a characteristic voltage plateau due to lithium stripping is simulated. The shape of the voltage plateau corresponds to the amount of previously plated lithium. The model correlates with experimental data of a commercial 18650-type NMC/C cell. The simulated amount of plated lithium is in the same range as in a previous neutron diffraction study with the same cell type. To induce lithium plating, the cells are charged with various C-rates at an ambient temperature of 0 °C. The measured voltage plateau caused by lithium stripping in the discharge is correctly described by simulation.

1. Introduction

Lithium-ion batteries are today's most important energy storage system for mobile applications due to their high specific energy and power density [1]. Nevertheless, lithium-ion batteries degrade during their lifetime by several aging mechanisms [2,3]. One main aging mechanism is the deposition of metallic lithium on the surface of the graphite anode [4], which occurs under certain operational conditions such as low temperatures [5–9], high charging currents [10–12] and a high state-of-charge (SOC) [11,13] during charging. Hence, lithium plating should be avoided by maintaining the maximum charging current, the minimum operating temperature and the upper cut-off voltage. However, especially for battery electric vehicles, fast charging is essential to compensate for the limited driving range.

The deposition of lithium is initially reversible, but part of the deposited lithium is irreversibly lost due to the reaction with the electrolyte or due to a loss of electrical contact during the dissolution, which both result in capacity loss. Lithium plating can also become a safety risk because of the growth of dendrites, which can possibly

penetrate the separator and short-circuit the electrodes, and because of exothermic reactions of lithium metal with the electrolyte [7]. Moreover, lithium plating can also occur after prolonged cycling due to pore clogging in the porous electrode [14].

Physicochemical models can be helpful to predict the onset of lithium deposition and the possible amount of deposited metallic lithium. It is also important to describe the altered voltage behavior due to the lithium dissolution, the so-called lithium stripping, during a subsequent discharge or rest period.

There are some models for lithium plating, but only a few models the backward reaction of lithium stripping. Arora et al. [15] firstly described the conditions for lithium deposition during overcharge. They extended Doyle's well-known model [16–19] with a side reaction described by a Butler-Volmer equation on the negative electrode and investigated lithium deposition under various operating conditions, with various cell designs and charging protocols. Perkins et al. [20] compared Arora's full-order model [15] with their own reduced-order model to develop a controls-oriented comprehensive cell degradation model. Hein and Latz [21] showed by their simulation on

---

microstructure scale that the voltage plateau during the stripping process not only depends on the amount of deposited lithium but also on the distribution in the electrode. Ge et al. [22] extended Arora's model [15] with temperature dependency according to the Arrhenius law for low temperature studies. Additionally, they compared their simulations with experimental data measured by nuclear magnetic resonance. Yang et al. [14] developed a lithium plating induced aging model, which predicts the transition from linear to nonlinear aging after prolonged cycling. Yang et al. [23] further used a concentration-dependent Butler-Volmer equation for their mathematical model for lithium plating and stripping. Ren et al. [24] added a second side reaction for the stripping process to Arora's model [15], which can roughly describe the voltage behavior during a rest period.

This work will extend the well-known model by Doyle, Fuller and Newman [16–18] with one side reaction for the modeling of lithium deposition according to Arora et al. [15] during charging. The backward side reaction describes the lithium stripping process taking into account the plated charge quantity. With this approach, the characteristic voltage plateau of lithium stripping is described during a subsequent discharge after lithium plating in a previous charge. All simulations are validated by experimental data of a commercial 18650-type NMC/C cell.

2. Model description

In this work, a physicochemical model is developed to analyze the behavior of lithium plating and lithium stripping based on the modeling approach of Doyle, Fuller and Newman [16–19], which rests on the concentrated solution and the porous electrode theory. The developed model is a one-dimensional representation of the cell, which is coupled to a second dimension representing the spherical active material particles, which is also known as a pseudo-two-dimensional (p2D) model.

2.1. Implementation of lithium plating and lithium stripping

Lithium plating and stripping are side reactions occurring on the surface of the negative electrode. The reactions of plating and stripping can be written in the following way:

$$Li^+ + e^- \rightleftarrows Li^0 \tag{1}$$
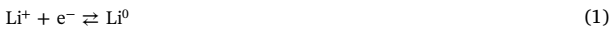
The forward reaction describes lithium plating and the backward reaction lithium stripping. The total local current density i_{tot} must be the sum of the current density of the main reaction $i_{main,neg}$, which is the intercalation respectively deintercalation, and the current densities of the side reactions lithium plating i_{lpl} and lithium stripping i_{lst}:

$$i_{tot} = i_{main,neg} + i_{lpl} + i_{lst} \tag{2}$$

The intercalation/deintercalation reaction is described by a Butler-Volmer equation where the driving force is the overpotential η_{main}, which is defined by the difference between the potentials of the solid and the liquid phase $\phi_s - \phi_l$ and the thermodynamic equilibrium potential ϕ^0:

$$\eta_{main} = \phi_s - \phi_l - \phi^0 \tag{3}$$

The charge-transfer current density i_{main} is calculated by

$$i_{main} = i_{0,main}\left(\exp\left(\frac{\alpha_a F}{RT}\eta_{main} \right) - \exp\left(\frac{-\alpha_c F}{RT}\eta_{main} \right) \right) \tag{4}$$

with the exchange current density for the intercalation/deintercalation reaction:

$$i_{0,main} = Fk_c^{\alpha_a} k_a^{\alpha_c} (c_{s,max} - c_{s,surf})^{\alpha_a} c_{s,surf}^{\alpha_c} \left(\frac{c_l}{c_{l,ref}} \right)^{\alpha_a} \tag{5}$$

The maximum possible concentration of intercalated lithium ions in the active material is given by $c_{s,max}$ and the lithium-ion concentration

in the electrolyte by c_l. Furthermore, k describes reaction rates and α expresses the charge-transfer coefficients. Subscripts a and c signify the anodic and cathodic direction, respectively. Moreover, the exchange current density is dependent on the surface concentration $c_{s,surf}$.

The side reaction for lithium plating is described by a Butler-Volmer equation as reported by Arora et al. [15]:

$$i_{lpl} = i_{0,lpl}\left(\exp\left(\frac{\alpha_{a,lpl}F}{RT}\eta_{lpl} \right) - \exp\left(\frac{-\alpha_{c,lpl}F}{RT}\eta_{lpl} \right) \right), \ \eta_{lpl} \leq 0 \ V \tag{6}$$

The exchange current density for the lithium plating reaction was derived by Ge et al. [22]:

$$i_{0,lpl} = Fk_{lpl}c_l^{\alpha_{a,lpl}} \tag{7}$$

The overpotential of both side reactions can be written as

$$\eta_{lpl} = \eta_{lst} = \phi_s - \phi_l - \phi^0_{Li^0/Li^+} \tag{8}$$

with the subscripts lpl and lst which consider lithium plating and lithium stripping side reactions. The equilibrium potential of both side reactions is regarded as 0 V versus Li^0/Li^+. The condition for lithium plating is $\eta_{lpl} \leq 0$ V, whereas the condition for lithium stripping is $\eta_{lpl} > 0$ V.

The side reaction in relation to lithium stripping can also be described by a Butler-Volmer equation with the same exchange current density but an additional correction term, in which q_{lpl} and q_{lst} is the amount of reversibly plated and stripped lithium, respectively. The correction term allows the stripping reaction to be stopped, when the reversibly amount of plated lithium has been consumed. Both Butler-Volmer equations enable that the current is zero when the overpotential is zero:

$$i_{lst} = i_{0,lpl}\left(\exp\left(\frac{\alpha_{a,lpl}F}{RT}\eta_{lpl} \right) - \exp\left(\frac{-\alpha_{c,lpl}F}{RT}\eta_{lpl} \right) \right)\frac{q_{lpl} - q_{lst}}{q_{lpl,max}}, \ \eta_{lpl} > 0 \ V \tag{9}$$

A brief overview of all used physicochemical parameters is given in Table 1. The equations of the equilibrium potentials for both electrodes as well as the electrolyte transport equations can be found in the appendix (A.1-A.5).

In this work, we assume that the lithium deposition reaction is fully reversible. That means the whole part of the deposited lithium is dissolved during the subsequent stripping process. This can be considered as valid for a few cycles since Howlett et al. [25] showed cycling efficiency of greater than 99 % for lithium metal electrodes. In a future work, we will extend the model to form irreversible products to get an irreversible loss of lithium inventory during extended cycling.

The ratio between the intercalation and the plating current while charging as well as between the deintercalation current and the stripping current while discharging depends on the temperature. Therefore, the physicochemical model is coupled with a thermal model.

2.2. Thermal model

The physicochemical model is coupled with a 0D thermal model, in which the heat is evenly distributed in the cell. The heat transfer is considered by convection

$$\dot{Q}_{conv} = hA_{cell}(T_{block} - T) \tag{10}$$

with the heat transfer coefficient h, the cell surface A_{cell}, the cell temperature T_{block} and the ambient temperature T. The radiation

$$\dot{Q}_{rad} = \varepsilon_{th}\sigma_B A_{cell}(T_{block}^4 - T^4) \tag{11}$$

in which ε_{th} is the emissivity and σ_B the Stefan-Boltzmann constant. Furthermore, the thermal mass of the cell is considered

$$\dot{Q}_{th} = mc_p\frac{\partial T_{block}}{\partial t} \tag{12}$$

Table 1
Physicochemical model parameters for a commercial 18650-type NMC/C cell.

Parameter	Anode	Separator	Cathode
Thickness l	79 μm [a]	25 μm [a]	67 μm [a]
Particle radius r_p	10.5 μm [a]		4.6 μm [a]
Solid phase fraction ε_s	0.56 [b]		0.56 [b]
Liquid phase fraction ε_l	0.3 [b]	0.45 [b]	0.3 [b]
Specific surface a^V	$3\varepsilon_s/r_p$		$3\varepsilon_s/r_p$
Equilibrium potential ϕ^0	see Equation (A.1) [26]		see Equation (A.2) [27]
Maximum Li$^+$ concentration $c_{s,max}$	31370 mol m^{-3} [28]		51385 mol m^{-3} [28]
Initial state of charge $\frac{c_{s,0}}{c_{s,max}}$ (25 °C $\mid$ 0 °C)	0.9 $\mid$ 0.78 [b]		0.394 $\mid$ 0.4 [b]
Activation energy of the diffusion $E_{a,D}$	1.5·10^4 J mol^{-1} [29]		1.5·10^4 J mol^{-1} [29]
Activation energy of the reaction $E_{a,k}$	3.5·10^4 J mol^{-1} [29]		3.5·10^4 J mol^{-1} [29]
Reaction rate constant k	1·10^{-11} m s^{-1} [30]		1·10^{-11} m s^{-1} [30]
Anodic charge-transfer coefficient α_a	0.5 [c]		0.5 [c]
Cathodic charge-transfer coefficient α_c	0.5 [c]		0.5 [c]
Solid diffusivity D_s	1·10^{-14} m^2 s^{-1} [30]		1·10^{-14} m^2 s^{-1} [6]
Electronic conductivity σ	100 S m^{-1} [31]		3.8 S m^{-1} [31]
MacMullin number N_M	12 [c]	12 [c]	12 [32]
Initial electrolyte concentration c_l		1000 mol m^{-3} [c]	
Electrolyte diffusivity D_l		see Equation (A.3) [33]	
Electrolyte ionic conductivity κ		see Equation (A.4) [33]	
Activity dependency $\frac{\partial \ln f \pm}{\partial \ln c_l}$		see Equation (A.5) [33]	
Transport number t_+		0.38 [34]	
Reaction rate constant lithium plating k_{lpl}	2.5·10^{-7} m s^{-1} [b]		
Anodic charge-transfer coefficient lithium plating $\alpha_{a,lpl}$	0.5 [c]		
Cathodic charge-transfer coefficient lithium plating $\alpha_{c,lpl}$	0.5 [c]		

[a] Measured.
[b] Fitted to measurements.
[c] Assumed.

with its specific heat capacity c_p and mass m.

The heat balancing equation results in

$$\dot{q}V_{cell} = mc_p\frac{\partial T_{block}}{\partial t} + hA_{cell}(T_{block} - T) + \varepsilon_{th}\sigma_B A_{cell}(T_{block}^4 - T^4) \quad (13)$$

in which V_{cell} is the volume of the cell.

The heat generation $\dot{q}$ is comprised of several components: the ohmic power losses of the liquid and solid phase, the irreversible heat produced by the charge-transfer and the reversible heat.

$$\dot{q} = \dot{q}_{ohm,l} + \dot{q}_{ohm,s} + \dot{q}_{irrev,\,main} + \dot{q}_{irrev,\,lpl} + \dot{q}_{irrev,\,lst} + \dot{q}_{rev,\,main} + \dot{q}_{rev,\,lpl}$$
$$+ \dot{q}_{rev,\,lst} \quad (14)$$

Since the reversible heat has only a significant influence at lower currents [35], no temperature-dependent equilibrium potentials are regarded in this work. Thus, Eq. (14) can be written as

$$\dot{q} = i_l \nabla\phi_l + i_{s,neg}\nabla\phi_s + i_{s,pos}\nabla\phi_s + a_{neg}^V i_{main,neg}\eta_{main,neg} + a_{pos}^V i_{pos}\eta_{pos}$$
$$+ a_{neg}^V i_{lpl}\eta_{lpl} + a_{neg}^V i_{lst}\eta_{lst} \quad (15)$$

dependent on the current densities of the solid and liquid phases i_s and i_l, the potentials ϕ_s and ϕ_l, as well as on the specific surface a^V, the local current densities and the overpotentials of the reactions. The parameters for the thermal model are summarized in Table 2.

Table 2
Thermal model parameters.

Parameter	
Specific heat capacity c_p	1000 J kg^{-1} K^{-1} [28]
Emissivity ε_{th}	0.8 [36]
Heat transfer coefficient h	25 W m^{-2} K^{-1} [a]

[a] Assumed

3. Experimental

The measurements were performed with a commercial 18650-type cylindrical cell with a layered metal oxide as cathode (LiNi$_{1/3}$Mn$_{1/3}$Co$_{1/3}$O$_2$) and graphite as anode. The nominal capacity is rated as 1.95 Ah during a 0.2C discharge at 25 °C. All C-rates in this paper are given relative to this nominal capacity. The measurements were performed on a Cell Test System (BaSyTec, Germany) and were carried out in a VT4021 climate chamber (Vötsch, Germany).

For the validation of the model, the cells were charged with a constant current (CC) of 0.2C from 3.0 V to the cut-off voltage of 4.2 V, followed by a constant voltage (CV) phase at 4.2 V until the charge current dropped below 0.05C. Afterwards, the cells were discharged with various C-rates (0.1C, 0.2C, 0.5C, 1C) to 3.0 V. The validation measurements were performed at an ambient temperature of 25 °C and 0 °C.

To induce lithium plating, the cells were charged with various C-rates (0.2C, 0.5C, 0.7C, 1C) to the cut-off voltage of 4.2 V at an ambient temperature of 0 °C, followed by a CV phase at 4.2 V until the charge current dropped below 0.05C. For the investigation of the voltage plateau caused by lithium stripping, the cells were subsequently discharged at a C-rate of 0.2C to the cut-off voltage of 3.0 V. For every condition, three cells were measured.

4. Results and discussion

4.1. Model validation

Fig. 1 shows the validation of the physicochemical and thermal model. The simulated cell voltage and surface temperature are compared with experimental results for discharge with 0.1C, 0.2C, 0.5C and 1C. As in all validation experiments, the charging current was only 0.2C, no lithium plating was expected. The simulations and experiments are performed at ambient temperatures of 25 °C as shown in Fig. 1a) and b) and at 0 °C in Fig. 1c) and d). The simulated and
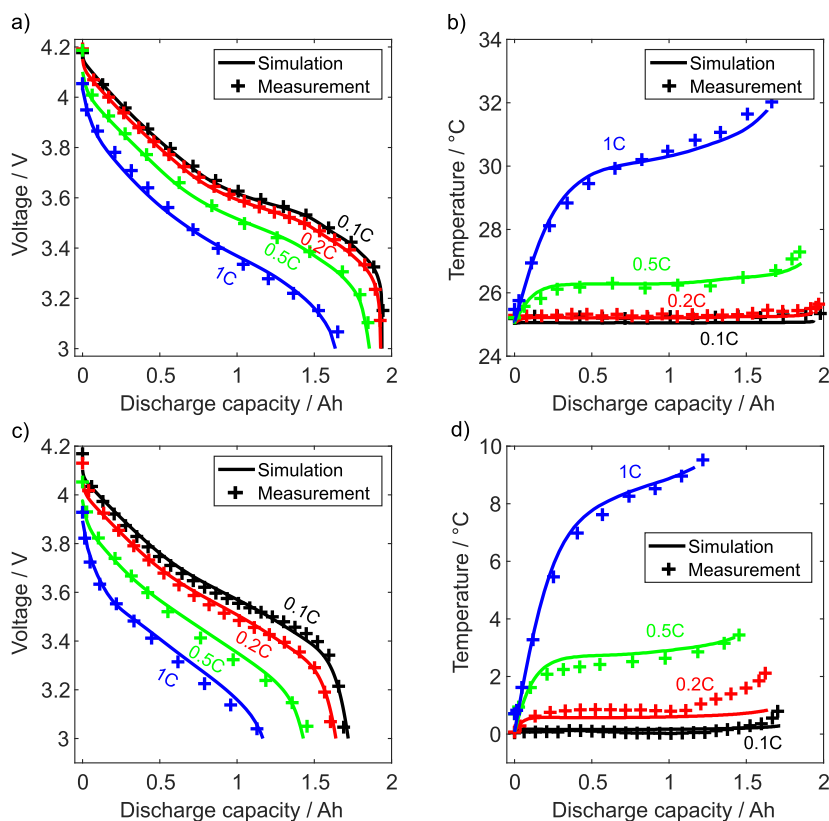
Fig. 1. Comparison of the simulation results (solid lines) with the experimental data (symbols) at different discharge rates. (a) Cell voltage and (b) surface temperature at an ambient temperature of 25 °C, (c) cell voltage and (d) surface temperature at an ambient temperature of 0 °C vs. discharge capacity.

experimental data are presented vs. discharge capacity for a better scaling in contrast to time representation. According to Fig. 1, the simulated cell voltage corresponds to the experimental data very well for all C-rates. The simulated temperature is in good agreement with the experimental data except for some small deviations at 0 °C.

4.2. Lithium plating

With a charging rate of 0.2C, the anode potential never drops below 0 V neither at the separator electrode interface nor at the current collector electrode interface at an ambient temperature of 0 °C (Fig. 2). Therefore, no lithium plating occurs at a charging rate of 0.2C. For the
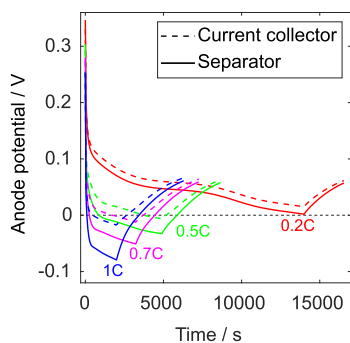

Fig. 2. Anode potential vs. Li^0/Li^+ over time at an ambient temperature of 0 °C at the electrode separator interface (solid lines) and at the electrode current collector interface (dashed lines).

other applied charging rates 0.5C, 0.7C and 1C, lithium plating starts at the electrode separator interface at 868 s, 259 s and 98 s, respectively, when the potential of the negative electrode falls below 0 V. The lowest anode potential always occurs at the anode/separator interface.

Later during charging, plating occurs in the whole electrode, as the propagation of the plating reaction proceeds from the separator electrode interface into the anode in the direction of the current collector of the anode. Lithium plating begins at the current collector electrode interface at 3749 s, 1743 s and 474 s for 0.5C, 0.7C and 1C, respectively.

In Fig. 3, the local volumetric current density of the three modeled reactions is depicted at the electrode separator interface. The 1C charging begins with regular intercalation until the anode potential drops below 0 V, at which lithium plating starts. Both reactions proceed simultaneously even though the intercalation current density has not reached its maximum yet. When switching to the CV phase at 1.064 Ah, the volumetric current density for lithium plating has its maximum and begins to reduce due to an increasing plating overpotential in consequence of a decreasing charging current. After the anode potential exceeds 0 V at 1.466 Ah, the volumetric current density of plating drops to zero and the dissolution of plated lithium – lithium stripping – starts.

The amount of deposited lithium can be predicted by simulation. Dependent on the charging current, the amount of plated lithium increases with higher charging currents, which can be seen in Fig. 4. The plated lithium is 0.141 Ah for a current of 0.5C, 0.230 Ah for 0.7C and 0.299 Ah for 1C. In relation to the nominal cell capacity of 1.95 Ah, the deposited lithium accounts for 7.2 %–15.3 %. These values are in the same range as the ones measured in a previous neutron diffraction study [12] with the same cell type under nearly the same conditions as the temperature was −2 °C. In that study, 5.5 % of lithium plating for a current of 0.5C was measured and 9.0 % for 1C. The quantity of lithium
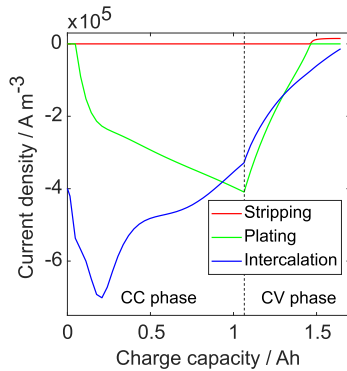
Fig. 3. Local volumetric current density of the intercalation (blue), plating (green) and stripping (red) reaction at the electrode separator interface vs. capacity during 1C CCCV charge. (For interpretation of the references to colour in this figure legend, the reader is referred to the Web version of this article.)
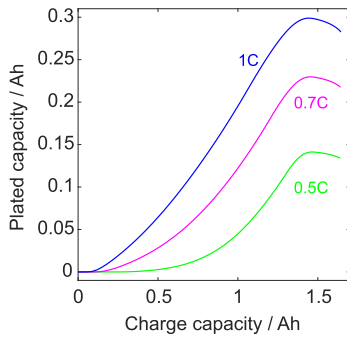

Fig. 4. Capacity of reversibly plated lithium vs. charge capacity for increasing charging currents.

plating is underestimated, as the calculations of the neutron diffraction experiment refer to the relaxation phase and do not consider the lithium stripping in the CV phase.

In this simulation, 8 mAh are already stripped in the CV phase at 0.5C, 13 mAh at 0.7C and 18 mAh at 1C.

4.3. Lithium stripping

The characteristic voltage plateau which correlates with the lithium stripping process is described in literature during discharge [8,9,37]
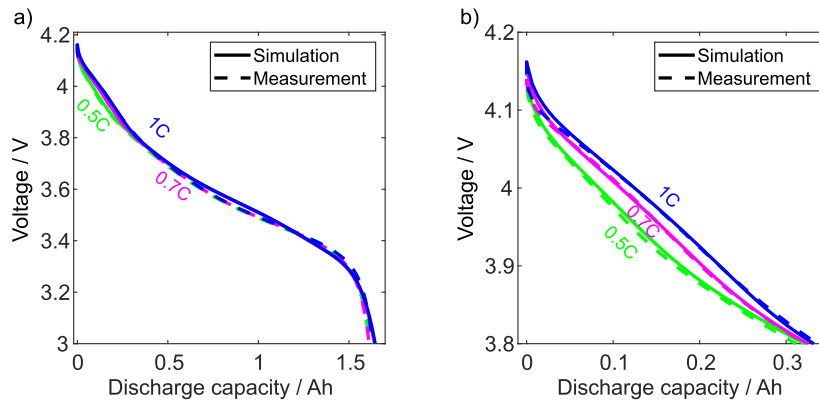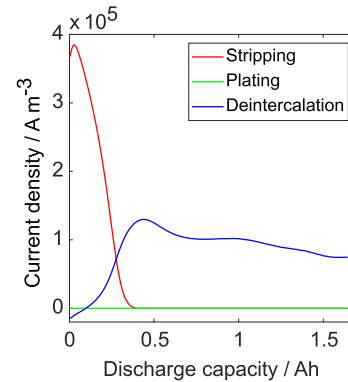

Fig. 6. Local volumetric current density of the deintercalation (blue), plating (green) and stripping (red) reaction at the electrode separator interface vs. discharge capacity after 1C charge. (For interpretation of the references to colour in this figure legend, the reader is referred to the Web version of this article.)

and relaxation [12,24,38]. In Fig. 5 a), the simulated voltage during discharging is compared with experimental data at an ambient temperature of 0 °C. The charging rates are set as mentioned before, but every discharge is carried out with a constant current of 0.2C.

With charging rates of 0.5C, 0.7C and 1C, lithium is deposited due to the negative anode potential (cf Fig. 2), and the voltage plateau is clearly visible during the subsequent discharges. The size of the plateau increases with increasing charging current which indicates that the plateau correlates with the amount of deposited lithium. The simulated voltage curves match with the experimental data for the voltage plateau and the position of the turning points very well, as can be seen in the magnification in Fig. 5 b). The deviation between simulation and measurement of the voltage plateau is less than 10 mV.

With the beginning of the discharge, the volumetric current density for lithium stripping increases immediately nearly to its maximum, which is approximately three times higher than the average deintercalation volumetric current density, which can be seen in Fig. 6. The high stripping current density at the beginning of the discharge results in a small deintercalation current during the discharge period. The lithium stripping volumetric current density reduces nearly constantly until all reversibly plated lithium is dissolved and the curve levels out at 0.4 Ah. Up to this state, the deintercalation current density increases strongly.

After charging with 0.2C, the stoichiometry x in Li_xC_6 decreases linearly when discharging with a constant current. The state of charge

Fig. 5. (a) Cell voltage vs. discharge capacity after previous 0.5C, 0.7C and 1C charge, simulation (solid lines) and measurement (dashed lines). (b) Magnification of the voltage plateau during lithium stripping.
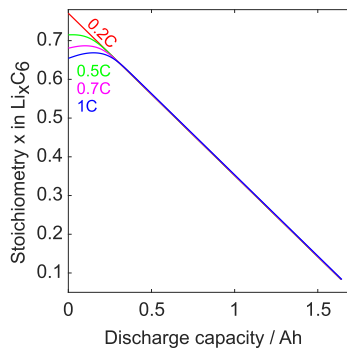
Fig. 7. Stoichiometry x in Li_xC_6 vs. discharge capacity.

of the graphite anode is lower for higher charging C-rates because of lithium plating and increased polarization. It can be seen in Fig. 7 that the highest C-rates show the lowest stoichiometries at the beginning of the discharge. The plated lithium dissolves in the discharge phase before deintercalation starts. This results in a slower decrease of the stoichiometry when lithium stripping takes place. For the high C-rates of 0.7C and 1C, the stoichiometry increases first by 0.9 % and 2.2 % until deintercalation of the anode starts. After all plated lithium is stripped, all curves collapse to one due to the same discharge rate.

This confirms earlier experimental studies by Zinth et al. [8] where they showed that the neutron diffraction signal corresponding to the state of charge of the graphite anode stays constant during a subsequent discharge until all reversibly plated lithium is dissolved (cf cycle III in Fig. 10 in their study).

5. Summary and conclusion

We have developed a pseudo-two-dimensional model which considers the phenomenon of lithium plating as well as lithium stripping. The model has been validated by experimental data and shows a very high agreement at both ambient temperatures of 25 °C and 0 °C. Four charging rates have been observed with these results: 0.2C does not indicate any lithium plating in contrast to 0.5C, 0.7C and 1C, at which the amount of plating increases with the C-rate. The characteristic voltage plateau during discharge due to lithium stripping can be illustrated very distinctly by simulation and correlates very highly with the measured data. Furthermore, the voltage plateau clearly increases with the increasing amount of lithium plating rising up to the start of the CV phase, after which it then decreases. In addition, the simulated amounts of plated lithium also match to the measurement data of a neutron diffraction study [12].

This model extension provides a foundation for plating detection so that novel charging methods can be developed, which are fast and safe. The impact of lithium plating and lithium stripping on cell aging will further be investigated in a future study.

Acknowledgement

Appendix A

Equilibrium potential of the negative electrode dependent on the degree of lithiation x by Safari et al. [26]:

$$\phi_{neg}^0 = 0.6379 + 0.5416 \cdot \exp(-305.5309x) + 0.044 \tanh\left(-\frac{x - 0.1958}{0.1088}\right) - 0.1978 \tanh\left(\frac{x - 1.0571}{0.0854}\right) - 0.6875 \tanh\left(\frac{x + 0.0117}{0.0529}\right)$$

$$- 0.0175 \tanh\left(\frac{x - 0.5692}{0.0875}\right) \tag{A.1}$$

Equilibrium potential of the positive electrode dependent on the degree of lithiation y by Stewart et al. [27]:

$$\phi_{pos}^0 = 6.0826 - 6.9922y + 7.1062y^2 - 0.54549 \cdot 10^{-4} \exp(124.23y - 114.2593) - 2.5947y^3 \tag{A.2}$$

Electrolyte phase diffusion coefficient D_l by Lundgren et al. [33]:

$$D_l = 7.588 \cdot 10^{-11} \exp\left(\frac{3536.9}{8.314}\left(\frac{1}{298.15} - \frac{1}{T}\right)\right)c_l^2 - 3.036 \cdot 10^{-10} \exp\left(\frac{3272}{8.314}\left(\frac{1}{298.15} - \frac{1}{T}\right)\right)c_l + 3.654 \cdot 10^{-10} \exp\left(\frac{8372.8}{8.314}\left(\frac{1}{298.15} - \frac{1}{T}\right)\right) \tag{A.3}$$

Ionic conductivity κ_l by Lundgren et al. [33]:

$$\kappa_l = \frac{1.147}{10} \cdot \exp\left(\frac{520}{8.314}\left(\frac{1}{298.15} - \frac{1}{T}\right)\right)c_l^3 - \frac{22.38}{10} \cdot \exp\left(\frac{1010}{8.314}\left(\frac{1}{298.15} - \frac{1}{T}\right)\right)c_l^{1.5} + \frac{29.15}{10} \cdot \exp\left(\frac{1270}{8.314}\left(\frac{1}{298.15} - \frac{1}{T}\right)\right)c_l \tag{A.4}$$

Activity dependence $\frac{\partial \ln f_\pm}{\partial \ln c_l}$ by Lundgren et al. [33]:

$$\frac{\partial \ln f_\pm}{\partial \ln c_l} = \frac{0.2731c_l^2 + 0.6352c_l + 0.4577}{(0.1291c_l^3 - 0.3517c_l^2 + 0.4893c_l + 0.5713) - 1} \tag{A.5}$$

References

[1] B. Scrosati, J. Garche, Lithium batteries, J. Power Sources 195 (2010) 2419–2430, https://doi.org/10.1016/j.jpowsour.2009.11.048.

[2] M. Broussely, P. Biensan, F. Bonhomme, P. Blanchard, S. Herreyre, K. Nechev, R.J. Staniewicz, Main aging mechanisms in Li ion batteries, J. Power Sources 146 (2005) 90–96, https://doi.org/10.1016/j.jpowsour.2005.03.172.

[3] J. Vetter, P. Novák, M.R. Wagner, C. Veit, K.-C. Möller, J.O. Besenhard, M. Winter, M. Wohlfahrt-Mehrens, C. Vogler, A. Hammouche, Ageing mechanisms in lithium-ion batteries, J. Power Sources 147 (2005) 269–281, https://doi.org/10.1016/j.jpowsour.2005.01.006.

[4] T. Waldmann, B.-I. Hogg, M. Wohlfahrt-Mehrens, Li plating as unwanted side reaction in commercial Li-ion cells – a review, J. Power Sources 384 (2018) 107–124, https://doi.org/10.1016/j.jpowsour.2018.02.063.

[5] J. Fan, S. Tan, Studies on charging lithium-ion cells at low temperatures, J. Electrochem. Soc. 153 (2006) A1081, https://doi.org/10.1149/1.2190029.

[6] M. Petzl, M. Kasper, M.A. Danzer, Lithium plating in a commercial lithium-ion battery – a low-temperature aging study, J. Power Sources 275 (2015) 799–807, https://doi.org/10.1016/j.jpowsour.2014.11.065.

[7] M. Fleischhammer, T. Waldmann, G. Bisle, B.-I Hogg, M. Wohlfahrt-Mehrens, Interaction of cyclic ageing at high-rate and low temperatures and safety in lithium-ion batteries, J. Power Sources 274 (2015) 432–439, https://doi.org/10.1016/j.jpowsour.2014.08.135.

[8] V. Zinth, C. von Lüders, M. Hofmann, J. Hattendorff, I. Buchberger, S. Erhard, J. Rebelo-Kornmeier, A. Jossen, R. Gilles, Lithium plating in lithium-ion batteries at sub-ambient temperatures investigated by in situ neutron diffraction, J. Power Sources 271 (2014) 152–159, https://doi.org/10.1016/j.jpowsour.2014.07.168.

[9] R.V. Bugga, M.C. Smart, 216th ECS Meeting, ECS, 2010, pp. 241–252.

[10] J.C. Burns, D.A. Stevens, J.R. Dahn, In-Situ detection of lithium plating using high precision coulometry, J. Electrochem. Soc. 162 (2015) A959–A964, https://doi.org/10.1149/2.0621506jes.

[11] T. Waldmann, M. Kasper, M. Wohlfahrt-Mehrens, Optimization of charging strategy by prevention of lithium deposition on anodes in high-energy lithium-ion batteries – electrochemical experiments, Electrochim. Acta 178 (2015) 525–532, https://doi.org/10.1016/j.electacta.2015.08.056.

[12] C. von Lüders, V. Zinth, S.V. Erhard, P.J. Osswald, M. Hofmann, R. Gilles, A. Jossen, Lithium plating in lithium-ion batteries investigated by voltage relaxation and in situ neutron diffraction, J. Power Sources 342 (2017) 17–23, https://doi.org/10.1016/j.jpowsour.2016.12.032.

[13] T. Waldmann, B.-I. Hogg, M. Kasper, S. Grolleau, C.G. Couceiro, K. Trad, B.P. Matadi, M. Wohlfahrt-Mehrens, Interplay of operational parameters on lithium deposition in lithium-ion cells, J. Electrochem. Soc. 163 (2016) A1232–A1238, https://doi.org/10.1149/2.0591607jes.

[14] X.-G. Yang, Y. Leng, G. Zhang, S. Ge, C.-Y. Wang, Modeling of lithium plating induced aging of lithium-ion batteries: transition from linear to nonlinear aging, J. Power Sources 360 (2017) 28–40, https://doi.org/10.1016/j.jpowsour.2017.05.110.

[15] P. Arora, M. Doyle, R.E. White, Mathematical modeling of the lithium deposition overcharge reaction in lithium-ion batteries using carbon-based negative electrodes, J. Electrochem. Soc. 146 (1999) 3543, https://doi.org/10.1149/1.1392512.

[16] M. Doyle, T.F. Fuller, J. Newman, Modeling of galvanostatic charge and discharge of the lithium/polymer/insertion cell, J. Electrochem. Soc. 140 (1993) 1526, https://doi.org/10.1149/1.2221597.

[17] C.M. Doyle, Design and Simulation of Lithium Rechargeable Batteries, Ph. D. Thesis (1995).

[18] T.F. Fuller, Simulation and optimization of the dual lithium ion insertion cell, J. Electrochem. Soc. 141 (1994) 1, https://doi.org/10.1149/1.2054684.

[19] J.S. Newman, K.E. Thomas-Alyea, Electrochemical Systems, third ed., Wiley-Interscience, Hoboken, NJ, 2004.

[20] R.D. Perkins, A.V. Randall, X. Zhang, G.L. Plett, Controls oriented reduced order modeling of lithium deposition on overcharge, J. Power Sources 209 (2012) 318–325, https://doi.org/10.1016/j.jpowsour.2012.03.003.

[21] S. Hein, A. Latz, Influence of local lithium metal deposition in 3D microstructures on local and global behavior of Lithium-ion batteries, Electrochim. Acta 201 (2016) 354–365, https://doi.org/10.1016/j.electacta.2016.01.220.

[22] H. Ge, T. Aoki, N. Ikeda, S. Suga, T. Isobe, Z. Li, Y. Tabuchi, J. Zhang, Investigating lithium plating in lithium-ion batteries at low temperatures using electrochemical model with NMR assisted parameterization, J. Electrochem. Soc. 164 (2017) A1050–A1060, https://doi.org/10.1149/2.0461706jes.

[23] X.-G. Yang, S. Ge, T. Liu, Y. Leng, C.-Y. Wang, A look into the voltage plateau signal for detection and quantification of lithium plating in lithium-ion cells, J. Power Sources 395 (2018) 251–261, https://doi.org/10.1016/j.jpowsour.2018.05.073.

[24] D. Ren, K. Smith, D. Guo, X. Han, X. Feng, L. Lu, M. Ouyang, J. Li, Investigation of lithium plating-stripping process in Li-ion batteries at low temperature using an electrochemical model, J. Electrochem. Soc. 165 (2018) A2167–A2178, https://doi.org/10.1149/2.0661810jes.

[25] P.C. Howlett, D.R. MacFarlane, A.F. Hollenkamp, High lithium metal cycling efficiency in a room-temperature ionic liquid, Electrochem. Solid State Lett. 7 (2004) A97. 10.1149/1.1664051.

[26] M. Safari, C. Delacourt, Modeling of a commercial graphite/LiFePO4 cell, J. Electrochem. Soc. 158 (2011) A562, https://doi.org/10.1149/1.3567007.

[27] S.G. Stewart, V. Srinivasan, J. Newman, Modeling the performance of lithium-ion batteries and capacitors during hybrid-electric-vehicle operation, J. Electrochem. Soc. 155 (2008) A664, https://doi.org/10.1149/1.2953524.

[28] S. Tippmann, D. Walper, L. Balboa, B. Spier, W.G. Bessler, Low-temperature charging of lithium-ion cells part I, J. Power Sources 252 (2014) 305–316, https://doi.org/10.1016/j.jpowsour.2013.12.022.

[29] Y. Ye, Y. Shi, N. Cai, J. Lee, X. He, Electro-thermal modeling and experimental validation for lithium ion battery, J. Power Sources 199 (2012) 227–238, https://doi.org/10.1016/j.jpowsour.2011.10.027.

[30] R. Chandrasekaran, Quantification of contributions to the cell overpotential during galvanostatic discharge of a lithium-ion cell, J. Power Sources 262 (2014) 501–513, https://doi.org/10.1016/j.jpowsour.2014.03.124.

[31] M. Doyle, Comparison of modeling predictions with experimental data from plastic lithium ion cells, J. Electrochem. Soc. 143 (1996) 1890, https://doi.org/10.1149/1.1836921.

[32] J. Landesfeind, A. Ehrl, M. Graf, W.A. Wall, H.A. Gasteiger, Direct electrochemical determination of thermodynamic factors in aprotic binary electrolytes, J. Electrochem. Soc. 163 (2016) A1254–A1264, https://doi.org/10.1149/2.0651607jes.

[33] H. Lundgren, M. Behm, G. Lindbergh, Electrochemical characterization and temperature dependency of mass-transport properties of LiPF 6 in EC:DEC, J. Electrochem. Soc. 162 (2015) A413–A420, https://doi.org/10.1149/2.0641503jes.

[34] L.O. Valøen, J.N. Reimers, Transport properties of LiPF[sub 6]-based Li-ion battery electrolytes, J. Electrochem. Soc. 152 (2005) A882, https://doi.org/10.1149/1.1872737.

[35] V.V. Viswanathan, D. Choi, D. Wang, W. Xu, S. Towne, R.E. Williford, J.-G. Zhang, J. Liu, Z. Yang, Effect of entropy change of lithium intercalation in cathodes and anodes on Li-ion battery thermal management, J. Power Sources 195 (2010) 3720–3729, https://doi.org/10.1016/j.jpowsour.2009.11.103.

[36] C. Kupper, W.G. Bessler, Multi-scale thermo-electrochemical modeling of performance and aging of a LiFePO 4/graphite lithium-ion cell, J. Electrochem. Soc. 164 (2017) A304–A320, https://doi.org/10.1149/2.0761702jes.

[37] M. Petzl, M.A. Danzer, Nondestructive detection, characterization, and quantification of lithium plating in commercial lithium-ion batteries, J. Power Sources 254 (2014) 80–87, https://doi.org/10.1016/j.jpowsour.2013.12.060.

[38] S. Schindler, M. Bauer, M. Petzl, M.A. Danzer, Voltage relaxation and impedance spectroscopy as in-operando methods for the detection of lithium plating on graphitic anodes in commercial lithium-ion cells, J. Power Sources 304 (2016) 170–180, https://doi.org/10.1016/j.jpowsour.2015.11.044.

Symbols

A_{cell}: cell surface area in m^2
a^V: specific surface in m^{-1}
c: lithium-ion concentration in mol m^{-3}
c_p: specific heat capacity in J kg^{-1} K^{-1}
F: Faraday constant, 96485 C mol^{-1}
h: heat transfer coefficient in W m^{-2} K^{-1}
i: local current density in A m^{-2}
i_0: exchange current density in A m^{-2}
k: reaction rate constant in m s^{-1}
m: mass in kg
q: local amount of reversible lithium in C mol^{-3}
$\dot{q}$: heat generation in W m^{-3}
$\dot{Q}$: heat transfer in W
R: universal gas constant, 8.314 J mol^{-1} K^{-1}
T: absolute temperature in K
T_{block}: resulting cell temperature in K
V_{cell}: cell volume in m^3
α: charge-transfer coefficient
ε_{th}: emissivity
η: overpotential in V
σ_B: Stefan-Boltzmann constant, 5.67·10^{-8} W m^{-2} K^{-4}
ϕ: electric potential in V
ϕ^0: thermodynamic equilibrium potential in V

Subscripts

a: anodic
c: cathodic
conv: convection
irrev: irreversible
l: liquid phase
Li: lithium
lpl: lithium plating
lst: lithium stripping
main: main reaction
neg: negative electrode
pos: positive electrode
rad: radiation
rev: reversible
s: solid phase
surf: surface
th: thermal
tot: total

7 Linear and Nonlinear Aging of Lithium-Ion Cells Investigated by Electrochemical Analysis and In-Situ Neutron Diffraction

In this chapter, we summarize the paper *Linear and Nonlinear Aging of Lithium-Ion Cells Investigated by Electrochemical Analysis and In-Situ Neutron Diffraction.*

In this work, we present an aging study on commercial 18650-type $C/LiNi_{0.33}Mn_{0.33}Co_{0.33}O_2$ lithium-ion cells under different testing procedures. Both linearly and nonlinearly aged cells are investigated by electrochemical analysis and in-situ neutron diffraction.

The general test procedure is as follows: the cells were discharged using a CC to a cut-off voltage of 2.75 V, followed by a CC charging step to a cut-off voltage of 4.2 V and a CV charging step with a cut-off current of 0.1 A. After each discharge and charge, resting times were applied. By varying the charging current, the discharging current and the resting time, four different test procedures were performed. At the beginning of the aging experiment and after every 100 cycles, checkup tests were performed to determine the cells' capacity and internal resistance. For all cycles and tests, we used an environmental chamber to keep the ambient temperature at 25 °C. The cells show a nonlinear capacity fade after a few hundred equivalent full cycles, if cycled with a standard charging and discharging rate of almost 1C, and different resting times of 900 s and 10 s. By increasing the discharging current to almost 2C or decreasing the charging current to roughly 0.7C, the lifetime improves and results in a linear capacity fade.

The neutron diffraction measurements were performed using a Debye–Scherrer geometry under ambient conditions at the high-resolution powder diffractometer SPODI, at the Heinz Maier-Leibnitz (FRM II) research reactor in Garching, Germany [88]. For the neutron diffraction experiment, two cells from every test procedure – which result in various SOHs – were selected and respectively charged or discharged to 4.2 V (100 % SOC) or 2.75 V (0 % SOC) using a CCCV protocol with a current of 1 A ($\approx$ C/2) and a cut-off current of 20 mA ($\approx$ C/100).

Equally to the work summarized in Chapter 4, we carried out Rietveld refinements of all neutron diffractograms to identify crystalline phases, estimate their phase fractions and derive lattice parameters to thus analyze the cyclable lithium content in the electrodes and structural changes caused by aging. The neutron diffraction experiment reveals the loss of lithium inventory as the dominant aging mechanism for both linearly- and nonlinearly-aged cells. Other aging mechanisms, like the structural degradation of anode or cathode active materials or the deactivation of active materials, could not be confirmed. This result is also confirmed by DVA.

The comparison between capacity loss determined by electrochemical analysis and neutron diffraction revealed an increasing capacity loss in the edge area of the electrodes with ongoing aging. We supposed two different dominant aging mechanisms, which are the growth of the solid electrolyte interphase in the early stage and marginal lithium deposition in the later stage.

After a few weeks of storage, checkup tests showed both capacity recovery or capacity loss dependent on the SOH as well as the SOC the cells were stored at. Linearly-aged cells that were fully charged for the neutron diffraction experiment revealed a capacity loss of less than 3.0 %, whereas the fully discharged ones pointed out a capacity recovery of less than 3.2 %, owing to lithium diffusion into or out of the anode overhang area [103], respectively. On the other hand, all nonlinearly-aged cells showed a capacity recovery due to lithium stripping, the partial reversible reaction of lithium deposition, as well as the chemical intercalation of lithium.

Finally, SEM images of uncycled and nonlinearly-aged cells qualitatively showed surface layer growth and morphology changes on the graphite anode, whereas the cathode particles appeared unchanged.

Author contribution   Jonas Keil initiated the idea of the experimental study investigating linear and nonlinear aging, designed and carried out the aging experiment, helped to design and to carry out the neutron diffraction experiment, accomplished the post-mortem analysis and analyzed and processed the data. Neelima Paul and Volodymyr Baran designed and carried out the neutron diffraction experiment as well as analyzed and processed the neutron diffraction data. Peter Keil helped to design the aging experiment and to process the data. The manuscript was written by Jonas Keil and was edited by Neelima Paul, Volodymyr Baran, Peter Keil, Ralph Gilles and Andreas Jossen. All authors discussed the data and commented on the results.

Linear and Nonlinear Aging of Lithium-Ion Cells Investigated by Electrochemical Analysis and In-Situ Neutron Diffraction

Jonas Keil, Neelima Paul, Volodymyr Baran, Peter Keil, Ralph Gilles, Andreas Jossen

Linear and Nonlinear Aging of Lithium-Ion Cells Investigated by Electrochemical Analysis and In-Situ Neutron Diffraction

Jonas Keil, [1,z] Neelima Paul, [2] Volodymyr Baran, [2] Peter Keil, [1] Ralph Gilles, [2] and Andreas Jossen [1]

[1]*Technical University of Munich (TUM), Institute for Electrical Energy Storage Technology (EES), 80333 Munich, Germany*
[2]*Technical University of Munich (TUM), Heinz Maier-Leibnitz Zentrum (MLZ), 85747 Garching, Germany*

In this paper, we present an aging study of commercial 18650-type $C/LiNi_{0.33}Mn_{0.33}Co_{0.33}O_2$ lithium-ion cells. The test procedure comprises varying charging currents, discharging currents and resting times between cycles. The cells show a nonlinear capacity fade after a few hundred equivalent full cycles, if cycled with a standard charging and discharging rate of almost 1C, and different resting times. By increasing the discharging current or decreasing the charging current, the lifetime improves and results in a linear capacity fade. The neutron diffraction experiment reveals a loss of lithium inventory as the dominant aging mechanism for both linearly- and nonlinearly-aged cells. Other aging mechanisms such as the structural degradation of anode or cathode active materials, or the deactivation of active materials, cannot be confirmed. With ongoing aging, we observe an increasing capacity loss in the edge area of the electrodes. Whereas the growth of the solid electrolyte interphase defines the early stage, linear aging, marginal lithium deposition is supposed to cause the later stage, nonlinear aging. Capacity recovery caused by lithium stripping and chemical intercalation is shown to be dependent on the cell's state of health.

Nowadays, lithium-ion battery technology is widely used both in mobile and stationary applications, such as consumer electronics, electric vehicles, and grid operations. The economic, sustainable and safe operation of these battery-energy-storage systems depends significantly on their aging behavior. In particular, the definition of a battery's end of life, and also a conceivable reuse of lithium-ion batteries in second life applications, are extensively discussed topics.[1–3]

Aging of lithium-ion cells generally means a decrease in its energy density and power capability, caused by the loss of capacity and the increase of impedance. In particular, aging can be separated into an early stage and a later stage. The former indicates decelerated or linear aging, whereas the latter describes accelerated or nonlinear aging. Furthermore, the aging mechanisms can be assigned to a loss of lithium inventory (LLI), a loss of active material and an impedance increase.[4–6] The main aging mechanisms are: electrolyte decomposition leading to solid electrolyte interphase (SEI) and cathode electrolyte interphase growth; contact loss of active material particles due to volume changes during cycling; a decrease in accessible surface area and porosity due to SEI growth; lithium deposition; transition-metal dissolution from the cathode; solvent co-intercalation; gas evolution with subsequent cracking of particles; binder decomposition; and current collector corrosion.[7–10]

SEI growth, the main aging mechanism under common operational conditions, results in a linear capacity fade on charge throughput, or a square-root-shaped capacity loss over time.[11] However, a nonlinear or accelerated capacity fade is caused by the deposition of metallic lithium on the graphite anode,[2] if the local anode potential becomes negative vs. Li/Li^+.[12,13] Low temperatures,[10,14–16] high charging currents[2,10,17] as well as a high state of charge (SoC)[18] favor lithium deposition. Lithium metal can react again with the electrolyte, forming additional SEI. Waldmann et al.[13] classify the terminology of lithium deposition and distinguish between homogeneous lithium plating and inhomogeneous, local or marginal, lithium deposition. Even at moderate temperatures and charging rates, lithium deposition may occur due to inhomogeneous current and potential distributions, as well as temperature gradients inside the cell.[2,10] Bach et al.[19] show local lithium deposition, caused by an unevenly compressed cell casing, at an ambient temperature of 20°C. Lithium plating or lithium deposition are partly reversible processes as long as the plated/deposited lithium exhibits an electrical contact to the active material of the negative electrode. In that case, there are basically two different reversible processes: lithium stripping during a subsequent discharge, or chemical intercalation during relaxation.[13]

There are various methods to characterize aging mechanisms and their underlying chemical, physical and mechanical processes. In general, a distinction is made between in-situ and ex-situ experiments. In situ refers to measurements that are performed on materials in their original position, i.e. without disassembling the battery.[20] Ex-situ measurements involve cell opening and sample preparation. The fact that further operation of the cell is not possible following ex-situ measurements, as well as the high risk of altering or contaminating the samples, are the main drawbacks of this method.[20–22] The most commonly used in-situ techniques are X-ray techniques, scanning probe microscopy, electron microscopy, optical techniques, magnetic (resonance) techniques and neutron techniques.[20] However, the metal casing of lithium-ion cells is generally impenetrable for electromagnetic waves, magnetic fields and electrons. Therefore, special cells including transparent windows are required for most spectroscopy and microscopy techniques.[21,23]

Neutron diffraction (ND) is a powerful analytical in-situ technique to study commercial lithium-ion cells. Rietveld analysis of neutron diffractograms can be used to determine the atomic structure, lattice parameters and particle size of crystalline anode (e.g. graphite) and cathode active materials (e.g. spinels, layered metal oxides or phospho-olivines).[21] Compared to X-ray diffraction, neutron diffraction shows a much higher sensitivity for light elements like lithium (especially in the vicinity of heavy elements) and is much more suitable for large cell formats due to the higher penetration depth of neutrons.[21] However, as a consequence of the high effort of neutron diffraction measurements, only a few studies have been published so far and they analyze degradation mechanisms in particular. Dolotko et al.[24] investigated cell fatigue of linearly-aged commercial $C/LiCoO_2$ cells at 25°C and 50°C, and observed a loss of mobile lithium due to SEI formation. This result is confirmed by Shiotani et al.[25] and Paul et al.[26] for 18650-type $C/LiNi_{0.33}Mn_{0.33}Co_{0.33}O_2$ cells. The aging of cells composed of different anode active materials, mesocarbon microbeads and needle coke, and a lithium-iron-phosphate (LFP) based cathode has been investigated by Paul et al.,[21] and showed that LLI was the dominant aging mechanism. Inhomogeneous lithium distribution affected by cell fatigue is shown by Cai et al.[27] and Mühlbauer et al.[28] Furthermore, Zinth et al.[29] and von Lüders et al.[15] investigated chemical intercalation through changes in LiC_6 and LiC_{12} peak intensities during a rest time immediately after severe lithium deposition at low temperatures.

zE-mail: jonas.keil@tum.de

Nevertheless, there is still little knowledge of how SEI growth, lithium deposition, lithium stripping and chemical intercalation interact during aging. In this context, we present an aging study of commercial 18650-type C/LiNi$_{0.33}$Mn$_{0.33}$Co$_{0.33}$O$_2$ lithium-ion cells with a focus on linear and nonlinear aging behavior, depending on the test procedure. We use electrochemical analysis and in-situ neutron diffraction to investigate the aging mechanisms. To the best of our knowledge, we firstly obtain structural information of both linearly- and nonlinearly-aged lithium-ion cells by using neutron diffraction.

Experimental

This section presents the investigated lithium-ion cells as well as the test conditions, the test procedure of the aging experiment and the design of the neutron diffraction experiment.

Cell information and test conditions.—We tested commercial 18650-type lithium-ion cells with a nominal capacity of 2.05 Ah and an energy density of 175 Wh kg^{-1}. The cells are composed of graphite as the anode and LiNi$_{0.33}$Mn$_{0.33}$Co$_{0.33}$O$_2$ as the cathode. We used a battery test system CTS (BaSyTec) to cycle the cells, and an environmental chamber MK 53 (Binder) to keep the ambient temperature at 25°C.

Aging experiment.—The general test procedure is as follows: the cells were discharged using a constant current step (CC$_{dch}$) to a cutoff voltage of 2.75 V, followed by a constant current charging step (CC$_{ch}$) to a cutoff voltage of 4.2 V and a constant voltage charging step (CV$_{ch}$) with a cutoff current of 0.1 A. After each discharge and charge, resting times (t_r) were applied. By varying the charging current, the discharging current and the resting time, four different test procedures were performed, as shown in Table I. We tested at least three cells for every test procedure. At the beginning of the aging experiment and after ev-

Table I. Test procedures of aging experiment with varying charging currents, discharging currents and resting times.

Test procedure	$I_{CC\,dch}$	t_r	$I_{CC\,ch}$	$I_{CV\,ch}$	t_r
# 1	−2 A	900 s	2 A	0.1 A	900 s
# 2	−2 A	10 s	2 A	0.1 A	10 s
# 3	−4 A	900 s	2 A	0.1 A	900 s
# 4	−2 A	900 s	1.4 A	0.1 A	900 s

ery 100 cycles, checkup tests were performed to determine the cells' capacity and internal resistance. The capacity is determined using a CCCV protocol with a current of 250 mA ($\approx$ C/10) and a cutoff current of 100 mA ($\approx$ C/20). The internal resistance $R_{dc,10s}$ in the time domain is derived from the voltage response, corresponding to a current step of 3 A with a pulse duration of 10 s. Additionally, differential voltage analysis (DVA) was obtained. For the neutron diffraction experiment, two cells from every test procedure were selected and respectively charged or discharged to 4.2 V (100% SoC) or 2.75 V (0% SoC) using a CCCV protocol with a current of 1A ($\approx$ C/2) and a cutoff current of 20 mA ($\approx$ C/100). We dis-/charged the cells five days before the neutron diffraction experiment started to guarantee relaxed states within the cells.

Neutron diffraction experiment.—The neutron diffraction measurements were performed using a Debye–Scherrer geometry under ambient conditions at the high-resolution powder diffractometer SPODI, at the Heinz Maier-Leibnitz (FRM II) research reactor in Garching, Germany.[30] Figure 1a shows the schematic of the instrument and the setup of the experiment. Neutrons with a wavelength of 0.1548 nm were incident on a rectangular cross section of 40 mm × 30 mm of the cell center, as shown in Figures 1b and 1c. The top
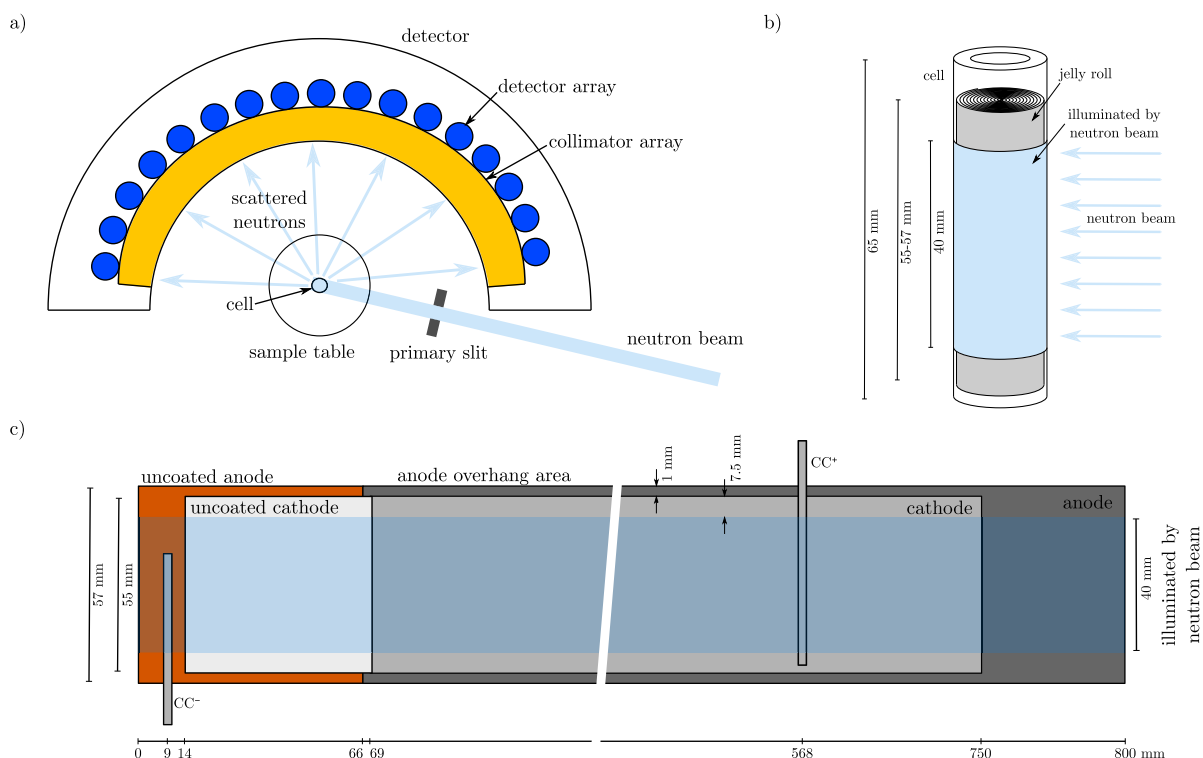

Figure 1. a) Schematic of high-resolution powder diffractometer SPODI and setup of neutron diffraction experiment, b) rectangular cross section of 40 mm height, illuminated by neutron beam, and c) schematic of electrode geometries of the investigated cell.

and bottom of the cell (approx. 25 mm in total) were not illuminated by the neutron beam, to avoid noisy signals from the cell holder and safety protection circuitry. A neutron detector array consisting of 80 vertical position-sensitive detectors with a Soller collimator in front of each, see Figure 1a, recorded the neutrons scattered by the cell.[30,31] The cells were continuously rotated during the entire measurement to obtain an average signal over cell volume. Five succeeding diffractograms were measured for each cell, with an acquisition time of 36 min each. Therefore, the total integration time for the obtained diffractograms was 3 h for each cell. We determined an instrumental resolution function with a $Na_2Ca_3Al_2F_{14}$ reference material, in order to calculate the full widths at half the maximum reflections from the cell. To describe the peak profile shape, a Thompson-Cox-Hastings pseudo-Voigt function was used.[32] A linear interpolation between selected data points was used to fit the background. Multi-phase Rietveld refinements of structural models for the neutron diffraction data were carried out using the FullProf software package.[33] Due to significant overlap of diffraction peaks from the steel housing and current collectors, and the strong preferred orientations of crystallites for these phases, structure-independent profile fits were used.

Post-mortem analysis.—Scanning electron microscopy (SEM) was used to qualitatively investigate the surface morphology of the electrodes of cycled and uncycled cells. The cells were opened in a glove box (M. Braun Inertgas-Systeme GmbH, Germany) under an argon atmosphere, subsequent to the aging experiment. We punched out electrode samples at different positions along the electrode and obtained images using a benchtop SEM (JCM-6000, JEOL Ltd., Japan) with an acceleration voltage of 15 kV.

Results and Discussion

Electrochemical characterization.—Figure 2 shows the mean values (solid lines) and standard deviations (light-colored) of the relative capacity and relative resistance over equivalent full cycles (EFC) for the various test procedures. The test procedures # 1 and # 2, which have the same charging and discharging currents and varying resting times, both show a nonlinear capacity fade, whereas # 3 and # 4, which have an increased discharging current or decreased charging current, give a linear capacity fade (see Figure 2a). The increase in the relative discharge resistance at 50% SoC is in accordance with the capacity loss and equally demonstrates either a nonlinear (test procedures # 1 and # 2) or linear (test procedures # 3 and # 4) behavior, as depicted in Figure 2b. As shown by Schuster et al.,[34] capacity fade and impedance rise correlate dependent on the operational strategies. Assuming an end of life of 80% state of health (SoH), the achievable battery life is as follows: # 1 ≈ 400 EFC, # 2 ≈ 550 EFC, # 3 ≈ 800 EFC and # 4 > 850 EFC. Shortening the relaxation time between cycles positively influences the lifetime by roughly 40%. At the same time, a higher discharging current and unchanged relaxation almost doubles the cell's lifetime. The strongest effect is shown by a reduced charging current, with a lifetime exceeding 850 EFC. It should be noted that these results are valid for this cell type and within the scope of this aging experiment. The temperature increase for all cells under various test conditions is of less than 2°C from the beginning to the ending of cycling, measured at the cell's surface.

Our original goal was to carry out the neutron diffraction experiment with both linearly- and nonlinearly-aged cells for every test procedure. Due to the fast capacity loss for cells cycled with test procedure # 1 and the absence of nonlinear aging for cells cycled with test procedure # 3 and # 4, we were only able to investigate differently aged cells for test procedure # 2. This results in 12 cells at different SoH, and in uncycled ones that were fully charged or discharged for the neutron diffraction experiment using a CCCV protocol with a current of 1A (≈ C/2) and a cutoff current of 20 mA (≈ C/100). The small currents were used to diminish polarization and to guarantee the same SoCs, i.e. the same cell voltages. Table II summarizes the cells and their respective SoH and SoC as investigated in the neutron diffraction experiment.
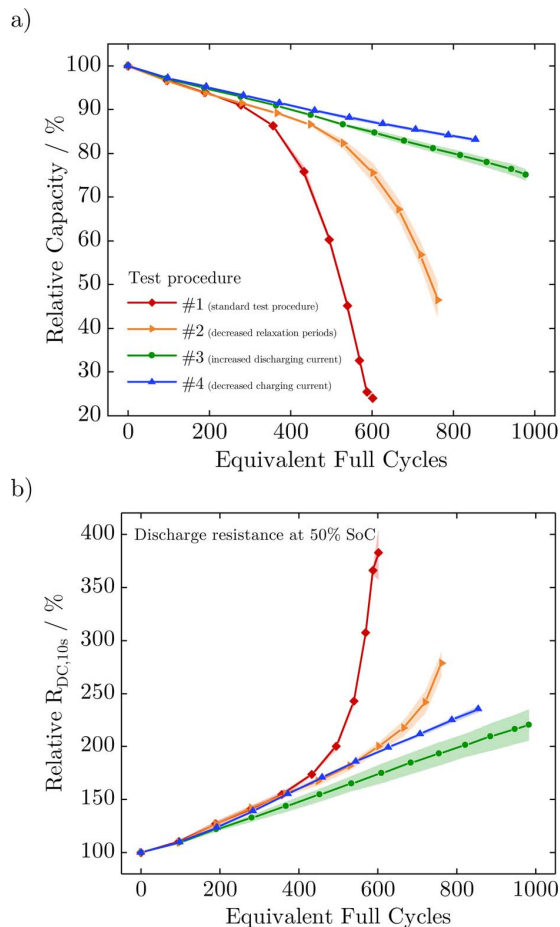
a)

b)

Figure 2. Mean values (solid lines) and standard deviations (light-colored) of the relative capacity (a) and relative resistance (b) over equivalent full cycles for the various test procedures.

Finally, we obtained differential voltage analysis to investigate the degradation mechanisms.[4,35] Figure 3 shows the measured differential voltage of cells for the various test procedures. Furthermore, Figure 3a depicts distinctive material markers that are phase changes of the lithiated graphite. According to Winter et al.,[36] the first one shows the transition from phase III+IV to phase II+IIL and the second from phase II+IIL to II+I. As these markers do not shift and Q_C remains constant, anode active material loss cannot be confirmed. Distinctive material markers that refer to the cathode cannot be assigned in the DVA curves. The absolute irreversible capacity loss Q_{cell} at remaining material markers of the anode reveals a loss of lithium inventory as the dominant aging mechanism for both linearly- and nonlinearly-aged cells.

Neutron diffraction.—Neutron diffractograms were taken for cells at various SoHs in their fully discharged state (0% SoC) as well as in their fully charged state (100% SoC). Rietveld refinements were carried out of all neutron diffractograms and structural information regarding all polycrystalline battery constituents obtained. Crystal structure models of LiC_6 and LiC_{12} for the anode and $Li_yNi_{0.33}Mn_{0.33}Co_{0.33}O_2$ for the cathode were used to analyze the diffraction patterns at 100% SoC. At 0% SoC, crystal structure models of graphite for the anode and $Li_yNi_{0.33}Mn_{0.33}Co_{0.33}O_2$ for the cathode were used to analyze the diffraction patterns. The difference in lithium content between 100% SoC and 0% SoC corresponds to the amount

Table II. Information on the cells investigated in the neutron diffraction experiment.

Test procedure	#1		#2		#3		#4		#2		uncycled	
Cell number	1	2	3	4	5	6	7	8	9	10	11	12
SoC for ND experiment/%	100	0	100	0	100	0	100	0	100	0	100	0
	CheckUp data before cycling											
Initial capacity/Ah	2.0575	2.0530	2.0576	2.0527	2.0604	2.0487	2.0676	2.0596	2.0556	2.0610	2.0673	2.0506
	CheckUp data after cycling and before neutron diffraction experiment											
Equivalent full cycles	599	604	767	770	975	982	852	856	278	278	0	0
Capacity/Ah	0.4920	0.4532	1.0153	0.9832	1.5295	1.5596	1.7129	1.7157	1.8815	1.8856	2.0673	2.0506
SoH/%	23.9	22.1	49.3	47.9	74.2	76.1	82.8	83.3	91.5	91.5	100.0	100.0

of cyclable lithium participating in the charge/discharge process. The loss of cyclable lithium due to aging is estimated by comparing the amount of cyclable lithium in the uncycled and aged cells. Thus, cyclable lithium losses reported in this work are calculated relative to the uncycled cell.

In Figure 4a, LiC_6 and LiC_{12} reflections of the lithiated anode material are clearly visible in the fully charged state of all cells. No LiC_z reflections with $z > 12$, corresponding to phases with low lithium content such as LiC_{18} or LiC_{24} or C, are observed in any cell. A decrease in the intensity of the LiC_6 (001) reflection peak and increase in the LiC_{12} (002) reflection peak with decreasing SoH (on aging) is observed. This is related to the decrease in lithium content within the anode. In Figure 4c, the C (002) reflection in the delithiated anode shows no noticeable shift in angular position on aging, which is an indication of the complete extraction of lithium from the anode at 0%

SoC, regardless of aging. We presume that the observed intensity reductions of the crystalline carbon peak of the aged cells occur due to diffusion of lithium into the anode overhang area, as all cells were measured for the same amount of time. Since no additional lithiated graphite reflections in this angular region are detected at 0% SoC, and no graphite reflections are detected at 100% SoC an absence of neither lithiated nor delithiated electrochemically detached anode active material can be concluded for all cells.

In Figure 4d, the NMC (003), NMC (006) and NMC (012) reflections of the cathode show angular shifts indicating that the lithium content in the lithiated cathode has decreased during aging. On the other hand, these reflections remain fairly similar on aging for the delithiated cathode, as can be seen in Figure 4b, showing that the amount of lithium being removed from the cathode at the upper voltage limit is similar for all cells.
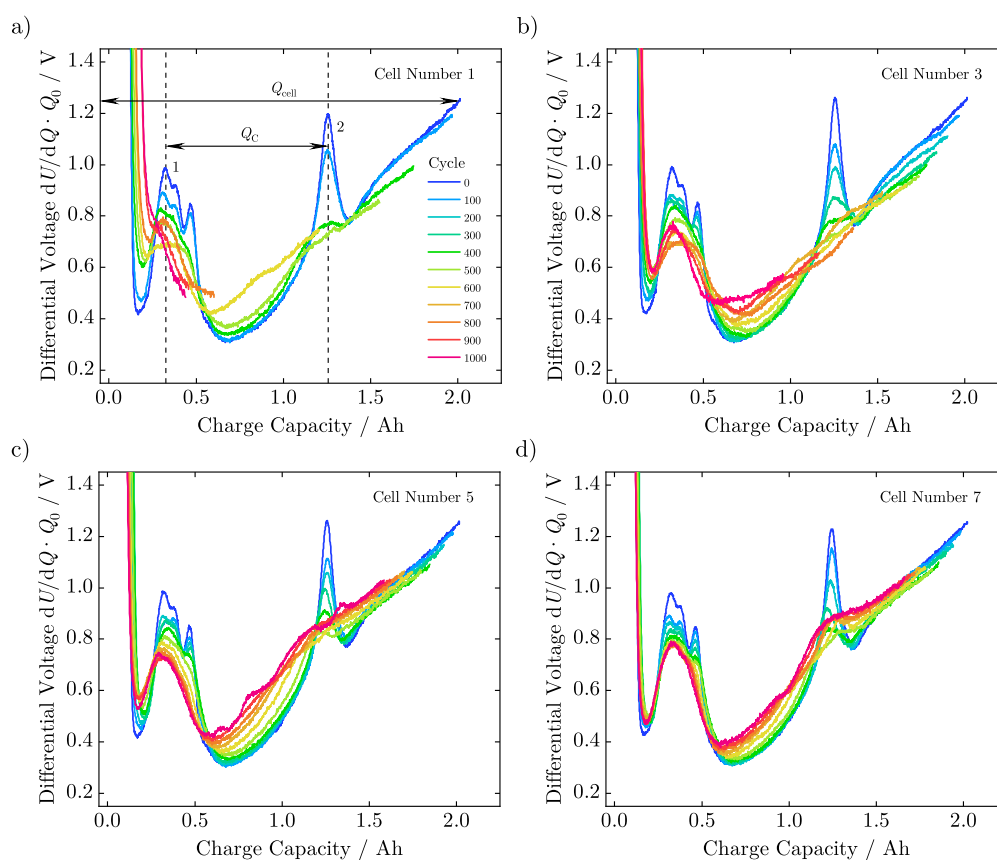
Figure 3. Measured differential voltage of cells from a) test procedure # 1, b) test procedure # 2, c) test procedure # 3, and d) test procedure # 4.
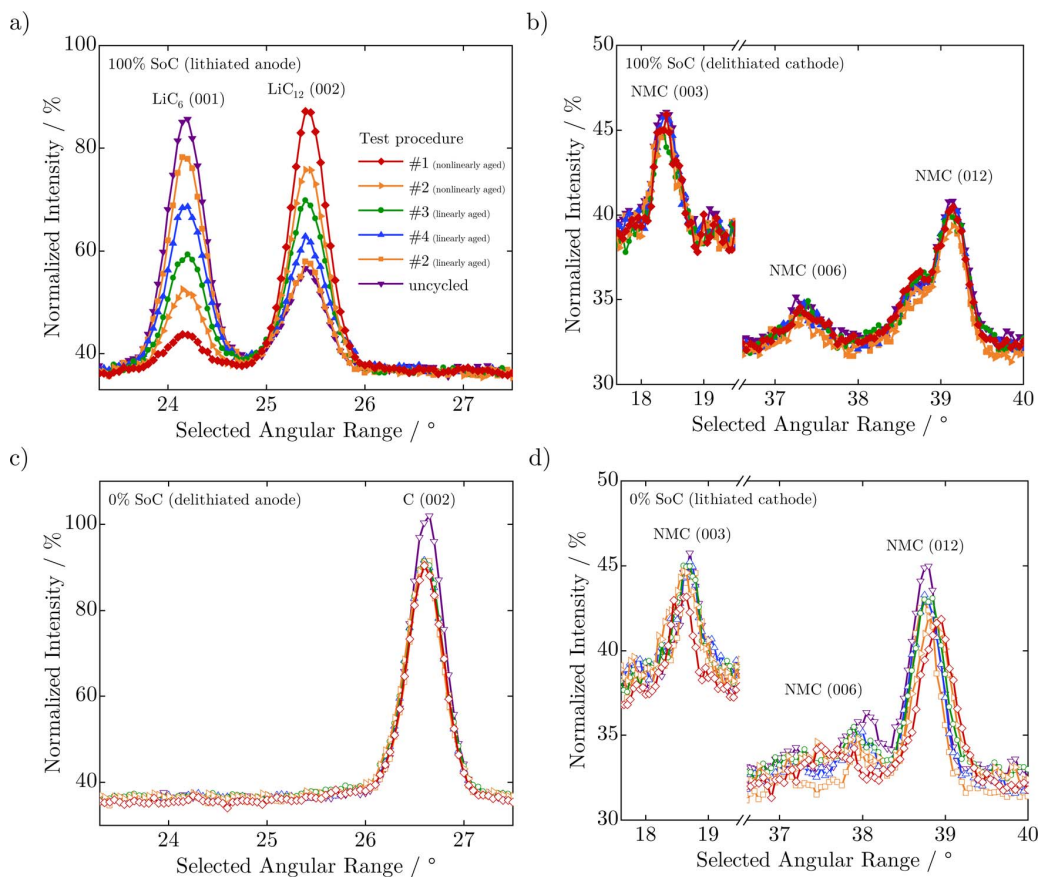
Figure 4. a) and c) present neutron diffraction data from a selected angular range, focusing on the prominent LiC_6 (001), LiC_{12} (002) and C (002) reflections of the anode, where changes in peak intensities of LiC_6 (001) and LiC_{12} (002) reflections indicate a reduction in lithium content in the anode on aging. b) and d) present selected angular range of neutron diffraction data, focusing on the NMC (003), NMC (006) and NMC (012) reflections of the cathode, which in spite of being weak in intensity, show angular shifts indicating a reduction in lithium content in the lithiated cathode on aging.

Figure 5 shows full neutron diffractograms of uncycled (a) and b)) and nonlinearly-aged (test procedure # 1, c) and d)) cells in their fully charged and fully discharged state, along with their Rietveld refinements. A high background due to the incoherent scattering of neutrons due to the hydrogen present in the electrolyte and separator is observed for all cells, which tends to increase with angle. From the Rietveld refinement of all cells, electrochemically accessible lithium content in their electrodes and lattice parameters was extracted and compared.

Differences in mean lithium content in anodes at 100% SoC and 0% SoC provide a reasonable estimation of cyclable lithium losses in the anode.[26] Thus, phase fractions of LiC_6 and LiC_{12} reflections were extracted from the Rietveld refinement of the complete neutron diffractograms of all cells at 100% SoC, and converted to molar fractions. Mean lithium concentrations were calculated as described by Senyshyn et al.[37] and shown as anode stoichiometries in Figure 6a. No significant differences in lattice parameters for the anode were observed as a consequence of aging.

No noticeable differences in the lattice parameter of the cathode are seen at 100% SoC, and the Rietveld refinements show a constant value of $z/c = 0.236$ for the refined fractional coordinate of the oxygen atoms at the 6c site (0,0,z) for all cells. This parameter gives an estimation of distances between oxygen layers, and the value obtained here is similar to the value obtained in earlier studies for NMC based 18650 cells.[24,26] Thus, the average charge at the oxygen ions is similar due to an identical lithium content in the cathodes.

However, the lattice parameter a, which has a constant value of 0.2816nm at 100% SoC, expands for all cells at 0% SoC. Its value at 0% SoC shows a systematic decrease with aging. On the other hand, the lattice parameter c contracts for all cells on discharge, due to the reduction in electrostatic repulsion between the oxygen layers following a decrease in the partial screening of charge by lithium ions. As a consequence of aging, all aged cells show a larger c lattice parameter and a smaller a lattice parameter at 0% SoC compared to their pristine condition, depending on their SoH. Such changes typically indicate a reduction in the amount of cyclable lithium content in the cathode and have also been reported previously.[26] From the different c/a values, lithium contents in $Li_yNi_{0.33}Mn_{0.33}Co_{0.33}O_2$ were calculated using Vegards law, as shown by Buchberger et al.,[38] and are shown as stoichiometries in Figure 6b for all cells at both SoCs.

Marginal lithium deposition.—The decrease of the stoichiometry x in the anode at 100% SoC, see Figure 6a, reveals a loss of lithium inventory as the dominant aging mechanism for both linearly- and nonlinearly-aged cells. This capacity loss causes a decrease of the stoichiometry y in the cathode at 0% SoC, as depicted in Figure 6b. Based on the stoichiometry changes, we calculated the loss of lithium inventory both for the anode and the cathode. These capacity losses – which were determined with neutron diffraction independently – match up.

Figure 7 shows the capacity loss for all cells investigated by electrochemical analysis as well as in-situ neutron diffraction. The amount of lost capacity emerging following neutron diffraction is always less
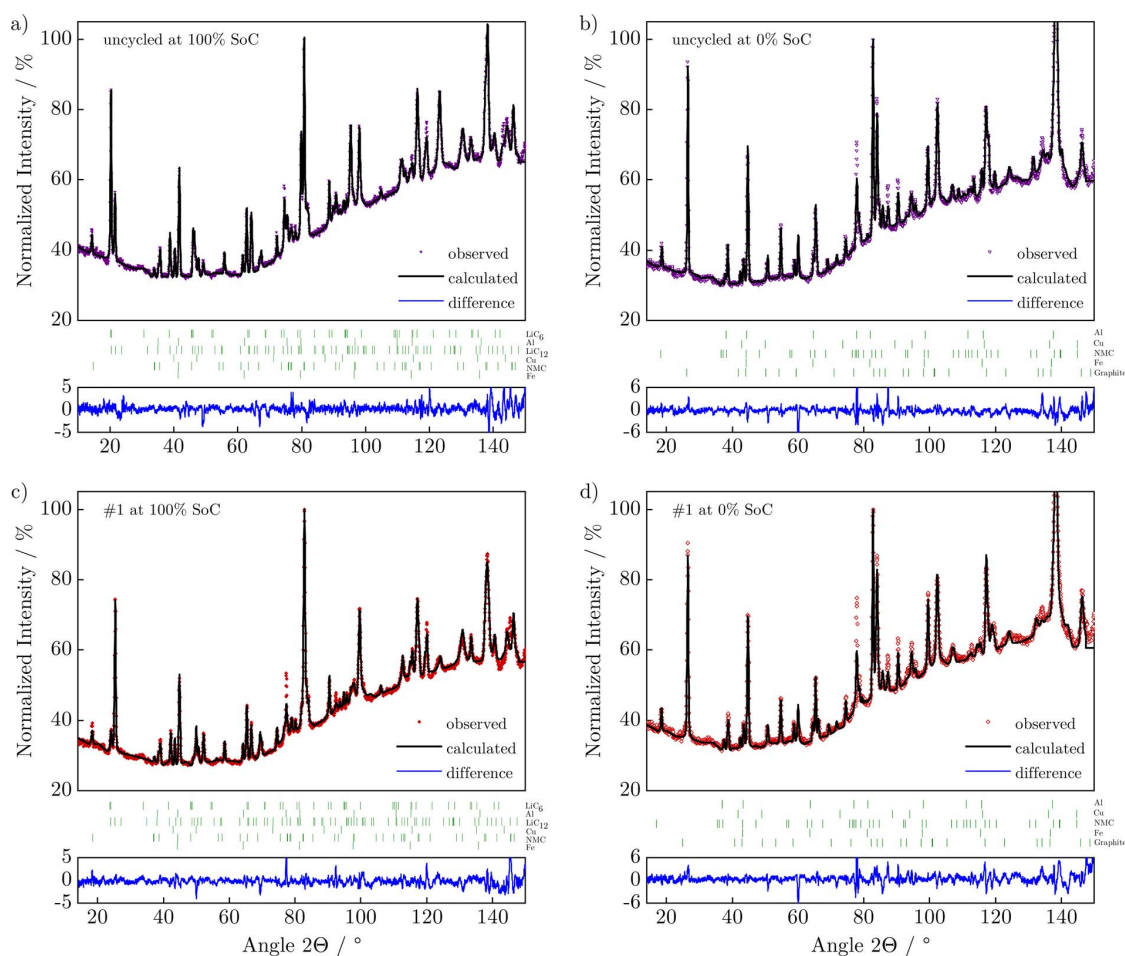
Figure 5. Neutron diffractograms with the full angular range of the a) uncycled cell at 100% SoC, b) uncycled cell at 0% SoC, c) nonlinearly-aged cell at 100% SoC, d) nonlinearly-aged cell at 0% SoC. The experimental data are shown by colored symbols whereas their Rietveld refinements are shown as black lines. The blue lines show differences between data and fit. The vertical bars (green) above the blue line indicate Bragg reflections corresponding to the crystalline phases in the cell (for 100% SoC from top to bottom: LiC_6, Al, LiC_{12}, Cu, NMC and Fe, and for 0% SoC from top to bottom: Al, Cu, NMC, Fe and graphite).

Figure 6. a) Anode stoichiometry x in Li_xC_6 and b) cathode stoichiometry y in $Li_yNi_{0.33}Mn_{0.33}Co_{0.33}O_2$ at different SoHs at 0% (open symbols) and 100% (solid symbols) SoC, respectively.

Figure 7. Comparison of the capacity loss determined by electrochemical analysis and in-situ neutron diffraction dependent on the SoH.
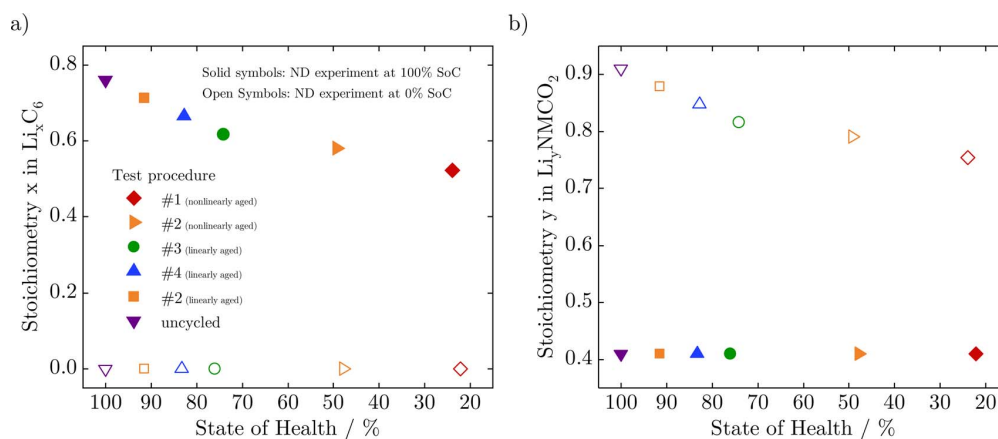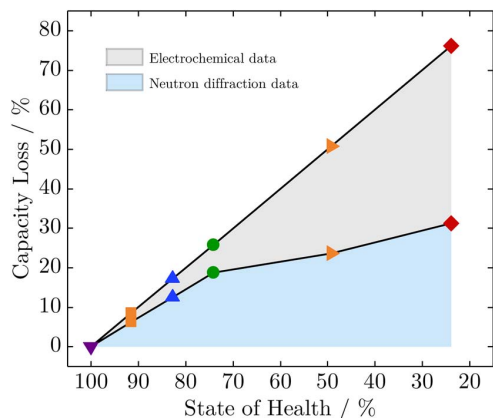
than the quantity determined by electrochemical analysis. Based on the setup of the neutron diffraction experiment, the top and bottom of the cell (approx. 25 mm in total compared to a cell height of 65 mm) were not illuminated by the neutron beam in order to avoid noisy signals from the cell holder and safety protection circuitry. Thus, 15 mm of the jelly roll is not captured by the neutron beam. Therefore, we are able to make a statement on the spatial distribution of aging and distinguish between the inner cell area and the edge area. The comparison between capacity loss determined by the two methods reveals an increasing capacity loss in the edge area of the electrodes with ongoing aging. Below an SoH of about 75%, the sharp decline indicates a prominent capacity loss in the edge area of the electrodes that are not illuminated by the neutron beam. We suppose two different dominant aging mechanisms that are the growth of the solid electrolyte interphase in the early stage and marginal lithium deposition in the later stage.

Senyshyn et al. revealed a non-homogeneity of the lithium distribution in the graphite anode by spatially resolved neutron diffraction.[37] Non-uniformity has been found in both radial and axial directions of 18650-type cells and is affected by a cell fatigue.[28] An inhomogeneous aging in combination with a marginal capacity loss is also in accordance with the observations by Cai et al.[27] and Birkenmaier et al.[39]

Capacity recovery.—Following the neutron diffraction experiment, the cells were stored for a few weeks in a safety environment because of radiation protection regulations at FRM II. Subsequently, we ran additional checkup tests. Figure 8a shows the relative capacities over equivalent full cycles, revealing both capacity recovery or capacity loss dependent on the SoH as well as the SoC the cells were stored at. Linearly-aged cells which were fully charged for the neutron diffraction experiment, reveal a capacity loss of less than 3.0%, whereas the fully discharged ones show a capacity recovery of less than 3.2%, as depicted in Figure 8b. This is in accordance with the investigations by Wilhelm et al.,[40] showing a decrease or increase in capacity due to lithium diffusion into or out of the anode overhang area following long-term storage. The anode overhang area, as depicted in Figure 1c, does not have cathode counterparts and is designed to avoid lithium deposition at the edges of the anode.

In contrast, all nonlinearly-aged cells show a capacity recovery. Cells that were stored at 0% SoC result in a higher recovery than those stored at 100% SoC. The effect of capacity recovery is consistent with lithium stripping, the partial reversible reaction of lithium deposition, as well as the chemical intercalation of lithium into the graphite.[13,16,41,42] The reason for a higher capacity recovery for nonlinearly-aged cells compared to linearly-aged ones seems to be that more lithium was deposited than was stored in the anode over-

hang area. Additionally, lithium deposition and lithium stripping likely proceed faster than lithium diffuses into or out of the anode overhang area.

Figures 8c and 8d show the relative internal resistance $R_{dc,10s}$ over equivalent full cycles and how it changes depending on the SoH. Linearly-aged cells reveal a decrease in resistance of less than 4.9%, independent of the SoC the cells were stored at, except the uncycled cells that show an increase in resistance of less than 5.0%. For the nonlinearly-aged cells, the resistance is inversely proportional to the capacity, showing a higher resistance decrease for discharged cells.

Table III summarizes the cells' capacities before and after neutron diffraction, depending on their SoH and SoC.

Post-mortem analysis.—SEM imaging discloses degradation mechanisms on the surface of cell components. The detectable phenomena are: the growth of films on electrodes; the clogging of pores; cracks in electrode coatings; the deformation of electrodes; changes on particle surfaces; and particle cracks.[22] At the end of the aging experiment, we opened a nonlinearly-aged cell cycled under test condition # 1 and an uncycled cell in an argon-filled glove box. Electrode samples were punched out in the middle part of both anode and cathode, and SEM images obtained. Primary and secondary particles are clearly visible for uncycled as well as nonlinearly-aged cathode samples, as depicted in Figures 9a and 9b. At the same time, the cathode microstructure seems to be unchanged, as also shown by Waldmann et al.[43] and Burns et al.[44] The anode, in contrast, reveals significant changes. Figure 9c shows the flake-shaped graphite particles from the uncycled anode, whereas the aged anode is shown in Figures 9d–9f at different magnifications. First of all, surface changes are attributed to SEI growth, which causes the clogging of pores and LLI.[43–45] Moreover, cracks in electrode coatings and particles due to mechanical stress caused by volume changes are visible.[46,47] Figure 9f and the observable morphology changes in particular support our theory of lithium deposition on graphite, as also shown by Honbo et al.[48] and Uhlmann et al.[49] Although SEM imaging neither reveals the amount of lost capacity nor distinguishes between SEI growth and lithium deposition, we have qualitatively confirmed the aging mechanisms determined by electrochemical analysis and neutron diffraction.

The cells were also opened to gain insights into their internal structure and electrode geometries. Figure 1c emphasizes the anode and cathode geometries, the anode overhang area and the inner cell area, illuminated by the neutron beam.

Conclusions

In this work, the linear and nonlinear aging of commercial 18650-type C/LiNi$_{0.33}$Mn$_{0.33}$Co$_{0.33}$O$_2$ lithium-ion cells was investigated. The cells were cycled under different test procedures at a controlled temperature of 25°C. In-situ neutron diffraction measurements were performed for cells at various SoHs in their fully discharged and charged states. After storage, additional checkup tests were run. Selected cells were opened in a glove box and surface morphologies were qualitatively investigated by SEM.

The main findings are as follows:

1. Cells aged with a standard charging and discharging rate of almost 1C, but different resting times, showed a nonlinear capacity fade after a few hundred equivalent full cycles. By increasing the discharging current or decreasing the charging current, the lifetime improved, resulting in a linear capacity fade. Shortening the relaxation time between cycles positively influenced the lifetime by roughly 40%, whereas a higher discharging current almost doubled the cell's lifetime.

2. The neutron diffraction experiment and differential voltage analysis revealed the loss of lithium inventory as the dominant aging mechanism for both linearly- and nonlinearly-aged cells. Other aging mechanisms, like the structural degradation of anode or cathode active materials or the deactivation of active materials could not be confirmed.
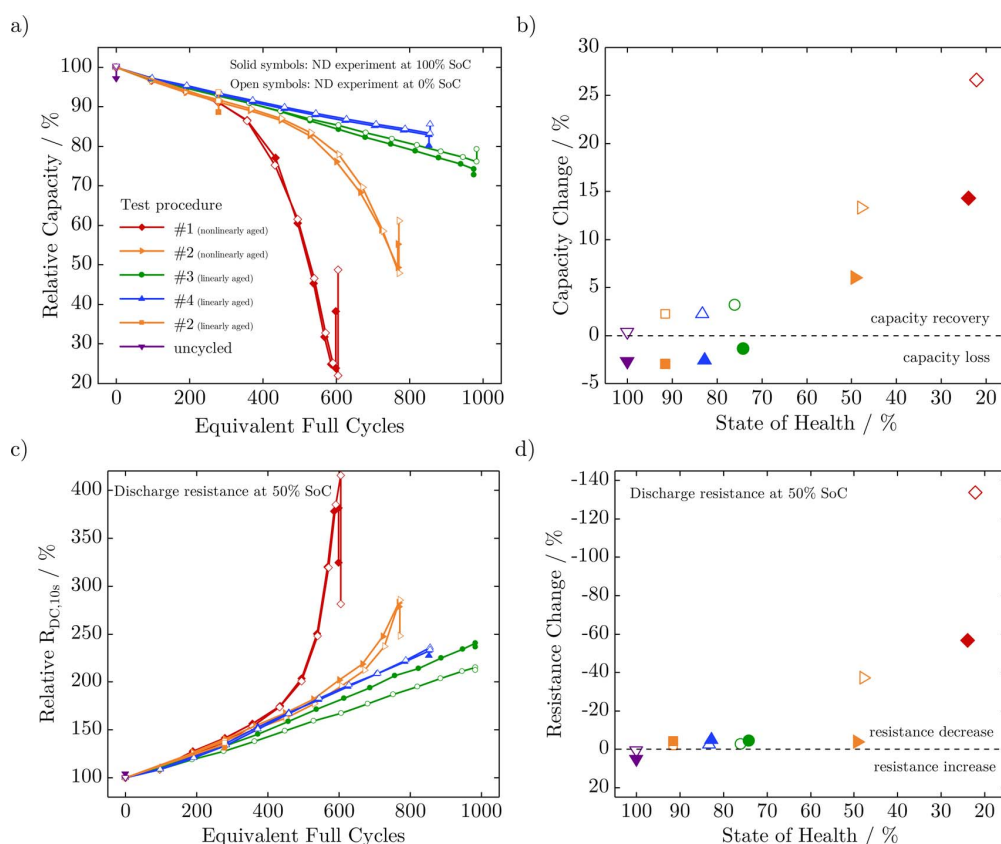
Figure 8. Capacity and resistance change after neutron diffraction experiment and storage due to radiation protection.

3. The comparison between capacity loss determined by electro-chemical analysis and neutron diffraction revealed an increasing capacity loss in the edge area of the electrodes with ongoing aging. We supposed two different dominant aging mechanisms that are the growth of the solid electrolyte interphase in the early stage and marginal lithium deposition in the later stage.

4. After a few weeks of storage, checkup tests showed both capacity recovery or capacity loss dependent on the SoH as well as the SoC the cells were stored at. Linearly-aged cells that were fully charged for the neutron diffraction experiment revealed a capacity loss of less than 3.0%, whereas the fully discharged ones pointed out a capacity recovery of less than 3.2%, owing to lithium diffusion into or out of the anode overhang area, respectively. On the other hand, all nonlinearly-aged cells showed a capacity recovery

due to lithium stripping, the partial reversible reaction of lithium deposition, as well as the chemical intercalation of lithium.

5. SEM images of uncycled and nonlinearly-aged cells qualitatively showed surface layer growth and morphology changes on the graphite anode, whereas the cathode particles appeared unchanged.

The results demonstrate the influence of operational strategies on the lifetime of lithium-ion cells. State-of-the-art battery-management systems reduce the charging current at high anode lithiation states and low temperatures, to prevent lithium deposition. Future enhancements, especially for fast-charging applications, may also take into account predicted and subsequent relaxation time and discharge currents, cell inhomogeneities and geometry, as well as the cell's SoH.

Table III. Information on the investigated cells and their capacity recovery after neutron diffraction experiment.

| Test procedure	#1		#2		#3		#4		#2		uncycled	
Cell number	1	2	3	4	5	6	7	8	9	10	11	12
SoC for ND experiment/%	100	0	100	0	100	0	100	0	100	0	100	0
CheckUp data after cycling and before neutron diffraction experiment												
Equivalent full cycles	599	604	767	770	975	982	852	856	278	278	0	0
Capacity/Ah	0.4920	0.4532	1.0153	0.9832	1.5295	1.5596	1.7129	1.7157	1.8815	1.8856	2.0673	2.0506
SoH/%	23.9	22.1	49.3	47.9	74.2	76.1	82.8	83.3	91.5	91.5	100.0	100.0
CheckUp data after cycling and after neutron diffraction experiment												
Capacity/Ah	0.7862	1.0008	1.1379	1.2553	1.4992	1.6246	1.6579	1.7615	1.8199	1.9305	2.0114	2.0594
SoH/%	38.2	48.7	55.3	61.2	72.8	79.3	80.2	85.5	88.5	93.7	97.3	100.4
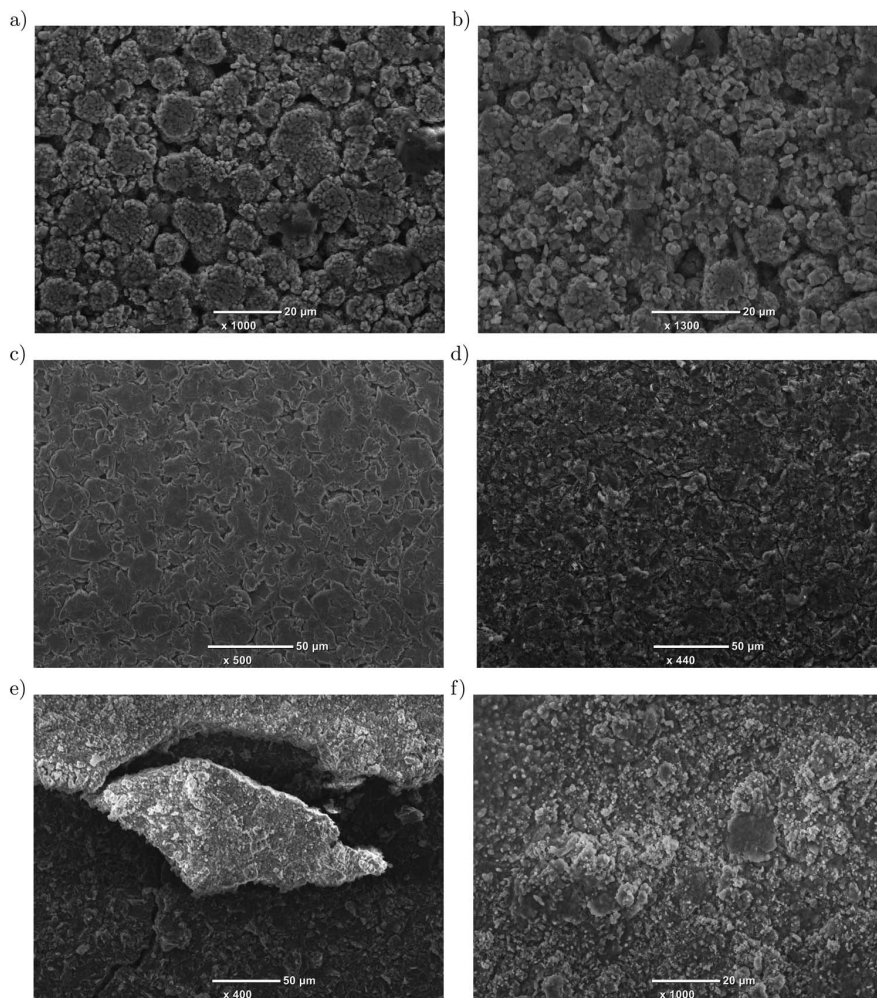
Figure 9. SEM images of electrode samples: a) cathode of uncycled cell, b) cathode of nonlinearly-aged cell, c) anode of uncycled cell and d)-f) anode of nonlinearly-aged cell at different magnifications.

ORCID

Jonas Keil https://orcid.org/0000-0002-0674-2676
Neelima Paul https://orcid.org/0000-0002-6906-1683
Volodymyr Baran https://orcid.org/0000-0003-2379-3632
Peter Keil https://orcid.org/0000-0003-4986-2413
Ralph Gilles https://orcid.org/0000-0003-2703-4369
Andreas Jossen https://orcid.org/0000-0003-0964-1405

References

1. J. Neubauer and A. Pesaran, "The ability of battery second use strategies to impact plug-in electric vehicle prices and serve utility energy storage applications," *Journal of Power Sources*, **196**, 10351 (2011).
2. S. F. Schuster, T. Bach, E. Fleder, J. Müller, M. Brand, G. Sextl, and A. Jossen, "Nonlinear aging characteristics of lithium-ion cells under different operational conditions," *Journal of Energy Storage*, **1**, 44 (2015).
3. R. Faria, P. Marques, R. Garcia, P. Moura, F. Freire, J. Delgado, and A. T. de Almeida, "Primary and secondary use of electric mobility batteries from a life cycle perspective," *Journal of Power Sources*, **262**, 169 (2014).
4. M. Dubarry, C. Truchot, and B. Y. Liaw, "Synthesize battery degradation modes via a diagnostic and prognostic model," *Journal of Power Sources*, **219**, 204 (2012).
5. Q. Zhang and R. E. White, "Capacity fade analysis of a lithium ion cell," *Journal of Power Sources*, **179**, 793 (2008).
6. J. Christensen and J. Newman, "Cyclable Lithium and Capacity Loss in Li-Ion Cells," *Journal of The Electrochemical Society*, **152**, A818 (2005).
7. V. Agubra and J. Fergus, "Lithium Ion Battery Anode Aging Mechanisms," *Materials (Basel, Switzerland)*, **6**, 1310 (2013).
8. P. Arora, "Capacity Fade Mechanisms and Side Reactions in Lithium-Ion Batteries," *Journal of The Electrochemical Society*, **145**, 3647 (1998).
9. C. R. Birkl, M. R. Roberts, E. McTurk, P. G. Bruce, and D. A. Howey, "Degradation diagnostics for lithium ion cells," *Journal of Power Sources*, **341**, 373 (2017).
10. J. Vetter, P. Novák, M. R. Wagner, C. Veit, K.-C. Möller, J. O. Besenhard, M. Winter, M. Wohlfahrt-Mehrens, C. Vogler, and A. Hammouche, "Ageing mechanisms in lithium-ion batteries," *Journal of Power Sources*, **147**, 269 (2005).
11. M. Ecker, N. Nieto, S. Käbitz, J. Schmalstieg, H. Blanke, A. Warnecke, and D. U. Sauer, "Calendar and cycle life study of Li(NiMnCo)O2-based 18650 lithium-ion batteries," *Journal of Power Sources*, **248**, 839 (2014).
12. S. Hein and A. Latz, "Influence of local lithium metal deposition in 3D microstructures on local and global behavior of Lithium-ion batteries," *Electrochimica Acta*, **201**, 354 (2016).

13. T. Waldmann, B.-I. Hogg, and M. Wohlfahrt-Mehrens, "Li plating as unwanted side reaction in commercial Li-ion cells – A review," *Journal of Power Sources*, **384**, 107 (2018).

14. M. Ouyang, Z. Chu, L. Lu, J. Li, X. Han, X. Feng, and G. Liu, "Low temperature aging mechanism identification and lithium deposition in a large format lithium iron phosphate battery for different charge profiles," *Journal of Power Sources*, **286**, 309 (2015).

15. C. von Lüders, V. Zinth, S. V. Erhard, P. J. Osswald, M. Hofmann, R. Gilles, and A. Jossen, "Lithium plating in lithium-ion batteries investigated by voltage relaxation and in situ neutron diffraction," *Journal of Power Sources*, **342**, 17 (2017).

16. M. Petzl, M. Kasper, and M. A. Danzer, "Lithium plating in a commercial lithium-ion battery – A low-temperature aging study," *Journal of Power Sources*, **275**, 799 (2015).

17. S. Tippmann, D. Walper, L. Balboa, B. Spier, and W. G. Bessler, "Low-temperature charging of lithium-ion cells part I: Electrochemical modeling and experimental investigation of degradation behavior," *Journal of Power Sources*, **252**, 305 (2014).

18. T. Waldmann, B.-I. Hogg, M. Kasper, S. Grolleau, C. G. Couceiro, K. Trad, B. P. Matadi, and M. Wohlfahrt-Mehrens, "Interplay of Operational Parameters on Lithium Deposition in Lithium-Ion Cells: Systematic Measurements with Reconstructed 3-Electrode Pouch Full Cells," *Journal of The Electrochemical Society*, **163**, A1232 (2016).

19. T. C. Bach, S. F. Schuster, E. Fleder, J. Müller, M. J. Brand, H. Lorrmann, A. Jossen, and G. Sextl, "Nonlinear aging of cylindrical lithium-ion cells linked to heterogeneous compression," *Journal of Energy Storage*, **5**, 212 (2016).

20. P. Harks, F. M. Mulder, and P. Notten, "In situ methods for Li-ion battery research: A review of recent developments," *Journal of Power Sources*, **288**, 92 (2015).

21. N. Paul, J. Wandt, S. Seidlmayer, S. Schebesta, M. J. Mühlbauer, O. Dolotko, H. A. Gasteiger, and R. Gilles, "Aging behavior of lithium iron phosphate based 18650-type cells studied by in situ neutron diffraction," *Journal of Power Sources*, **345**, 85 (2017).

22. T. Waldmann, A. Iturrondobeitia, M. Kasper, N. Ghanbari, F. Aguesse, E. Bekaert, L. Daniel, S. Genies, I. J. Gordon, M. W. Löble, E. de Vito, and M. Wohlfahrt-Mehrens, "Review—Post-Mortem Analysis of Aged Lithium-Ion Batteries: Disassembly Methodology and Physico-Chemical Analysis Techniques," *Journal of The Electrochemical Society*, **163**, A2149 (2016).

23. J. Wandt, C. Marino, H. A. Gasteiger, P. Jakes, R.-A. Eichel, and J. Granwehr, "Operando electron paramagnetic resonance spectroscopy – formation of mossy lithium on lithium anodes during charge–discharge cycling," *Energy & Environmental Science*, **8**, 1358 (2015).

24. O. Dolotko, A. Senyshyn, M. J. Mühlbauer, K. Nikolowski, F. Scheiba, and H. Ehrenberg, "Fatigue Process in Li-Ion Cells: An In Situ Combined Neutron Diffraction and Electrochemical Study," *Journal of The Electrochemical Society*, **159**, A2082 (2012).

25. S. Shiotani, T. Naka, M. Morishima, M. Yonemura, T. Kamiyama, Y. Ishikawa, Y. Ukyo, Y. Uchimoto, and Z. Ogumi, "Degradation analysis of 18650-type lithium-ion cells by operando neutron diffraction," *Journal of Power Sources*, **325**, 404 (2016).

26. N. Paul, J. Keil, F. M. Kindermann, S. Schebesta, O. Dolotko, M. J. Mühlbauer, L. Kraft, S. V. Erhard, A. Jossen, and R. Gilles, "Aging in 18650-type Li-ion cells examined with neutron diffraction, electrochemical analysis and physico-chemical modeling," *Journal of Energy Storage*, **17**, 383 (2018).

27. L. Cai, K. An, Z. Feng, C. Liang, and S. J. Harris, "In-situ observation of inhomogeneous degradation in large format Li-ion cells by neutron diffraction," *Journal of Power Sources*, **236**, 163 (2013).

28. M. J. Mühlbauer, O. Dolotko, M. Hofmann, H. Ehrenberg, and A. Senyshyn, "Effect of fatigue/aging on the lithium distribution in cylinder-type Li-ion batteries," *Journal of Power Sources*, **348**, 145 (2017).

29. V. Zinth, C. von Lüders, M. Hofmann, J. Hattendorff, I. Buchberger, S. Erhard, J. Rebelo-Kornmeier, A. Jossen, and R. Gilles, "Lithium plating in lithium-ion batteries at sub-ambient temperatures investigated by in situ neutron diffraction," *Journal of Power Sources*, **271**, 152 (2014).

30. M. Hoelzel, A. Senyshyn, N. Juenke, H. Boysen, W. Schmahl, and H. Fuess, "High-resolution neutron powder diffractometer SPODI at research reactor FRM II," *Nuclear Instruments and Methods in Physics Research Section A: Accelerators, Spectrometers, Detectors and Associated Equipment*, **667**, 32 (2012).

31. R. Gilles, B. Krimmer, H. Boysen, and H. Fuess, "Status of the new structure powder diffractometer (SPODI) at the FRM-II in Garching," *Applied Physics A: Materials Science & Processing*, **74**, s148 (2002).

32. P. Thompson, D. E. Cox, and J. B. Hastings, "Rietveld refinement of Debye–Scherrer synchrotron X-ray data from Al_2O_3," *Journal of Applied Crystallography*, **20**, 79 (1987).

33. T. Roisnel and J. Rodríguez-Carvajal, "WinPLOTR: A Windows Tool for Powder Diffraction Pattern Analysis," *Materials Science Forum*, **378–381**, 118 (2001).

34. S. F. Schuster, M. J. Brand, C. Campestrini, M. Gleissenberger, and A. Jossen, "Correlation between capacity and impedance of lithium-ion cells during calendar and cycle life," *Journal of Power Sources*, **305**, 191 (2016).

35. P. Keil and A. Jossen, "Calendar Aging of NCA Lithium-Ion Batteries Investigated by Differential Voltage Analysis and coulomb Tracking," *Journal of The Electrochemical Society*, **164**, A6066 (2016).

36. M. Winter, J. O. Besenhard, M. E. Spahr, and P. Novák, "Insertion Electrode Materials for Rechargeable Lithium Batteries," *Advanced Materials*, **10**, 725 (1998).

37. A. Senyshyn, M. J. Mühlbauer, O. Dolotko, M. Hofmann, and H. Ehrenberg, "Homogeneity of lithium distribution in cylinder-type Li-ion batteries," *Scientific reports*, **5**, 18380 (2015).

38. I. Buchberger, S. Seidlmayer, A. Pokharel, M. Piana, J. Hattendorff, P. Kudejova, R. Gilles, and H. A. Gasteiger, "Aging Analysis of Graphite/$LiNi_{1/3}Mn_{1/3}Co_{1/3}O_2$ Cells Using XRD, PGAA, and AC Impedance," *Journal of The Electrochemical Society*, **162**, A2737 (2015).

39. C. Birkenmaier, B. Bitzer, M. Harzheim, A. Hintennach, and T. Schleid, "Lithium Plating on Graphite Negative Electrodes: Innovative Qualitative and Quantitative Investigation Methods," *Journal of The Electrochemical Society*, **162**, A2646 (2015).

40. J. Wilhelm, S. Seidlmayer, P. Keil, J. Schuster, A. Kriele, R. Gilles, and A. Jossen, "Cycling capacity recovery effect: A coulombic efficiency and post-mortem study," *Journal of Power Sources*, **365**, 327 (2017).

41. T. Waldmann and M. Wohlfahrt-Mehrens, "Effects of rest time after Li plating on safety behavior—ARC tests with commercial high-energy 18650 Li-ion cells," *Electrochimica Acta*, **230**, 454 (2017).

42. M. V. Avdeev, A. A. Rulev, V. I. Bodnarchuk, E. E. Ushakova, V. I. Petrenko, I. V. Gapon, O. V. Tomchuk, V. A. Matveev, N. K. Pleshanov, E. Y. Kataev, L. V. Yashina, and D. M. Itkis, "Monitoring of lithium plating by neutron reflectometry," *Applied Surface Science*, **424**, 378 (2017).

43. T. Waldmann, M. Wilka, M. Kasper, M. Fleischhammer, and M. Wohlfahrt-Mehrens, "Temperature dependent aging mechanisms in Lithium-ion batteries – A Post-Mortem study," *Journal of Power Sources*, **262**, 129 (2014).

44. J. C. Burns, A. Kassam, N. N. Sinha, L. E. Downie, L. Solnickova, B. M. Way, and J. R. Dahn, "Predicting and Extending the Lifetime of Li-Ion Batteries," *Journal of The Electrochemical Society*, **160**, A1451 (2013).

45. B. Stiaszny, J. C. Ziegler, E. E. Krauß, J. P. Schmidt, and E. Ivers-Tiffée, "Electrochemical characterization and post-mortem analysis of aged $LiMn_2O_4$–$Li(Ni_{0.5}Mn_{0.3}Co_{0.2})O_2$/graphite lithium ion batteries. Part I: Cycle aging," *Journal of Power Sources*, **251**, 439 (2014).

46. K. Zhao, M. Pharr, J. J. Vlassak, and Z. Suo, "Fracture of electrodes in lithium-ion batteries caused by fast charging," *Journal of Applied Physics*, **108**, 073517 (2010).

47. V. Tarnopolskiy, J. Kalhoff, M. Nádherná, D. Bresser, L. Picard, F. Fabre, M. Rey, and S. Passerini, "Beneficial influence of succinic anhydride as electrolyte additive on the self-discharge of 5 V $LiNi_{0.4}Mn_{1.6}O_4$ cathodes," *Journal of Power Sources*, **236**, 39 (2013).

48. H. Honbo, K. Takei, Y. Ishii, and T. Nishida, "Electrochemical properties and Li deposition morphologies of surface modified graphite after grinding," *Journal of Power Sources*, **189**, 337 (2009).

49. C. Uhlmann, J. Illig, M. Ender, R. Schuster, and E. Ivers-Tiffée, "In situ detection of lithium metal plating on graphite in experimental cells," *Journal of Power Sources*, **279**, 428 (2015).

8 Electrochemical Modeling of Linear and Nonlinear Aging of Lithium-Ion Cells

Within this chapter, the paper *Electrochemical Modeling of Linear and Nonlinear Aging of Lithium-Ion Cells* is presented.

In this publication, we present an electrochemical aging model with SEI formation, SEI re-formation due to cracking of the layer during graphite expansion, lithium plating when the potential of the negative electrode becomes negative vs. Li/Li$^+$, and subsequent lithium stripping once the potential becomes positive again. The model considers the transition from an early stage, linear to a later stage, nonlinear capacity fade.

Figure 8.1 shows the electrochemical main and side reactions at the graphite particle surface.
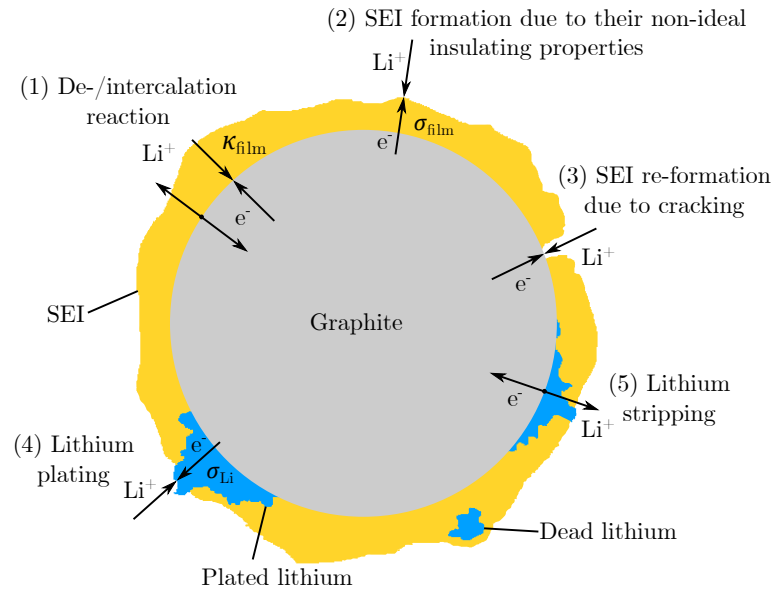
Figure 8.1: Illustration of the electrochemical reactions at the graphite particle surface.

We distinguish between the transport of two species through the negative electrode surface film – lithium ions, on the one hand, and electrons on the other hand. This corresponds to the assumption that the film exhibits a maximum conductivity for lithium ions κ_{film} and an insulation conductivity for electrons σ_{film} [25; 93; 104]. While the lithium de-/intercalation reaction is unimpeded by a high conductivity of lithium ions through the film (1), SEI formation results from their non-ideal insulating properties for electrons (2). Additional SEI re-formation is caused by cracking of the layer during graphite expansion and is unaffected by any transport limitations through the film (3). Lithium plating takes place once the overpotential becomes negative vs. Li/Li$^+$ (4). As soon as lithium has been plated and the overpotential becomes positive vs. Li/Li$^+$, the lithium stripping reaction proceeds by partly dissolving the plated lithium (5) [13]. Considering the different ionic and electronic conductivities, our approach results in different potential drops for the overpotentials of the main and SEI formation

reaction. By taking this approach, we are able to differentiate between the aging phenomena of capacity and power fade [93].

Figures 8.2, 8.3, 8.4 depict the Butler-Volmer kinetics for the main de-/intercalation reaction, the SEI re-/formation side reaction, and the lithium plating and lithium stripping side reaction. The equations for the exchange current density and the overpotential are summarized for each main and side reaction. For a thorough modeling of lithium stripping, we developed a novel approach considering the charge quantity of plated and stripped lithium as well as the ratio of reversibly plated lithium.

The following equations appear in the figure:

$$i_n = i_{0,n} \left(\exp\left(\frac{\alpha_{a,n} F}{RT} \eta_n \right) - \exp\left(-\frac{\alpha_{c,n} F}{RT} \eta_n \right) \right)$$

$$\eta_{neg} = \Phi_s - \Phi_l - E_{\mathrm{Eq},neg} - i_{neg} R_{Li^+}$$

$$\eta_{pos} = \Phi_s - \Phi_l - E_{\mathrm{Eq},pos}$$

oxidation / deintercalation
$Li\Theta_s \rightleftharpoons Li^+ + \Theta_s + e^-$

overall reaction

anodic / forward reaction

i_0

$-i_0$

Overpotential in V

cathodic / backward reaction

reduction / intercalation
$Li^+ + \Theta_s + e^- \rightleftharpoons Li\Theta_s$
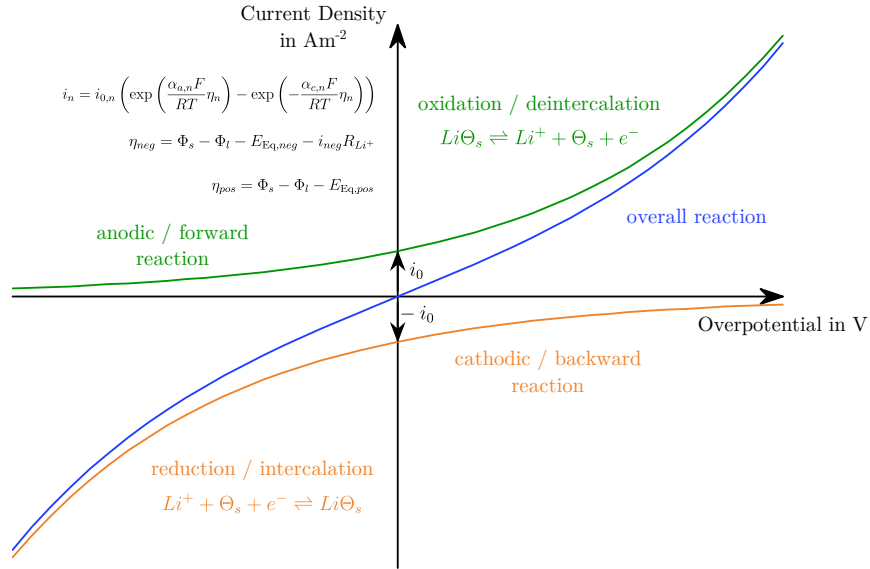
Figure 8.2: Butler-Volmer kinetics of the main de-/intercalation reaction.

$$i_{\mathrm{SEI,form}} = -i_{0,\mathrm{SEI}} \exp\left(-\frac{\alpha_{c,\mathrm{SEI}} F}{RT} \eta_{\mathrm{SEI,form}} \right)$$

$$\eta_{\mathrm{SEI,form}} = \Phi_s - \Phi_l - E_{\mathrm{Eq,SEI}} - i_{\mathrm{SEI,form}} R_{e^-}$$

$$i_{\mathrm{SEI,re-form}} = -i_{0,\mathrm{SEI}} \, f_{exp}(x) \, \exp\left(-\frac{\alpha_{c,\mathrm{SEI}} F}{RT} \eta_{\mathrm{SEI,re-form}} \right)$$

$$\eta_{\mathrm{SEI,re-form}} = \Phi_s - \Phi_l - E_{\mathrm{Eq,SEI}}$$

$-i_{0,\mathrm{SEI}}$

Overpotential in V

cathodic / backward reaction

reductive SEI forming reactions
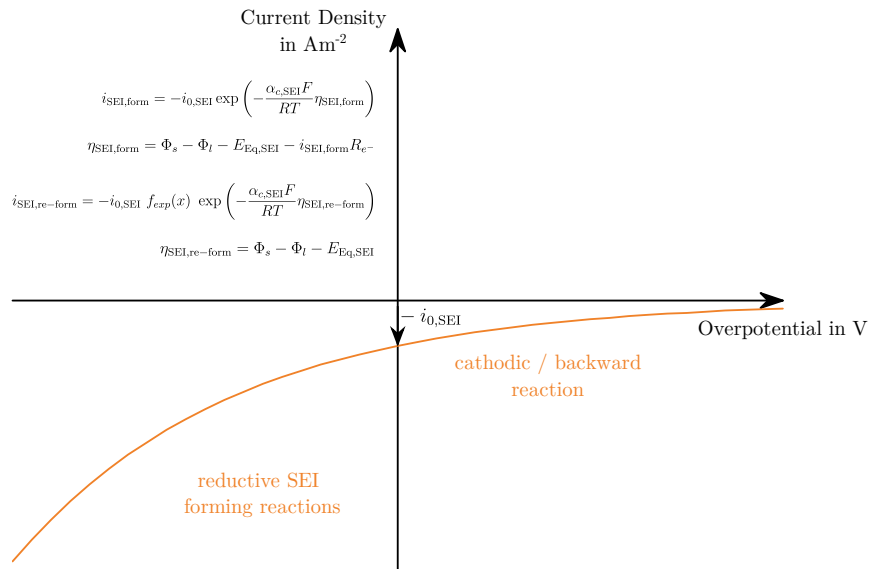
Figure 8.3: Butler-Volmer kinetics of the SEI re-/formation side reaction.

$$i_{lpl} = i_{0,lpl} \left(\exp\left(\frac{\alpha_{a,lpl}F}{RT} \eta_{lpl} \right) - \exp\left(\frac{-\alpha_{c,lpl}F}{RT} \eta_{lpl} \right) \right), \eta_{lpl} \leq 0$$

$$i_{lst} = i_{0,lst} \left(\exp\left(\frac{\alpha_{a,lst}F}{RT} \eta_{lst} \right) - \exp\left(\frac{-\alpha_{c,lst}F}{RT} \eta_{lst} \right) \right) \left(\frac{\xi q_{lpl} - q_{lst}}{q_{ref}} \right), \eta_{lst} > 0$$

$$\eta_{lpl} = \eta_{lst} = \Phi_s - \Phi_l - E_{Eq,lpl/lst}$$

Current Density in Am^{-2}

lithium stripping
$Li(s) \rightleftharpoons Li^+ + e^-$

$E_{Eeq,lpl/lst} = 0$ V

Overpotential in V

lithium plating
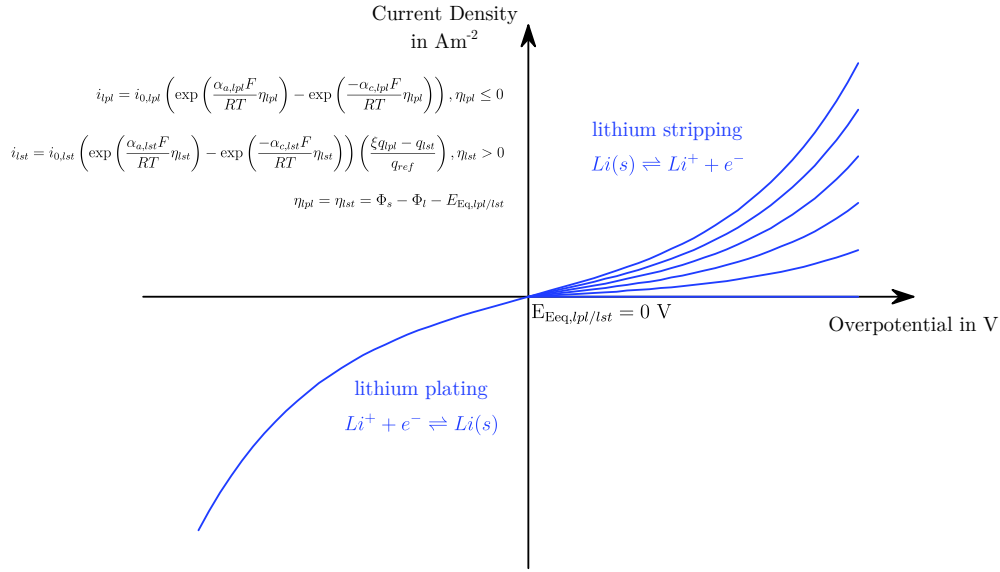$Li^+ + e^- \rightleftharpoons Li(s)$

Figure 8.4: Butler-Volmer kinetics of the lithium plating and lithium stripping side reaction.

The electrochemical model considers effective transport parameters, temperature-dependent variables and is coupled with a 0D thermal model.

Finally, the model is applied to the testing procedure #2 of the aging experiment in the publication *Linear and Nonlinear Aging of Lithium-Ion Cells Investigated by Electrochemical Analysis and In-Situ Neutron Diffraction* (see Table I and Figure 2) that is shown in Chapter 7. As depicted in Figure 8.5, the model describes linear and nonlinear aging and accurately reveals the onset and slope on nonlinear aging.
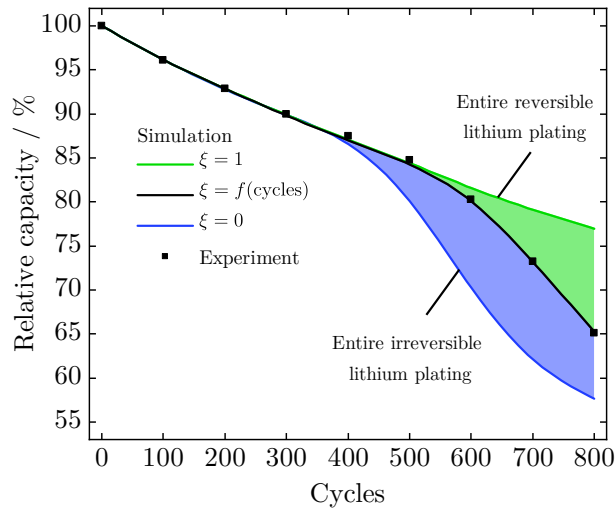

Figure 8.5: Comparison of experimental data (symbols) and simulation results (lines) with varying lithium plating reversibility. $\xi = 1$ denotes entire reversible and $\xi = 0$ entire irreversible lithium plating.

Author contribution   Jonas Keil initiated the idea of an electrochemical modeling approach depicting linear and nonlinear aging, developed, parametrized and validated the model, carried out the simulation studies and analyzed and processed the data. The manuscript was written by Jonas Keil and was edited by Andreas Jossen. All authors discussed the data and commented on the results.

Electrochemical Modeling of Linear and Nonlinear Aging of Lithium-Ion Cells

Jonas Keil, Andreas Jossen

Electrochemical Modeling of Linear and Nonlinear Aging of Lithium-Ion Cells

Jonas Keil[z] and **Andreas Jossen**

Technical University of Munich (TUM), Institute for Electrical Energy Storage Technology (EES), D-80333 Munich, Germany

We present an electrochemical aging model with solid electrolyte interphase (SEI) formation, SEI re-formation due to cracking of the layer during graphite expansion, lithium plating when the potential of the negative electrode becomes negative vs Li/Li$^+$, and subsequent lithium stripping once the potential becomes positive again. The model considers the transition from an early stage, linear to a later stage, nonlinear capacity fade. While SEI re-/formation define linear aging, the onset and slope of nonlinear aging is simulated based on the ratio of reversibly and irreversibly plated lithium. With ongoing aging, more lithium is plated irreversibly so that less lithium is stripped. The simulation data agree very well with experimental data on commercial 18 650-type lithium-nickel-cobalt-manganese-oxide vs graphite (NCM/C) cells.

List of symbols

A	Surface area, m^2
a	Specific surface area, m^{-1}
C	Capacity, Ah
c	Lithium-ion concentration, mol m^{-3}
c_p	Specific heat capacity, J kg^{-1} K^{-1}
D	Diffusivity, m^2 s^{-1}
Ea	Activation energy, J mol^{-1}
E_{Eq}	Equilibrium potential, V
F	Faraday's constant, 96 485 As mol^{-1}
f	Function/factor
$f_\pm$	Mean molar activity coefficient
h	Heat transfer coefficient, W m^{-2} K^{-1}
h_{ss}	Height, m
I	Current, A
i	Current density, A m^{-2}
i_0	Exchange current density, A m^{-2}
k	Reaction rate, m s^{-1}
l	Length, m
M	Molar mass, kg mol^{-1}
m	Mass, kg
N_M	MacMullin's number
$\dot{Q}$	Heat transfer, W
q	Charge quantity, C m^{-2}
$\dot{q}$	Heat generation, W m^{-3}
R_{ss}	Film resistance, Ωm^2
R	Universal gas constant, 8.314 J K^{-1} mol^{-1}
r	Radius, m
T	Temperature, K
t	Time, s
t_+	Transport number
V	Volume, m^3
x	Negative electrode stoichiometry
y	Positive electrode stoichiometry

Greek

α	Charge-transfer coefficient
δ	Thickness, m
ε	Volume fraction
ε_{th}	Emissivity
η	Overpotential, V

κ	Ionic conductivity, S m^{-1}
Φ	Potential, V
Ψ	Temperature-dependent variable
ρ	Density, kg m^{-3}
σ	Electronic conductivity, S m^{-1}
σ_B	Stefan-Boltzmann constant, 5.67×10^{-8} W m^{-2} K^{-4}
ξ	Ratio of reversibly plated lithium

Subscripts

0	Initial
a	Anodic
c	Cathodic
cell	Cell
ch	Charge
conv	Convection
cor	Correction
dch	Discharge
eff	Effective
exp	Expansion
e$^-$	Electron/electronic
film	Film
∞	Ambient
Li	Lithium
Li$^+$	Lithium-ion/ionic
l	Liquid phase
lpl	Lithium plating
lst	Lithium stripping
max	Maximum
N	Nominal
n	Negative/positive electrode
neg	Negative electrode
ohm	Ohmic
p	Particle
pos	Positive electrode
rad	Radiation
reac	Reaction
ref	Reference
rev	Reversible
SEI	Solid electrolyte interphase
SEI,form	SEI formation
SEI,re-form	SEI re-formation
s	Solid phase
sep	Separator
ss	Subscript
th	Thermal

[z]E-mail: jonas.keil@tum.de

Lithium-ion batteries are today's most important battery-energy-storage technology and are used both in mobile and stationary applications, such as consumer electronics, electric vehicles, and grid operations. The aging behavior of lithium-ion batteries mainly defines their economic and sustainable usage. In particular, the determination, estimation and prediction of the battery's state of health (SOH), remaining useful life (RUL) and end of life (EOL) are current challenges.

Aging of lithium-ion cells in general means the loss of capacity and the increase of impedance that results in a decrease in energy density and also power capability.[1] The main aging mechanisms are: solid electrolyte interphase (SEI) formation due to electrolyte decomposition, SEI re-formation caused by cracking of the layer, lithium plating, a decrease in accessible surface area and porosity due to SEI growth, contact loss of active material particles due to volume changes during cycling, cathode electrolyte interphase (CEI) growth and transition-metal dissolution from the cathode, solvent co-intercalation, gas evolution with subsequent cracking of particles, binder decomposition, and current collector corrosion.[1–4] These aging mechanisms can be assigned to a loss of lithium inventory (LLI), a loss of active material and an impedance increase.[1]

SEI re-/formation is the main aging mechanism for common operational conditions and the majority of lithium-ion cell compositions. It results in a decelerated or linear capacity fade on charge throughput, or a square-root-shaped capacity loss over time and defines the early stage of aging. The later stage of aging is characterized by an accelerated or nonlinear capacity fade that is caused by lithium plating on the graphite anode if the local anode potential becomes negative vs Li/Li$^+$.[5,6] A high polarization caused by high charging currents in conjunction with low temperatures and a high state of charge (SOC) favor lithium plating.[7–9] However, even at moderate temperatures and charging rates, and due to temperature gradients and mechanical stress inside the cell, inhomogeneous current and potential distributions may cause lithium plating.[10–13] On the one hand, plated lithium can irreversibly react with the electrolyte, forming additional SEI. On the other hand, lithium plating is partly reversible as long as the metallic lithium exhibits an electrical contact to the active material of the negative electrode.[14] The literature distinguishes between two different reversible processes that are lithium stripping during a subsequent discharge and chemical intercalation during relaxation.[6]

Electrochemical models—based on physical-chemical equations—are adapted to investigate and describe the behavior of lithium-ion cells, especially their underlying aging mechanisms. The best-known electrochemical model is the pseudo two-dimensional (P2D) model developed by Newman, Doyle and Fuller.[15–18] The model considers kinetics and reaction rates as well as transport equations of charge and mass and is based on the theory of porous electrode and on the theory of concentrated solution.[18] On the one hand, the model is computationally intensive, but on the other hand, it represents the most accurate model of lithium-ion cells.

Lithium plating models are described in the previous literature, but only a few model lithium stripping as the backward reaction of lithium plating and fewer investigate cycling and the effect on aging. Arora et al.[2] first described a lithium plating side reaction by a Butler–Volmer equation on the negative electrode that occurs during overcharge. Tang et al.[19] investigated the effect of lithium plating at electrode edges caused by local overpotentials and showed that anode overhang area successfully prevents lithium deposition. Hein, Latz and co-workers[20,21] introduced an electrochemical model considering both lithium plating and lithium stripping. Their model shows a characteristic voltage plateau during discharge due to the dissolution of reversibly plated lithium. Furthermore, their 3D microstructure modeling approach reveals the most probable position for lithium plating.[5] Tippmann et al.[7] built up an electrochemical model considering lithium plating for low-temperature charging. Their experimental results on degradation qualitatively correlate with the modeled anode potential. Legrand et al.[22] investigated lithium plating through charge transfer limitations that

occur at short-time scales. However, diffusion limitations in the solid insertion compound occur at long-time scales and have not been examined. A lithium plating model at subzero temperatures was introduced by Ge et al.[23] and validated by nuclear magnetic resonance (NMR) measurements. Yang et al.[24] presented an aging model considering SEI growth and lithium plating based on cathodic Tafel equations. While the anode porosity decreases during cycling, lithium plating exponentially increases and causes accelerated capacity loss and resistance rise. In a further work, Yang and co-workers[25] extended their model considering lithium stripping to model the characteristic voltage plateau during relaxation or discharge after severe lithium deposition. Differential voltage analysis assesses the amount of deposited lithium. This model is focused on one charging/discharging cycle and does not consider long-term cycling or aging. Ren et al.[26] also modeled the characteristic voltage plateau due to lithium plating and lithium stripping side reactions at low temperatures. Differential voltage analysis is used as quantitative, non-destructive lithium plating detection. Finally, Xu et al.[27] modeled the effect of dead lithium on the cell's capacity and voltage.

In this paper, we present an electrochemical long-term cycling aging model at ambient temperature with SEI formation,[28] SEI re-formation,[29] lithium plating and lithium stripping[30] side reactions on the negative electrode described by adjusted Butler-Volmer equations. With this novel approach, we control the ratio of reversibly and irreversibly plated lithium. Accordingly, the model considers the transition from an early stage, linear to a later stage, nonlinear capacity fade, and determines the onset and slope of nonlinear aging. We compare the simulation results to experimental data on commercial 18 650-type NCM/C cells.

Model Development

Based on the pseudo two-dimensional (P2D) electrochemical model by Newman, Doyle and Fuller,[15–18] we developed an aging model considering SEI formation, SEI re-formation as well as lithium plating and lithium stripping side reactions within the negative electrode. The model for a common NCM/graphite cell is set up using COMSOL Multiphysics® 5.4. All governing equations of the P2D model and the theories of porous electrodes and concentrated solutions have been considerably shown in literature,[15–18] so that we focus on the model extension with regard to the side reactions.

Figure 1 shows the electrochemical main and side reactions at the graphite particle surface. We distinguish between the transport of two species through the negative electrode surface film—lithium-ions, on the one hand, and electrons on the other hand. This corresponds to the assumption that the film exhibits a maximum
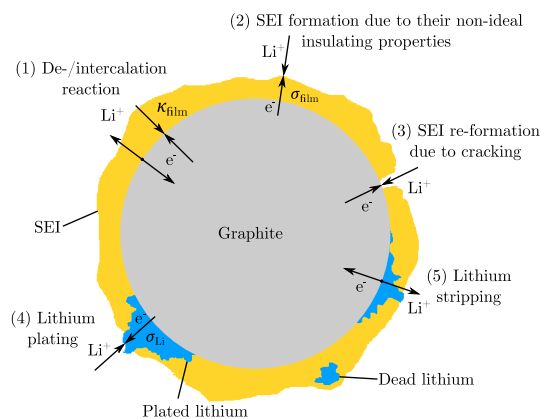

Figure 1. Illustration of the electrochemical reactions at the graphite particle surface.

conductivity for lithium-ions κ_{film} and an insulation conductivity for electrons σ_{film}.[29,31,32] While the lithium de-/intercalation reaction is unimpeded by a high conductivity of lithium-ions through the film (1), SEI formation results from their non-ideal insulating properties for electrons (2). Additional SEI re-formation is caused by cracking of the layer during graphite expansion and is unaffected by any transport limitations through the film (3). Lithium plating takes place once the overpotential becomes negative vs Li/Li$^+$ (4). As soon as lithium has been plated and the overpotential becomes positive vs Li/Li$^+$, the lithium stripping reaction proceeds by partly dissolving the plated lithium (5).[6] Considering the different ionic and electronic conductivities, our approach results in different potential drops for the overpotentials of the main and SEI formation reaction. By taking this approach, we are able to differentiate between the aging phenomena of capacity and power fade.[29] The resistances R_{Li^+} and R_{e^-} are given by the thickness of the film δ_{film} and the ionic and electronic conductivity κ_{film} and σ_{film}, respectively

$$R_{\text{Li}^+} = \frac{\delta_{\text{film}}}{\kappa_{\text{film}}} \tag{1}$$

$$R_{\text{e}^-} = \frac{\delta_{\text{film}}}{\sigma_{\text{film}}} \tag{2}$$

The SEI re-formation considers no potential drop as no film limits the transport. Compared to the ionic and electronic conductivities of the film, the conductivity of metallic lithium σ_{Li} is better by several orders of magnitude. Therefore, these very low potential drops for the overpotentials of the plating and stripping side reactions are neglected in the model.

In summary, we consider the loss of lithium inventory and the increase in impedance based on this modeling approach and the implementations of side reactions, which are shown in the following subsections.

De-/intercalaction reaction.—The current density i of the lithium de-/intercalation reaction is calculated by the Butler-Volmer equation

$$i_n = i_{0,n}\left(\exp\left(\frac{\alpha_{a,n}F}{RT}\eta_n\right) - \exp\left(-\frac{\alpha_{c,n}F}{RT}\eta_n\right)\right) \tag{3}$$

where the index n symbolizes the negative or positive electrode, i_0 is the exchange current density, α_a and α_c are the anodic and cathodic charge-transfer coefficients, F, R and T represent Faraday's constant, the universal gas constant and the cell temperature, respectively. The overpotential η_{neg} of the main reaction at the negative electrode is obtained by the solid phase potential Φ_s, the liquid phase potential Φ_l, the negative electrode equilibrium potential $E_{\text{Eq,neg}}$ and the potential drop $i_{\text{neg}}R_{\text{Li}^+}$[29]

$$\eta_{\text{neg}} = \Phi_s - \Phi_l - E_{\text{Eq,neg}} - i_{\text{neg}}R_{\text{Li}^+} \tag{4}$$

The potential drop by a cathode electrolyte interphase (CEI) at the positive electrode is left out of consideration in this work. Therefore, the overpotential η_{pos} is defined as

$$\eta_{\text{pos}} = \Phi_s - \Phi_l - E_{\text{Eq,pos}} \tag{5}$$

with the positive electrode equilibrium potential $E_{\text{Eq,pos}}$. Table I shows the chosen parameters—measured, taken from the literature and estimated—for the above introduced model at 25 °C.

Modeling SEI formation and SEI re-formation.—We distinguish between SEI formation due to its non-ideal insulating properties and SEI re-formation due to cracking of the layer. Both are modeled as irreversible side reactions by cathodic Tafel equations. The current density for SEI formation is calculated by

$$i_{\text{SEI,form}} = -i_{0,\text{SEI}} \exp\left(-\frac{\alpha_{c,\text{SEI}}F}{RT}\eta_{\text{SEI,form}}\right) \tag{6}$$

with the SEI's exchange current density $i_{0,\text{SEI}}$ and cathodic charge-transfer coefficient $\alpha_{c,\text{SEI}}$. The overpotential $\eta_{\text{SEI,form}}$ is calculated by

$$\eta_{\text{SEI,form}} = \Phi_s - \Phi_l - E_{\text{Eq,SEI}} - i_{\text{SEI,form}}R_{\text{e}^-} \tag{7}$$

where $i_{\text{SEI,form}}R_{\text{e}^-}$ symbolizes the potential drop due to the insulating conductivity of the SEI for electrons. Due to its non-ideal insulating properties, the solid electrolyte interphase grows continuously. However, this formation slows down over time or with cycles due to the increasing potential drop caused by the growth of the film.

SEI re-formation considers an expansion factor f_{exp} dependent on the stoichiometry x as depicted in Fig. 2. This expansion factor is the gradient of a graphite expansion curve as previously introduced and as already implemented in an electrochemical SEI model by Kindermann et al.[29]

$$i_{\text{SEI,re-form}} = -i_{0,\text{SEI}} \, f_{\text{exp}}(x) \, \exp\left(-\frac{\alpha_{c,\text{SEI}}F}{RT}\eta_{\text{SEI,re-form}}\right) \tag{8}$$

The overpotential $\eta_{\text{SEI,re-form}}$ considers no *iR* drop

$$\eta_{\text{SEI,re-form}} = \Phi_s - \Phi_l - E_{\text{Eq,SEI}} \tag{9}$$

Modeling lithium plating and lithium stripping.—The current density of the lithium plating side reaction is calculated by a Butler-Volmer equation, as reported by Arora et al.[36]

$$i_{\text{lpl}} = i_{0,\text{lpl}}\left(\exp\left(\frac{\alpha_{a,\text{lpl}}F}{RT}\eta_{\text{lpl}}\right) - \exp\left(\frac{-\alpha_{c,\text{lpl}}F}{RT}\eta_{\text{lpl}}\right)\right), \eta_{\text{lpl}} \leqslant 0 \text{ V} \tag{10}$$

with the lithium plating exchange current density $i_{0,\text{lpl}}$ and the anodic and cathodic charge-transfer coefficients $\alpha_{a,\text{lpl}}$ and $\alpha_{c,\text{lpl}}$. This equation is valid as long as the overpotential η_{lpl} is less than or equal to 0 V. Once the overpotential becomes positive again and as long as reversibly plated lithium exists, lithium stripping takes place

$$i_{\text{lst}} = i_{0,\text{lst}}\left(\exp\left(\frac{\alpha_{a,\text{lst}}F}{RT}\eta_{\text{lst}}\right) - \exp\left(\frac{-\alpha_{c,\text{lst}}F}{RT}\eta_{\text{lst}}\right)\right)$$
$$\times f\left(\frac{\xi q_{\text{lpl}} - q_{\text{lst}}}{q_{\text{cor}}}\right), \eta_{\text{lst}} > 0 \text{ V} \tag{11}$$
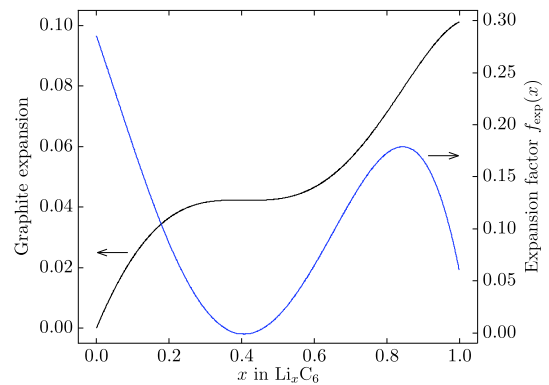

Figure 2. Graphite expansion and expansion factor $f_{\text{exp}}(x)$ as a function of stoichiometry x.

where f is a damping function (as shown in Fig. 3), q_{lpl} and q_{lst} describe the charge quantity of plated and stripped lithium, ξ is the ratio of reversibly plated lithium and q_{cor} denotes a correction variable to ensure valid units. The damping function enables the lithium stripping reaction to be stopped as soon as all reversibly plated lithium has been dissolved. In contrast to a step function, the damping function is based on a Sigmoid function to ensure a stable numeric solver. Irreversibly plated lithium has lost its electrical contact to the negative electrode and is also called dead lithium, as shown in Fig. 1. The overpotentials are defined as

$$\eta_{lpl} = \eta_{lst} = \Phi_s - \Phi_l - E_{Eq,lpl/lst} \qquad [12]$$

with the equilibrium potentials $E_{Eq,lpl} = E_{Eq,lst} = 0$ V. Here, the potential drop iR is left out of consideration due to the aforementioned high conductivity of metallic lithium.

Film growth.—We consider a surface film on the graphite particles that is composed of SEI and metallic lithium

$$\delta_{film} = \delta_{0,film} - \frac{(q_{SEI,form} + q_{SEI,re-form})M_{SEI}}{F\rho_{SEI}} - \frac{(q_{lpl} + q_{lst})M_{Li}}{F\rho_{Li}} \qquad [13]$$
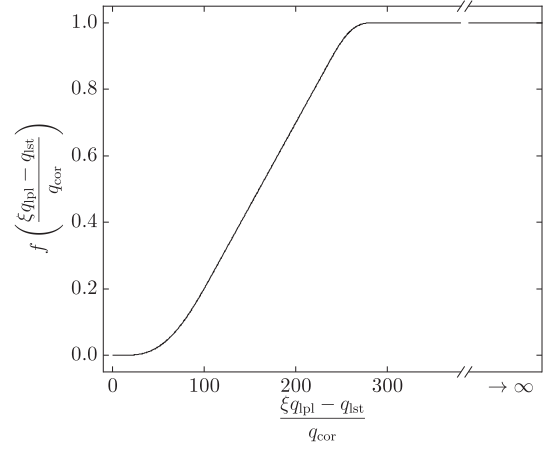

Figure 3. Damping function—which is based on a Sigmoid function—for the adjusted Butler-Volmer equation of the lithium stripping side reaction dependent on the ratio of reversibly plated lithium ξ, the charge quantities of plated and stripped lithium q_{lpl} and q_{lst}, and the correction variable q_{cor}.

Table I. Electrochemical model parameters measured from a Sanyo UR18650E cell labeled with superscript *m*. The superscript *e* indicates estimated values.

Parameter	Negative electrode	Separator	Positive electrode
Geometry			
Thickness l	70 μm [m]	20 μm [m]	60 μm [m]
Mean particle radius r_p	10 μm [m]		4 μm [m]
Solid phase fraction ε_s	0.59 [e]		0.61 [e]
Liquid phase fraction ε_l	0.3 [e]	0.45 [e]	0.3 [e]
Thermodynamics			
Equilibrium voltage E_{Eq}	see Fig. A·1 [m]		see Fig. A·1 [m]
Maximum Li$^+$ concentration $c_{s,max}$	31 370 mol m^{-3} [33]		51 385 mol m^{-3} [7]
Initial state of charge $\dfrac{c_{s,0}}{c_{s,max}}$	0.8 [e]		0.4 [e]
Kinetics			
Reaction rate constant k_n	1.5×10^{-11} m s^{-1} [e]		1.5×10^{-11} m s^{-1} [e]
Activation energy Ea_{k_n}	1×10^4 J mol^{-1} [e]		1×10^4 J mol^{-1} [e]
Anodic charge-transfer coefficient α_a	0.5 [e]		0.5 [e]
Cathodic charge-transfer coefficient α_c	0.5 [e]		0.5 [e]
Transport			
Solid diffusivity D_s	9×10^{-11} m^2 s^{-1} [e]		2.6×10^{-13} m^2 s^{-1} [e]
Activation energy Ea_{D_s}	5×10^4 J mol^{-1} [34]		2.5×10^4 J mol^{-1} [34]
Solid conductivity σ	100 S m^{-1} [e]		3.8 S m^{-1} [e]
Parameter		Electrolyte	
Electrolyte concentration c_l		1000 mol m^{-3} [e]	
Electrolyte diffusivity D_l		see Eq. 23 [35]	
Electrolyte conductivity κ		see Eq. 24 [35]	
Activity dependency $\dfrac{\partial \ln f_\pm}{\partial \ln c_l}$		see Eq. 25 [35]	
Transport number t_+		0.38 [35]	
Parameter		Cell	
Nominal capacity C_N		2.05 Ah [m]	
Radius r_{cell}		9 mm [m]	
Height h_{cell}		65 mm [m]	
Mass m_{cell}		45 g [m]	
Cell surface area A_{cell}		4.1846×10^{-3} m^2	
Cell volume V_{cell}		1.654×10^{-5} m^3	

with their molar masses M_{SEI} and M_{Li} and densities ρ_{SEI} and ρ_{Li}. $\delta_{0,film}$ symbolizes the initial film thickness. The charge quantities q are calculated by integrating the side reaction current densities. Cathodic current densities ($i_{SEI,form}$, $i_{SEI,re-form}$ and i_{lpl}) have a minus-sign and anodic current densities (i_{lst}) a plus-sign. Therefore, SEI formation, SEI re-formation and lithium plating cause the film to grow, whereas lithium stripping partly dissolves it.

Effective transport.—Furthermore, we consider effective transport parameters for the electrolyte diffusion coefficient D_l, the ionic conductivity κ and the electronic conductivity σ

$$D_{l,\text{eff}} = \frac{1}{N_M} D_l \qquad [14]$$

$$\kappa_{\text{eff}} = \frac{1}{N_M} \kappa \qquad [15]$$

$$\sigma_{\text{eff}} = \frac{1}{N_M} \sigma \qquad [16]$$

where MacMullin's number N_M describes the influence of porosity and tortuosity changes in the negative and positive electrode. In the literature, MacMullin's number is mostly given as a function depending on the porosity. However, especially for small porosities caused by film growth and pore clogging, adequate experimental data is missing. Based on simulation results by Xu et al.,[27] we assume an almost linearly increasing function depending on the cycles. Figure 4 shows both the considered MacMullin's number and its reciprocal.

Finally, Table II shows all parameters for the SEI re-/formation and lithium plating/stripping side reaction definitions.

Thermal model.—The electrochemical model is coupled with a 0D thermal model that simulates an evenly distributed heat in the cell. The total heat generation $\dot{q}$ is comprised of ohmic heat $\dot{q}_{ohm}$, reaction heat $\dot{q}_{reac}$ and reversible heat $\dot{q}_{rev}$

$$\dot{q} = \dot{q}_{ohm} + \dot{q}_{reac} + \dot{q}_{rev} = i_l \nabla \Phi_l + i_s \nabla \Phi_s \\ + \sum_i a_i i_i \left(\eta_i + T \frac{\partial E_{Eq,i}}{\partial T} \right) \qquad [17]$$

with the electrolyte current density i_l and electrode current density i_s. Index i symbolizes the partial reactions at the negative and positive electrode. The entropy for both electrodes is given in the Appendix (see Fig. A·2). The heat transfer is considered by convection
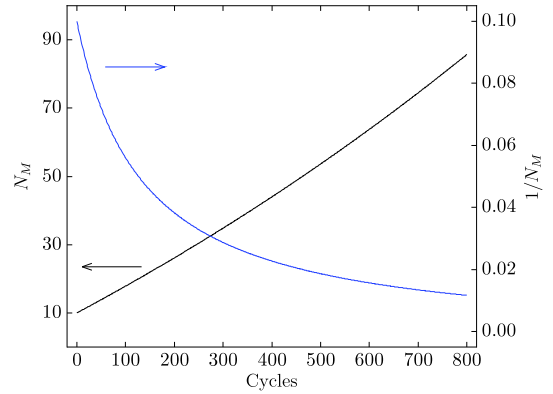

Figure 4. MacMullin's number and its reciprocal as a function of cycles.

$$\dot{Q}_{conv} = hA_{cell}(T - T_\infty) \qquad [18]$$

with the heat transfer coefficient h, the cell's surface A_{cell} and temperature T as well as the ambient temperature T_∞. The radiation is calculated by

$$\dot{Q}_{rad} = \varepsilon_{th} \sigma_B A_{cell}(T^4 - T_\infty^4) \qquad [19]$$

in which ε_{th} describes the emissivity and σ_B the Stefan–Boltzmann constant. In addition, the cell's thermal mass is considered by

$$\dot{Q}_{th} = m_{cell} c_p \frac{\partial T}{\partial t} \qquad [20]$$

with its mass m_{cell} and specific heat capacity c_p. Hence, the governing equation is given by

$$m_{cell} c_p \frac{\partial T}{\partial t} = V_{cell} \frac{1}{l} \int_{x=0}^{l} \dot{q} \; dx - hA_{cell}(T - T_\infty) \\ - \varepsilon_{th} \sigma_B A_{cell}(T^4 - T_\infty^4) \qquad [21]$$

with the thickness of a cell layer $l = l_{neg} + l_{sep} + l_{pos}$. All cell design information is listed in Tables I, and Table III shows the parameters of the thermal model.

Temperature-dependent variables.—The temperature dependency of the anodic and cathodic reaction rate constants k_a and k_c

Table II. Electrochemical model parameters for the side reaction definitions. The superscript *e* indicates estimated values.

Parameter	Value
SEI re-/formation equilibrium potential $E_{Eq,SEI}$	0.4 V [37]
SEI re-/formation exchange current density $i_{0,SEI}$	1×10^{-6} A m^{-2} ^{e}
SEI re-/formation cathodic charge-transfer coefficient $\alpha_{c,SEI}$	0.5 ^{e}
SEI density ρ_{SEI}	1690 kg m^{-3} [38]
SEI molar mass M_{SEI}	0.162 kg mol^{-1} [38]
Li$^+$ conductivity κ_{film}	see Eq. 24[35]
e$^-$ conductivity σ_{film}	1×10^{-8} S m^{-1} [29]
Initial film thickness $\delta_{0,film}$	5 nm ^{e}
Lithium plating/stripping equilibrium potential $E_{Eq,lpl}/E_{Eq,lst}$	0 V [30]
Lithium plating/stripping exchange current density $i_{0,lpl}/i_{0,lst}$	1 A m^{-2} ^{e}
Lithium plating/stripping anodic charge-transfer coefficient $\alpha_{a,lpl}/\alpha_{a,lst}$	0.5 ^{e}
Lithium plating/stripping cathodic charge-transfer coefficient $\alpha_{c,lpl}/\alpha_{c,lst}$	0.5 ^{e}
Lithium density ρ_{Li}	534 kg m^{-3}
Lithium molar mass M_{Li}	6.94×10^{-3} kg mol^{-1}
Correction variable q_{cor}	1 C m^{-2} ^{e}
Ratio of reversibly plated lithium ξ	f(cycles), see Fig. 7

Table III. Thermal model parameters. The superscript *e* indicates estimated values.

Parameter	Value
Specific heat capacity c_p	$1000 \, \text{J kg}^{-1} \, \text{K}^{-1}$ [7]
Heat transfer coefficient h	$10 \, \text{W m}^{-2} \, \text{K}^{-1}$ [e]
Emissivity ε_{th}	0.8 [39]
Ambient temperature T_∞	298 K
Entropy $\frac{\partial E_{Eq}}{\partial T}$	see Fig. A·2 [40,41]

and the diffusion coefficients in the negative and positive active material $D_{s,neg}$ and $D_{s,pos}$ are described by the Arrhenius equation

$$\Psi = \Psi_{ref} \exp\left(\frac{E_{a,\Psi}}{R}\left(\frac{1}{T_{ref}} - \frac{1}{T}\right)\right) \quad [22]$$

with $E_{a,\Psi}$ as the activation energy. Ψ marks the dependent variable and Ψ_{ref} its reference value at the reference temperature T_{ref}.

The temperature dependency of the diffusion coefficient in the electrolyte D_l, the liquid phase conductivity κ and the thermodynamic factor $\frac{\partial \ln f_\pm}{\partial \ln c_l}$ are given by Valøen et al.[35] in Eqs. 23, 24 and 25.

Experimental

We tested commercial Sanyo UR18650E lithium-ion cells to validate our modeling approach and simulation results. The cells with a nominal capacity of 2.05 Ah and an energy density of $175 \, \text{Wh kg}^{-1}$ are composed of graphite as negative electrode and NCM111 as positive electrode. We used a battery test system CTS (BaSyTec) to cycle the cells, and an environmental chamber MK 53 (Binder) to control their ambient temperature.

At the beginning, we ran rate capability tests with new cells under different discharge currents (C/10, C/5, C/2, 1C and 2C) at 25 °C and 0 °C for model validation. Two more new cells were opened in an argon filled glove box, half cells with Li_xC_6/Li and $\text{Li}_y(\text{Ni}_{0.33}\text{Co}_{0.33}\text{Mn}_{0.33})\text{O}_2$/Li were assembled and equilibrium potentials vs Li/Li^+ were measured (see Fig. A·1). Additionally, we measured the cells' cross section area, the thickness of the electrodes and separator and the mean particle radii (see Table I).

For the aging experiment, we kept the ambient temperature at 25 °C. Three cells were cycled as follows: constant current discharge (CC$_{dch}$) with -2 A to the cut-off voltage of 2.75 V, followed by constant current charge (CC$_{ch}$) with 2 A to the cut-off voltage of 4.2 V and constant voltage charge (CV$_{ch}$) with the cut-off current of 0.1 A. Resting times of 10 s were applied after each discharge and charge. At the beginning of the aging experiment and after every 100 cycles, checkup cycles were performed to determine the cells' capacity.

Results and Discussion

Model validation.—The simulated cell voltages and temperatures of the electrochemical and thermal model are shown in Fig. 5 and compared to the experimental data for discharge with C/10, C/5, C/2,
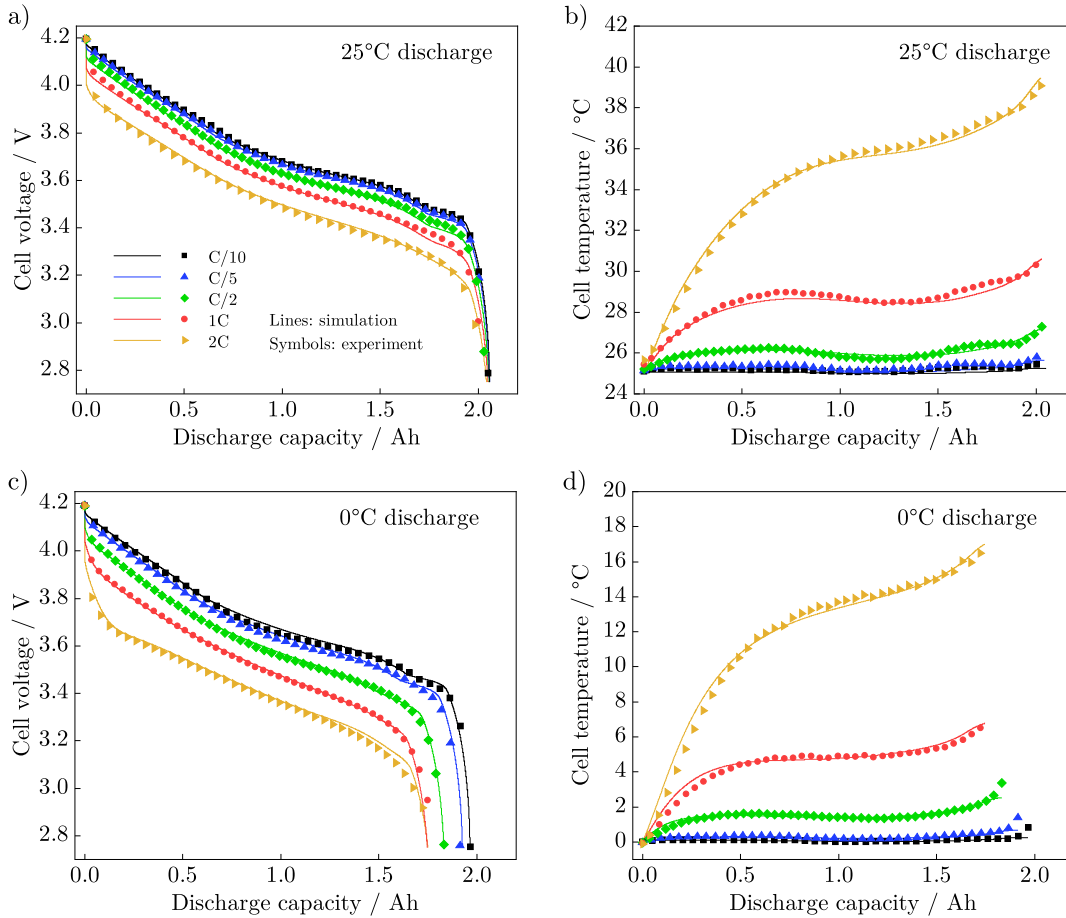

Figure 5. Comparison of simulation results (lines) and experimental data (symbols) for different discharge rates. Cell voltage (a) and cell temperature (b) at an ambient temperature of 25 °C, and cell voltage (c) and cell temperature (d) at an ambient temperature of 0 °C.
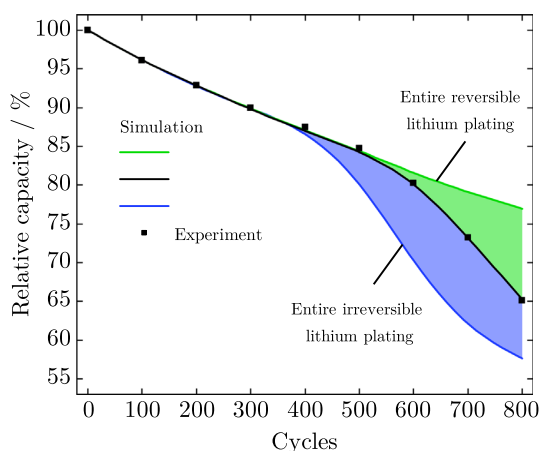
Figure 6. Comparison of experimental data (symbols) and simulation results (lines) with varying lithium plating reversibility. $\xi = 1$ denotes entire reversible and $\xi = 0$ entire irreversible lithium plating.

Figure 7. Changing ratio of reversibly plated lithium ξ over cycles.

1C and 2C at ambient temperatures of 25 °C and 0 °C. We calculated mean absolute errors (MAE) and root mean square errors (RMSE) to assess the deviation between model and experiment. At 25 °C, the maximum MAEs are 14 mV (2 C) and 0.2 °C (2 C) and the maximum RMSEs are 21 mV (2 C) and 0.25 °C (2 C). At 0 °C, the maximum MAEs are 19 mV (2 C) and 0.3 °C (2 C) and the maximum RMSEs are 23 mV (2 C) and 0.4 °C (2 C). Therefore, the simulation results are in very good agreement with the experimental data for all C-rates as well as for both temperatures.

Reversible and irreversible lithium plating.—Figure 6 shows the measured cell's relative capacity determined in the checkup cycles of the aging experiment (symbols). In the early stage that is arising from the beginning of cycling to about cycle 500, an almost linear or square-root-shaped, decelerating capacity loss is seen. Thereafter, an accelerating, nonlinear capacity loss denotes the later stage with a relative capacity of 65% after 800 cycles. Usually, an end of life is defined by falling below a relative capacity of 80% that is reached for this cell after 600 cycles, already within the stage of accelerated capacity loss. In a former study,[13] we showed that the loss of lithium inventory is the dominant aging mechanism within the scope of this aging experiment. Electrochemical characterization and post-mortem analysis revealed solid electrolyte interphase growth and lithium plating induced capacity loss.

Based on our electrochemical modeling approach and by setting the ratio of reversibly plated lithium ξ to one, we are able to simulate sole SEI formation and re-formation. Lithium plating may still take place but is plated completely reversibly and will be stripped subsequently. The simulation result is shown by the green line in Fig. 6 that is an almost linear or square-root-shaped capacity loss during cycling. The slope of the curve is fitted by the SEI re-/formation exchange current density $i_{0,SEI}$.

In contrast, the entire irreversible lithium plating is modeled by setting the ratio of reversibly plated lithium ξ to zero. No lithium stripping side reaction takes place anymore. The blue line in Fig. 6 shows the simulation result that exhibits an early stage, linear capacity loss and an accelerating capacity loss, starting at about cycle 400. Compared to the measurements, the simulation results in an earlier and more intense capacity loss.

Finally, the black line in Fig. 6 shows the simulated relative capacity considering a changing ratio of reversibly plated lithium ξ over cycles. With this approach, we assume that the amount of reversibly plated lithium decreases with ongoing cycling. In other words, the more lithium is plated, the more lithium is irreversibly plated. With an MAE of 0.17% and an RMSE of 0.25%, the simulation results are in very good agreement with the experimental
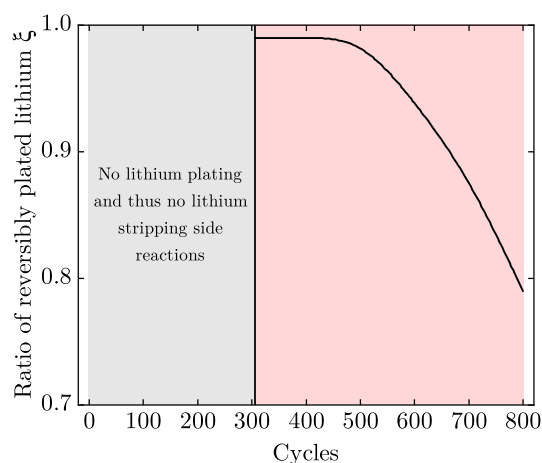
data. Based on our modeling approach, we are able to simulate both linear and nonlinear aging as well as to define the onset and slope of nonlinear aging. Differentiating between reversible and irreversible lithium plating and their impact on capacity loss is also consistent to operando lithium plating quantifications using incremental capacity analysis shown by Ansean et al.[42]

The fitted ratio of reversibly plated lithium ξ over cycles is shown in Fig. 7. Up to cycle 306, no lithium plating and thus no lithium stripping side reactions take place, as the potential of the negative electrode is always positive vs Li/Li^+. As soon as this potential becomes negative and lithium is plated, we assume ξ to be 0.99 since Howlett et al.[43] showed a cycling efficiency of greater than 99% for lithium metal electrodes. To obtain a linear aging behavior, the cycling efficiency remains constant for about one hundred cycles. However, the efficiency declines with ongoing cycling due to degradation mechanisms, inhomogeneous current and potential distributions, and deposit morphology changes.[12,13,43,44] The change in the ratio of reversibly plated lithium concurs with the onset and slope of nonlinear aging in Fig. 6. In the end, the ratio is of less than 80% which means that one fifth is irreversibly plated.

Cell voltage and capacity loss.—Figure 8 shows the simulated cell voltages (lines) compared to experimental data (symbols) over discharge capacity obtained from checkup cycles. With minimum
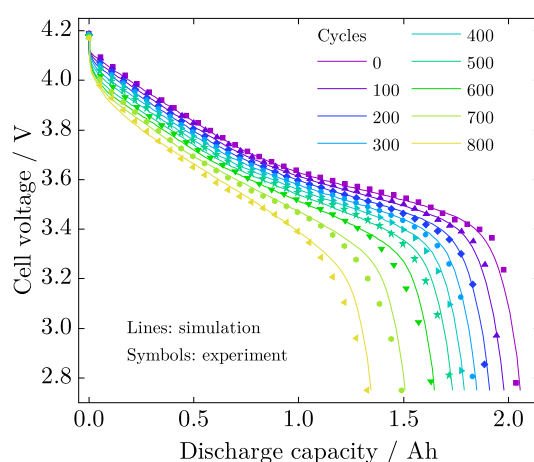

Figure 8. Comparison of simulation results (lines) and experimental data (symbols) of cell voltage over discharge capacity obtained from checkup cycles.
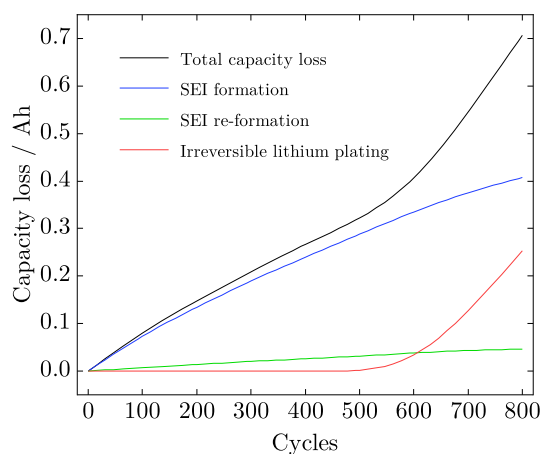
Figure 9. Entire capacity loss caused by SEI formation, SEI re-formation and irreversible lithium plating shown over cycles.

errors of 8 mV (MAE) and 12 mV (RMSE) for cycle 200 and maximum errors of 27 mV (MAE) and 44 mV (RMSE) for cycle 700, the results are in very good agreement. Furthermore, the simulation results show that the model considers capacity as well as power fade.

The capacity loss over cycles is depicted in Fig. 9. SEI formation shows a decelerated, square-root-shaped behavior over cycles, as the

potential drop increases due to the growth of the film. However, SEI re-formation considers no influencing film and potential drop, and thus results in an almost linear capacity loss. Only by cause of capacity loss and shortened charge/discharge cycles, SEI re-formation decelerates. In contrast, irreversible lithium plating is unobtrusive over many cycles, but subsequently causes the nonlinear capacity fade between 500 and 800 cycles. After 800 cycles, about two thirds of the capacity loss are caused by SEI re-/formation and one third by irreversible lithium plating.

Characteristics of side reactions over cycling.—The following subsection shows the characteristics of SEI re-/formation and lithium plating/stripping over cycling based on simulation results. Figure 10 depicts the cyclic cell voltage (a) and main reaction current density (b). With ongoing aging, the total cycle time decreases as the cell's capacity fades. Moreover, the resistance rise causes higher polarization that shortens the CC phase and extends the CV phase during charging. Both capacity and power loss—which in turn cause the energy loss of the cell—are clearly recognizable based on the cell voltage.

Figure 10c depicts the side reaction current density of SEI formation (solid lines) and re-formation (dotted lines). For both, the current density declines while discharging and rises again while charging the cell. The maximum of current density corresponds to the transition from CC to CV charging, as the driving overpotentials are at a maximum. With ongoing aging, less SEI formation occurs because the total cycle time is getting shorter, but mainly because of the increasing potential drop caused by the growth of the film. In contrast, no *iR* drop is considered for SEI re-formation. As expected, SEI re-/formation is characterized by a decelerating behavior over
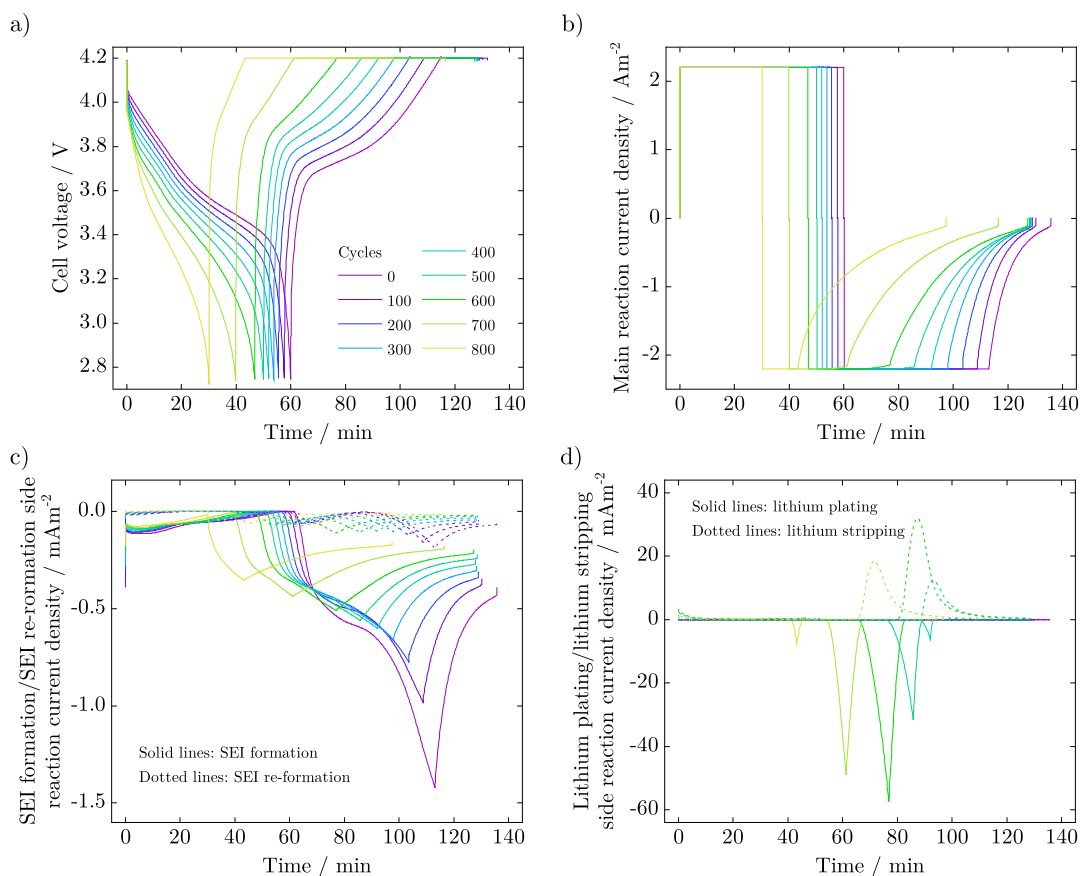

Figure 10. Simulation results of a discharge-charge cycle: cell voltage (a), current density of the main reaction (b), SEI formation/re-formation (c) and lithium plating/stripping (d) over time.
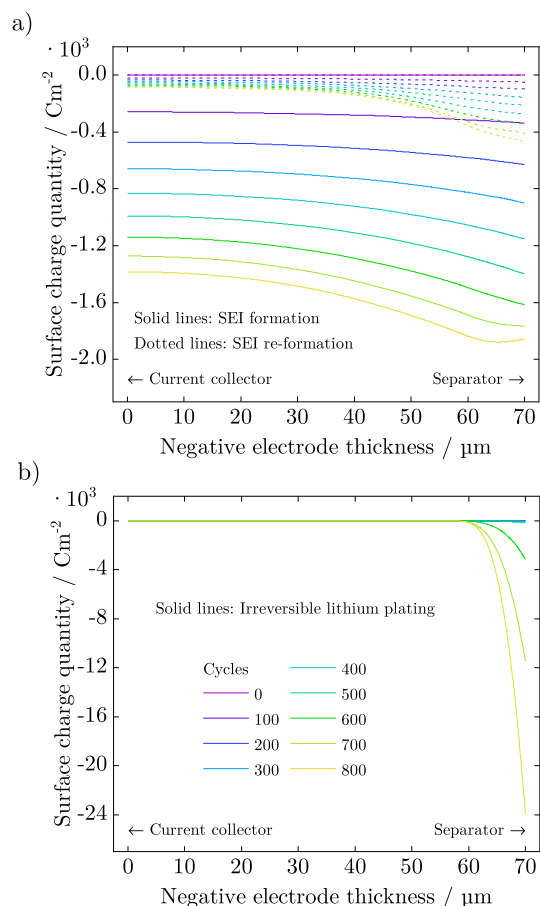
Figure 11. Surface charge quantities of SEI formation and re-formation (a) and irreversible lithium plating (b) over the thickness of the negative electrode.

Figure 12. Stoichiometry *x* of the negative electrode (a) and *y* of the positive electrode (b) at end-of-charge (EOC) and end-of-discharge (EOD) showing their shifts over cycles.

cycling. In addition, the results show a higher SEI re-/formation for higher cell voltages, which means for higher SOCs.

The lithium plating and lithium stripping side reaction densities are shown in Fig. 10d. As soon as the local potential of the graphite anode becomes negative vs Li/Li^+, lithium plating takes place, which reveals its maximum at the transition from the CC to the CV charging phase as well. Due to the decreasing main reaction current density in the CV charging phase, the cell's polarization also decreases. Once the driving overpotential becomes positive vs Li/Li^+, subsequent lithium stripping dissolves the reversibly plated lithium. The lithium stripping side reaction density forms a maximum and diminishes towards the end of charging. In the subsequent discharging phase, the remaining amount of reversibly plated lithium is dissolved which causes a characteristic voltage plateau if the amount is big enough.[30] Furthermore, lithium plating firstly appears after a few hundred cycles and increases and then declines again with ongoing cycling. Finally, this is caused by the capacity loss, the increasing polarization, the shortened CC and extended CV phases —and therefore the reduced time when lithium plating can occur— and the transition from a stage I to a stage II potential plateau in the negative electrode caused by LLI (see Fig. 12).

Integrating the side reaction current densities results in surface charge quantities, which are shown in Fig. 11 over the thickness of the negative electrode. SEI formation and re-formation (solid and dotted lines in Fig. 11a, respectively) take place in the entire electrode. However, the SEI grows faster at the negative electrode/ separator interface. In contrast, irreversible lithium plating occurs on
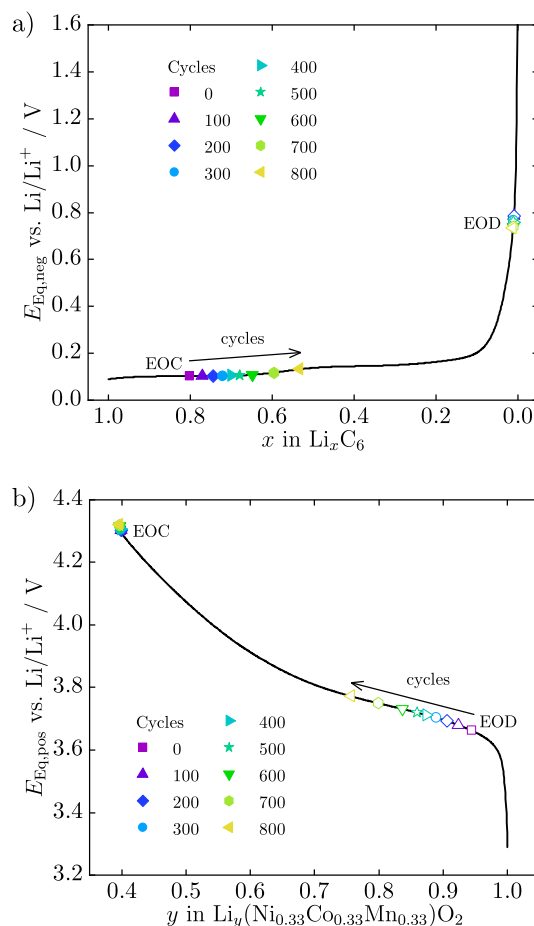
the outer edge of the negative electrode at its interface to the separator,[5,24] as shown in Fig. 11b. At the interface of the negative electrode and its current collector, the overpotential vs Li/Li^+ is always positive and no lithium is deposited. Finally, much more lithium is spatially deposited compared to SEI re-/formation, that is based on the difference in the magnitude of the side reaction current densities, as depicted in Figs. 10c and 10d.

Figure 12 shows the shifts in stoichiometry—which is the inter-calation degree—over cycles of the negative and positive electrode at end-of-charge (EOC) and end-of-discharge (EOD) as a consequence of capacity fade. As expected, the stoichiometry of the negative electrode at EOC decreases with ongoing aging due to LLI. The declining change in stoichiometry up to cycle 500, which increases subsequently, reveals the linear and nonlinear aging behavior. While the LLI effects a transition from a stage I to a stage II potential plateau in the negative electrode, the potential of the positive electrode slightly increases at EOC, which is defined by the cutoff-voltage of the cell at 4.2 V, which is the difference between the negative and positive electrode potential. As a result of the transition of the potential plateaus, the lithium plating side reaction diminishes with ongoing aging.

At the EOD, the stoichiometry of the positive electrode decreases with ongoing aging based on the LLI as the dominant aging mechanism. Again, the change in stoichiometry results from the decelerating capacity loss due to SEI re-/formation and the subsequent accelerated capacity loss caused by irreversible lithium plating. Furthermore, the stoichiometry is a relative but not absolute

variable and thus the shifts are not equidistant for the negative and positive electrode.

Conclusions

In this paper, we introduced a pseudo two-dimensional electrochemical aging model that describes the transition from a linear to a nonlinear aging behavior. Besides the main aging mechanisms of SEI formation and re-formation, we presented a novel approach for modeling reversible and irreversible lithium plating and lithium stripping. The model agrees very well with experimental aging data on commercial 18 650-type NCM/C cells and accurately reveals the onset and slope of nonlinear aging. Furthermore, the simulation results are in very good agreement with experimental data for discharge at different C-rates and at ambient temperatures of 25 °C and 0 °C. Future work will incorporate the model into a multi-dimensional modeling approach to investigate inhomogeneous aging and to get a more thorough understanding of the impact of different charging strategies, tab and electrode designs, and temperature conditioning on spatial cell degradation.

Appendix

Measured equilibrium potential curves dependent on the degree of lithiation x and y for the negative and positive active material are shown in Fig. A·1. The entropic coefficient of the reversible heat is derived from the literature[40,41] and shown in Fig. A·2.

We consider transport parameters of the electrolyte as functions of temperature T, lithium-ion concentration in the liquid phase c_l and transport number t_+ as measured by Valøen et al.[35] The analytical dependencies for electrolyte diffusivity D_l, conductivity κ and activity $\frac{\partial \ln f_\pm}{\partial \ln c_l}$ are described by

$$D_l = (10^{-4.43 - \frac{54}{T-(229+5\,c_l)} - 0.22\,c_l}) \cdot 10^{-4} \qquad [23]$$

$$\begin{aligned}\kappa = 0.1\,c_l\,(&-10.5 + 0.074\,T - 6.96 \cdot 10^{-5}\,T^2 \\ &+ 0.668\,c_l - 0.0178\,c_l\,T + 2.8 \cdot 10^{-5}\,c_l\,T^2 \\ &+ 0.494\,c_l^2 - 8.86 \cdot 10^{-4}\,c_l^2\,T)^2\end{aligned} \qquad [24]$$

$$\begin{aligned}&\frac{\partial \ln f_\pm}{\partial \ln c_l} \\ &= \frac{0.601 - 0.24\,c_l^{0.5} + 0.982\,c_l^{1.5}\,(1 - 0.0052\,(T - 294))}{1 - t_+} - 1\end{aligned}$$
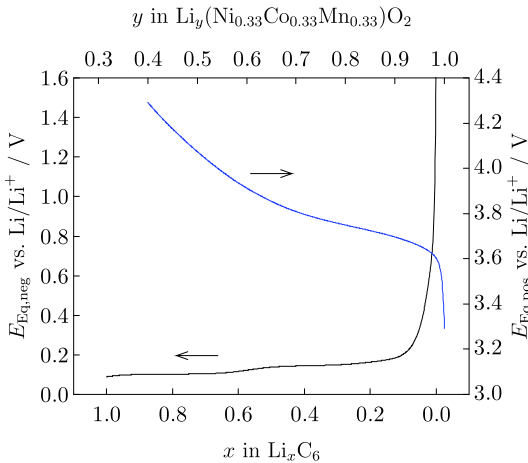$$[25]$$

Figure A·1. Equilibrium potential for the negative and positive electrode.
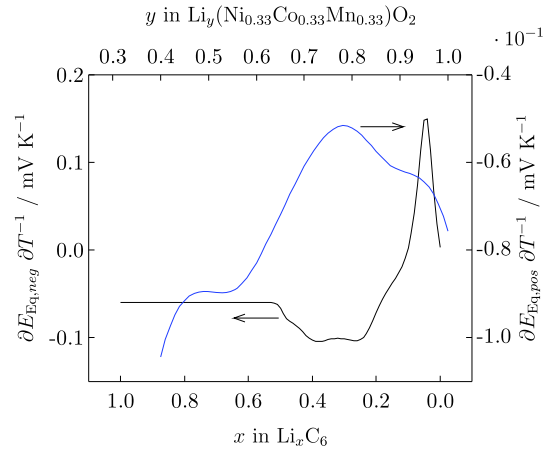

Figure A·2. Entropy of the negative[41] and positive electrode.[40]

ORCID

Jonas Keil ⓘ https://orcid.org/0000-0002-0674-2676

References

1. C. R. Birkl, M. R. Roberts, E. McTurk, P. G. Bruce, and D. A. Howey, "Degradation diagnostics for lithium ion cells." *Journal of Power Sources*, **341**, 373 (2017).
2. P. Arora, "Capacity fade mechanisms and side reactions in lithium-ion batteries." *J. Electrochem. Soc.*, **145**, 3647 (1998).
3. J. Vetter, P. Novák, M. R. Wagner, C. Veit, K.-C. Möller, J. O. Besenhard, M. Winter, M. Wohlfahrt-Mehrens, C. Vogler, and A. Hammouche, "Ageing mechanisms in lithium-ion batteries." *Journal of Power Sources*, **147**, 269 (2005).
4. T. Waldmann et al., "Review–post-mortem analysis of aged lithium-ion batteries: disassembly methodology and physico-chemical analysis techniques." *J. Electrochem. Soc.*, **163**, A2149 (2016).
5. S. Hein and A. Latz, "Influence of local lithium metal deposition in 3D microstructures on local and global behavior of lithium-ion batteries." *Electrochimica Acta*, **201**, 354 (2016).
6. T. Waldmann, B.-I. Hogg, and M. Wohlfahrt-Mehrens, "Li plating as unwanted side reaction in commercial Li-ion cells–a review." *Journal of Power Sources*, **384**, 107 (2018).
7. S. Tippmann, D. Walper, L. Balboa, B. Spier, and W. G. Bessler, "Low-temperature charging of lithium-ion cells part I: Electrochemical modeling and experimental investigation of degradation behavior." *Journal of Power Sources*, **252**, 305 (2014).
8. T. Waldmann, B.-I. Hogg, M. Kasper, S. Grolleau, C. G. Couceiro, K. Trad, B. P. Matadi, and M. Wohlfahrt-Mehrens, "Interplay of operational parameters on lithium deposition in lithium-ion cells: systematic measurements with reconstructed 3-electrode pouch full cells." *J. Electrochem. Soc.*, **163**, A1232 (2016).
9. I. D. Campbell, M. Marzook, M. Marinescu, and G. J. Offer, "How observable is lithium plating? differential voltage analysis to identify and quantify lithium plating following fast charging of cold lithium-ion batteries." *J. Electrochem. Soc.*, **166**, A725 (2019).
10. B. Rieger, S. F. Schuster, S. V. Erhard, P. J. Osswald, A. Rheinfeld, C. Willmann, and A. Jossen, "Multi-directional laser scanning as innovative method to detect local cell damage during fast charging of lithium-ion cells." *Journal of Energy Storage*, **8**, 1 (2016).
11. V. Zinth, C. von Lüders, J. Wilhelm, S. V. Erhard, M. Hofmann, S. Seidlmayer, J. Rebelo-Kornmeier, W. Gan, A. Jossen, and R. Gilles, "Inhomogeneity and relaxation phenomena in the graphite anode of a lithium-ion battery probed by in situ neutron diffraction." *Journal of Power Sources*, **361**, 54 (2017).
12. S. V. Erhard et al., "Simulation and measurement of the current density distribution in lithium-ion batteries by a multi-tab cell approach." *J. Electrochem. Soc.*, **164**, A6324 (2017).
13. J. Keil, N. Paul, V. Baran, P. Keil, R. Gilles, and A. Jossen, "Linear and nonlinear aging of lithium-ion cells investigated by electrochemical analysis and in-situ neutron diffraction." *J. Electrochem. Soc.*, **166**, A3908 (2019).
14. V. Zinth, C. von Lüders, M. Hofmann, J. Hattendorff, I. Buchberger, S. Erhard, J. Rebelo-Kornmeier, A. Jossen, and R. Gilles, "Lithium plating in lithium-ion batteries at sub-ambient temperatures investigated by in situ neutron diffraction." *Journal of Power Sources*, **271**, 152 (2014).
15. M. Doyle, "Modeling of galvanostatic charge and discharge of the lithium/polymer/insertion cell." *J. Electrochem. Soc.*, **140**, 1526 (1993).
16. T. F. Fuller, "Simulation and optimization of the dual lithium ion insertion cell." *J. Electrochem. Soc.*, **141**, 1 (1994).
17. M. Doyle, "Design and simulation of lithium rechargeable batteries." *Dissertation*, University of California, Berkeley (1995), https://escholarship.org/uc/item/6j87z0sp.

18. J. S. Newman and K. E. Thomas-Alyea, *Electrochemical Systems* (J. Wiley, Hoboken, N.J.) 3rd ed. (2004).
19. M. Tang, P. Albertus, and J. Newman, "Two-dimensional modeling of lithium deposition during cell charging." *J. Electrochem. Soc.*, **156**, A390 (2009).
20. S. Hein, M. Petzl, M. Danzer, and A. Latz, "Simulation of lithium plating and stripping during low temperature operation of li-ion battery." *UECT 2014* (2014), https://elib.dlr.de/92058/.
21. S. Hein and A. Latz, "Lithium plating and stripping in the framework of a 3d electrochemical model." *ECS Trans.*, **69**, 3 (2015).
22. N. Legrand, B. Knosp, P. Desprez, F. Lapicque, and S. Raël, "Physical characterization of the charging process of a Li-ion battery and prediction of Li plating by electrochemical modelling." *Journal of Power Sources*, **245**, 208 (2014).
23. H. Ge, T. Aoki, N. Ikeda, S. Suga, T. Isobe, Z. Li, Y. Tabuchi, and J. Zhang, "Investigating lithium plating in lithium-ion batteries at low temperatures using electrochemical model with nmr assisted parameterization." *J. Electrochem. Soc.*, **164**, A1050 (2017).
24. X.-G. Yang, Y. Leng, G. Zhang, S. Ge, and C.-Y. Wang, "Modeling of lithium plating induced aging of lithium-ion batteries: transition from linear to nonlinear aging." *Journal of Power Sources*, **360**, 28 (2017).
25. X.-G. Yang, S. Ge, T. Liu, Y. Leng, and C.-Y. Wang, "A look into the voltage plateau signal for detection and quantification of lithium plating in lithium-ion cells." *Journal of Power Sources*, **395**, 251 (2018).
26. D. Ren, K. Smith, D. Guo, X. Han, X. Feng, L. Lu, M. Ouyang, and J. Li, "Investigation of lithium plating-stripping process in li-ion batteries at low temperature using an electrochemical model." *J. Electrochem. Soc.*, **165**, A2167 (2018).
27. S. Xu, K.-H. Chen, N. P. Dasgupta, J. B. Siegel, and A. G. Stefanopoulou, "Evolution of dead lithium growth in lithium metal batteries: experimentally validated model of the apparent capacity loss." *J. Electrochem. Soc.*, **166**, A3456 (2019).
28. N. Paul, J. Keil, F. M. Kindermann, S. Schebesta, O. Dolotko, M. J. Mühlbauer, L. Kraft, S. V. Erhard, A. Jossen, and R. Gilles, "Aging in 18 650-type Li-ion cells examined with neutron diffraction, electrochemical analysis and physico-chemical modeling." *Journal of Energy Storage*, **17**, 383 (2018).
29. F. M. Kindermann, J. Keil, A. Frank, and A. Jossen, "A SEI modeling approach distinguishing between capacity and power fade." *J. Electrochem. Soc.*, **164**, E287 (2017).
30. C. von Lüders, J. Keil, M. Webersberger, and A. Jossen, "Modeling of lithium plating and lithium stripping in lithium-ion batteries." *Journal of Power Sources*, **414**, 41 (2019).
31. P. Verma, P. Maire, and P. Novák, "A review of the features and analyses of the solid electrolyte interphase in Li-ion batteries." *Electrochimica Acta*, **55**, 6332 (2010).
32. K. Xu, "Nonaqueous liquid electrolytes for lithium-based rechargeable batteries." *Chem. Rev.*, **104**, 4303 (2004).
33. M. Safari and C. Delacourt, "Modeling of a commercial graphite/LiFePO4 cell." *J. Electrochem. Soc.*, **158**, A562 (2011).
34. W. Fang, O. J. Kwon, and C.-Y. Wang, "Electrochemical-thermal modeling of automotive Li-ion batteries and experimental validation using a three-electrode cell." *International Journal of Energy Research*, **34**, 107 (2010).
35. L. O. Valoen and J. N. Reimers, "Transport properties of LiPF[sub 6]-based li-ion battery electrolytes." *J. Electrochem. Soc.*, **152**, A882 (2005).
36. P. Arora, "Mathematical modeling of the lithium deposition overcharge reaction in lithium-ion batteries using carbon-based negative electrodes." *J. Electrochem. Soc.*, **146**, 3543 (1999).
37. P. Ramadass, B. Haran, P. M. Gomadam, R. White, and B. N. Popov, "Development of first principles capacity fade model for li-ion cells." *J. Electrochem. Soc.*, **151**, A196 (2004).
38. A. Awarke, S. Pischinger, and J. Ogrzewalla, "Pseudo 3d modeling and analysis of the sei growth distribution in large format Li-ion polymer pouch cells." *J. Electrochem. Soc.*, **160**, A172 (2012).
39. C. Kupper and W. G. Bessler, "Multi-scale thermo-electrochemical modeling of performance and aging of a lifepo 4/graphite lithium-ion cell." *J. Electrochem. Soc.*, **164**, A304 (2017).
40. V. V. Viswanathan, D. Choi, D. Wang, W. Xu, S. Towne, R. E. Williford, J.-G. Zhang, J. Liu, and Z. Yang, "Effect of entropy change of lithium intercalation in cathodes and anodes on Li-ion battery thermal management." *Journal of Power Sources*, **195**, 3720 (2010).
41. J. Mao, W. Tiedemann, and J. Newman, "Simulation of temperature rise in Li-ion cells at very high currents." *Journal of Power Sources*, **271**, 444 (2014).
42. D. Anseán, M. Dubarry, A. Devie, B. Y. Liaw, V. M. García, J. C. Viera, and M. González, "Operando lithium plating quantification and early detection of a commercial LiFePO4 cell cycled under dynamic driving schedule." *Journal of Power Sources*, **356**, 36 (2017).
43. P. C. Howlett, D. R. MacFarlane, and A. F. Hollenkamp, "High lithium metal cycling efficiency in a room-temperature ionic liquid." *Electrochimica Acta*, **7**, A97 (2004).
44. M. Wetjen, D. Pritzl, R. Jung, S. Solchenbach, R. Ghadimi, and H. A. Gasteiger, "Differentiating the degradation phenomena in silicon-graphite electrodes for lithium-ion batteries." *J. Electrochem. Soc.*, **164**, A2840 (2017).

9 Conclusion and Outlook

In this thesis, the linear and nonlinear aging of lithium-ion cells was investigated by means of aging experiments, electrochemical and post-mortem analysis, neutron diffraction and physicochemical modeling.

Starting with fundamentals of lithium-ion cell aging, the main aging mechanisms are presented which are the formation and re-formation of the solid electrolyte interphase, lithium plating and lithium stripping, particle fracture and structural changes and decomposition of the positive electrode. The aging mechanisms can be assigned to the degradation modes of loss of lithium-ion inventory, loss of active material in the negative electrode and loss of active material in the positive electrode.

Furthermore, methods for characterizing aging mechanisms and their state of the art are shown. While in-situ measurements are performed on materials in their original position, i.e. without disassembling the battery, ex-situ measurements involve cell opening and sample preparation. Most of the spectroscopy and microscopy techniques are performed on materials or require special cells including transparent windows. In contrast, neutron diffraction shows a high sensitivity for light elements like lithium and is suitable for large cell formats and commercially produced cells due to the high penetration depth of neutrons.

The state of the art of modeling lithium-ion cell aging is presented focusing on physicochemical modeling which considers kinetics and reaction rates, transport equations of charge and mass as well as the theory of porous electrode and the theory of concentrated solution. Although there are physicochemical SEI re-/formation and lithium plating models, only a few include lithium stripping as the backward reaction of lithium plating and even fewer investigate cycling and the effect on aging.

We performed aging experiments at controlled temperatures on 18650-type $C/LiNi_{0.33}Mn_{0.33}Co_{0.33}O_2$ lithium-ion cells with special consideration of varying stress conditions to investigate the interaction of SEI re-/formation, lithium plating and lithium stripping. Cells aged with a standard charging and discharging rate of almost 1C, but different resting times, showed a nonlinear capacity fade after a few hundred equivalent full cycles. By increasing the discharging current or decreasing the charging current, their lifetime improved, resulting in a linear capacity fade. Shortening the relaxation time between cycles positively influenced the lifetime by roughly 40 %, whereas a higher discharging current almost doubled the cell's lifetime.

We applied electrochemical analysis, post-mortem analysis and in-situ neutron diffraction to investigate the underlying degradation mechanisms. The neutron diffraction experiment and differential voltage analysis revealed the loss of lithium inventory as the dominant aging mechanism for both linearly- and nonlinearly-aged cells. Other aging mechanisms, like the structural degradation of anode or cathode active materials or the deactivation of active materials, could not be confirmed. SEM images of uncycled and nonlinearly-aged cells qualitatively showed surface layer growth and morphology changes on the graphite anode, whereas the cathode particles appeared unchanged. The comparison between capacity loss determined by electrochemical analysis and neutron diffraction revealed an increasing capacity loss in the edge area of the electrodes with ongoing aging. We supposed two different dominant

aging mechanisms, which are the growth of the SEI in the early stage and marginal lithium deposition in the later stage. After a few weeks of storage, checkup tests showed both capacity recovery or capacity loss dependent on the SOH as well as the SOC the cells were stored at. Linearly-aged cells that were fully charged for the neutron diffraction experiment revealed a capacity loss of less than $3.0\,\%$, whereas the fully discharged ones pointed out a capacity recovery of less than $3.2\,\%$, owing to lithium diffusion into or out of the anode overhang area, respectively. On the other hand, all nonlinearly-aged cells showed a capacity recovery due to lithium stripping, the partial reversible reaction of lithium deposition, as well as the chemical intercalation of lithium. These results hold true for the investigated cells and the performed aging experiments.

A central part of this thesis is the development of physicochemical side reaction models for SEI re-/formation, lithium plating and lithium stripping, and the development of a physicochemical aging model considering the transition from linear to nonlinear aging. Firstly, we developed an aging model considering SEI re-/formation in the negative electrode. We implemented SEI formation on intact graphite particles as a first side reaction and SEI re-formation due to cracking of the SEI layer caused by the expansion and contraction of the graphite particles during cycling as a second side reaction. Both side reactions are considered to be irreversible and implemented by cathodic Tafel equations. Integrating the side reaction current gives a charge quantity that results in the thickness of the SEI layer. The resistance of the SEI layer is proportional to the thickness and increases over time. It causes an additional overpotential for the main and side reactions. This model simulates the early stage, linear aging of lithium-ion cells. Secondly, we introduced a new SEI modeling approach that distinguishes between the transport of lithium ions, on the one hand, and electrons through the SEI, on the other hand. This is in accordance with the assumption that the SEI possesses two ideal properties – a maximum conductivity for lithium ions (κ_{SEI}) and an insulating conductivity for electrons (σ_{SEI}). The model results in a different ohmic drop for the driving potential of the main intercalation reaction at the negative electrode and the SEI forming reaction. This results in a more accurate representation of the SEI and enables us to differentiate between capacity and power fade. Thirdly, we developed a physicochemical model considering both lithium plating and lithium stripping side reactions. The model simulates reversible lithium plating and the characteristic voltage plateau due to lithium stripping during a subsequent discharge after lithium plating in a previous charge. The side reactions are described by adapted Butler-Volmer equations including a novel approach which considers a correction term for the amount of reversibly plated and stripped lithium. Finally, we developed an electrochemical aging model with SEI formation, SEI re-formation due to cracking of the layer during graphite expansion, lithium plating when the potential of the negative electrode becomes negative vs. Li/Li$^+$, and subsequent lithium stripping once the potential becomes positive again. The model considers the transition from an early stage, linear to a later stage, nonlinear capacity fade.

Outlook

As an outlook, additional aging experiments can be performed on other cell chemistries, designs and formats, testing procedures, and boundary conditions. Especially silicon-graphite anodes and high-voltage cathodes are of interest here. Neutron diffraction should be further used to investigate the inhomogeneous aging while taking into account the inhomogeneous lithium distribution as investigated by Senyshyn, Mühlbauer and co-workers [52; 105; 106] as well as Cai et al. [51].

Similar to the experiments, the developed aging models can be applied to other cell chemistries, designs

and formats, testing procedures, and boundary conditions. The effect of structured electrodes [93] and changing porosities [84] on the aging behavior need to be further investigated based on detailed degradation models. Additionally, the model needs to be incorporated into a multi-dimensional modeling approach [37; 107; 108] to investigate and to get a more thorough understanding of inhomogeneous aging. The modeling of lithium plating and lithium stripping can be extended while taking into account the surface of plated lithium. For this, the detailed knowledge of lithium deposition and dissolution on a microstructure level including dendritic and mossy structures is needed.

Finally, the model can be applied to develop (fast) charging methods [109; 110] while considering the degradation mechanisms and cell limitations to keep the cell in a phase of linear aging. Next to the cell's SOC and temperature, its current SOH, inhomogeneities as well as predicted and subsequent relaxation times and discharging currents may also be taken into account to control the charging current in a battery management system.

List of References

[1] P. Arora. "Capacity Fade Mechanisms and Side Reactions in Lithium-Ion Batteries". In: *Journal of The Electrochemical Society* 145.10 (1998), p. 3647. ISSN: 00134651. DOI: 10.1149/1.1838857.

[2] J. Vetter et al. "Ageing mechanisms in lithium-ion batteries". In: *Journal of Power Sources* 147.1-2 (2005), pp. 269–281. ISSN: 03787753. DOI: 10.1016/j.jpowsour.2005.01.006.

[3] C. R. Birkl, M. R. Roberts, E. McTurk, P. G. Bruce, and D. A. Howey. "Degradation diagnostics for lithium ion cells". In: *Journal of Power Sources* 341 (2017), pp. 373–386. ISSN: 03787753. DOI: 10.1016/j.jpowsour.2016.12.011.

[4] J. S. Edge et al. "Lithium ion battery degradation: what you need to know". In: *Physical chemistry chemical physics : PCCP* 23.14 (2021), pp. 8200–8221. DOI: 10.1039/d1cp00359c.

[5] A. Jossen and W. Weydanz. *Moderne Akkumulatoren richtig einsetzen*. 1. Auflage. Neusäß: Ubooks-Verlag, 2006. ISBN: 3937536019.

[6] J. Garche and C. K. Dyer, eds. *Encyclopedia of electrochemical power sources*. Amsterdam and Boston: Academic Press and Imprint of Elsevier, 2009. ISBN: 978-0-444-52745-5.

[7] B. Scrosati, J. Garche, and W. Tillmetz, eds. *Advances in battery technologies for electric vehicles*. Vol. number 80. Woodhead Publishing in energy. Cambridge, UK: Woodhead Publishing, an imprint of Elsevier, 2015. ISBN: 978-1-78242-377-5.

[8] S. F. Schuster, T. Bach, E. Fleder, J. Müller, M. Brand, G. Sextl, and A. Jossen. "Nonlinear aging characteristics of lithium-ion cells under different operational conditions". In: *Journal of Energy Storage* 1 (2015), pp. 44–53. DOI: 10.1016/j.est.2015.05.003.

[9] S. F. Schuster. "Reuse of Automotive Lithium-Ion Batteries: An Assessment from the Cell Aging Perspective". Dissertation. Technical University of Munich, 2016.

[10] T. C. Bach, S. F. Schuster, E. Fleder, J. Müller, M. J. Brand, H. Lorrmann, A. Jossen, and G. Sextl. "Nonlinear aging of cylindrical lithium-ion cells linked to heterogeneous compression". In: *Journal of Energy Storage* 5 (2016), pp. 212–223. DOI: 10.1016/j.est.2016.01.003.

[11] D. Anseán, M. Dubarry, A. Devie, B. Y. Liaw, V. M. García, J. C. Viera, and M. González. "Operando lithium plating quantification and early detection of a commercial LiFePO 4 cell cycled under dynamic driving schedule". In: *Journal of Power Sources* 356 (2017), pp. 36–46. ISSN: 03787753. DOI: 10.1016/j.jpowsour.2017.04.072.

[12] X.-G. Yang, Y. Leng, G. Zhang, S. Ge, and C.-Y. Wang. "Modeling of lithium plating induced aging of lithium-ion batteries: Transition from linear to nonlinear aging". In: *Journal of Power Sources* 360 (2017), pp. 28–40. ISSN: 03787753. DOI: 10.1016/j.jpowsour.2017.05.110.

[13] T. Waldmann, B. Hogg, and M. Wohlfahrt-Mehrens. "Li plating as unwanted side reaction in commercial Li-ion cells – A review". In: *Journal of Power Sources* 384 (2018), pp. 107–124. ISSN: 03787753. DOI: 10.1016/j.jpowsour.2018.02.063.

[14] N. Paul et al. "Aging in 18650-type Li-ion cells examined with neutron diffraction, electrochemical analysis and physico-chemical modeling". In: *Journal of Energy Storage* 17 (2018), pp. 383–394. DOI: 10.1016/j.est.2018.03.016.

[15] F. M. Kindermann, J. Keil, A. Frank, and A. Jossen. "A SEI Modeling Approach Distinguishing between Capacity and Power Fade". In: *Journal of The Electrochemical Society* 164.12 (2017), E287–E294. ISSN: 00134651. DOI: 10.1149/2.0321712jes.

[16] C. von Lüders, J. Keil, M. Webersberger, and A. Jossen. "Modeling of lithium plating and lithium stripping in lithium-ion batteries". In: *Journal of Power Sources* 414 (2019), pp. 41–47. ISSN: 03787753. DOI: 10.1016/j.jpowsour.2018.12.084.

[17] J. Keil, N. Paul, V. Baran, P. Keil, R. Gilles, and A. Jossen. "Linear and Nonlinear Aging of Lithium-Ion Cells Investigated by Electrochemical Analysis and In-Situ Neutron Diffraction". In: *Journal of The Electrochemical Society* 166.16 (2019), A3908–A3917. ISSN: 00134651. DOI: 10.1149/2.1271915jes.

[18] J. Keil and A. Jossen. "Electrochemical Modeling of Linear and Nonlinear Aging of Lithium-Ion Cells". In: *Journal of The Electrochemical Society* 167.11 (2020), p. 110535. ISSN: 00134651. DOI: 10.1149/1945-7111/aba44f.

[19] V. Agubra and J. Fergus. "Lithium Ion Battery Anode Aging Mechanisms". In: *Materials (Basel, Switzerland)* 6.4 (2013), pp. 1310–1325. ISSN: 1996-1944. DOI: 10.3390/ma6041310.

[20] V. A. Agubra and J. W. Fergus. "The formation and stability of the solid electrolyte interface on the graphite anode". In: *Journal of Power Sources* 268 (2014), pp. 153–162. ISSN: 03787753. DOI: 10.1016/j.jpowsour.2014.06.024.

[21] D. Aurbach. "A short review of failure mechanisms of lithium metal and lithiated graphite anodes in liquid electrolyte solutions". In: *Solid State Ionics* 148.3-4 (2002), pp. 405–416. ISSN: 01672738. DOI: 10.1016/S0167-2738(02)00080-2.

[22] D. Aurbach, B. Markovsky, G. Salitra, E. Markevich, Y. Talyossef, M. Koltypin, L. Nazar, B. Ellis, and D. Kovacheva. "Review on electrode–electrolyte solution interactions, related to cathode materials for Li-ion batteries". In: *Journal of Power Sources* 165.2 (2007), pp. 491–499. ISSN: 03787753. DOI: 10.1016/j.jpowsour.2006.10.025.

[23] M. Broussely, P. Biensan, F. Bonhomme, P. Blanchard, S. Herreyre, K. Nechev, and R. J. Staniewicz. "Main aging mechanisms in Li ion batteries". In: *Journal of Power Sources* 146.1-2 (2005), pp. 90–96. ISSN: 03787753. DOI: 10.1016/j.jpowsour.2005.03.172.

[24] R. Hausbrand, G. Cherkashinin, H. Ehrenberg, M. Gröting, K. Albe, C. Hess, and W. Jaegermann. "Fundamental degradation mechanisms of layered oxide Li-ion battery cathode materials: Methodology, insights and novel approaches". In: *Materials Science and Engineering: B* 192 (2015), pp. 3–25. ISSN: 09215107. DOI: 10.1016/j.mseb.2014.11.014.

[25] P. Verma, P. Maire, and P. Novák. "A review of the features and analyses of the solid electrolyte interphase in Li-ion batteries". In: *Electrochimica Acta* 55.22 (2010), pp. 6332–6341. ISSN: 00134686. DOI: 10.1016/j.electacta.2010.05.072.

[26] T. Waldmann et al. "Review—Post-Mortem Analysis of Aged Lithium-Ion Batteries: Disassembly Methodology and Physico-Chemical Analysis Techniques". In: *Journal of The Electrochemical Society* 163.10 (2016), A2149–A2164. ISSN: 00134651. DOI: 10.1149/2.1211609jes.

[27] E. Peled. "The Electrochemical Behavior of Alkali and Alkaline Earth Metals in Nonaqueous Battery Systems—The Solid Electrolyte Interphase Model". In: *Journal of The Electrochemical Society* 126.12 (1979), p. 2047. ISSN: 00134651. DOI: 10.1149/1.2128859.

[28] J. B. Goodenough and Y. Kim. "Challenges for Rechargeable Li Batteries". In: *Chemistry of Materials* 22.3 (2010), pp. 587–603. ISSN: 0897-4756. DOI: 10.1021/cm901452z.

[29] T. Liu et al. "In situ quantification of interphasial chemistry in Li-ion battery". In: *Nature nanotechnology* 14.1 (2019), pp. 50–56. DOI: 10.1038/s41565-018-0284-y.

[30] N. Legrand, B. Knosp, P. Desprez, F. Lapicque, and S. Raël. "Physical characterization of the charging process of a Li-ion battery and prediction of Li plating by electrochemical modelling". In: *Journal of Power Sources* 245 (2014), pp. 208–216. ISSN: 03787753. DOI: 10.1016/j.jpowsour.2013.06.130.

[31] X.-G. Yang, S. Ge, T. Liu, Y. Leng, and C.-Y. Wang. "A look into the voltage plateau signal for detection and quantification of lithium plating in lithium-ion cells". In: *Journal of Power Sources* 395 (2018), pp. 251–261. ISSN: 03787753. DOI: 10.1016/j.jpowsour.2018.05.073.

[32] S. Tippmann, D. Walper, L. Balboa, B. Spier, and W. G. Bessler. "Low-temperature charging of lithium-ion cells part I: Electrochemical modeling and experimental investigation of degradation behavior". In: *Journal of Power Sources* 252 (2014), pp. 305–316. ISSN: 03787753. DOI: 10.1016/j.jpowsour.2013.12.022.

[33] T. Waldmann, B. Hogg, M. Kasper, S. Grolleau, C. G. Couceiro, K. Trad, B. P. Matadi, and M. Wohlfahrt-Mehrens. "Interplay of Operational Parameters on Lithium Deposition in Lithium-Ion Cells: Systematic Measurements with Reconstructed 3-Electrode Pouch Full Cells". In: *Journal of The Electrochemical Society* 163.7 (2016), A1232–A1238. ISSN: 00134651. DOI: 10.1149/2.0591607jes.

[34] I. D. Campbell, M. Marzook, M. Marinescu, and G. J. Offer. "How Observable Is Lithium Plating? Differential Voltage Analysis to Identify and Quantify Lithium Plating Following Fast Charging of Cold Lithium-Ion Batteries". In: *Journal of The Electrochemical Society* 166.4 (2019), A725–A739. ISSN: 00134651. DOI: 10.1149/2.0821904jes.

[35] B. Rieger, S. Schlueter, S. V. Erhard, and A. Jossen. "Strain Propagation in Lithium-Ion Batteries from the Crystal Structure to the Electrode Level". In: *Journal of The Electrochemical Society* 163.8 (2016), A1595–A1606. ISSN: 00134651. DOI: 10.1149/2.0431608jes.

[36] V. Zinth et al. "Inhomogeneity and relaxation phenomena in the graphite anode of a lithium-ion battery probed by in situ neutron diffraction". In: *Journal of Power Sources* 361 (2017), pp. 54–60. ISSN: 03787753. DOI: 10.1016/j.jpowsour.2017.06.060.

[37] S. V. Erhard. "Mehrdimensionale elektrochemisch-thermische Modellierung von Lithium-Ionen-Batterien". Dissertation. Technical University of Munich, 2017.

[38] V. Zinth, C. von Lüders, M. Hofmann, J. Hattendorff, I. Buchberger, S. Erhard, J. Rebelo-Kornmeier, A. Jossen, and R. Gilles. "Lithium plating in lithium-ion batteries at sub-ambient temperatures investigated by in situ neutron diffraction". In: *Journal of Power Sources* 271 (2014), pp. 152–159. ISSN: 03787753. DOI: 10.1016/j.jpowsour.2014.07.168.

[39] M. Ebner, F. Marone, M. Stampanoni, and V. Wood. "Visualization and quantification of electrochemical and mechanical degradation in Li ion batteries". In: *Science (New York, N.Y.)* 342.6159 (2013), pp. 716–720. DOI: 10.1126/science.1241882.

[40] B. Rieger. "Methodik zur Simulation des mechanischen Verhaltens von Lithium-Ionen-Zellen". Dissertation. Technical University of Munich, 2017.

[41] X. H. Liu, L. Zhong, S. Huang, S. X. Mao, T. Zhu, and J. Y. Huang. "Size-dependent fracture of silicon nanoparticles during lithiation". In: *ACS nano* 6.2 (2012), pp. 1522–1531. DOI: 10. 1021/nn204476h.

[42] P. Harks, F. M. Mulder, and P. Notten. "In situ methods for Li-ion battery research: A review of recent developments". In: *Journal of Power Sources* 288 (2015), pp. 92–105. ISSN: 03787753. DOI: 10.1016/j.jpowsour.2015.04.084.

[43] N. Paul, J. Wandt, S. Seidlmayer, S. Schebesta, M. J. Mühlbauer, O. Dolotko, H. A. Gasteiger, and R. Gilles. "Aging behavior of lithium iron phosphate based 18650-type cells studied by in situ neutron diffraction". In: *Journal of Power Sources* 345 (2017), pp. 85–96. ISSN: 03787753. DOI: 10.1016/j.jpowsour.2017.01.134.

[44] J. Wandt, C. Marino, H. A. Gasteiger, P. Jakes, R.-A. Eichel, and J. Granwehr. "Operando electron paramagnetic resonance spectroscopy – formation of mossy lithium on lithium anodes during charge–discharge cycling". In: *Energy & Environmental Science* 8.4 (2015), pp. 1358–1367. ISSN: 1754-5692. DOI: 10.1039/C4EE02730B.

[45] M. Dubarry, C. Truchot, and B. Y. Liaw. "Synthesize battery degradation modes via a diagnostic and prognostic model". In: *Journal of Power Sources* 219 (2012), pp. 204–216. ISSN: 03787753. DOI: 10.1016/j.jpowsour.2012.07.016.

[46] C. Pastor-Fernández, K. Uddin, G. H. Chouchelamane, W. D. Widanage, and J. Marco. "A Comparison between Electrochemical Impedance Spectroscopy and Incremental Capacity-Differential Voltage as Li-ion Diagnostic Techniques to Identify and Quantify the Effects of Degradation Modes within Battery Management Systems". In: *Journal of Power Sources* 360 (2017), pp. 301–318. ISSN: 03787753. DOI: 10.1016/j.jpowsour.2017.03.042.

[47] P. Keil. "Aging of Lithium-Ion Batteries in Electric Vehicles". Dissertation. Technical University of Munich, 2017.

[48] M. Wetjen, M. Trunk, L. Werner, R. Gernhäuser, B. Märkisch, Z. Révay, R. Gilles, and H. A. Gasteiger. "Quantifying the Distribution of Electrolyte Decomposition Products in Silicon-Graphite Electrodes by Neutron Depth Profiling". In: *Journal of The Electrochemical Society* 165.10 (2018), A2340–A2348. ISSN: 00134651. DOI: 10.1149/2.1341810jes.

[49] O. Dolotko, A. Senyshyn, M. J. Mühlbauer, K. Nikolowski, F. Scheiba, and H. Ehrenberg. "Fatigue Process in Li-Ion Cells: An In Situ Combined Neutron Diffraction and Electrochemical Study". In: *Journal of The Electrochemical Society* 159.12 (2012), A2082–A2088. ISSN: 00134651. DOI: 10.1149/2.080212jes.

[50] S. Shiotani, T. Naka, M. Morishima, M. Yonemura, T. Kamiyama, Y. Ishikawa, Y. Ukyo, Y. Uchimoto, and Z. Ogumi. "Degradation analysis of 18650-type lithium-ion cells by operando neutron diffraction". In: *Journal of Power Sources* 325 (2016), pp. 404–409. ISSN: 03787753. DOI: 10.1016/j.jpowsour.2016.06.026.

[51] L. Cai, K. An, Z. Feng, C. Liang, and S. J. Harris. "In-situ observation of inhomogeneous degradation in large format Li-ion cells by neutron diffraction". In: *Journal of Power Sources* 236 (2013), pp. 163–168. ISSN: 03787753. DOI: 10.1016/j.jpowsour.2013.02.066.

[52]   M. J. Mühlbauer, O. Dolotko, M. Hofmann, H. Ehrenberg, and A. Senyshyn. "Effect of fatigue/ageing on the lithium distribution in cylinder-type Li-ion batteries". In: *Journal of Power Sources* 348 (2017), pp. 145–149. ISSN: 03787753. DOI: `10.1016/j.jpowsour.2017.02.077`.

[53]   C. von Lüders, V. Zinth, S. V. Erhard, P. J. Osswald, M. Hofmann, R. Gilles, and A. Jossen. "Lithium plating in lithium-ion batteries investigated by voltage relaxation and in situ neutron diffraction". In: *Journal of Power Sources* 342 (2017), pp. 17–23. ISSN: 03787753. DOI: `10.1016/j.jpowsour.2016.12.032`.

[54]   V. Ramadesigan, P. W. C. Northrop, S. De, S. Santhanagopalan, R. D. Braatz, and V. R. Subramanian. "Modeling and Simulation of Lithium-Ion Batteries from a Systems Engineering Perspective". In: *Journal of The Electrochemical Society* 159.3 (2012), R31–R45. ISSN: 00134651. DOI: `10.1149/2.018203jes`.

[55]   A. Jokar, B. Rajabloo, M. Désilets, and M. Lacroix. "Review of simplified Pseudo-two-Dimensional models of lithium-ion batteries". In: *Journal of Power Sources* 327 (2016), pp. 44–55. ISSN: 03787753. DOI: `10.1016/j.jpowsour.2016.07.036`.

[56]   M. Armand and J.-M. Tarascon. "Building better batteries". In: *Nature* 451.7179 (2008), pp. 652–657. ISSN: 1476-4687. DOI: `10.1038/451652a`. URL: `https://www.nature.com/articles/451652a`.

[57]   Alejandro A. Franco. "Multiscale modelling and numerical simulation of rechargeable lithium ion batteries: concepts, methods and challenges". In: *RSC Advances* 3.32 (2013), pp. 13027–13058. DOI: `10.1039/C3RA23502E`.

[58]   C. Menictas, M. Skyllas-Kazacos, and T. M. Lim. *Advances in Batteries for Medium and Large-Scale Energy Storage*. Vol. 67. Woodhead Publishing Series in Energy. Amsterdam: Elsevier Science, 2015. ISBN: 9781782420224. URL: `http://gbv.eblib.com/patron/FullRecord.aspx?p=1901693`.

[59]   A. A. Franco, M. L. Doublet, and W. G. Bessler, eds. *Physical Multiscale Modeling and Numerical Simulation of Electrochemical Devices for Energy Conversion and Storage*. Green Energy and Technology. London: Springer London, 2016. ISBN: 978-1-4471-5676-5. DOI: `10.1007/978-1-4471-5677-2`.

[60]   M. Doyle. "Modeling of Galvanostatic Charge and Discharge of the Lithium/Polymer/Insertion Cell". In: *Journal of The Electrochemical Society* 140.6 (1993), p. 1526. ISSN: 00134651. DOI: `10.1149/1.2221597`.

[61]   T. F. Fuller. "Simulation and Optimization of the Dual Lithium Ion Insertion Cell". In: *Journal of The Electrochemical Society* 141.1 (1994), pp. 1–10. ISSN: 00134651. DOI: `10.1149/1.2054684`.

[62]   M. Doyle. "Design and Simulation of Lithium Rechargeable Batteries". Dissertation. University of California, Berkeley, 1995. URL: `http://escholarship.org/uc/item/6j87z0sp#`.

[63]   J. S. Newman and K. E. Thomas-Alyea. *Electrochemical systems*. 3rd ed. Hoboken, N.J.: J. Wiley, 2004. ISBN: 978-0-471-47756-3.

[64]   J. Newman and W. Tiedemann. "Porous-electrode theory with battery applications". In: *AIChE Journal* 21.1 (1975), pp. 25–41. ISSN: 0001-1541. DOI: `10.1002/aic.690210103`.

[65]   Dong Zhang, Branko N. Popov, and Ralph E. White. "Modeling Lithium Intercalation of a Single Spinel Particle under Potentiodynamic Control". In: *Journal of The Electrochemical Society* 147.3 (2000), p. 831. ISSN: 00134651. DOI: `10.1149/1.1393279`. URL: `https://iopscience.iop.org/article/10.1149/1.1393279`.

[66]   Kristen A. Severson et al. "Data-driven prediction of battery cycle life before capacity degradation". In: *Nature Energy* 4.5 (2019), pp. 383–391. ISSN: 2058-7546. DOI: 10.1038/s41560-019-0356-8. URL: https://www.nature.com/articles/s41560-019-0356-8.

[67]   Peter M. Attia et al. "Closed-loop optimization of fast-charging protocols for batteries with machine learning". In: *Nature* 578.7795 (2020), pp. 397–402. ISSN: 1476-4687. DOI: 10.1038/s41586-020-1994-5. URL: https://www.nature.com/articles/s41586-020-1994-5.

[68]   J. Jia, J. Liang, Y. Shi, J. Wen, X. Pang, and J. Zeng. "SOH and RUL Prediction of Lithium-Ion Batteries Based on Gaussian Process Regression with Indirect Health Indicators". In: *Energies* 13.2 (2020), p. 375. DOI: 10.3390/en13020375.

[69]   B. Wu, W. D. Widanage, S. Yang, and X. Liu. "Battery digital twins: Perspectives on the fusion of models, data and artificial intelligence for smart battery management systems". In: *Energy and AI* 1 (2020), p. 100016. ISSN: 26665468. DOI: 10.1016/j.egyai.2020.100016.

[70]   Darius Roman, Saurabh Saxena, Valentin Robu, Michael Pecht, and David Flynn. "Machine learning pipeline for battery state-of-health estimation". In: *Nature Machine Intelligence* 3.5 (2021), pp. 447–456. ISSN: 2522-5839. DOI: 10.1038/s42256-021-00312-3. URL: https://www.nature.com/articles/s42256-021-00312-3.

[71]   Chinedu I. Ossai and Ifeanyi P. Egwutuoha. "Real-time state-of-health monitoring of lithium-ion battery with anomaly detection, Levenberg–Marquardt algorithm, and multiphase exponential regression model". In: *Neural Computing and Applications* 33.4 (2021), pp. 1193–1206. ISSN: 1433-3058. DOI: 10.1007/s00521-020-05031-1. URL: https://link.springer.com/article/10.1007/s00521-020-05031-1.

[72]   P. Arora. "Mathematical Modeling of the Lithium Deposition Overcharge Reaction in Lithium-Ion Batteries Using Carbon-Based Negative Electrodes". In: *Journal of The Electrochemical Society* 146.10 (1999), p. 3543. ISSN: 00134651. DOI: 10.1149/1.1392512.

[73]   M. Doyle. "Comparison of Modeling Predictions with Experimental Data from Plastic Lithium Ion Cells". In: *Journal of The Electrochemical Society* 143.6 (1996), p. 1890. ISSN: 00134651. DOI: 10.1149/1.1836921.

[74]   M. Safari, M. Morcrette, A. Teyssot, and C. Delacourt. "Multimodal Physics-Based Aging Model for Life Prediction of Li-Ion Batteries". In: *Journal of The Electrochemical Society* 156.3 (2009), A145. ISSN: 00134651. DOI: 10.1149/1.3043429.

[75]   S. Hein, M. Petzl, M. Danzer, and A. Latz. "Simulation of lithium plating and Stripping during low temperature Operation of Li-ion battery". In: *UECT 2014* (2014).

[76]   S. Hein and A. Latz. "Lithium Plating and Stripping in the Framework of a 3D Electrochemical Model". In: *ECS Transactions* 69.1 (2015), pp. 3–5. ISSN: 1938-6737. DOI: 10.1149/06901.0003ecst.

[77]   S. Hein and A. Latz. "Influence of local lithium metal deposition in 3D microstructures on local and global behavior of Lithium-ion batteries". In: *Electrochimica Acta* 201 (2016), pp. 354–365. ISSN: 00134686. DOI: 10.1016/j.electacta.2016.01.220.

[78]   M. Tang, P. Albertus, and J. Newman. "Two-Dimensional Modeling of Lithium Deposition during Cell Charging". In: *Journal of The Electrochemical Society* 156.5 (2009), A390. ISSN: 00134651. DOI: 10.1149/1.3095513.

[79] I. Laresgoiti, S. Käbitz, M. Ecker, and D. U. Sauer. "Modeling mechanical degradation in lithium ion batteries during cycling: Solid electrolyte interphase fracture". In: *Journal of Power Sources* 300 (2015), pp. 112–122. ISSN: 03787753. DOI: 10.1016/j.jpowsour.2015.09.033.

[80] H. Ge, T. Aoki, N. Ikeda, S. Suga, T. Isobe, Z. Li, Y. Tabuchi, and J. Zhang. "Investigating Lithium Plating in Lithium-Ion Batteries at Low Temperatures Using Electrochemical Model with NMR Assisted Parameterization". In: *Journal of The Electrochemical Society* 164.6 (2017), A1050–A1060. ISSN: 00134651. DOI: 10.1149/2.0461706jes.

[81] D. Ren, K. Smith, D. Guo, X. Han, X. Feng, L. Lu, M. Ouyang, and J. Li. "Investigation of Lithium Plating-Stripping Process in Li-Ion Batteries at Low Temperature Using an Electrochemical Model". In: *Journal of The Electrochemical Society* 165.10 (2018), A2167–A2178. ISSN: 00134651. DOI: 10.1149/2.0661810jes.

[82] S. Xu, K.-H. Chen, N. P. Dasgupta, J. B. Siegel, and A. G. Stefanopoulou. "Evolution of Dead Lithium Growth in Lithium Metal Batteries: Experimentally Validated Model of the Apparent Capacity Loss". In: *Journal of The Electrochemical Society* 166.14 (2019), A3456–A3463. ISSN: 00134651. DOI: 10.1149/2.0991914jes.

[83] X. Zhao, Y. Yin, Y. Hu, and S.-Y. Choe. "Electrochemical-thermal modeling of lithium plating/stripping of Li(Ni0.6Mn0.2Co0.2)O2/Carbon lithium-ion batteries at subzero ambient temperatures". In: *Journal of Power Sources* 418 (2019), pp. 61–73. ISSN: 03787753. DOI: 10.1016/j.jpowsour.2019.02.001.

[84] D. Müller, T. Dufaux, and K. P. Birke. "Model-Based Investigation of Porosity Profiles in Graphite Anodes Regarding Sudden-Death and Second-Life of Lithium Ion Cells". In: *Batteries* 5.2 (2019), p. 49. DOI: 10.3390/batteries5020049.

[85] Sanyo. *UR18650E Datasheet.*

[86] M. Winter, J. O. Besenhard, M. E. Spahr, and P. Novák. "Insertion Electrode Materials for Rechargeable Lithium Batteries". In: *Advanced Materials* 10.10 (1998), pp. 725–763. ISSN: 0935-9648. DOI: https://doi.org/10.1002/(SICI)1521-4095(199807)10:10<725::AID-ADMA725>3.0.CO;2-Z.

[87] R. Gilles, B. Krimmer, H. Boysen, and H. Fuess. "Status of the new structure powder diffractometer (SPODI) at the FRM-II in Garching". In: *Applied Physics A: Materials Science & Processing* 74.0 (2002), s148–s150. ISSN: 0947-8396. DOI: 10.1007/s003390201739.

[88] M. Hoelzel, A. Senyshyn, N. Juenke, H. Boysen, W. Schmahl, and H. Fuess. "High-resolution neutron powder diffractometer SPODI at research reactor FRM II". In: *Nuclear Instruments and Methods in Physics Research Section A: Accelerators, Spectrometers, Detectors and Associated Equipment* 667 (2012), pp. 32–37. ISSN: 01689002. DOI: 10.1016/j.nima.2011.11.070.

[89] M. Hoelzel, A. Senyshyn, and O. Dolotko. "SPODI: High resolution powder diffractometer". In: *Journal of large-scale research facilities JLSRF* 1 (2015). DOI: 10.17815/jlsrf-1-24.

[90] Heinz Maier-Leibnitz Zentrum. *SPODI - High resolution powder diffractometer.* 2021-04-28. URL: https://mlz-garching.de/spodi (visited on 04/28/2021).

[91] P. Thompson, D. E. Cox, and J. B. Hastings. "Rietveld refinement of Debye–Scherrer synchrotron X-ray data from Al 2 O 3". In: *Journal of Applied Crystallography* 20.2 (1987), pp. 79–83. ISSN: 0021-8898. DOI: 10.1107/S0021889887087090.

[92]   T. Roisnel and J. Rodríquez-Carvajal. "WinPLOTR: A Windows Tool for Powder Diffraction Pattern Analysis". In: *Materials Science Forum* 378-381 (2001), pp. 118–123. DOI: 10.4028/www.scientific.net/MSF.378-381.118.

[93]   F. M. Kindermann. "Implications of Current Density Distribution in Lithium-Ion Battery Graphite Anodes on SEI Formation". Dissertation. Technical University of Munich, 2017.

[94]   A. Jokar, B. Rajabloo, M. Désilets, and M. Lacroix. "An Inverse Method for Estimating the Electrochemical Parameters of Lithium-Ion Batteries". In: *Journal of The Electrochemical Society* 163.14 (2016), A2876–A2886. ISSN: 00134651. DOI: 10.1149/2.0191614jes.

[95]   D. A. G. Bruggeman. "Berechnung verschiedener physikalischer Konstanten von heterogenen Substanzen. I. Dielektrizitätskonstanten und Leitfähigkeiten der Mischkörper aus isotropen Substanzen". In: *Annalen der Physik* 416.7 (1935), pp. 636–664. ISSN: 00033804. DOI: 10.1002/andp.19354160705.

[96]   L. O. Valoen and J. N. Reimers. "Transport Properties of LiPF[sub 6]-Based Li-Ion Battery Electrolytes". In: *Journal of The Electrochemical Society* 152.5 (2005), A882. ISSN: 00134651. DOI: 10.1149/1.1872737.

[97]   *COMSOL Multiphysics*. 2021-05-24. URL: https://www.comsol.de/comsol-multiphysics (visited on 05/24/2021).

[98]   *MathWorks MATLAB*. 2021-05-24. URL: https://de.mathworks.com/products/matlab.html (visited on 05/24/2021).

[99]   *COMSOL LiveLink*. 2021-05-24. URL: https://www.comsol.de/livelink-for-matlab (visited on 05/24/2021).

[100] I. Buchberger, S. Seidlmayer, A. Pokharel, M. Piana, J. Hattendorff, P. Kudejova, R. Gilles, and H. A. Gasteiger. "Aging Analysis of Graphite/LiNi 1/3 Mn 1/3 Co 1/3 O 2 Cells Using XRD, PGAA, and AC Impedance". In: *Journal of The Electrochemical Society* 162.14 (2015), A2737–A2746. ISSN: 00134651. DOI: 10.1149/2.0721514jes.

[101] M. Ecker, N. Nieto, S. Käbitz, J. Schmalstieg, H. Blanke, A. Warnecke, and D. U. Sauer. "Calendar and cycle life study of Li(NiMnCo)O2-based 18650 lithium-ion batteries". In: *Journal of Power Sources* 248 (2014), pp. 839–851. ISSN: 03787753. DOI: 10.1016/j.jpowsour.2013.09.143.

[102] K. Kleiner, P. Jakes, S. Scharner, V. Liebau, and H. Ehrenberg. "Changes of the balancing between anode and cathode due to fatigue in commercial lithium-ion cells". In: *Journal of Power Sources* 317 (2016), pp. 25–34. ISSN: 03787753. DOI: 10.1016/j.jpowsour.2016.03.049.

[103] J. Wilhelm, S. Seidlmayer, P. Keil, J. Schuster, A. Kriele, R. Gilles, and A. Jossen. "Cycling capacity recovery effect: A coulombic efficiency and post-mortem study". In: *Journal of Power Sources* 365 (2017), pp. 327–338. ISSN: 03787753. DOI: 10.1016/j.jpowsour.2017.08.090.

[104] K. Xu. "Nonaqueous Liquid Electrolytes for Lithium-Based Rechargeable Batteries". In: *Chemical Reviews* 104.10 (2004), pp. 4303–4418. ISSN: 0009-2665. DOI: 10.1021/cr030203g.

[105] A. Senyshyn, M. J. Mühlbauer, O. Dolotko, M. Hofmann, and H. Ehrenberg. "Homogeneity of lithium distribution in cylinder-type Li-ion batteries". In: *Scientific reports* 5 (2015), p. 18380. DOI: 10.1038/srep18380.

[106] M. J. Mühlbauer, D. Petz, V. Baran, O. Dolotko, M. Hofmann, R. Kostecki, and A. Senyshyn. "Inhomogeneous distribution of lithium and electrolyte in aged Li-ion cylindrical cells". In: *Journal of Power Sources* 475 (2020), p. 228690. ISSN: 03787753. DOI: 10.1016/j.jpowsour.2020.228690.

[107] J. Sturm, A. Rheinfeld, I. Zilberman, F. B. Spingler, S. Kosch, F. Frie, and A. Jossen. "Modeling and simulation of inhomogeneities in a 18650 nickel-rich, silicon-graphite lithium-ion cell during fast charging". In: *Journal of Power Sources* 412 (2019), pp. 204–223. ISSN: 03787753. DOI: 10.1016/j.jpowsour.2018.11.043.

[108] J. Sturm, A. Frank, A. Rheinfeld, S. V. Erhard, and A. Jossen. "Impact of Electrode and Cell Design on Fast Charging Capabilities of Cylindrical Lithium-Ion Batteries". In: *Journal of The Electrochemical Society* 167.13 (2020), p. 130505. ISSN: 00134651. DOI: 10.1149/1945-7111/abb40c.

[109] T. Waldmann, M. Kasper, and M. Wohlfahrt-Mehrens. "Optimization of Charging Strategy by Prevention of Lithium Deposition on Anodes in high-energy Lithium-ion Batteries – Electrochemical Experiments". In: *Electrochimica Acta* 178 (2015), pp. 525–532. ISSN: 00134686. DOI: 10.1016/j.electacta.2015.08.056.

[110] C. von Lüders. "Experimentelle und simulative Untersuchung von Lithium-Plating und Lithium-Stripping in Lithium-Ionen-Zellen". Dissertation. Technical University of Munich, 2019.

List of Publications

1. Frank M. Kindermann, **Jonas Keil**, Alexander Frank, Andreas Jossen: A SEI Modeling Approach Distinguishing between Capacity and Power Fade. In: *Journal of The Electrochemical Society* 164 (12), E287–E294, 2017.

2. Neelima Paul, **Jonas Keil**, Frank M. Kindermann, Sebastian Schebesta, Oleksandr Dolotko, Martin J. Mühlbauer, Ludwig Kraft, Simon V. Erhard, Andreas Jossen, Ralph Gilles: Aging in 18650-type Li-ion cells examined with neutron diffraction, electrochemical analysis and physicochemical modeling. In: *Journal of Energy Storage* 17, 383–394, 2018.

3. Katharina Rumpf, Alexander Rheinfeld, Markus Schindler, **Jonas Keil**, Tobias Schua, Andreas Jossen: Influence of Cell-to-Cell Variations on the Inhomogeneity of Lithium-Ion Battery Modules. In: *Journal of The Electrochemical Society* 165 (11), A2587–A2607, 2018.

4. Christian von Lüders, **Jonas Keil**, Markus Webersberger, Andreas Jossen: Modeling of lithium plating and lithium stripping in lithium-ion batteries. In: *Journal of Power Sources* 414, 41–47, 2019.

5. **Jonas Keil**, Neelima Paul, Volodymyr Baran, Peter Keil, Ralph Gilles, Andreas Jossen: Linear and Nonlinear Aging of Lithium-Ion Cells Investigated by Electrochemical Analysis and In-Situ Neutron Diffraction. In: *Journal of The Electrochemical Society* 166 (16), A3908-A3917, 2019.

6. **Jonas Keil**, Andreas Jossen: Electrochemical Modeling of Linear and Nonlinear Aging of Lithium-Ion Cells. In: *Journal of The Electrochemical Society* 167, 110535, 2020.